

**DYNAMIC CHARACTERIZATION OF A MAGNETO-RHEOLOGICAL FLUID
DAMPER AND SYNTHESIS OF A SEMI-ACTIVE SUSPENSION SEAT**

Xiao Qing Ma

A Thesis

in

the Department

of

Mechanical and Industrial Engineering

Presented in Partial Fulfillment of the Requirements
for the Degree of Doctor of Philosophy at
Concordia University
Montréal, Québec, Canada

September 2006

© Xiao Qing Ma, 2006



Library and
Archives Canada

Bibliothèque et
Archives Canada

Published Heritage
Branch

Direction du
Patrimoine de l'édition

395 Wellington Street
Ottawa ON K1A 0N4
Canada

395, rue Wellington
Ottawa ON K1A 0N4
Canada

Your file Votre référence

ISBN: 978-0-494-23842-4

Our file Notre référence

ISBN: 978-0-494-23842-4

NOTICE:

The author has granted a non-exclusive license allowing Library and Archives Canada to reproduce, publish, archive, preserve, conserve, communicate to the public by telecommunication or on the Internet, loan, distribute and sell theses worldwide, for commercial or non-commercial purposes, in microform, paper, electronic and/or any other formats.

The author retains copyright ownership and moral rights in this thesis. Neither the thesis nor substantial extracts from it may be printed or otherwise reproduced without the author's permission.

AVIS:

L'auteur a accordé une licence non exclusive permettant à la Bibliothèque et Archives Canada de reproduire, publier, archiver, sauvegarder, conserver, transmettre au public par télécommunication ou par l'Internet, prêter, distribuer et vendre des thèses partout dans le monde, à des fins commerciales ou autres, sur support microforme, papier, électronique et/ou autres formats.

L'auteur conserve la propriété du droit d'auteur et des droits moraux qui protègent cette thèse. Ni la thèse ni des extraits substantiels de celle-ci ne doivent être imprimés ou autrement reproduits sans son autorisation.

In compliance with the Canadian Privacy Act some supporting forms may have been removed from this thesis.

Conformément à la loi canadienne sur la protection de la vie privée, quelques formulaires secondaires ont été enlevés de cette thèse.

While these forms may be included in the document page count, their removal does not represent any loss of content from the thesis.

Bien que ces formulaires aient inclus dans la pagination, il n'y aura aucun contenu manquant.


Canada

ABSTRACT

DYNAMIC CHARACTERIZATION OF A MAGNETO-RHEOLOGICAL FLUID DAMPER AND SYNTHESIS OF A SEMI-ACTIVE SUSPENSION SEAT

Xiao Qing Ma, Ph. D.
Concordia University, 2006

From the point of view of suspension damper, semi-active dampers with only minimal power requirement could be applied to achieve variable damping to enhance suspension performance under complex vibration and shock environments. Magneto-rheological (MR) fluid based dampers offer significant potential for realizing semi-actively controlled variable damping with only minimal power. The MR-fluid dampers invariably exhibit considerable hysteresis, while the damping force varies with the intensity of applied electro-magnetic field and the nature of vibration in a highly nonlinear manner. A simulation model based on symmetric and asymmetric sigmoid functions is developed to fully characterize the properties of a MR-damper as function of excitation and control current. A comprehensive laboratory test program is undertaken to characterize the damping properties of a MR damper under wide ranges of excitations and control current. The essential fundamental features are identified for the modeling task, while the model parameters are identified using multi-parameter error minimization techniques. The validity of the proposed generic model is thoroughly examined by comparing the model response with the measured data under a wide range of excitations, particularly the force saturation and the hysteresis behaviour. An independent current function is further derived that could be integrated to reported regression-based hysteresis models to enhance their prediction abilities. From the results of the study, it is concluded that the refined Bouc-Wen and the proposed generalized sigmoid function model can

fully characterized the nonlinear MR damping behaviour as function of applied current and excitation.

A nonlinear analytical model of a pneumatic suspension seat including the motion limiting stops is developed for synthesis and analyses of the MR-damping control algorithms. The validity of the passive suspension seat model is thoroughly examined under various deterministic and random vibration excitations of varying intensities. The results suggest that attenuation of shock as well as vibration imposes difficulties design compromise of the passive damper. Owing to the strongly nonlinear properties of the suspension-seat and the MR-damper, such as hysteresis, saturation and end-stop impacts, a 'hi-lo' semi-active control algorithm is synthesized to realized modulation of the control current and thus the damping force following the skyhook control law. A continuous modulation function is further synthesized and integrated to ensure smooth transition between the 'hi' and 'lo' states. A relative position control is further introduced to limit the frequency and severity of shock motions caused by end-stop impacts. A set of performance measures is proposed to assess the characteristics of the semi-active and the resulting integrated controller under a wide range of excitations, including deterministic excitations of continuous and transient nature and random excitations of different vehicles. The potential performance benefits of the controller design are further investigated through a hardware-in-the-loop test and simulation program. The results are used to demonstrate the validity of the MR-damper and suspension seat models, and effectiveness of the control algorithm.

ACKNOWLEDGEMENTS

The author is sincerely grateful to her supervisors, Dr. Subhash Rakheja and Dr. Chun–Yi Su, for their initiation of the project and their constant guidance and dedication throughout the thesis work. Their valuable advice and contributions have helped to realize this dissertation results.

The author would like to acknowledge the technical support provided by Mr. Danius Juras and Mr. José Esteves in realizing the experimental setups. The assistance provided by Mr. Cédric Boudinet in formulating the HIL platform is further appreciated. The author thanks her colleague, Dr. Enrong Wang, for his encouragement and collaborations.

Financial support provided by the Institut de recherche en santé et en sécurité du travail du Quebec (IRSST) scholarship, FCAR scholarship, Concordia External Grant Holder Doctoral Scholarship and NSERC-CHRP grant are gratefully acknowledged.

Finally, the author would like to dedicate this thesis to her dear daughter, Jessie Zheng.

TABLE OF CONTENTS

TABLE OF CONTENTS.....	VI
LIST OF FIGURES	XI
LIST OF TABLES.....	XIX
NOMENCLATURE.....	XX
CHAPTER 1 INTRODUCTION AND LITERATURE REVIEW.....	1
1.1 Introduction.....	1
1.2 Review of Relevant Literature.....	4
1.2.1 Effects of Whole-body Vibration (WBV) and Shocks.....	5
1.2.2 Control of Whole-body Vibration and Shock.....	6
1.2.3 Suspension Seat System.....	7
1.2.4 Active and Semi-active Suspensions	12
1.2.5 Semi-active and Active Suspension Seats.....	15
1.2.6 MR/ER-fluids Suspension	18
1.2.7 Performance Analysis of Suspension Seats	25
1.3 Scope and Objectives of the Dissertation Research.....	27
1.3.1 Objectives of the Dissertation Research	29
1.4 Organization of the Dissertation	30
CHAPTER 2 CHARACTERIZATION AND MODELING THE HYSTERETIC PROPERTIES OF A MR-FLUID DAMPER.....	33
2.1 Introduction.....	33
2.2 Characterization of Damping Properties.....	36
2.2.1 Experimental Methodology	36
2.2.2 Force-velocity and Force-displacement Characteristics	39
2.3 Synthesis of a Generalized Sigmoid Model.....	43

2.3.1	Generalized Characteristic Parameters	44
2.3.2	Synthesis of the Characteristic Curves	45
2.3.3	Influence of Control Current.....	47
2.3.4	Synthesis of the Overall Model.....	55
2.4	Model Validation.....	56
2.5	Summary	61
CHAPTER 3 DEVELOPMENT AND RELATIVE ASSESSMENTS OF CURRENT DEPENDENT HYSTERESIS MODELS		63
3.1	Introduction.....	63
3.2	Critical Review of Reported Models	64
3.3	MR-Damper Properties and Modeling Considerations.....	66
3.4	Current Dependent Hysteresis --- A Generalized Model Structure.....	69
3.5	Generalized Model Structure Implementation.....	70
3.5.1	Nonlinear Hysteretic Biviscous Model [102]	71
3.5.2	Polynomial Function Model [77].....	74
3.5.3	Extended Bouc-Wen Hysteresis Model [73].....	75
3.5.4	Generalized Sigmoid Hysteretic Model.....	78
3.6	Parameters Identification	79
3.7	Relative Assessments of Proposed Modified Models.....	82
3.8	Errors Analysis.....	92
3.9	Summary	101
CHAPTER 4 MODELING AND ANALYSE OF A PASSIVE SUSPENSION SEAT		103
4.1	Introduction.....	103
4.2	Model Development.....	107
4.2.1	Nonlinear Cushion Model.....	108

4.2.2	Suspension Forces.....	114
4.3	Excitation Signals	118
4.3.1	Vehicular Vertical Vibration.....	119
4.4	Suspension Seat Model Validation.....	122
4.4.1	Deterministic Excitations.....	122
4.4.2	Random Vehicular Excitations.....	125
4.5	Performance Criteria.....	126
4.6	Damping Requirements of Suspension Seats	128
4.6.1	Low Frequency Vehicular Vibration	130
4.6.2	High Frequency Vehicular Vibration	137
4.6.3	Acceleration Transmissibility	139
4.6.4	Transient Excitation	140
4.7	Discussions	143
CHAPTER 5	SYNTHESIS AND ANALYSES OF THE SEMI-ACTIVE SUSPENSION SEAT CONTROLLERS	146
5.1	Introduction.....	146
5.2	Development of the Suspension Seat with MR Damper	148
5.3	Responses of MR Suspension Seat under Constant Currents.....	149
5.3.1	Harmonic Excitations.....	150
5.3.2	Transient Excitations.....	152
5.3.3	Vehicular Excitations	156
5.3.4	Influences of MR-damper Hysteresis	157
5.4	Formulation of Controller Synthesis.....	160
5.4.1	Control Algorithm.....	161
5.5	Response Characteristics of Suspension Seat with ‘hi-lo’ Control.....	166
5.5.1	Harmonic Excitations.....	166

5.5.2	Transient Excitations.....	169
5.5.3	Vehicular Excitations	174
5.6	Integrated End-stop Impact Control (IC).....	178
5.6.1	Formulation of the Control Algorithm.....	179
5.7	Response Characteristics of MR-suspension Seat with Integrated Control...181	
5.7.1	Harmonic Excitations.....	181
5.7.2	Transient Excitations.....	186
5.7.3	Vehicular Excitations	195
5.8	Summary.....	201
CHAPTER 6	HARDWARE-IN-THE-LOOP TEST AND ANALYSES	203
6.1	Introduction.....	203
6.2	Development of the Hardware-in-the-loop Test and Simulation Platform	205
6.2.1	Description of HIL Test System.....	205
6.2.2	Design of the Digital Damper Power Supply (DPS)	209
6.2.3	dSPACE Communication and Interface Window Design.....	210
6.3	Experiment Methodology	213
6.3.1	Excitation Signals and Control Methods	213
6.4	Responses to Harmonic Excitations.....	215
6.4.1	Constant Current Inputs	215
6.4.2	Semi-active Damping.....	218
6.5	Responses to Transient Excitations.....	222
6.5.1	Constant Current Inputs	222
6.5.2	Semi-active Damping.....	224
6.6	Responses to Vehicular Excitations	228
6.6.1	Constant Current Inputs	228

6.6.2	Semi-active Damping.....	229
6.7	Summary.....	233
CHAPTER 7	CONCLUSIONS AND RECOMMENDATIONS FOR FUTURE WORK.....	235
7.1	Highlights and Major Contributions of the Study.....	235
7.2	Major Conclusions.....	239
7.3	Recommendations for Further Studies.....	241
REFERENCES	243

LIST OF FIGURES

Figure 1.1:	Cross linkage mechanism of seat suspension.	9
Figure 1.2:	Schematics of passive, active and semi-active suspensions.	12
Figure 1.3:	Schematic configuration of the test MR damper.....	20
Figure 2.1:	A pictorial view of the MR damper test system (1-Servo-controller; 2-Data acquisition; 3-DC power supply; 4-Temperature monitor; 5-Force transducer; 6-MR-damper; 7-Hydraulic actuator).	37
Figure 2.2:	Time-history of response and excitation under a harmonic excitation ($A_r = 6.25$ mm; $f_r = 2.5$ Hz; and $i = 0.50$ A).	40
Figure 2.3:	Measured damper responses as functions of applied current under a harmonic excitation ($A_r = 6.25$ mm; and $f_r = 2.5$ Hz).	41
Figure 2.4:	Force-velocity characteristics as functions of: (a) applied current, $A_r = 6.35$ mm, $f_r = 7.5$ Hz; and (b) frequency, $A_r = 6.35$ mm, $i = 0.75$ A.	41
Figure 2.5:	Generalized hysteretic f - v characteristics.....	44
Figure 2.6:	Measured transition force f_t as a function of i and v_m	46
Figure 2.7:	Variations in high velocity slope β_h with i and v_m	50
Figure 2.8:	Variations in low velocity slope β_l with i and v_m	52
Figure 2.9:	Variations in zero-force velocity intercept v_h with i and v_m	54
Figure 2.10:	Comparison of simulation results with the measured data under different operating conditions: (a) $A_r = 2.54$ mm, $f_r = 0.5$ Hz; (b) $A_r = 6.35$ mm, $f_r = 12.5$ Hz; (c) $A_r = 6.35$ mm, $f_r = 15.0$ Hz (..... Measured; ——— Simulation).	57
Figure 2.11:	Comparison of simulation results with the measured data under different operating frequencies: (a) $A_r = 6.35$ mm, $f_r = 1.5$ Hz; (b) $A_r = 12.5$ mm, $f_r = 5.0$ Hz; (c) $A_r = 6.35$ mm, $f_r = 7.5$ Hz; (d) $A_r = 6.35$ mm, $f_r = 7.5$ Hz (..... Measured; ——— Simulation).	58
Figure 2.12:	Comparison of simulation and experimental results: (a) $A_r = 6.35$ mm, $i = 0.75$ A, $f_r = 15.0, 12.5, 10.0, 7.5, 5.0, 2.5, 1.5$ and 0.5 Hz, from the outside loop to the inside loop; (b) $f_r = 2.5$ Hz, $i = 0.75$ A, $A_r = 18.75, 12.5, 6.35$ and 2.54 mm, from the outside loop to the inside loop.	59

Figure 2.13: Simulation results attained under an arbitrary displacement excitation and control current: (a) time-history of displacement; (b) time-history of control current; and (c) time-history of damping force response.....	61
Figure 3.1: Measured f - v characteristics of a MR-damper illustrating variations with: (a) applied current, $A_r = 6.35$ mm, $f_r = 1.5$ Hz; (b) excitation frequency, $A_r = 6.35$ mm, $i = 0.75$ A; (c) excitation amplitude, $f_r = 2.5$ Hz, $i = 0.75$ A.	67
Figure 3.2: Nonlinear Hysteretic Biviscous Model [102].	72
Figure 3.3: Bouc-Wen model [88] and extended Bouc-Wen model [73].	76
Figure 3.4: Comparisons of results from the modified piecewise linear biviscous model with the measured data under $A_r = 6.25$ mm at: (a) $f_r = 1.5$ Hz; (b) $f_r = 2.5$ Hz; (c) $f_r = 5.0$ Hz (..... Measured; ——— Simulation).	84
Figure 3.5: Comparisons of results from the modified polynomial model with the measured data under $A_r = 6.25$ mm at: (a) $f_r = 1.5$ Hz; (b) $f_r = 2.5$ Hz; $i = 0.25$ A; (c) $f_r = 2.5$ Hz; $i = 0.75$ A.	86
Figure 3.6: Comparisons of results from the modified extended Bouc-Wen model with the measured data under $A_r = 6.25$ mm at: (a) $f_r = 1.5$ Hz; (b) $f_r = 2.5$ Hz; (c) $f_r = 5.0$ Hz; (..... Measured; ——— Simulation).	87
Figure 3.7: Comparisons of results from the generalized hysteretic sigmoid model with the measured data under $A_r = 6.25$ mm at: (a) $f_r = 1.5$ Hz; (b) $f_r = 2.5$ Hz; (c) $f_r = 5.0$ Hz; (..... Measured; ——— Simulation).	89
Figure 3.8: Comparisons of results attained from the original models with the measured data under 6.25 mm harmonic displacement excitation at 1.5 Hz: (a) nonlinear hysteretic biviscous model [102]; (b) extended Bouc-Wen model [73]; (c) polynomial function model [77]; (d) variations in selected polynomial function model coefficients with applied current (..... Measured;—— Simulation).	91
Figure 3.9: The damping force prediction error of the modified piecewise linear biviscous model as function of: (a) applied current, $A_r = 6.35$ mm, $f_r = 1.5$ Hz; and (b) excitation frequency, $A_r = 6.35$ mm, $i = 0.5$ A.	94
Figure 3.10: The damping force prediction error of the modified polynomial model as function of: applied current $A_r = 6.35$ mm, $f_r = 1.5$ Hz.	95
Figure 3.11: The damping force prediction error of the modified extended Bouc-Wen model as function of: (a) applied current, $A_r = 6.35$ mm, $f_r = 1.5$ Hz; and (b) excitation frequency, $A_r = 6.35$ mm, $i = 0.5$ A.	96
Figure 3.12: The damping force prediction error of the generalized hysteretic sigmoid model as function of: (a) applied current, $A_r = 6.35$ mm, $f_r = 1.5$ Hz; and (b)	

excitation frequency, $A_r = 6.35$ mm, $i = 0.5$ A.	97
Figure 3.13: Comparisons of the damping force errors of modified models under $A_r = 6.35$ mm, $f_r = 1.5$ Hz: (a) $i = 0.5$ A; and (b) $i = 1.5$ A.	99
Figure 3.14: Comparisons of the damping force error of modified models under $A_r = 6.35$ mm, $i = 0.5$ A at: (a) 2.5 Hz; and (b) 5.0 Hz.	100
Figure 4.1: Two-DOF combined human-suspension seat model.	108
Figure 4.2: Measured static force-deflection characteristics of a typical seat cushion.	110
Figure 4.3: Comparisons of cushion model responses with the measured data under different excitation frequencies and preloads: (a) 1.5 Hz, 40 kg preload; (b) 2.0 Hz, 40 kg preload; (c) 2.5 Hz, 40 kg preload; (d) 40, 55, 66 kg preloads.	113
Figure 4.4: Force-velocity characteristics of a typical hydraulic damper.	115
Figure 4.5: Force-deflection characteristics of the: (a) elastic element of suspension mechanism; and (b) end-stops.	117
Figure 4.6: Comparisons of measured friction force with the model results as function of preload and deflection.	118
Figure 4.7: Time history of transient excitation.	119
Figure 4.8: PSD of vertical acceleration of selected vehicles and the corresponding amplified signals: (a) Bus & BusA; (b) EM1 & EM1A; (c) Snow & SnowA.	121
Figure 4.9: Comparisons of measured and computed responses: (a) acceleration transmissibility of the suspension seat; and (b) time histories of mass acceleration under a harmonic displacement excitation ($A_r = 55$ mm and $f_r = 1.25$ Hz).	124
Figure 4.10: Comparison of the mass acceleration response of the model with the experimental data under transient excitation.	125
Figure 4.11: Comparisons of measured and computed acceleration PSD responses of the seat-suspension subject to: (a) Bus and BusA; and (b) EM1 and EM1A excitations.	126
Figure 4.12: Influences of variation in damping parameters (C_{cl} and p) on the SEAT and VDVR responses under: (a) Bus; (b) BusA; and (c) BusA2.	132
Figure 4.13: Comparison of the peak acceleration under Bus, BusA and BusA2 excitations, influenced by variations in damping parameters of: (a) C_{cl} ; and	

(b) p	133
Figure 4.14: Influences of variation in damping parameters (γ_c and γ_e) on the <i>SEAT</i> and <i>VDVR</i> responses under: (a) Bus; and (b) BusA.	134
Figure 4.15: Influence of variation in damping parameters (C_{cl} and p) on the <i>SEAT</i> and <i>VDV</i> ratio responses of suspension seat under: (a) EM1; and (b) EM1A.	136
Figure 4.16: Comparison of the peak acceleration under EM1 and EM1A excitations, influenced by variations in damping parameters of: (a) C_{cl} ; and (b) p	136
Figure 4.17: Influence of variation in damping parameters (γ_c and γ_e) on the <i>SEAT</i> and <i>VDV</i> ratio responses of suspension seat under:(a) EM1; (b) EM1A.....	137
Figure 4.18: Influence of variation in damping parameters (C_{cl} and p) on the <i>SEAT</i> and <i>VDV</i> ratio responses of suspension seat subject to excitation signals: (a) Snow; and (b) SnowA.....	138
Figure 4.19: Influence of variation in damping parameters (C_{cl} and p) on the acceleration transmissibility response of the suspension seat.	140
Figure 4.20: Influence of variations in damping coefficient C_{cl} on the suspension seat responses under transient excitation ($A_p = 55$ mm).	141
Figure 4.21: Influence of selected asymmetric factor p of damping coefficient on the weighted and unweighted of the <i>SEAT</i> and <i>VDV</i> ratio of the suspension seat subject to transient excitation.....	142
Figure 5.1: Combined rigid human-suspension seat model equipped with MR-damper.	149
Figure 5.2: Influence of applied current on the occupant mass acceleration transmissibility response of the MR-damped suspension seat model.....	151
Figure 5.3: Comparison of acceleration transmissibility responses of the model with hydraulic and MR-damper with the measured data of the hydraulic suspension seat.....	152
Figure 5.4: Time history of transient excitations of different peak magnitudes (1.5 Hz).	153
Figure 5.5: Influence of applied current on the body mass acceleration \ddot{x}_o , damping force f_d and end-stop force F_b , of the MR-damper suspension seat model subject to a 55 mm peak transient excitation.	154
Figure 5.6: Comparison of responses, body acceleration \ddot{x}_o , damping force f_d and end-stop force F_b , of MR-damper suspension seat model under three different peak magnitude of transient excitations (applied constant current i	

$= 0.12\text{A})$	155
Figure 5.7: Comparison of acceleration PSD responses of suspension seat models with the MR-damper (0.12 A) and the hydraulic passive damper under Bus and BusA excitations.	157
Figure 5.8: Comparison of acceleration PSD responses of suspension seat models with the MR-damper (0.12 A) and the hydraulic passive damper under EM1 and EM1A excitations.....	157
Figure 5.9: Comparison of acceleration transmissibility of the body mass of the suspension seat model employing hysteresis and mean damping force model (0.12 A).	158
Figure 5.10: Comparison of responses of the suspension seat model with mean and hysteresis damper models under a harmonic excitation ($A_r = 25 \text{ mm}$; $f_r = 1.25 \text{ Hz}$; $i = 0.12 \text{ A}$): (a) body acceleration \ddot{x}_o ; (b) $f-v$ characteristics of the MR-dampers.	159
Figure 5.11: Comparison of acceleration responses of the suspension seat model with mean and hysteresis $f-v$ damper models under transient excitation (peak displacement amplitude = 55 mm).....	160
Figure 5.12: Continuous variations in the command current i_c of a ‘hi-lo’ control algorithm and the effects of smoothing.	164
Figure 5.13: Continuous variations in the control current i_c of a ‘hi-lo’ control algorithm and the effects of the proportionality factor p_c ($\xi_c = 10$)......	165
Figure 5.14: Schematic of the general structure of the semi-active MR-damping control scheme based on skyhook and continuous modulation algorithm.....	166
Figure 5.15: Comparison of acceleration transmissibility characteristics of semi-active suspension seat with different value of control gain G	168
Figure 5.16: Comparison of acceleration transmissibility characteristics of the semi-active suspension seat with selected control gain with those attained under constant currents.	168
Figure 5.17: Comparison of the control current with smoothing and without smoothing while semi-active skyhook-based controller applied ($A_r=25\text{mm}$; $f_r=1.25\text{Hz}$; $G=1$).	169
Figure 5.18: Influence of controller gain on the response characteristics of the semi-active suspension seat to a transient excitation (peak displacement = 55 mm).	171
Figure 5.19: Influence of peak displacement amplitudes of the transient excitation on the	

semi-actively suspension responses ($G=1$).	172
Figure 5.20: Influence of peak displacement amplitudes of the transient excitation on the semi-actively suspension responses ($G=3$).	173
Figure 5.21: Comparisons of the PSD of body mass acceleration responses of the semi-active and constant current suspension seats under a bus excitation for different gains: (a) Bus; and (b) BusA.	175
Figure 5.22: Comparisons of the PSD of body mass acceleration responses of the semi-active and constant current suspension seats under class I construction vehicle excitation for different gains: (a) EM1; (b) EM1A.	177
Figure 5.23: Influence of relative position control on the responses of the suspension with integrated controller under different magnitudes of harmonic excitations ($f_r = 1.25$ Hz; $G = 3$; $\delta_s = 0.6$).	183
Figure 5.24: Influence of position margin on the responses of the suspension with integrated control under a relatively higher excitation magnitude ($f_r = 1.25$ Hz; $G = 3$; $A_r = 0.112$ m).	185
Figure 5.25: Transient response characteristics of the suspension with integrated control under different magnitudes of transient excitations ($G = 1$; $\delta_s = 0.6$).	187
Figure 5.26: Transient response characteristics of the suspension with integrated control ($A_p = 0.115$ m; $G = 1$; and $\delta_s = 0.7$).	188
Figure 5.27: Transient response characteristics of the suspension with integrated control ($A_p = 0.115$ m; $G = 1$; and $\delta_s = 0.8$).	189
Figure 5.28: Influence of peak transient excitation amplitude (A_p) on the response characteristics of the suspension with integrated control ($G = 3$; $\delta_s = 0.7$).	192
Figure 5.29: Influence of position margin (δ_s) on the response characteristics of the suspension with integrated control under a transient excitation ($A_p = 0.132$ m; $G = 3$).	193
Figure 5.30: The response characteristics of the suspension seat with integrated control and higher limiting current (Transient excitation: $A_p = 0.132$ m; $G = 7$; $i_H = 2.5$ A; $\delta_s = 0.7$).	194
Figure 5.31: Comparisons of the weighted and unweighted SEAT and VDVR measures of different suspension seats subject to 'Bus' excitation.	197
Figure 5.32: Comparisons of the weighted and unweighted SEAT and VDVR measures of different suspension seats subject to 'BusA' excitation.	197

Figure 5.33: Comparisons of the weighted and unweighted SEAT and VDVR measures of different suspension seats subject to 'BusA2' excitation.	198
Figure 5.34: Comparisons of the weighted and unweighted SEAT and VDVR measures of different suspension seats subject to 'EM1' excitation.....	200
Figure 5.35: Comparisons of the weighted and unweighted SEAT and VDVR measures of different suspension seats subject to 'EM1A' excitation.	200
Figure 5.36: Influences of controller gain (G) and position margin (δ_s) on the <i>SEAT</i> and <i>VDVR</i> responses of the suspension seats with integrated control subject to 'EM1A' excitation.	201
Figure 6.1: Schematic diagram of the HIL test system comprising the MR-damper hardware, the suspension seat model and the interface.	206
Figure 6.2: Schematic diagram of the interface between the hardware and the software.	207
Figure 6.3: A pictorial view of HILS for the proposed suspension seat (1- DPS; 2- I/O board ; 3- Temperature monitor; 4- Hydraulic actuator; 5-LVDT & LVT; 6- MR-damper; 7- Force sensor).	208
Figure 6.4: The damper power supply circuit (DA2- Command signal from I/O board; AD3- Feedback for the PID controller).	210
Figure 6.5: The designed layout of the interface window of the HIL test and simulation platform.....	212
Figure 6.6: Comparisons of model and measured responses of the suspension seat with the MR damper hardware subject to 0.1 A constant current and a harmonic excitation ($f_r = 1.5$ Hz and $A_r = 25$ mm).	216
Figure 6.7: Comparison of the computed and measured f - v characteristics of the MR-damper in the damper installing direction under a harmonic excitation ($i = 0.1$ A, $f_r = 1.5$ Hz, $A_r = 25$ mm).	217
Figure 6.8: Comparisons of the body mass acceleration transmissibility responses derived from the measured data and the model of the MR suspension seat with MR-damper ($i = 0$ and 0.1 A).	218
Figure 6.9: Comparisons of measured and computed acceleration transmissibility responses of the suspension seat employing the proposed skyhook-based semi-active damping control with two different control gains.	220
Figure 6.10: Comparisons of the computed and measured responses of the suspension seat model employing the proposed semi-active skyhook-based MR-damping under a harmonic excitation ($f_r = 1.5$ Hz, $A_r = 20$ mm and $G =$	

3).	221
Figure 6.11: Comparisons of model and measured responses of the suspension seat with a constant current MR damping under transient excitations ($i = 0.1$ A; $A_p = 27.5$ mm).	223
Figure 6.12: Comparisons of model and measured responses of the suspension seat with a constant current MR damping under transient excitations ($i = 0.1$ A; $A_p = 42.5$ mm).	224
Figure 6.13: Comparisons of computed and measured responses of the suspension seat employing the proposed semi-active damping control under 42.5 mm transient excitation ($G = 1$).	225
Figure 6.14: Comparisons of computed and measured responses of the suspension seat employing the proposed semi-active damping control under 42.5 mm transient excitation ($G = 3$).	226
Figure 6.15: Comparisons of computed and measured responses of the suspension seat employing the proposed semi-active damping control under 66 mm transient excitation ($G = 3$).	227
Figure 6.16: Comparisons of PSD of the measured and computed body mass acceleration of the suspension seat with a constant current MR damping ($i = 0.1$ A) subject to vehicular vertical vibration: (a) Bus; (b) BusA; (c) EM1; (d) EM1A.	229
Figure 6.17: Comparisons of PSD of the measured and computed body acceleration of the suspension seat employing semi-active damping control with different control gains (excitation: Bus).	231
Figure 6.18: Comparisons of PSD of the measured and computed body acceleration of the suspension seat employing semi-active damping control with different control gains (excitation: BusA).	231
Figure 6.19: Comparisons of PSD of the measured and computed body acceleration of the suspension seat employing semi-active damping control with different control gains (excitation: EM1).	232
Figure 6.20: Comparisons of PSD of the measured and computed body acceleration of the suspension seat employing semi-active damping control with different control gains (excitation: EM1A).	233

LIST OF TABLES

Table 2.1: Test matrix.	39
Table 2.2: High Velocity Slope β_h as function of v_m and i	50
Table 2.3: Low Velocity Slope β_l as function of v_m and i	52
Table 2.4: Model parameters identified from the measured data.....	56
Table 3.1: Identified parameters for hysteresis loop of all models.	82
Table 3.2: Identified parameters for the current dependent function in all modified models.	82
Table 4.1: The model parameters.....	112
Table 4.2: The coefficients of the vertical acceleration transfer functions describing the vertical vibration characteristic of an urban bus (Bus), a sidewalk snowplow (Snow) and a class I construction vehicle (EM1).	122
Table 4.3: Frequency-weighted and unweighted VDV and rms acceleration values of excitations.	128
Table 5.1: The peak displacement magnitudes of transient excitations that initiate end-stop impacts of different suspensions.	195

NOMENCLATURE

A	Constant parameter of Bouc-Wen hysteron expression
A_{m1}, A_{m2}	Coefficients of transfer functions of vertical vehicular vibration
A_p	Peak displacement magnitude of transient excitation (m)
A_r	Amplitude of harmonic displacement excitation (m)
a_{wb}, a_{wo}	Frequency-weighted rms base and response accelerations
$Bus, BusA$	Vertical vibration of an urban bus and amplified by 150%
C_{cl}	Damping coefficient of the low-speed compression mode of hydraulic damper (Ns/m)
c	Viscous damping coefficient (Ns/m)
c_0, c_1	Viscous damping coefficients of the Bouc-Wen model (Ns/m)
c_{po}, c_{pr}	Pre- and post-yield linear damping rates
c_{t0}, c_{t1}	Cushion damping coefficients in compression and rebound
d_c, d_e	Suspension travel in compression and rebound (m)
$d_m^{(c)}, d_m^{(e)}$	Maximum deformation of the buffers (m)
$EMI, EMIA$	Vertical vibration of class I earthmoving machinery and amplified by 150%
F_b	End-stop force (N)
F_c	Total cushion force (N)
F_d	Damping force due to an inclined hydraulic damper (N)
F_{dv}	Vertical damping force due to hydraulic damper (N)
F_f	Friction force (N)

F_h	Hysteresis function describing hysteresis damping force (N)
F_s	Spring force (N)
F_{sb}	Damper seal friction force (N)
f_d	Damping force due to an inclined MR-damper (N)
f_{dm}	Measured damping force (N)
f_{dv}	Vertical damping force due to MR-damper (N)
f_h	Zero-velocity force intercept (N)
f_m	Maximum damping force corresponding to v_m (N)
f_r	Frequency of harmonic excitation (Hz)
f_t	Transition mean damping force (N)
G	Control gain
g	Acceleration due to gravity (m/s^2)
$H(s)$	Transfer function
h_{cl}, h_{el}	Transition displacements for the top and bottom buffers (m)
i	Applied constant current (A)
i_H	Maximum damper current (A)
i_c	Command current (A)
i_d	Control current (A)
i_z	‘Hi’ state damper current
k_b	Bending stiffness of the pan (N/m)
k_{c1}, k_{c2}	Linear stiffness coefficients of the bottom buffer (N/m)

k_{e1}, k_{e2}	Linear stiffness coefficients of the top buffer (N/m)
k_s	Normalized stiffness (N/m)
k_{t0}, k_{t1}	Linear and nonlinear stiffness coefficients of cushion
M_c, M_{ce}	CM multipliers
m_o, m_s	Seated (body) mass and suspension mass (kg)
p	Damping asymmetry factor
T_c	Free thickness of cushion (m)
u	Voltage applied to the current driver of the damper (V)
VDV	Vibration dose value
VDVR	Vibration dose value ratio
v	Damping velocity (m/s)
v_c, v_e	Transition velocities (m/s)
	Transition velocity from low- to high-speed rebound mode of hydraulic damper (m/s)
v_h	Zero-force velocity intercept (m/s)
v_m	Peak damper velocity (m/s)
v_t	Transition velocity corresponding to onset of force-limiting (m/s)
W_k	Frequency weighting function
x	Damper displacement (m)
x_0	Initial piston displacement due to compression of the gas (m)
x_{t0}	Initial spring displacement of the accumulator (m)
x_1, x_2	Absolute displacements of springs k_{s0} and k_{s1} (m)

x_b	Displacement of base excitation (m)
$\dot{x}_{b1}, \dot{x}_{b2}$	Transition velocities between pre-and post-yield curves (m/s)
x_o	Displacement of seated body mass (m)
x_{os}	Cushion deformation (m)
x_s	Suspension mass displacement (m)
x_{sb}	Suspension relative displacement (m)
\dot{x}_{sb}	Relative velocity of suspension (m/s)
z	Bouc-Wen yield-force function
z_c, z_{ce}	Condition functions
β_l, β_h	Low and high speed damping coefficients (Ns/m)
δ_s	Position margin
γ_c, γ_e	Compression and rebound damping reduction factors
ε	Pressure drop due to the MR effect (yield) stress
η	Proportion of free thickness of the cushion
θ, θ_0	Inclination angles of the damper (rad)
ξ_c, ξ_{ce}	Smoothing factors

CHAPTER 1

INTRODUCTION AND LITERATURE REVIEW

1.1 Introduction

Whole-body vibration (WBV) and shock exposure among occupational drivers has been around since the advent of vehicles and many studies have shown the probable link between exposure and related adverse effects to the muscle-skeletal system of exposed drivers [1-4]. Although the amount of vibration and shock experienced by an operator of mobile equipment is also determined by driving speed, vehicle maintenance, vehicle load, vehicle suspension, vehicle size and seat type, etc., the whole-body vibration and shock basically arise from the road roughness [1, 5]. Adverse health outcomes associated with whole-body vibration and shock exposure have been well documented and include damage to the nervous, circulatory and digestive systems.

The whole-body vibration and shock exposures have been mostly considered focusing off-road vehicles (especially agricultural or earth-moving machinery) and heavy road vehicles (trucks or buses) [1, 6-9]. In view of the severe health and safety risks posed by exposure to these vibration and shock environments, a series of suspension systems such as chassis, cab and seat suspension are introduced to improve the ride quality. The chassis or cab suspensions are invariably developed to achieve a compromise among different conflicting measures, namely satisfactory ride, road-holding, handling and directional performances. A secondary suspension at the seat is thus considered vital

for attenuating potentially harmful WBV, which predominate along the vertical axis.

The shock and vibration transmission performance characteristics of low natural frequency suspension seats, widely employed in off-road and heavy road vehicles, strongly depend upon the component properties and the nature of vertical vibration environment of the target vehicle [3, 10-12]. The limited travel of such seats often causes impacts against the end-stops and thus transmits shock motions to the seated occupant. Many studies have concluded that a lightly damped suspension-seat can provide effective isolation from the road-induced vibration, while the driver's protection from shock motion necessitates high suspension damping.

A vast number of variable damping concepts based upon semi-active or active suspension have evolved during the past 40 years, to provide better compromise among different conflicting performance measures. However, the implementations of these suspensions have been limited due to high cost, hardware complexities and the power demand [13-17]. Owing to their rapid response and low power requirements, electric-rheological (ER) or magneto-rheological (MR) fluid suspensions have been considered as attractive, alternatives for realizing variable damping. The ER dampers require high working voltage, while the MR dampers need only minimal power, usually in the order of 1 to 2 Amps at 12-24V. The MR dampers are thus considered meritorious for achieving controllable high damping forces over a broad temperature range. The MR dampers could thus be considered as ideal candidates for enhancement of the shock and vibration attenuation performance of a suspension seat. The switching discontinuities,

damper hysteresis and limited bandwidth of the controlled damper, however, may degrade the performance. The controller design thus forms the most important task.

The MR dampers offer high viscous damping at low velocities in the pre-yield condition, while the post-yield saturation at high velocities can be characterized by low viscous damping. While the variations in the low-velocity rise and post-yield saturation can be achieved in a highly rapid manner with only minimal current, the force-velocity properties exhibit considerable hysteresis that depends upon applied control current and excitations. A large number of analytical models based upon different describing functions have evolved in recent years to describe the nonlinear properties of the MR-dampers, such as the Bingham plastic, nonlinear hysteretic biviscous, polynomial function, extended Bouc-Wen hysteresis model. However, only a few of the reported models could accurately characterize the nonlinear damping properties over a wide range of excitation conditions and applied current. A number of control concepts have been developed to achieve variable MR-damping in a semi-active manner. These include the “skyhook”, “sliding-mode” and “clipped semi-active” control schemes [18-21]. All of these studies consider mean force-velocity (f - v) characteristics of the damper, while neglecting the hysteretic behaviour. The hysteretic f - v properties of a damper could yield considerable errors in the tracking control [22].

This dissertation research focuses on the development of a controller design to realize variable damping properties of a MR-damper for applications in vehicle suspension seats. For this purpose, a generalized sigmoid hysteretic f - v model of the

MR-fluid damper is developed to characterize direct current controlled hysteretic damping properties as a function of the nature of excitation and the applied current. An independent sigmoid function in current is further proposed that could be integrated to the well-known biviscous, polynomial and extended Bouc-Wen models to enhance their prediction abilities. Furthermore, the influences of suspension design parameter on the shock and vibration performance characteristics of suspension seats are investigated through development and analysis of a nonlinear model under different types of excitation. This suspension seat with the passive hydraulic damper being replaced by a controllable MR-damper is further considered as the plant, while designing the controllers. Owing to the strongly nonlinear properties of the MR-damper, two different control algorithms based on skyhook formulations and similarly adaptive concept are explored. The performance characteristics of the MR suspension seat with and without the controlled damper are investigated under various excitations and are assessed in the laboratory through development of a hardware-in-the-loop (HIL) test platform.

1.2 Review of Relevant Literature

The design, analysis and developments in semi-active MR suspension seats encompass several challenges in characterization and modeling of MR damper, synthesis of semi-active controller, analysis of suspension seat, characterization of vehicular vibration and shock, etc. The relevant reported studies in these areas are thus reviewed to build the essential background and scope of the dissertation research. The reviewed

studies, grouped under the relevant topics, are discussed in the following sections.

1.2.1 Effects of Whole-body Vibration (WBV) and Shocks

Occupational drivers of heavy road and off-road vehicles are routinely exposed to severe levels of vibration and shocks caused by vehicle interactions with the terrain irregularities [1, 5, 8, 9, 33]. The severity of such shock and vibration transmitted to the seated driver tends to be considerably more in off-road vehicles employed in agriculture, construction, forestry and mining sectors. Such vibration also occurs in the low frequency range, up to 15 Hz. The suspension seats are thus designed with low natural frequency in the 1.25 to 1.5 Hz range to achieve effective vibration isolation [2, 7, 11]. The primary suspensions of heavy road vehicles also exhibit the vertical mode resonance of the sprung mass within the same frequency range which often causes the suspension seat to exceed its permissible travel and transmit severe shock motions to the seated driver.

Prolonged exposure to high magnitude vibration and repeated shocks of low frequency nature has been associated with an array of health disorders among the drivers, namely the disorders of the spine and the supporting musculoskeletal structure [1, 3, 4]. Moreover, exposure to such vehicular vibration and shocks has been known to interfere with the driver's comfort and working efficiency. It is generally agreed that the risk of spinal injury and lower back pain increases with magnitude of vibration and exposure duration. High magnitudes of shock motions, such as those encountered in a trucking accident, can cause compressive fracture of the spine (acute risk), while chronic exposure

to lower levels can lead to disc degeneration and lower back pain [24, 25]. In addition to the increased health risks, drivers who experience frequent bottoming and topping of the suspension-seat have reported increased levels of fatigue [24, 26]. Suspension topping and bottoming also presents a safety risk, as these events can cause the driver to temporarily lose control of the vehicle.

1.2.2 Control of Whole-body Vibration and Shock

It has been widely recognized that health and safety risks posed by occupational exposure to whole-body vibration can be considerably reduced by minimizing the magnitudes of vibration transmitted to the human occupant [7, 27]. Off-road vehicles, due to their interactions with uneven terrains, are known to yield high magnitudes of translation and rotational vibration. The magnitudes of longitudinal and lateral vibrations in some off-road vehicles may approach or exceed those along the vertical axis [1]. Upon recognizing high magnitudes of translational and rotational vibration, a concept in multi-axis seat vibration isolator has been proposed in the early 80's [28]. The commercial suspension seats, employed in heavy road and off-road vehicles, however, are designed to attenuate vibration in the vertical mode only, since the attenuation of vibration along all the other axes needs complex suspension mechanisms. The vertical mode suspension seats are known to yield vibration isolation superior to that of the conventional seats, since the suspensions are designed with natural frequency well below the frequency of dominant vibration.

The performance characteristics of suspension seats, comprising either mechanical or pneumatic springs and passive dampers, have been extensively investigated under different types of excitations via field or laboratory assessments and analyses of coupled suspension seat-occupant modes [5, 29-32]. Under low-level floor vibration, a suspension mechanism may exhibit lock-up behavior due to inherent Coulomb friction. Under higher levels of continuous vibration, a suspension seat may yield either attenuation or amplification of vibration depending upon the nature of vibration. Under even higher magnitudes of vehicular vibration, the suspension may exceed its free travel limit and result in repetitive impacts with the end-stops, thereby causing shock motions [10, 27]. The ride vibration environment of many heavy road vehicles, specifically those employed in urban public transport sector, often include shock motions arising from interactions of tires with extreme road irregularities, such as pot holes, rut formations and drain covers. The shock motions transmitted to operators of urban buses are known to be more frequent and more severe. The suspension seats employed in many off-road vehicles are also subjected to end-stop impacts, while operating on relatively rough terrains. The isolation of drivers from the shock and vibration environment of such vehicles thus necessitates the design of suspension seats that can minimize both the transmission of continuous vibration and shock motions to the operator.

1.2.3 Suspension Seat System

Occupational vehicle drivers are constantly exposed to high magnitude and low

frequency whole-body vibration, which has been associated with an array of health disorders among the drivers [1]. Consequently, low natural frequency suspension seats are widely employed in vehicles in the forestry, construction, industrial, mining and freight and passenger transportation sectors [2, 33]. Considerable advancements have also been made to enhance the ride performance through designs of primary wheel suspensions, specifically for the buses and trucks. Similar efforts for the off-road and industrial vehicles, however, have been limited due to constraints imposed for preservation of their roll stability. Soft suspension seats employed in heavy road and off-road vehicles also yield considerable magnitudes of repetitive shock motions, specifically under abrupt or high magnitude excitations, due to limited suspension travel and motion limiting stops.

The maximum seat suspension travel is limited to about 100 mm or less in the off-road vehicles to ensure safer vehicle control and accessibility for the driver. The travel limiting of the suspension seat is invariably achieved by introducing either elastic or rigid bump stops in compression and rebound. Figure 1.1 illustrates schematic of a typical guiding linkage of the suspension together with the location of the compression and extension end-stop buffers. Conventional suspension seats use rubber buffers to reduce the severity of such end-stop impacts [1]. The considerably high stiffness characteristics of these rubber buffers cause high magnitude resonant oscillations of the suspension and thus transmit high levels of shock and vibration to the driver. These shock motions tend to be quite severe for the drivers of vehicles operating on the relatively

rough urban roads, construction sites, sidewalks, ice-covered roads and off-road terrains. End-stop impacts in a suspension seat cause high levels of shock and vibration arising from impacts, and thus driver discomfort [30].

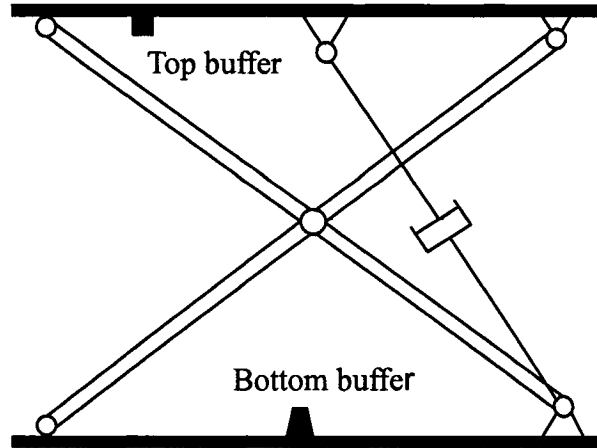


Figure 1.1: Cross linkage mechanism of seat suspension.

In earlier studies, vertical suspension seats have often been characterized by a two degree-of-freedom (DOF) dynamic system, in which the seat cushion, suspension spring and suspension damper have been simplified as linear elements, while the end-stop buffer properties have seldom been considered [11, 34]. Analytical models incorporating nonlinearities due to shock absorber damping, Coulomb friction force and elastic limit stops have been proposed in a few studies [28, 30, 31, 35]. Boileau et al. [31] established that consideration of end-stop impacts poses contradictory design requirements for suspension seats. In Europe, a major consortium of both research institutes and seat manufacturers undertook a study with objectives of developing test methods for

suspension seat end-stop impacts, improving buffer and suspension design and finally reducing the shock and vibration transmitted to the driver. Wu et al. [36] proposed a comprehensive analytical model of a typical elastic buffer to incorporate its nonlinear force-deflection and energy dissipation properties; meanwhile, the results of the optimization study revealed that soft and thick buffers with linear stiffness characteristics over a large range of deflection are highly desirable for reducing the severity of end-stop impacts. Rebelle [27] developed a numerical model of a suspension seat rather than characterizing the individual components to optimize the end-stop buffer. Such an approach thus prevents considering the effects of variations in the parameters of the individual components.

The influence of seat cushion designs on the seating comfort and driver posture has been evaluated through a number of subjective and objective studies. A study performed by Ng et al. [37] reported that an adequate driver-seat support could reduce the stresses in muscles of the back, buttocks and legs caused by prolonged sitting during daily driving activities. A subjective survey of the heavy-duty truck operators was performed to identify their seat design preferences and specific ailments experienced by the drivers [26]. Thakurta et al. [4] evaluated the seating comfort related to various seat zones through subjective studies and correlated the comfort assessments to measured driver-seat interface pressure under static loads. The polyurethane foam widely used in seat cushion design has complex mechanical properties and the human perception of ride comfort is closely related with these properties [38, 39]. The effects of the composition, density and

thickness of polyurethane foam and contouring of the seat on vibration transmission have also been studied [34, 40]. The polyurethane foam seats exhibit highly nonlinear visco-elastic properties depending upon the excitation magnitude and frequency content, and the seated body weight [3]. The vast majority of the studies on seat cushion models consider lumped and properties, while neglecting the hysteresis and dependence upon the body weight and nature of excitation [28, 31, 35, 41]. Such a linear cushion model yields large errors under high magnitude vibration, which may also induce bending deformations of the seat pan. A nonlinear seat cushion model was subsequently developed and validated by Wu [30]. Although this model was proposed based on systematic identification of the cushion's force-deflection and force-velocity characteristics, the hysteresis property was not considered. Furthermore, the application of model required prior knowledge of the excitation frequency.

The static and dynamic properties of the suspension mechanisms, such as kinematics design, stroke, elastic properties, Coulomb friction and elastic properties of the motion limiting buffers, mostly influence the shock and vibration attenuation characteristics of a suspension seat. The suspension seats invariably employ either mechanical or pneumatic spring elements in conjunction with a guidance mechanism to ensure nearly vertical motion of the seat. The response behavior of a suspension seat is directly affected by the stiffness characteristics of the spring element. Furthermore, the magnitude of friction force is attributed to shock absorber seals, various sliding contact surfaces and linkage joints. On the other hand, the parameterized models of spring elements and friction force,

proposed in earlier studies or by Wu [30], employed linear relationship by the way of mean curves, assuming negligible contributions due to hysteresis.

1.2.4 Active and Semi-active Suspensions

A wide range of variable damping concepts have evolved to maximize the passenger comfort, increase the handling stability and reduce the tire-induced road damage [7, 18]. Controllable damping devices have been proposed to realize the intelligent vehicle suspension designs. The vehicle suspensions, in general, can be categorized in three groups based on the energy properties, namely active and semi-active suspensions. The relative structures of passive, semi-active and active suspension dampers are illustrated in Figure 1.2, using a single-DOF formulation. A vast number of active and semi-active suspension structures have been proposed since the early 1950's, which could generate variable damping and suspension forces in accordance with the varying excitation and response variables to satisfy various conflicting design requirements [7, 16, 42, 43].

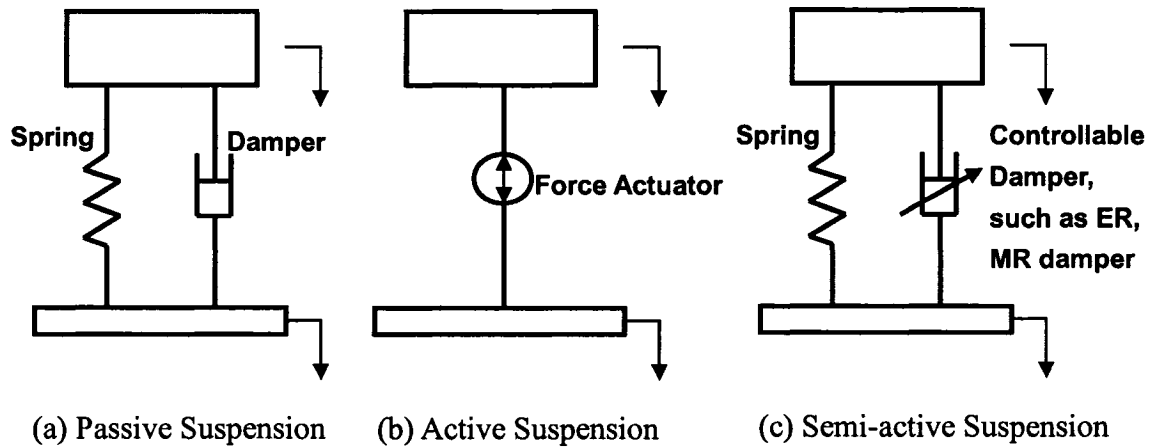


Figure 1.2: Schematics of passive, active and semi-active suspensions.

The passive suspensions offer limited performance due to uncontrollable nature of the dampers; they can only temporarily store and dissipate energy at a constant rate, and the forces generated depend on the local relative motions. The active suspensions refer to those, where the passive components are replaced by a high performance hydraulic or pneumatic or electro-magnetic force generator with a high bandwidth valve and hydraulic power supply. It can generate forces in response to varying response and excitation variables, but requires considerable external power. A semi-active suspension generally offers controllable damping forces with only minimal power requirement, and can thus provide variable rate of energy dissipation. Owing to the high cost and power requirement of a fully-active suspension, the semi-active suspensions are considered to be more meritorious for vehicle suspension applications.

A number of studies have explored different concepts in active suspension and controller synthesis. Crosby *et al.* [42] proposed the concept of an active damper for shock and vibration control. Thompson [16] demonstrated that the performance of active suspensions is definitely superior to that of the classical suspensions. Perisse [14, 15] proposed and investigated a new control policy, as an application of a cascade regulator plant. The proposed policy was applied to active a suspension seat, as an example, to illustrate the theoretical and experimental feasibility of the active vibration control system. However, from a technical point of view, an active suspension cannot be applied without a host of parametric measurements including velocities and deflections, which yield complexities in implementation apart from the high cost and power.

A vast number of semi-active vibration control systems have been proposed and investigated since the early 70's, as alternative to the high cost and high power active control systems [42, 44, 45]. Most studies in the area of semi-active suspensions involved either a single or a two DOF dynamic model representing a single wheel-suspension, often referred to as the quarter-car model. Semi-active suspensions generally involve a variable damper, where the damping force is modulated through valve flows in response to changing excitations. A study by Margolis [45] examined the effects of using realistic feedback signals when controlling the active and semi-active suspension systems. The study suggested several feedback control strategies for semi-active suspension system, such that the performance could approach to that of a fully active suspension. Hwang et al. [46] presented a method for performance assessment of a continuously controlled semi-active suspension using hardware-in-the-loop (HIL) simulation technique. The design and synthesis of a controller strongly depends on the target measure, such as ride quality, handling, roll control and rattle-space. Owing to the conflicting nature of most of the measures, the controller design has a challenging task. Youn et al. [44] proposed a semi-active optimal control law on the basis of a weighted performance index comprising ride comfort, road holding and suspension rattle space, and presented relative performance characteristics of passive, active and semi-active suspension designs. The study concluded that a semi-active suspension could offer performance benefits comparable to that of a fully-active suspension. This finding concurs with the conclusion derived by Margolis [45]. The reported semi-active control schemes, however, generally

do not consider the transient responses associated with switching of the command input, which may cause undesirable effects on the suspension performance.

Semi-active dampers based upon magneto-rheological (MR) fluids have recently evolved to achieve variable damping to enhance suspension performance under complex vibration and shock environments. These dampers offer considerable potential to realize variable damping with minimal time delays and power consumption, but exhibit significant hysteresis. The presence of hysteresis makes the task of controller synthesis a difficult one. Many studies have reported the performance characteristics of vehicle suspensions developed on the basis of the well-known skyhook or ground-hook semi-active control methods [29, 47], apart from the passive optimal control algorithms [36] and the more power-demanding active control systems [8]. A number of optimal control techniques for the active and semi-active suspensions have also been studied and applied to vehicles [16, 43, 48].

1.2.5 Semi-active and Active Suspension Seats

The suspension seat is designed not only for attenuating the vibration but also to provide adequate postural support for the driver with adequate seated height [36, 49, 50]. Thus, the semi-active and active suspension design methods have been widely applied in the design of vehicle seats, especially for the heavy load and off-road vehicles. Grimm et al. [51] designed a fully active seat suspension for farm vehicles using a hydraulic actuator. They used a simple displacement compensator to control the actuator using the

relative displacement of the seat and the acceleration of either the base or seat, as a result, the seat performance was improved when compared with a passive suspension seat. Stein and Ballo [52] proposed an active electro-pneumatic system which controls vibration performance of the seat by controlling the air flow in and out of a pneumatic spring. This active vibration control system requires a considerable amount of power. Perisse and Jezequel [14] developed an active seat suspension on the basis of the principal of improving ride passenger comfort by reducing transmitted seat acceleration. To control the dynamics of the seat suspension, an original feedback control command with a reversible electromechanical actuator was achieved. The root locus method and the linearization technology of small perturbations around the equilibrium were employed to synthesize the regulator for this active control seat.

Wu and Chen [53] applied an active vibration controller for reducing undesired low-amplitude vertical vibration in a vehicle seat. During the derivation of control algorithm, the reference signal supplied to the control plant was assumed as the displacement of excitation, while the feedback error signals were defined as the seat acceleration. One algorithm of the adaptive controls, the filtered-x least mean squares algorithm is adopted in this active controlled vehicle seat. However, the performance of controlled seat is only evaluated under a pulse excitation and low magnitude continuous vibration. Guclu [54] analyzed the dynamic behavior of a nonlinear vehicle model having active suspension and a PID controlled passenger seat suspension. The results showed that the ride comfort could be enhanced by adding a controlled actuator to generate the

desired suspension force under the passenger seat. In general, an active suspension seat can effectively overcome the limitations of a passive one, but involves high power and high cost. Consequently, the investigations on semi-active suspension seat have been considered quite attractive by many researchers, particularly with the evolution of the high bandwidth ER and MR fluid dampers.

Bouazara et al. [50] combined a 3-D vehicle model with an optimal non-linear active seat in order to analyze the safety and comfort performance and presented the relative performance of passive, semi-active and active suspension seats. The semi-active and active dampers are characterized by force generators in accordance with the control laws based upon suspension mass velocity. Optimal model parameters are selected using the sequential unconstrained minimization technique with an objective to minimize the acceleration due to vibration transmitted to the occupant mass. Wu and Griffin [36] focused on reducing the occurrence and severity of end-stop impacts in a suspension seat by employing an additional on-off controlled ER-fluid damper. However, the development of a semi-active ER-fluid damper within a suspension seat is somewhat complex, since it requires considerable high voltage. A MR-fluid damper on the other hand requires only low voltage. McManus et al. [55] investigated the potential benefits of a semi-active MR-damper in reducing the occurrence and severity of end-stop impacts of a low natural frequency suspension seat. However, the measured results did not show improvement in vibration attenuation performance over the fixed damping suspension. Choi et al. [49] proposed a semi-active MR suspension seat by implementing a PID

controller, which was also judged applicable to commercial vehicles. The performance characteristics of a full-car equipped with a prototype MR seat were evaluated using the hardware-in-the-loop (HIL) simulation technique, while the responses to repeated shocks caused by the end-stop impacts were not considered. Choi and Wereley [56] developed a semi-active nonlinear optimal control algorithm appropriate for the MR suspension seat coupled with a mechanical-equivalent model of the human body to account for the energy absorbed by the body. The study concluded that a MR suspension seat could yield considerable reductions in transmitted vibration under idealized broad-band excitations.

1.2.6 MR/ER-fluids Suspension

Controllable fluids are materials that respond to an applied electric or magnetic field with a change in their rheological behavior. These materials are commonly referred to as electro-rheological (ER) or magneto-rheological (MR) fluids. Magneto-rheological fluids, discovered by Rabinow [57], exhibit rapid, reversible and tunable transition from a free-flowing state to a semi-solid state upon the application of an external magnetic field. MR-fluids developed by the Lord Corporation [58-60] possess many attractive features, such as high yield strength, low viscosity and stable hysteretic behavior over a broad temperature range. MR-fluids have thus been applied in many devices, such as rotary brakes, vibration dampers and MR sponge dampers. Most devices that use MR fluids can be classified as having either fixed poles (pressure driven flow mode) or relatively moveable poles (direct-shear mode) [61]. The servo-valves and dampers belong to the

fixed poles devices, while the clutches, brakes, chucking and locking device are the moveable poles devices. Some of these MR fluids products have been successfully applied in the primary or secondary vehicle suspensions and vibration control of structures [49, 59, 62-65]. MR-fluid dampers have been developed in recent years to achieve variable damping in response to changing excitation and responses [49, 65]. It has been suggested that MR elastomers will also find applications where stiffness or resonance tenability is sought [66, 67].

A MR damper, developed by Lord Corporation for applications in secondary vehicle suspension is schematically shown in Figure 1.3. The damper consists of a nitrogen-charged accumulator, two MR-fluid chambers separated by a piston with an annular orifice, and electromagnetic coils. The variations in viscous and shear properties of the fluid, caused by the applied magnetic field, yield variations in the damping force. A dc current, limited to 2 A at 12 V, serves as the command signal for the coils.

MR dampers offer high viscous damping corresponding to low velocities in the pre-yield condition, while the post-yield saturation corresponding to high velocities can be characterized by a considerably lower viscous damping coefficient. The requirement of adequate ride, road-holding, handling and directional control performance of road vehicles entails variable damping [68] that could be achieved with MR dampers with only minimal power consumption. Owing to the rheology of MR fluid in terms of its shear stress-strain rate behavior, the damper exhibits highly nonlinear force-velocity characteristics attributed to the hysteresis and force-limiting properties of the fluid, which

are further dependent on the intensity of applied magnetic field, and displacement and velocity of the piston [69]. The development of an effective controller for realizing desirable variations in damping requires accurate characterization of the hysteretic force-velocity characteristics in the pre- and post-yield conditions. Consequently, considerable efforts have been made for characterizing the MR-damper properties. A number of linear piecewise linear and nonlinear models based upon either the regression formulations or the physical system have been proposed.

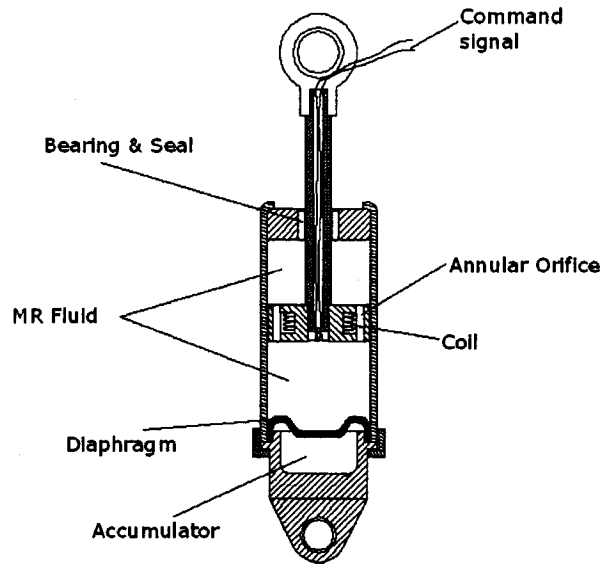


Figure 1.3: Schematic configuration of the test MR damper.

These models may be grouped into three broad categories based upon the modeling approach. These include: the piecewise continuous damper models; the dynamic structure equivalent models; and the dynamic characteristic equivalent models. The piecewise continuous damper models characterize the nonlinear and hysteretic properties by either

equivalent linear or piecewise linear viscous damping constants, such as Bingham plastic model [70, 71], nonlinear biviscous model and nonlinear hysteretic biviscous model [72]. The dynamic structure equivalent models include the famous Bouc-Wen model [5, 59, 64, 73] and the viscoelastic-plastic model [74-76]. The dynamic characteristic equivalent models attempt to describe the dynamic hysteresis properties on the basis of regression functions such as those proposed by Choi et al. [77] and Wang et al. [69, 78]. Moreover, Leva [79] adopted an iterative and discrete method called linear-in-the-parameters NARX (nonlinear auto regressive with exogenous input) model to describe the hysteretic properties of electro-rheological (ER) and magneto-rheological (MR) dampers.

Design and synthesis of a controller to realize desirable variations in the damping properties continues to be a challenging task, mostly due to the strongly nonlinear and hysteretic properties of the damper. The presence of hysteresis can lead to a number of undesirable effects, including loss of stability and robustness, limit cycle oscillations and steady-state and transient tracking errors [80-82]. The damper and synthesis of a controller can be greatly simplified through development of a reliable model that can accurately predict the nonlinear hysteresis behaviour. A few studies have thus proposed models for characterizing the hysteretic properties of the MR dampers [69, 72, 73, 75, 77]. These models adapt kinds of modeling structures and identify the model parameters using the experimental measured data. The general validity of these models over a wide range of operating, excitation and response conditions has not been demonstrated.

Active vibration control systems have become a topic of considerable interest in

recent years, although the concept is not new, particularly for vehicles. In order to improve ride, handling and comfort performances, a number of concepts in active suspension have been proposed. A large number of analytical and experimental studies have been reported on active and semi-active suspensions [8, 14, 15, 42, 83, 84]. Passive suspension systems temporarily store and dissipate energy on the basis of fixed suspension properties. The performance enhancements of such suspension are thus limited to identification of optimal stiffness and damping coefficients. Active suspensions systems in general employ a high performance force generator in the form of hydraulic or pneumatic actuators with hydraulic/pneumatic power supply, and can add or dissipate energy in response to changing excitation and response [14, 42, 85]. Such suspensions thus yield superior performance in terms of ride and handling characteristics of vehicle [16, 45]. Although a vast number of active suspension and controller concept have evolved over the past 40 years, their implementation in such applications have been prohibitive due to high associated cost, power requirements and added weight.

Semi-active suspensions generally adopt controllable dampers instead of the conventional hydraulic dampers and require only low level power to modulate the damping properties in accordance with a control law based upon the excitation and response variables. A number of studies have suggested that semi-active suspensions yield only marginal performance gain, which is mostly attributed to limited controller bandwidth, limited damping force range of hydraulic dampers, switching discontinuities of valves, etc. [6, 47, 86, 87]. Magneto-rheological fluids offer considerable potential for

developing adaptive semi-active suspensions, since they offer wide variations in fluid viscosity with applied current and thus high damping bandwidth. Moreover, the variations in damping force are achieved in the absence of control valves, while the fluid responds to magnetic field in a highly rapid manner in the order of a few milliseconds under a low level voltage [88]. In a recent study, the potential benefits of MR damper suspension seat have been investigated for reducing the incidence and severity of end-stop impacts through laboratory experiments [55]. The suspension seat employed a MR-damper operating at 12 V excitation and a rotary potentiometer served as the feedback from the controller.

As mentioned above, the MR fluid dampers exhibit complex nonlinearities such as hysteresis and magnetic field saturation. A nonlinear controller may be synthesized using different approaches, such as that based upon linearization of the nonlinear dynamic system [89, 90], the nonlinear PID controller [49, 91], the inverse model control scheme [92] or the inverse compensator [90, 93], the adaptive control algorithm [80], fuzzy logic control and dynamic neural network control method [21]. These techniques, however, have not been applied for the vehicle suspension systems which comprise only a few of components or elements possessing hysteretic characteristics. The identification of a practical control scheme thus forms the necessary task for vehicle suspension controller design. Furthermore, an adaptively controlled vehicle suspension system, based upon magneto-rheological (MR) properties of fluids, could offer considerable potential for performance enhancement of both, primary (wheel) as well as secondary (seat)

suspensions applications, with minimal power and weight requirements.

A number of semi-active control schemes have been synthesized with varying performance objectives of the vehicle suspension [49, 18-21]. The well-known “skyhook” control law was initially proposed by Karnopp et al. [86] to limit the resonant oscillations of the sprung mass and to achieve improved attenuation of vibration in the isolation range of frequencies. Yokoyama et al. [19] synthesized a sliding mode controller, in which a “skyhook” model is used as the reference model for tracking control. This study concluded that the skyhook reference model could yield superior vibration isolation performance of the MR-damper when considered in conjunction with a quarter-car model. Liao et al. [20] utilized the LQG control law with acceleration feedback to realize damper force tracking with reference to an optimal damping force, in which the state variables are estimated from the acceleration responses using the Kalman estimator. Guo et al. [21] employed the neural network control strategy including an error back propagation algorithm with quadratic momentum of the multi-layer forward neural networks. Choi et al. [18] applied the PID control law to track the desired damping force for a full-vehicle model.

Some of these concepts have also been applied for suspension seats to achieve improved shock and vibration isolation performance [36, 49, 52, 54, 55]. A recent study on assessment of a suspension seat with controlled MR-damping, has demonstrated the suspension effectiveness in limiting the shock motions by eliminating end-stop impacts [55]. The measured results did not show improvement in vibration attenuation

performance over the fixed damping suspension. Another study has shown improved vibration isolation, while the end-stop impact performance was not considered [49]. While a few studies have attempted the implementation of this control methodology for enhancement of shock and vibration attenuation performance, the contributions due to hysteresis and switching discontinuity are invariably ignored.

1.2.7 Performance Analysis of Suspension Seats

Performance analysis of suspension seats can be categorized into two groups on the basis of the methodology employed, namely, experimental and analytical methods. The international standard ISO-2631 [94] provides the guidance for the evaluation of human exposure to whole-body vibration, defining the means to evaluate periodic, random and transient vibration with respect to human responses: health, comfort, perception and motion sickness. The international standard ISO-7096 [95] provides guidance on performance analyses of suspension seats through laboratory experiments. The method requires the use of human subjects with specific body masses. The vibration isolation properties of suspension seats are thus widely evaluated through laboratory tests involving either human subjects or equivalent rigid masses [10, 24, 96, 97]. The laboratory studies have utilized a whole-body vehicular vibration simulator that can synthesize the vibration environment of different vehicles [1, 30]. The simulator comprises a seat platform supported on two servo-hydraulic actuators and a servo-control system interfaced with a digital signal generator. The response characteristics of the seats,

evaluated in terms of accelerations due to excitation and transmitted vibration under different excitations, are assessed in accordance with the measures defined in ISO 2631-1 (1997) in view of human exposure to vibration and shock, and the vibration attenuation performance of suspension seats [55, 98]. The basic evaluation methods include the frequency-weighted *rms* (root mean square) acceleration, vibration dose value (*VDV*), seat effective amplitude transmissibility (*SEAT*), *VDV* ratio and peak acceleration of the seated mass. The frequency-weighting whose transfer function is defined in ISO 2631-1 (1997) within the pass-band of 0.4-100 Hz, is applied to the response acceleration time histories.

While the experimental methods allow for consideration of the dynamic interactions of the body and the seat, these methods generally yield large inter-subject variability and involve repetitive trials with representative human subject samples. Alternatively, a few studies have employed analytical methods for assessing suspension seat performance and to derive design guidelines. These studies have thus developed linear models of suspension seat, which were also validated using the experimental results [27, 33, 99, 100]. The general model for the suspension seat is formulated upon integration of either linear or nonlinear component models. The human body is generally represented by a rigid mass, assuming that human body yields negligible contributions to the coupled system dynamics at low frequencies. This is evident from the measured apparent mass properties of the human body, which resembles that of a rigid mass at frequencies below 2 Hz [97, 101]. Single and multi-DOF mechanical-equivalent models of the seated body

have also been developed and integrated to the suspension seat model [3, 30, 31]. These models are developed on the basis of measured apparent mass characteristics of the seated body exposed to vertical whole-body vibration. Such models could be effectively applied for performance analyses of suspension seat with a MR-damper and synthesis of the controllers.

1.3 Scope and Objectives of the Dissertation Research

The design and analysis of suspension seats can be effectively performed using modeling and simulation techniques to examine the suspension's behavior under known excitation. The controller synthesis for a MR damper, however, necessitates a thorough characterization of the MR-damper, particularly its nonlinear hysteretic and force-saturation properties. The development of a model of the MR-damper forms the foremost challenging task, which could facilitate controller development, if proven effective. The nonlinear variations in the damping force attributed to hysteresis and force-limiting are expected to pose considerable complexities in the model development and the controller design. The presence of such nonlinearities may deteriorate the system performance in view of force-tracking and could induce system instability. The dependence of the hysteresis and force saturation on the intensity the applied magnetic field forms the second challenging task, which is lacking in most of reported models. The force-velocity properties of MR-dampers exhibit considerable hysteresis that depends not only on the applied current but also on the nature of the response and excitation variables.

The ride vibration environment of vehicles employed in highway transportation of freight and passengers, and in some of the off-road sectors, comprises low to medium levels of vibration of continuous nature and occasional shock motions. On the other hand, the suspension seats employed in many off-road vehicles are also believed to be subject to end-stop impacts while operating on relatively rough terrains. The attenuation performance under steady-state vibration and prevention of end-stop impacts under high magnitude vibration and shock, however, poses contradictory design requirements for the suspension seats. A lightly damped and soft suspension is considered desirable for effective attenuation of continuous vibration of low to medium levels, provided that the excitation occurs at frequencies well above the seat's natural frequency. The attenuation of high magnitude vibration and shock, on the other hand, requires suspension designs with higher damping and stiffness to prevent end-stop impacts. In environments involving combinations of low, medium and high levels of continuous vibration and shocks, means of achieving variable damping are highly desirable to adapt to the varying excitations. This can be attempted through development and integration of either active or semi-active damping mechanisms within the suspension.

A number of intelligent suspension seats based upon active and semi-active controls have evolved since the past 40 years. The application of a fully-active suspension at the seat, however, is most likely prohibitive due to associated high cost and requirement of power for the servo-actuator system. The limited bandwidth of the semi-active dampers based upon hydraulic flow modulation, on the other hand, resulted in only marginal

benefits. The ER and MR fluids, which exhibit significant variations in their rheological properties within the duration of 10 ms, offer attractive potential to realize variable damping with high bandwidth. The MR fluids are considered to be superior to ER fluids due to their low power requirement and high yield strength. A number of designs of MR-dampers for vehicular suspension applications have thus evolved in recent years.

1.3.1 Objectives of the Dissertation Research

The overall goal is to contribute towards attenuation of continuous vibration and discontinuous shocks transmitted to the occupants by designing controllers for the suspension seat equipped with a MR-fluid damper. The dissertation objective thus deals with an adequate compromise between the performances under both the continuous vibration and end-stop impacts. The specific objectives of the dissertation research are formulated as follows:

- (a) Characterize the hysteretic force-velocity ($f-v$) and force-displacement ($f-d$) properties of a MR-damper under a wide range of applied current, and excitation frequency and amplitude.
- (b) Synthesize a generalized model for describing the force-saturation and hysteretic force-velocity characteristics of the MR damper as functions of the excitation and applied current.
- (c) Assess the effectiveness of the proposed model synthesis under a wide range of excitation and current condition through systematic laboratory experiments and simulations.
- (d) Propose a generalized model formulation comprising an independent function in current that may be implemented to different reported models for enhancing their prediction abilities.

- (e) Identify the model parameters and demonstrate the validity and limitation of the modified models using the measured data.
- (f) Develop an analytical model upon integrating the nonlinear component models to assess its vibration transmission performance under different types of deterministic and random excitations.
- (g) Investigate the influences of the passive damping parameters and identify damping requirements under different types of excitations.
- (h) Synthesize a sky-hook semi-active control algorithm in conjunction with the selected suspension seat and the MR-damper. Assess the control algorithm in view of the seat performance under various excitation signals and compare the performance characteristics with those of the passively damped suspension.
- (i) Derive an adaptive semi-active control algorithm to reduce the frequency of end-stop impacts under the limited free travel.
- (j) Develop a hardware-in-the-loop (HIL) simulation and platform for assessment and tuning of the controllers using a prototype damper subject to different types of excitation signals.

1.4 Organization of the Dissertation

This dissertation is organized into seven chapters describing systematic developments in realizing the stated objectives. The relevant reported studies are reviewed in appropriate chapters highlighting the scope and research contributions of the dissertation research. In Chapter 2, the properties of a prototype MR-damper are described through extensive laboratory measurements to characterize the hysteretic force properties under wide ranges of excitation magnitudes of control currents. A phenomenological model is realized upon formulation and integration of component functions describing the pre-yield hysteresis, saturated hysteresis loop, linear rise and current-induced rise. The model parameters are identified and the model validity is

demonstrated.

Chapter 3 further investigates a generalized but independent current-dependent hysteresis model which is implemented to a number of reported hysteresis models to enhance their prediction abilities over a range of applied currents. The parameters of the modified models are identified and the errors between the modified models results and the measured data are analyzed to demonstrate the effectiveness of the current-dependent function.

In Chapter 4, a generalized model of a comprising the component models is used to study the desirable damping properties under different types of excitations. A refined cushion model is also proposed. A set of performance measures is described to assess the performance of passive suspension seats under different types of excitation signals. The limitations of the passive suspension seat are identified for different excitation spectra.

In Chapter 5, a 'hi-lo' semi-active skyhook-based control algorithm (SC) is formulated to realize controlled MR-damping to improve the vibration isolation performance of the suspension seat. In order to further improve the shock attenuation performance of seat under high intensity excitations by limiting the frequency and severity of end-stop impacts, an integrated control scheme (IC) is synthesized by introducing a relative position control to the semi-active skyhook-based control algorithm. The performance characteristics of the MR-damper suspension seat model with the proposed controllers are assessed over a range of excitation. The contributions due to hysteresis effects and the role of the smoothing function are further discussed.

Chapter 6 presents the development of a hardware-in-the-loop (HIL) test and simulation platform, for further tuning of the proposed semi-active controllers and validation of the analytical formulations. The HIL technique could provide a realistic and repeatable testing environment with a relative low power hydraulic actuator. The open loop and close loop suspension seat systems are evaluated under various different conditions and excitation signals, while the responses including the displacement, velocity, acceleration and forces are recorded. The results are discussed to demonstrate the effectiveness of the proposed controller synthesis.

Finally, the highlights of the dissertation research, conclusions and recommendations for further studies are presented in Chapter 7.

CHAPTER 2

CHARACTERIZATION AND MODELING THE HYSTERETIC PROPERTIES OF A MR-FLUID DAMPER

2.1 Introduction

A wide range of Magneto-rheological (MR) fluid-based dampers are currently being explored for their potential implementation in various systems, such as vibration control devices and vehicle suspension. A number of analytical and experimental studies have clearly established superior potential performance benefits of MR dampers in vehicle applications in relation to conventional hydraulic dampers [18, 49, 55, 73-76, 102]. The MR dampers offer high viscous damping corresponding to low velocities in the pre-yield condition, while the post-yield saturation corresponding to high velocities can be characterized by a considerably lower viscous damping coefficient. The requirement of variable damping for the base or seat suspension of vehicles [18, 47, 51, 54, 63, 85], could be achieved with MR dampers with only minimal power consumption.

The MR damper is considered to be a continuously controlled semi-active damper, since it offers variable damping force with minimal power requirement, unlike a fully active suspension which could add or remove energy depending upon the demand with the help of an elaborate power supply. The semi-active controlled MR fluid dampers offer rapid variations in damping properties in a reliable fail-safe manner, since they continue to provide adequate damping in a passive manner in the event of control hardware malfunction [103]. Although a vast number of semi-active variable damping concepts

based upon hydraulic flows modulation and electro-rheological (ER) fluids have been developed, definite advantages of the MR-fluid dampers have been clearly established, such as significantly higher yield stress and wider operating temperature [73-76, 102, 103].

Owing to the rheology of the MR fluid in terms of its shear stress-strain rate behavior, the damper exhibits highly non-linear variations in damping force, attributed to the hysteresis and force-limiting properties of the fluid as functions of intensity of applied magnetic field, and displacement and velocity of the piston. The development of an effective controller for realizing desirable variations in damping requires accurate characterization of hysteretic force-velocity (f - v) characteristics of the MR damper in the pre-yield condition and force saturation in the post-yield condition. In view of its highly non-linear properties, considerable attempts are being made to study their dynamic behavior for model synthesis and for developing effective control algorithms [49, 72-74, 102].

Spencer *et al.* [73] proposed a damper model on the basis of the Bouc-Wen hysteresis model. The model, however, poses inherent difficulties in predicting essential parameters and in realizing control systems for desired tracking control performance. Bingham plastic model has been proposed assuming rigid material behavior in the pre-yield, while the shear flow in the post-yield is characterized by a viscous damping coefficient [76, 102]. Assuming the material to be plastic in both pre- and post-yield conditions, Stanway *et al.* [72] proposed a nonlinear model, where the pre-yield force is characterized by

considerably high viscous damping. On the basis of this model, Wereley *et al.* [76, 102] proposed a nonlinear hysteretic bilinear model by fitting the force-velocity characteristics using four parameters: pre- and post-yield viscous damping coefficients, yield force and zero-force velocity intercept.

The above models, however, do not include the effects of continually varying nonlinear control current. Moreover, hysteretic damping force generated by a MR-damper not only depends upon the intensity of the magnetic field but also upon the excitation frequency and amplitude. This dependence of the hysteretic force on the nature of excitation has not yet been accurately characterized. In this chapter, a generalized model is proposed to characterize the biviscous hysteretic force characteristics of a magneto-rheological (MR) fluid damper using symmetric and asymmetric sigmoid functions on the basis of fundamental force generation mechanism, observed qualitative trends and measured data under wide range of control and excitation conditions. Extensive laboratory measurements were performed to characterize the hysteretic force properties of a MR damper under a wide range of magnitudes of control current and excitation conditions (frequency and stroke). The global model is realized upon formulation and integration of component functions describing pre-yield hysteresis, saturated hysteresis loop, linear rise and current-induced rise. The validity of the proposed model is demonstrated by comparing the simulation results with the measured data in terms of hysteretic force-displacement ($f-d$) and force-velocity ($f-v$) characteristics under a wide range of test conditions. The proposed model could be effectively applied

for characterizing the damper hysteresis and for development of a semi-active controller for implementation in vehicular suspension applications.

2.2 Characterization of Damping Properties

A MR damper RD-1005-3, developed by Lord Company and schematically shown in Figure 1.3, is considered for characterizing its damping properties in the laboratory. The damper consists of a nitrogen-charged accumulator and two MR-fluid chambers separated by a piston with orifices and coils. The variations in viscous and shear properties of the fluid, caused by the applied magnetic field, cause variations in the damping force. A dc current, limited to 2 A, serves as the command signal as well as the input for the coils. The considered damper could provide a total travel of about 2 inches (about 50 mm). Laboratory tests are performed to characterize the f - v and f - d properties of candidate MR-damper over a wide range of excitation condition.

2.2.1 Experimental Methodology

The force-velocity and force-displacement characteristics of the test MR damper are measured in the laboratory to characterize the damper hysteresis over a range of excitations. The damper is installed on an electro-hydraulic vibration exciter between the exciter and a fixed inertial frame through a force transducer, as pictorially shown in Figure 2.1. Position (LVDT) and velocity (LVT) sensors are installed on the exciter to measure the instantaneous position and velocity of the damper piston. The damper is

subject to harmonic displacement excitations of different constant amplitudes at selected discrete frequencies. The force, velocity and displacement data, acquired through a data acquisition board, were directly imported into an Excel worksheet using dynamic data exchange to obtain an on-line display of the hysteretic f - v characteristics. A dual regulated DC power supply was used to supply the command current to the damper. A thermocouple was also mounted on the damper body to monitor the damper temperature. The experimental data under each condition were acquired in the vicinity of a defined temperature range ($30 \pm 10^\circ\text{C}$), so as to suppress the thermal effects in the characterization task.

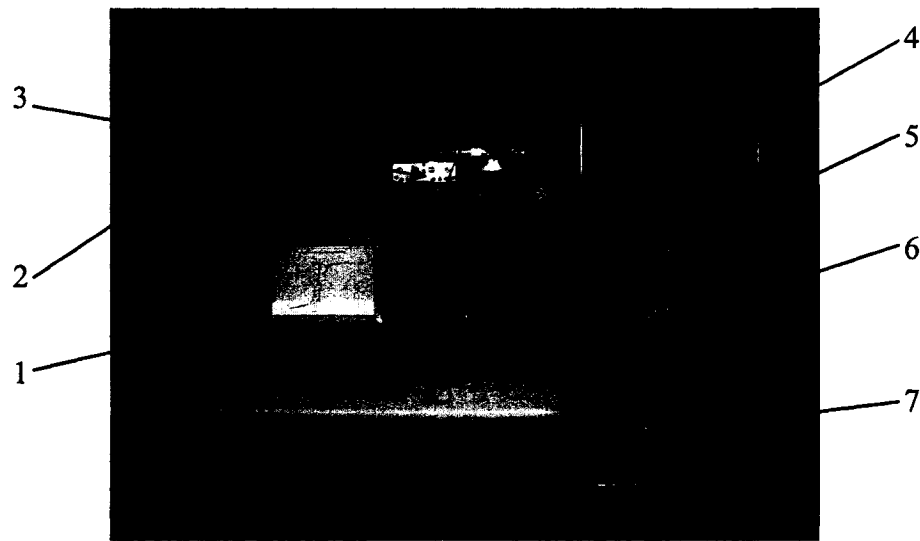


Figure 2.1: A pictorial view of the MR damper test system (1-Servo-controller; 2-Data acquisition; 3-DC power supply; 4-Temperature monitor; 5-Force transducer; 6-MR-damper; 7-Hydraulic actuator).

The hysteretic force-velocity characteristics of the MR-fluid damper are measured under sinusoidal displacement excitations in the 0 to 15 Hz frequency range, which is

considered to represent the range of predominant vehicular ride motions along the vertical axis [99]. The tests are performed with constant magnitudes of displacement, ranging from 2.5 to 18.75 mm, and control currents to the coil in the range 0 to 1.5 A. A total of 203 tests were performed corresponding to different combinations of frequency (0.1, 0.5, 1.5, 2.5, 5.0, 7.5, 10.0, 12.5 and 15.0 Hz), stroke (2.5, 6.35, 12.5 and 18.75 mm), and control current (0.0, 0.25, 0.5, 0.75, 1.0, 1.25 and 1.5 A). The amplitudes of displacement excitations at higher frequencies were limited to lower values to ensure damper operation within safe velocity limits. Table 2.1 summarizes the test matrix.

The measurements were initially performed under low amplitude excitation at a frequency of 0.1 Hz. The measured force was considered to represent the seal friction, assuming negligible contributions due to MR-fluid damping at extremely low velocities. The damper was then subjected to a selected excitation condition and current using the servo-controller and the voltage-current circuit, respectively. The force, velocity and displacement signals were acquired in the steady-state as the body temperature approaches 30 °C. The measured signals were displayed in the form of time-histories and curves in $f-v$ and $f-d$ corresponding to each test condition. The acquired data are subsequently analyzed to characterize important properties of the MR-fluid damper.

Table 2.1: Test matrix.

Amplitude (A_r)	Current (i)	Frequency f_r (Hz)									
		0.1	0.5	1.5	2.5	5.0	7.5	10	12.5	15	
2.5 mm	0	x	x	x	x	x	x	x	x	x	
	0.25 A	x	x	x	x	x	x	x	x	x	
	0.50 A	x	x	x	x	x	x	x	x	x	
	0.75 A	x	x	x	x	x	x	x	x	x	
	1.00 A	x	x	x	x	x	x	x	x	x	
	1.25 A	x	x	x	x	x	x	x	x	x	
	1.50 A	x	x	x	x	x	x	x	x	x	
6.35 mm	0	x	x	x	x	x	x	x	x	x	
	0.25 A	x	x	x	x	x	x	x	x	x	
	0.50 A	x	x	x	x	x	x	x	x	x	
	0.75 A	x	x	x	x	x	x	x	x	x	
	1.00 A	x	x	x	x	x	x	x	x	x	
	1.25 A	x	x	x	x	x	x	x	x	x	
	1.50 A	x	x	x	x	x	x	x	x	x	
12.5 mm	0	x	x	x	x	x	x				
	0.25 A	x	x	x	x	x	x				
	0.50 A	x	x	x	x	x	x				
	0.75 A	x	x	x	x	x	x				
	1.00 A	x	x	x	x	x	x				
	1.25 A	x	x	x	x	x	x				
	1.50 A	x	x	x	x	x	x				
18.75 mm	0	x	x	x	x	x					
	0.25 A	x	x	x	x	x					
	0.50 A	x	x	x	x	x					
	0.75 A	x	x	x	x	x					
	1.00 A	x	x	x	x	x					
	1.25 A	x	x	x	x	x					
	1.50 A	x	x	x	x	x					

2.2.2 Force-velocity and Force-displacement Characteristics

As an example, Figures 2.2 and 2.3 illustrate the measured force, velocity and displacement time-histories together with force-displacement (f - d) and force-velocity (f - v)

characteristics as a function of the control current (i) under $A_r = 6.25$ mm and $f_r = 2.5$ Hz, where A_r , f_r are respectively defined as the amplitude and frequency of the harmonic excitation. It should be noted that the force-displacement loops in Figure 2.3 (a) follow a clockwise path with increasing time, while the force-velocity loops in Figure 2.3 (b) follow the counterclockwise path with increasing time. The results shown in Figure 2.3 clearly show strong dependence of damper hysteresis in the pre-yield condition on the applied current. The f - v characteristics further show the post-yield force-limiting behavior that also relies strongly on the applied current. Such nonlinear damper properties are further dependent upon the excitation frequency and amplitude, as evident from Figure 2.4.

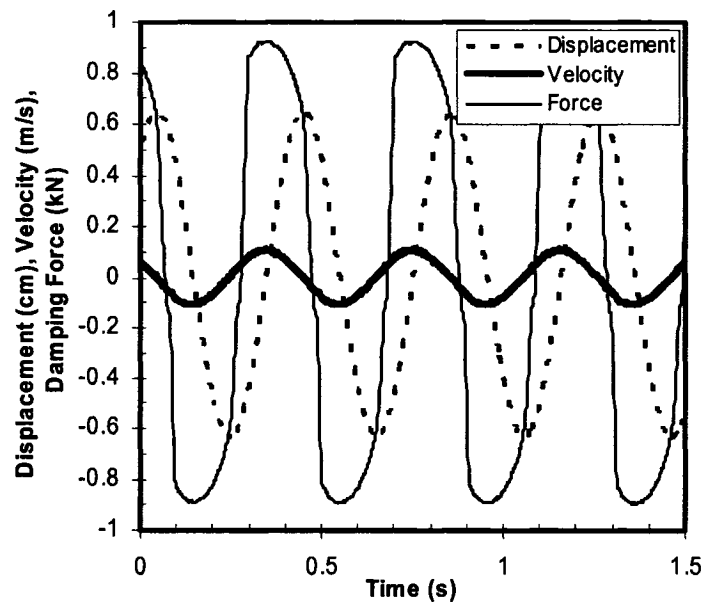


Figure 2.2: Time-history of response and excitation under a harmonic excitation ($A_r = 6.25$ mm; $f_r = 2.5$ Hz; and $i = 0.50$ A).

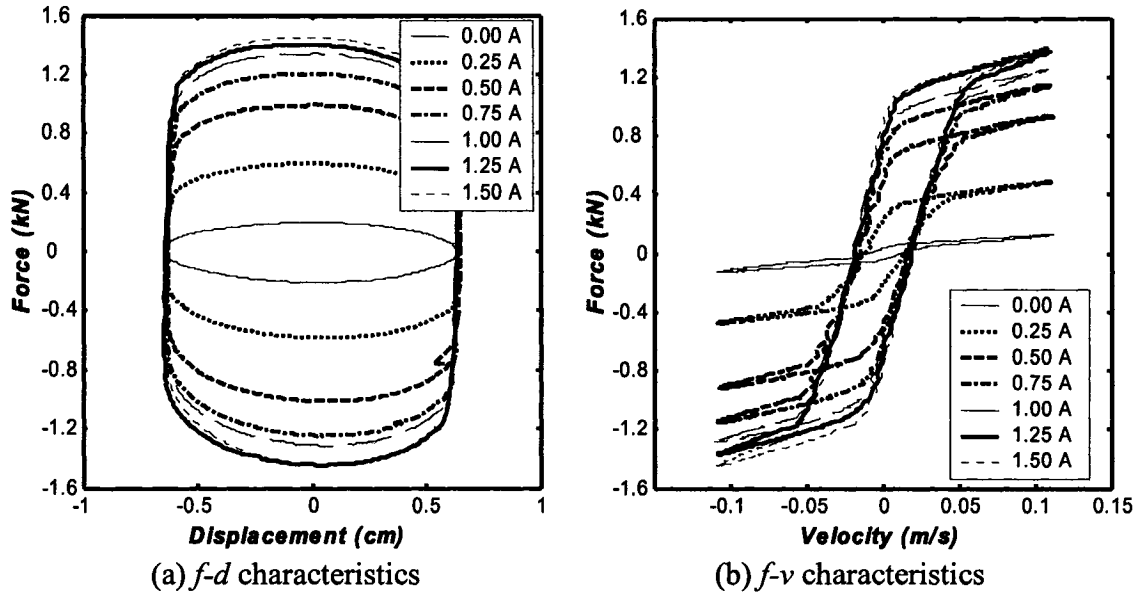


Figure 2.3: Measured damper responses as functions of applied current under a harmonic excitation ($A_r = 6.25$ mm; and $f_r = 2.5$ Hz).

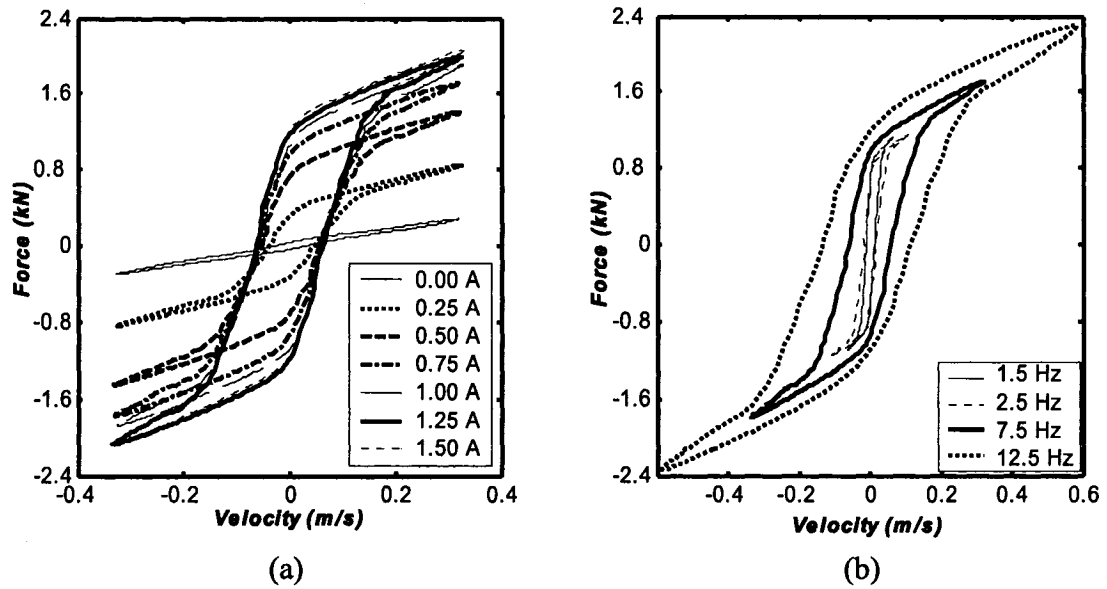


Figure 2.4: Force-velocity characteristics as functions of: (a) applied current, $A_r = 6.35$ mm, $f_r = 7.5$ Hz; and (b) frequency, $A_r = 6.35$ mm, $i = 0.75$ A.

Considering that the performance characteristics of suspension dampers are mainly evaluated in terms of $f-v$ properties; further data analysis and model synthesis is limited to

this data alone. The data acquired under extremely low frequency $f_r = 0.1$ Hz and $A_r = 2.5$ mm, was used to evaluate the contribution due to seal friction alone. The results revealed negligible seal friction in relation to the fluid hysteresis.

The essential dynamic behavior of the MR damper required for model synthesis can be deduced from the $f-d$ and $f-v$ characteristics, shown in Figures 2.2 to 2.4, and summarized below:

- *Incremental Feature:* The $f-v$ characteristics of MR dampers can be generally represented as symmetric bi-nonlinear curves with significant hysteresis at lower velocities (pre-yield), followed by linearly increasing force at higher velocities (post-yield). A force-limiting behavior is also evident during transition between low and high velocity responses. This behavior is also evident in the $f-v$ characteristics of typical hydraulic dampers with low-speed bleed flows and high speed blow-off valves [105]. The damping force may thus be characterized as an incremental function of velocity in the pre- and post-yield conditions.
- *Passive Behavior:* The MR damper exhibits almost viscous property when zero control current is applied (passive property), as evident from the near elliptical $f-d$ curve and nearly linear $f-v$ curve with relatively small hysteresis (Figure 2.3 (b) and (c)).
- *Controllability:* The damping force increases considerably with magnitude of control current. The measured yield force (force developed at the onset of post-yield saturation) corresponding to either $dv/dt < 0$ (upper $f-v$ curve) or $dv/dt > 0$ (lower $f-v$ curve) can be observed with increasing control currents. The rate of increase in force magnitude is approximately linear under lower current levels ($< 0.5 A$), which tends to gradually decrease under higher values of applied current ($0.5 \sim 1.25 A$). A further increase in current ($> 1.25 A$) yields saturation of the damping force.
- *Hysteretic Phenomenon:* The damper hysteresis progresses along counterclockwise path with increasing time (Figure 2.3 (c)). The upper curve in the $f-v$ characteristics reflects force variation with decreasing velocities ($dv/dt < 0$), while the lower curve corresponds to force with increasing velocities ($dv/dt > 0$). The mean slope of hysteretic loop, referred to as the viscous damping coefficient, is dependent upon both the control current and excitation

conditions (frequency and stroke).

- *Viscous Character*: Given a control current, the MR damper would yield nearly identical f - v curves under same excitation velocity that may be realized from different combinations of frequency and stroke. The damping force can therefore be expressed as a function of piston velocity and control current, with appropriate consideration of the force-limiting behavior.

2.3 Synthesis of a Generalized Sigmoid Model

A number of models have been proposed to characterize the hysteretic damping properties of MR-damper on the basis of various require functions. These models generally do not create the current dependence, which is clearly evident from the experimental results. The selected reported models are critically reviewed in Chapter 3. General overall structure and modifications of model are proposed to enhance their applicability for MR-damper. The f - v characteristics of the MR damper reveal pronounced nonlinear hysteresis and force-limiting properties. Hysteresis is a widely known phenomenon commonly encountered in a broad spectrum of physical systems. Structures invariably exhibit hysteresis, especially when the response becomes inelastic [22, 104]. The model synthesis of such systems thus poses a challenging task. In this study, the equivalent characteristic method is applied on the basis of experimental data to achieve a model synthesis in the form of a nonlinear algebraic function to fully characterize the hysteretic characteristics of the MR damper. The model also builds upon the observed features to enhance an understanding of the underlying damping mechanism, and relationships between the hysteresis and nature of excitation (frequency and stroke).

2.3.1 Generalized Characteristic Parameters

The typical f - v characteristics of a MR damper, corresponding to specific magnitudes of velocity and control current, can be represented by a general hysteresis loop shown in Figure 2.5. The mean damping characteristics, frequently used to evaluate the overall system response [99, 105], can also be easily derived from the loop as shown by the bold curve. The model synthesis can be obtained from the generalized hysteresis loop with appropriate considerations of the features observed from the experimental data. The essential parameters required to formulate the model are described below. Owing to the symmetry, the parameters are described for compression alone ($v \geq 0$).

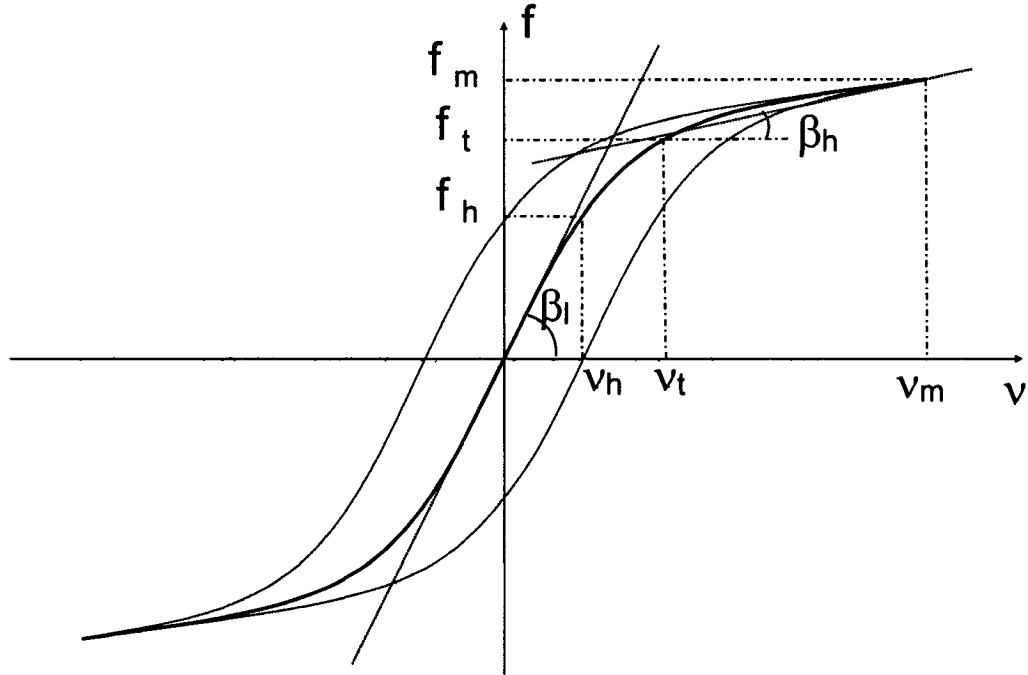


Figure 2.5: Generalized hysteretic f - v characteristics.

- *Maximum Velocity* (v_m , m/s): Maximum velocity of the damper piston determined from the excitation frequency and stroke.

- *Maximum Force* (f_m , N): Maximum force developed by the MR damper corresponding to specified v_m and control current i .
- *Zero-Force Velocity Intercept* (v_h , m/s): Piston velocity corresponding to zero damping force under given i and excitation condition.
- *Zero-Velocity Force Intercept* (f_h , N): Damping force corresponding to zero velocity under given i and excitation condition.
- *Transition Velocity* (v_t , m/s): Piston velocity corresponding to onset of force-limiting property (post-yield condition) leading to linearly increasing force and saturation, as derived from the mean curve. The transition velocity is obtained from the intersection point (f_t , v_t) of the tangent curves drawn to the mean f - v curve near $v = 0$ and to the mean curve in the post-yield (slope = β_h), as shown in Figure 2.5.
- *Transition Force* (f_t , N): Mean damping force corresponding to v_t .
- *Low Velocity Slope* (β_l , Ns/m): Slope of the mean f - v curve at $v = 0$, representing low speed viscous damping coefficient.
- *High Velocity Slope* (β_h , Ns/m): Slope of the mean f - v curve at v_t , representing high-speed viscous damping coefficient.

2.3.2 Synthesis of the Characteristic Curves

The family of f - v hysteresis curves for the MR damper (Figure 2.4) is described by three distinct properties: *saturated hysteresis loop*, *linear rise* and *current-induced rise*.

The various curves attained at increasing control currents may be considered as an amplification of the passive characteristics ($i = 0$). A saturated hysteresis loop in the absence of linear rise, $f_s(v + v_h)$, can be formulated by the symmetric sigmoid function with bi-deflexion in the lateral axis:

$$f_s(v + v_h) = f_t \frac{1 - e^{-\alpha(v+v_h)}}{1 + e^{-\alpha(v+v_h)}} \quad (2.1)$$

where v is the instantaneous relative velocity of the damper piston and α is a constant used to adjust the slope of the hysteresis curve.

The linear rise segment of the curves which relates to the force-limiting property in the post-yield condition can be expressed by the linear function, $c_v(v)$, which is often referred to as high velocity damping coefficient:

$$c_v(v) = 1 + k_v |v| \quad (2.2)$$

where k_v is a constant describing the influence of excitation condition on the linear rise.

Equations (2.1) and (2.2) allow the formulation of a general hysteresis loop as shown in Figure 2.6.

$$f(v + v_h) = f_t \frac{1 - e^{-\alpha(v+v_h)}}{1 + e^{-\alpha(v+v_h)}} (1 + k_v |v|) \quad (2.3)$$

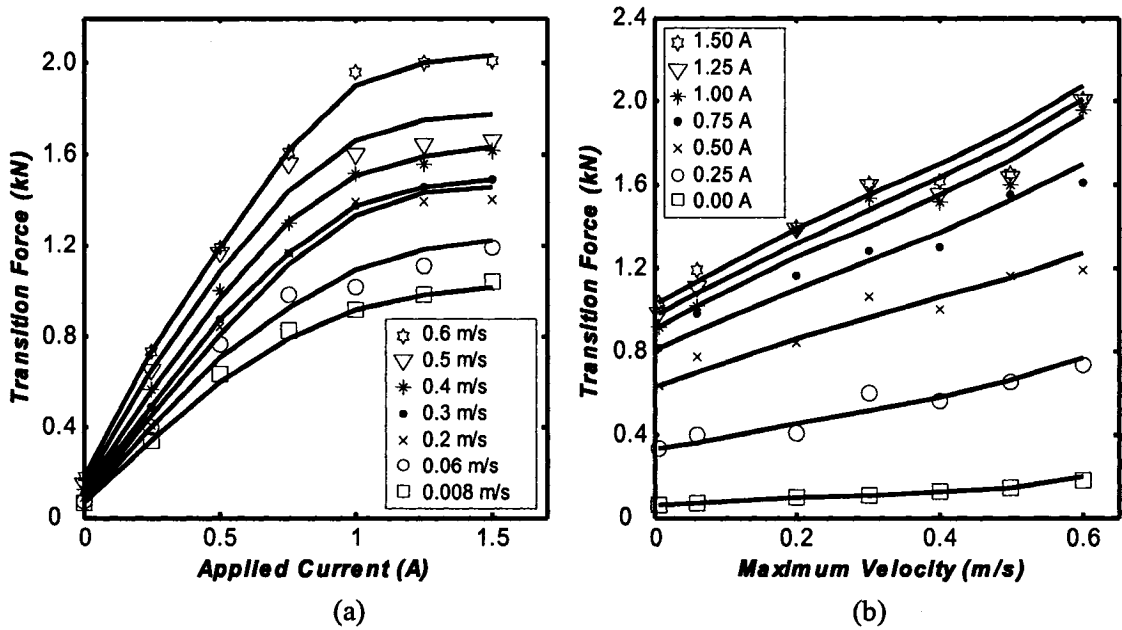


Figure 2.6: Measured transition force f_t as a function of i and v_m .

2.3.3 Influence of Control Current

If the current-induced rise is considered as a shift of the f - v curve, the role of control current in the model synthesis can be modeled as a gain $c_i(i)$ limiting the force to f_i . The gain function, $c_i(i)$, is derived with systematic considerations of the relationships between f_t, v_h, α and k_v corresponding to given excitation condition and control current. This requires the derivation of rather complex relationships among the various characteristic parameters (f_t, v_h, α, k_v) and excitation conditions, as described below.

A. Transition force f_t

The experimental data suggest strong dependence of f_t on both the applied constant current i , and on the excitation condition (v_m). The transition force may thus be expressed as:

$$f_t = f_0 c_e c_i \quad (2.4)$$

where f_0 denotes the constant base value of f_t taken as the seal friction force, while coefficients c_e and c_i describe the influence of v_m and i on f_t , respectively. This is evident from the variation of measured transition force as a function of v_m and i , as shown in Figure 2.6. The results also show the nonlinear incremental behavior that can be characterized by an *asymmetric sigmoid function* with a certain bias in the lateral axis. Consequently, the control current gain c_i is expressed as:

$$f_i(i) = 1 + \frac{k_2}{1 + e^{-a_2(i+I_0)}} - \frac{k_2}{1 + e^{-a_2 I_0}} \quad (2.5)$$

where k_2 and a_2 are positive constants, and I_0 is an arbitrary constant. Equation (2.5) yields a unit value of f_i for a passive damper ($i = 0$).

The evolution of f_i in relation to v_m with varying control current i can also be observed from the measured data plotted in Figure 2.6 (b). The data suggests that f_i can be expressed by an exponential function of v_m . The coefficient c_e is thus formulated as:

$$c_e(v_m) = 1 + e^{a_1 v_m} \quad (2.6)$$

where a_1 is a positive constant used to adjust the rising rate of the exponent v_m . It should be noted that the maximum velocity v_m is not a directly measurable quantity. It is however essential to derive a relationship between the hysteretic characteristics and v_m , which would enhance the synthesis for implementation over a broad range of operating conditions. The measured data (Figures 2.3 and 2.4) clearly show that the damper response is strongly dependent upon excitation frequency $2\pi f_r$ and stroke A_r . Although these excitation conditions can be equivalently expressed by the maximum velocity for harmonic motion, $v_m = 2\pi f_r A_r$, v_m can not be directly measured in real time, specifically under random excitations. Alternatively, the magnitude of v_m can be derived from the instantaneous position x and acceleration \ddot{x} :

$$v_m = 2\pi f_r A_r = \sqrt{(\dot{x})^2 - \ddot{x}x} \quad (2.7)$$

where $\dot{x} = v$ and $\ddot{x} = dv/dt$ are the instantaneous piston velocity and acceleration, respectively.

Upon substituting for f_i and c_e from Equations (2.5) and (2.6) into (2.4), the transition force f_t may be expressed as:

$$f_t = f_0(1 + e^{a_1 v_m})(1 + \frac{k_2}{1 + e^{-a_2(i+I_0)}} - \frac{k_2}{1 + e^{-a_2 I_0}}) \quad (2.8)$$

B. Linear rise coefficient k_v

The rate of linear rise at high velocities β_h can be estimated from the mean f - v curve, as shown in Figure 2.5:

$$\beta_h = \frac{f_m - f_t}{v_m - v_t} \quad (2.9)$$

where the parameters f_m, f_t, v_m and v_t are characteristic parameters, deduced from the measured data corresponding to different values of current i . Equation (2.9) is solved to calculate the slope of the high velocity region as a function of v_m and i . Figure 2.7 further shows the dependence of β_h on v_m and i , as derived from the measured data. The results show exponential decay in β_h with increasing v_m under a constant control current i , and a gradual increase with i under a specified v_m . The identical trends are also evident from the computed results presented in the Table 2.2.

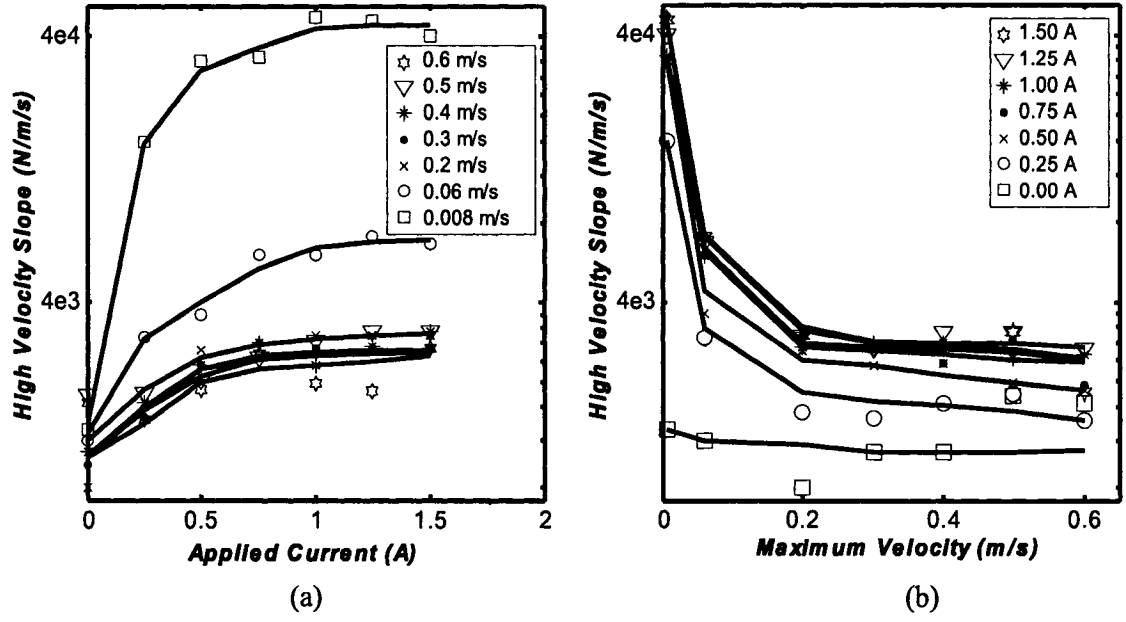


Figure 2.7: Variations in high velocity slope β_h with i and v_m .

Table 2.2: High Velocity Slope β_h as function of v_m and i .

v_m (m/s)	0.008	0.06	0.2	0.3	0.4	0.5	0.6
i (A)	High Velocity Slope β_h (Ns/m)						
0.00	333	300	200	274	274	445	417
0.25	4000	733	384	367	414	450	360
0.50	8000	900	657	573	580	497	467
0.75	8333	1500	670	700	700	617	637
1.00	11667	1500	744	667	580	717	490
1.25	11333	1767	744	667	680	767	460
1.50	10000	1667	744	668	772	767	667

The effect of i on β_h can be further obtained from the analysis of the general formulation of the hysteresis model, described in Equation (2.3). Owing to the saturation property of the sigmoid function, the rate of change of force with respect to velocity

corresponding to higher velocities yields following relationship between β_h and the linear rise coefficient k_v .

$$\beta_h = f_i k_v = f_0 c_e f_i k_v \quad (2.10)$$

The above relation reveals that β_h depends on both the excitation condition v_m , and on the control current i . The measured data presented in Figure 2.7 further suggests that the excitation condition has a relatively small effect at higher velocities. Considering that the coefficient c_e increases exponentially with v_m , the linear rise coefficient k_v can be expressed as:

$$k_v = k_1 e^{-a_4 v_m} \quad (2.11)$$

where k_1 and a_4 are positive constants.

C. *Hysteresis slope coefficient α*

The low velocity slope β_l of the hysteretic loop, shown in Figure 2.5, can be derived from the characteristic parameters f_h and v_h , as $\beta_l = f_h/v_h$. Table 2.3 summarizes the slope values for different values of v_m and i . Figure 2.8 further illustrates the variations in β_l with v_m and i , as derived from the measured data under selected excitation conditions. The results show trends identical to those observed for high velocity slope in Figure 2.7, namely the rapidly decaying β_l with increasing v_m .

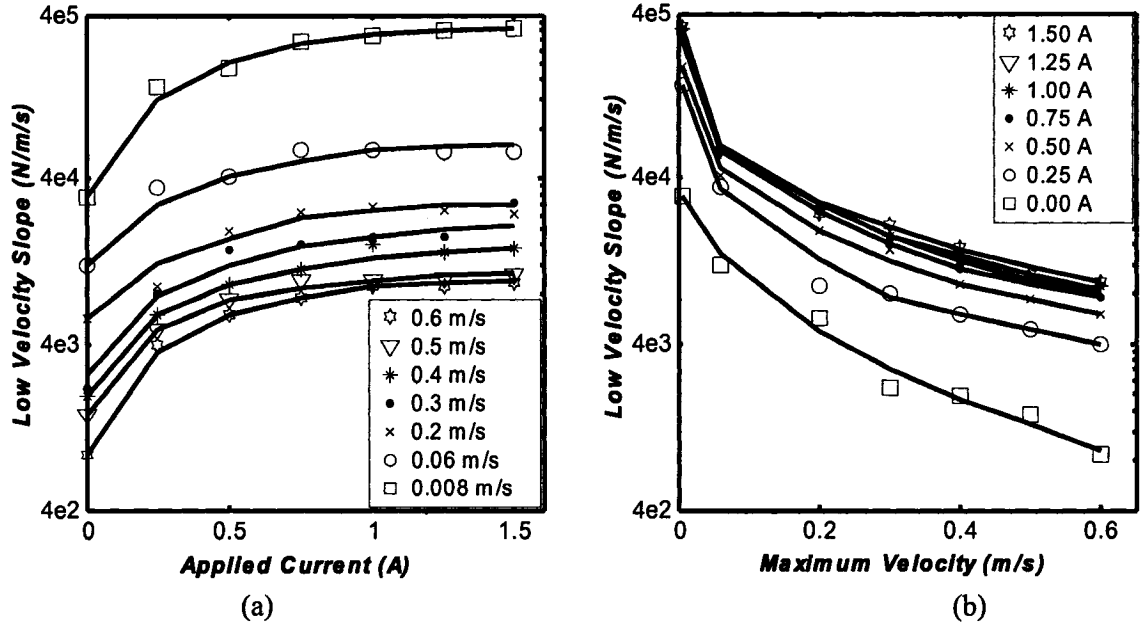


Figure 2.8: Variations in low velocity slope β_l with i and v_m .

Table 2.3: Low Velocity Slope β_l as function of v_m and i .

v_m (m/s)	0.008	0.06	0.2	0.3	0.4	0.5	0.6
i (A)	Low Velocity Slope β_l (Ns/m)						
0.00	7692	3000	1429	550	485	372	216
0.25	36250	8720	2270	2010	1500	1240	1000
0.50	47429	10200	4760	3750	2280	1867	1530
0.75	68205	14837	6230	4033	2860	2463	1904
1.00	74286	14810	6710	4453	2990	2442	2232
1.25	80909	14570	6464	4485	3590	2518	2236
1.50	81333	14500	6110	7222	3822	2600	2340

The low speed slope could also be calculated from Equation (2.3), by taking the rate of change of force with respect to velocity corresponding to $v = 0$, such that:

$$\beta_l = \frac{1}{2} \alpha f_i = \frac{1}{2} \alpha f_0 c_e f_i \quad (2.12)$$

Considering that the coefficient c_e increases exponentially with v_m , the hysteresis slope coefficient α can be expressed as:

$$\alpha = \frac{a_0}{1 + k_0 v_m} \quad (2.13)$$

where a_0 and k_0 are positive constants of the decreasing function α .

D. Zero-force velocity intercept v_h

Zero force velocity intercept v_h , shown in Figure 2.5, strongly affects the shape of the hysteresis curve, specifically the width of the hysteretic loop. The variations in v_h with v_m for different values of i and variations in v_h with i for different values v_m , deduced from the measured data further presented in Figure 2.9. The results show a strong dependence of v_h not only on the excitation condition v_m , but also on the control current i . The dependence of v_h on i for given values of v_m can be formulated by an asymmetric function similar to that defined for $c_i(i)$ in Equation (2.5). The dependence of v_h on v_m for given values of i can be described by a linear function in v_m . Furthermore, the sign of v_h can be determined from $\text{sign}(dv/dt)$. For $dv/dt = 0$, the velocity v approaches its maximum value v_m and the two enveloping curves converge. The zero-force velocity intercept can thus be expressed as a function of v_m and i in the following manner:

$$v_h = \text{sign}(\ddot{x}) k_4 v_m \left(1 + \frac{k_3}{1 + e^{-a_3(i+I_1)}} - \frac{k_3}{1 + e^{-a_3 I_1}} \right) \quad (2.14)$$

where a_3, k_3, k_4 and I_1 are positive constants.

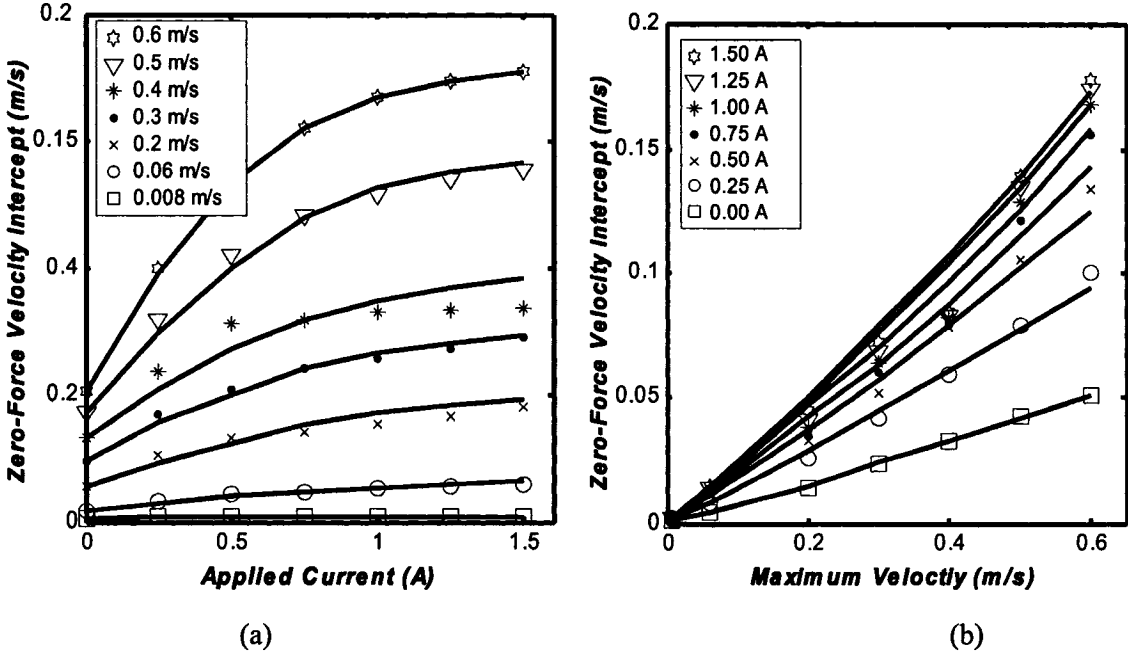


Figure 2.9: Variations in zero-force velocity intercept v_h with i and v_m .

E. Nature of excitation v_m

The nature of excitation refers to the peak velocity v_m , which is not a directly measurable quantity. It is, however, essential to derive a relationship between the hysteretic force characteristics and v_m , which would enhance the synthesis for implementation over a broad range of operating conditions. The measured data shown in Figures 2.3 and 2.4, illustrates that the damper response is strongly dependent upon the excitation frequency f_r and stroke A_r . Although these excitation conditions can be equivalently expressed by the maximum velocity for harmonic motion, $v_m = 2\pi f_r A_r$, v_m can not be directly measured in real time, specifically under random excitations. Alternatively, the magnitude of v_m can be estimated from the instantaneous displacement x ,

velocity \dot{x} and acceleration \ddot{x} of the damper piston, such that:

$$v_m = \sqrt{(\dot{x})^2 - \ddot{x}x} \quad (2.15)$$

where $\dot{x} = v$ is the instantaneous velocity of the damper piston.

2.3.4 Synthesis of the Overall Model

The overall model synthesis can be established from the generalized hysteresis loop model, Equation (2.3), by integrating above formulations which describe the nonlinear dependence of force on control current:

$$f_d = f_i(i) \frac{1 - e^{-\alpha(v+v_h)}}{1 + e^{-\alpha(v+v_h)}} (1 + k_v |v|) \quad (2.16)$$

where the current and excitation dependent functions which were formulated in the above section are summarized below:

$$\begin{aligned} f_i(i) &= f_0 (1 + e^{a_1 v_m}) \left(1 + \frac{k_2}{1 + e^{-a_2(i+I_0)}} - \frac{k_2}{1 + e^{-a_2 I_0}} \right) \\ v_h &= \text{sign}(\ddot{x}) k_4 v_m \left(1 + \frac{k_3}{1 + e^{-a_3(i+I_1)}} - \frac{k_3}{1 + e^{-a_3 I_1}} \right) \\ \alpha &= \frac{a_0}{1 + k_0 v_m}; \quad k_v = k_1 e^{-a_4 v_m}; \quad v_m = \sqrt{(\dot{x})^2 - \ddot{x}x} \end{aligned} \quad (2.17)$$

The overall model requires identification of a total of 13 parameters (f_0 , I_0 , I_1 , a_0 , a_1 , a_2 , a_3 , a_4 , k_0 , k_1 , k_2 , k_3 and k_4) from the measured data. It should be noted that the above hysteretic model can be easily simplified to the mean f - v model by letting $k_4 = 0$. (i.e. $v_h = 0$), and the number of parameters to be identified can be reduced from 13

to 10.

The measured data acquired under a wide range of excitation conditions and control current has been thoroughly analyzed to identify the model parameters for the particular damper consider and are summarized in Table 2.4.

Table 2.4: Model parameters identified from the measured data.

Parameter	Value	Parameter	Value
a_0	990	k_0	112.5
$a_1, (\text{m/s})^{-1}$	1.75	k_1	5.55
a_2, A^{-1}	2.85	k_2	19.4
a_3, A^{-1}	1.55	k_3	2.90
$a_4, (\text{m/s})^{-1}$	4.60	k_4	0.095
I_0, A	0.05	f_0, N	45.6
I_1, A	-0.08		

2.4 Model Validation

The proposed model synthesis, Equation (2.16), has been analyzed under a wide range of excitation conditions (stroke and frequency) and control current. The simulation results are compared with the measured data to evaluate the effectiveness of the model. The comparisons show reasonably good agreements between the simulation results and the test data, over the entire range of test conditions considered, with the exception of those attained under low levels of command current.

Figures 2.10 and 2.11 show comparisons of simulation results in terms of force-velocity characteristics with the measured data under a number of the test

conditions, as examples, to demonstrate the validity of the proposed model. The results also show the force-displacement response under 6.35 mm excitation at 7.5 Hz. The comparison of the f - d curves, attained from simulation and measured data under different values of control current, show similar degree of agreement.

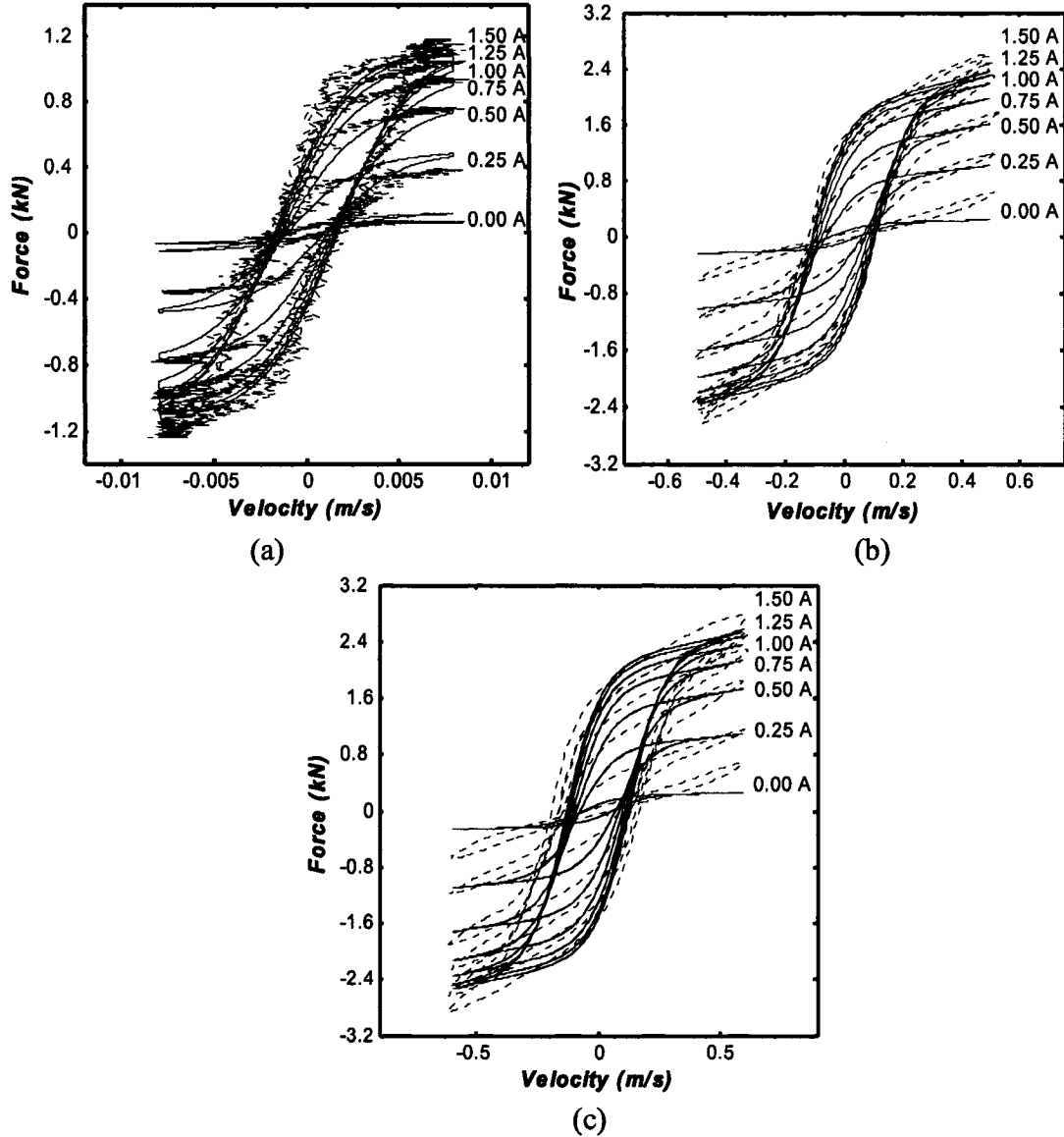


Figure 2.10: Comparison of simulation results with the measured data under different operating conditions: (a) $A_r=2.54$ mm, $f_r=0.5$ Hz; (b) $A_r=6.35$ mm, $f_r=12.5$ Hz; (c) $A_r=6.35$ mm, $f_r=15.0$ Hz (..... Measured; ——— Simulation).

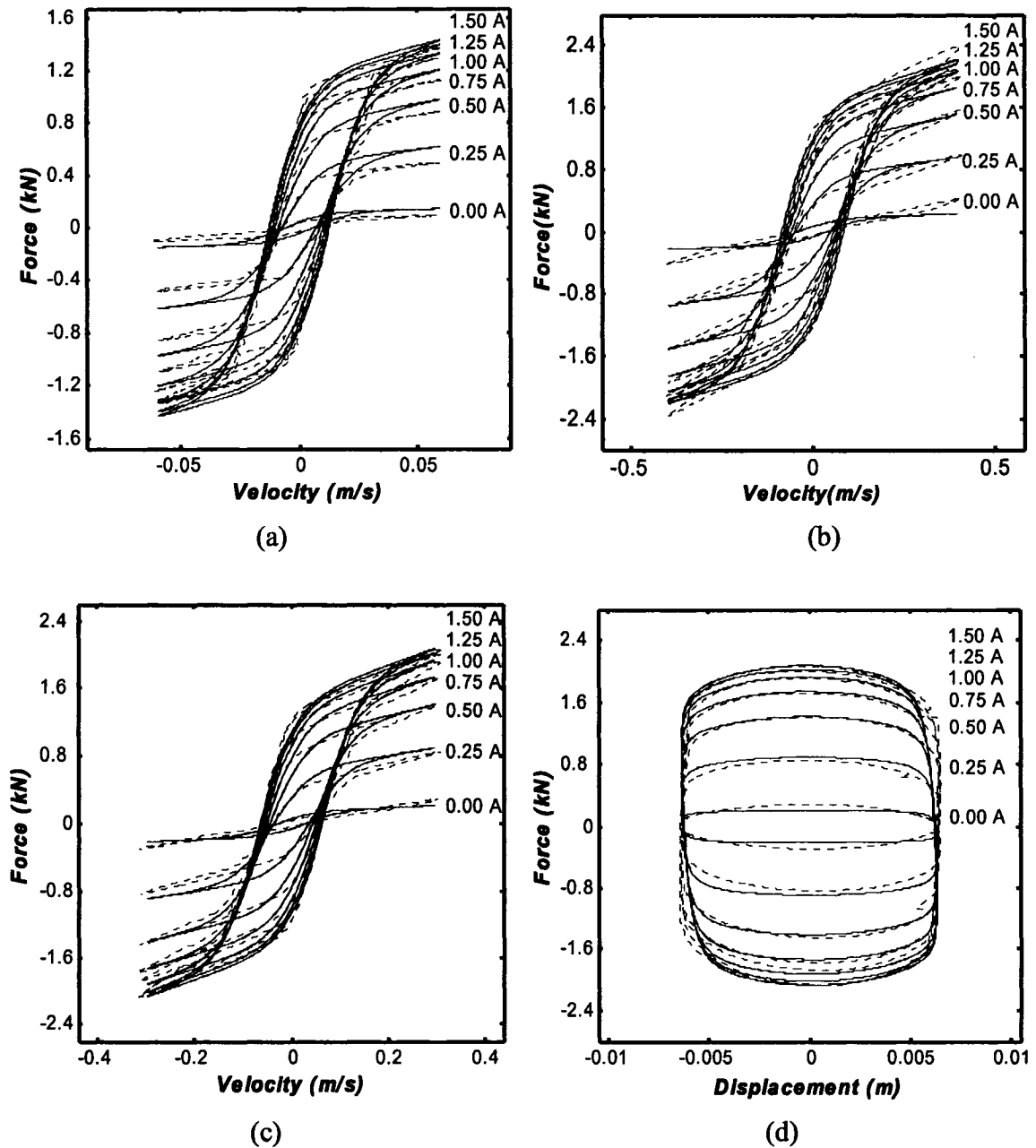


Figure 2.11: Comparison of simulation results with the measured data under different operating frequencies: (a) $A_r=6.35$ mm, $f_r=1.5$ Hz; (b) $A_r=12.5$ mm, $f_r=5.0$ Hz; (c) $A_r=6.35$ mm, $f_r=7.5$ Hz; (d) $A_r=6.35$ mm, $f_r=7.5$ Hz (..... Measured; — Simulation).

Figure 2.12 illustrates comparisons of simulations results with the measured data under different excitation frequencies and velocities, corresponding to $i = 0.75$ A. The

results show similar degree of agreement under the entire ranges of frequency and peak velocity considered in the study.

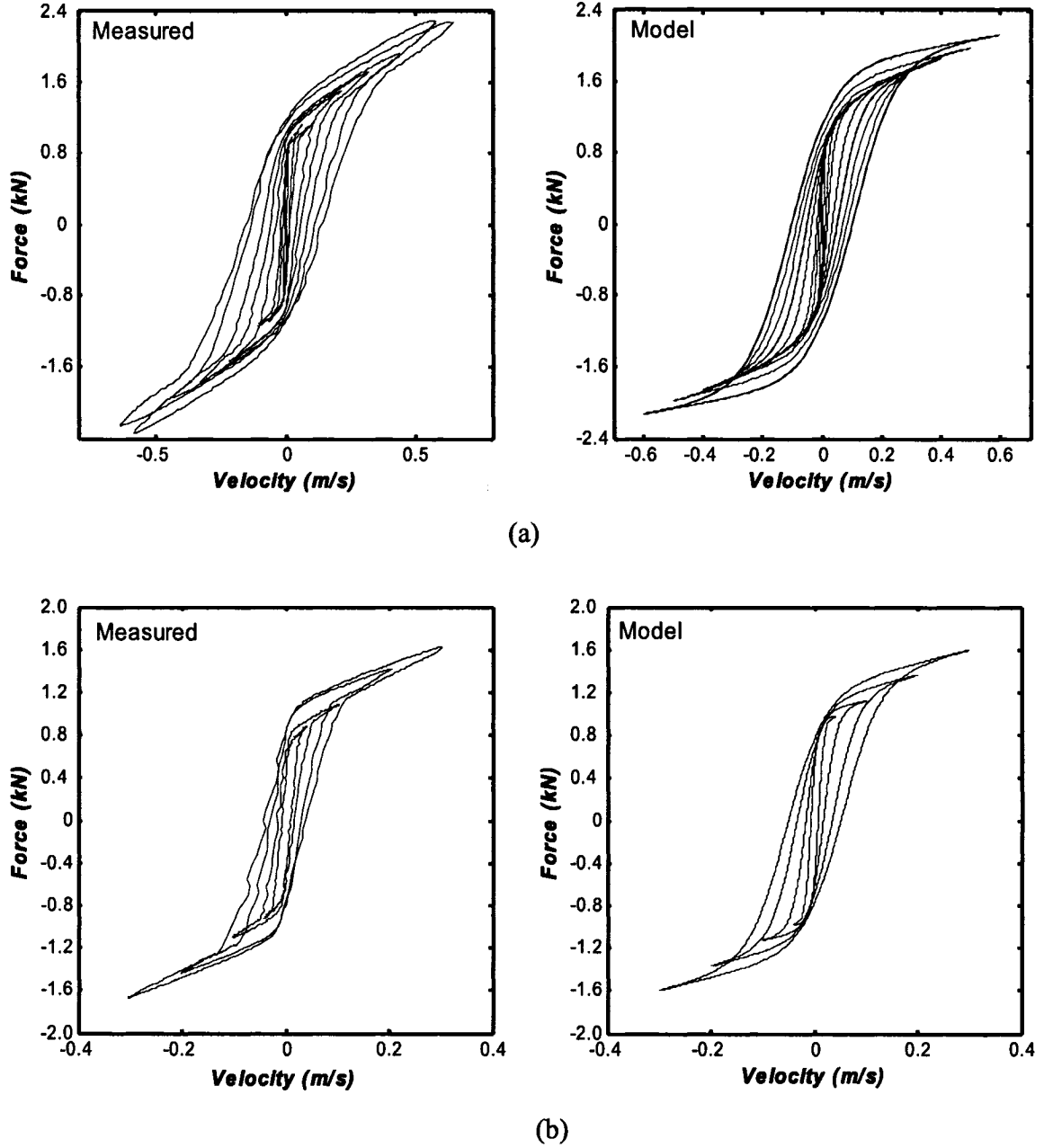
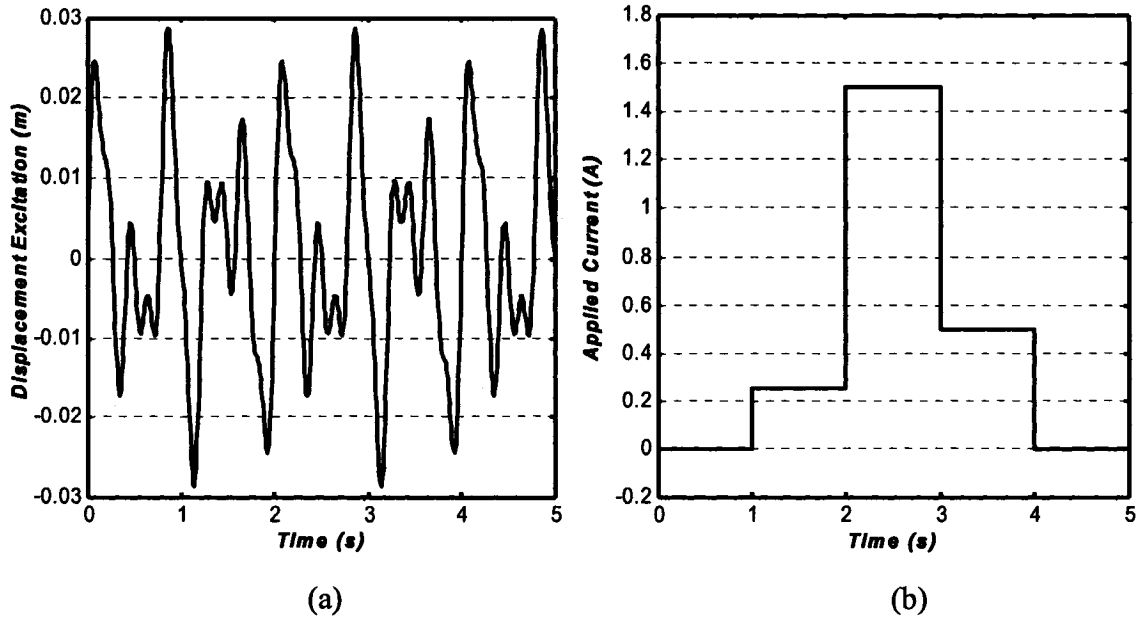
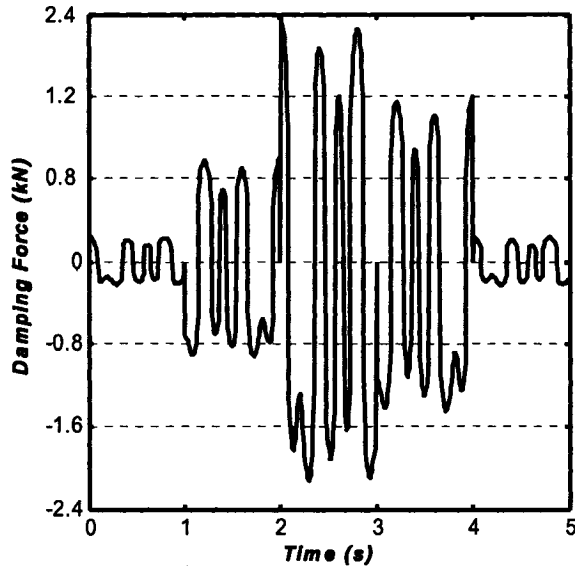


Figure 2.12: Comparison of simulation and experimental results: (a) $A_r = 6.35$ mm, $i = 0.75$ A, $f_r = 15.0, 12.5, 10.0, 7.5, 5.0, 2.5, 1.5$ and 0.5 Hz, from the outside loop to the inside loop; (b) $f_r = 2.5$ Hz, $i = 0.75$ A, $A_r = 18.75, 12.5, 6.35$ and 2.54 mm, from the outside loop to the inside loop.

The effectiveness of the synthesized model is further investigated through simulation performed with an arbitrary complex harmonic piston displacement signal composed of three harmonics with frequencies of 0.5, 2.5 and 5.0 Hz and respective amplitudes of 6.35, 12.5 and 12.5 mm. The control current is also varied using a multi-step signal with amplitudes of 0.0, 0.25, 1.5, 0.5 and 0.0 A, while the time duration of each step is limited to 1 s. It should be noted that this control current also represents the coil current as stated earlier. Equation (2.16) is solved to derive the damping force developed by the MR-damper model under prescribed displacement excitation and control current. Figure 2.13 shows the damping force response together with the excitation and command current signals. The results show a strong correlation between the peak damping force and the magnitude of command current and the displacement excitation.





(c)

Figure 2.13: Simulation results attained under an arbitrary displacement excitation and control current: (a) time-history of displacement; (b) time-history of control current; and (c) time-history of damping force response.

2.5 Summary

A generalized model synthesis is proposed to characterize the hysteretic force-velocity characteristics of a controllable MR damper under a wide range of sinusoidal excitation conditions (frequency and displacement amplitude) and magnitudes of control current. The essential features of the model are derived on the basis of measured force-displacement, force-velocity and seal friction properties of a MR damper attained under a wide range of excitation conditions. The model formulation is systematically realized on the basis of the fundamental force generation mechanism and observed qualitative trends of the measured data. The global model synthesis is realized by integrating the components describing the excitation and current dependent hysteretic

linear rise in the pre-yield condition, force limiting in the post-yield condition, zero-force velocity intercept, zero-velocity force intercept and yield force corresponding to onset of saturation. Simulations are performed to assess the effectiveness of the proposed model synthesis and results obtained under wide range of simulation conditions are compared with those obtained from the measured data. The results show reasonably good agreements between the simulation results and the measured data, irrespective of the excitation conditions and control current. It is thus concluded that the proposed model can effectively describe the nonlinear steady state hysteretic dynamic properties of the controllable MR damper and can thus be effectively used to design optimal semi-active controller for implementation in vehicle suspension.

CHAPTER 3

DEVELOPMENT AND RELATIVE ASSESSMENTS OF CURRENT DEPENDENT HYSTERESIS MODELS

3.1 Introduction

The magneto-rheological (MR) fluid-based dampers, with their superior damping modulation potential, are increasingly being used in various vibration control applications. In recent years, many experimental and analytical studies have clearly demonstrated the enhanced potentials of MR dampers in realizing variable damping with desired response time and minimal power requirement [18, 88, 103]. The MR dampers offer high viscous damping corresponding to low velocities in the pre-yield condition, while the post-yield saturation corresponding to high velocities can be characterized by a considerably lower viscous damping coefficient [102]. These studies have shown highly nonlinear damping properties of the MR-damper, particularly the hysteresis, force-saturation and the force transition at the onset of the post-yield. Moreover, these are further dependent upon the intensity of the applied magnetic field, displacement and velocity of the piston and nature of excitation in a highly nonlinear manner [106].

In this chapter, a number of reported models are evaluated in terms of their ability to predict hysteretic f - v properties of the MR-dampers over a range of excitations and applied current. A model modification is proposed that can be generally applied to these models to enhance their prediction abilities in view of the dependence on the control current, and excitation and response. The proposed modification involves the formulation

and integration of a nonlinear function describing the control current dependency of the hysteretic damping force. The modified model syntheses are further evaluated to demonstrate their improved prediction performance on the basis of the measured data acquired for a MR damper under a wide range of current and excitation conditions.

3.2 Critical Review of Reported Models

The nonlinear variations in damping force attributed to hysteresis and force-limiting are considered to pose complexities in controller design and force tracking. Considerable efforts have been made to mathematically characterize the properties, particularly the hysteresis and force-limiting nonlinearities, in order to utilize the full potential of the MR dampers through simple controller designs [103]. A large number of analytical models based upon different describing functions have evolved in recent years to describe the nonlinear properties of the MR-dampers [73-78, 102, 106]. The Bingham plastic model was proposed assuming rigid material behavior in the pre-yield, while the shear flow in the post-yield is characterized by a viscous damping coefficient [68]. Assuming the material to be plastic in both pre- and post-yield conditions, Stanway et al. [72] proposed a nonlinear model, where the pre-yield force is characterized by a considerably high viscous damping coefficient. On the basis of this model, Wereley et al. [102] proposed a nonlinear hysteretic bilinear model by fitting the force-velocity characteristics using four characteristic parameters: pre- and post-yield viscous damping coefficients, yield force and zero-force velocity intercept.

Dyke [88] proposed a damper model on the basis of the widely used Bouc-Wen hysteresis model. The model, however, poses inherent difficulties in predicting essential parameters and in realizing control systems for desired tracking performance. Based on this model, Spencer et al. [73] further derived an extended Bouc-Wen hysteresis dynamic model, which considered the effect of applied current as a linear function. Choi et al. [77] proposed a model on the basis of two polynomial functions to characterize the hysteresis nonlinearities of a MR damper. The model, however, could not ensure the convergence of the two curves at the extremities. While the reported models, nonlinear hysteretic biviscous model [102], Bouc-Wen hysteresis model [73], polynomial describing function model [77], characterize the damping force hysteresis reasonably well, the dependence of the hysteresis and force-saturation on the continually varying control current is not considered. Moreover, the hysteretic damping force generated by a MR-damper depends not only upon the intensity of the magnetic field but also upon the excitation frequency and amplitude of the damper motion. This dependence of the hysteretic force on the nature of excitation has not yet been accurately characterized. A generalized sigmoid hysteresis model was proposed to synthesis the nonlinear damping properties as a function of the current, as described in the previous chapter.

The force-velocity (f - v) characteristics of MR-dampers exhibit strong dependence on two primary factors: (i) control current; and (ii) the magnitude and frequency of excitation and response [78, 106]. The vast majority of the reported models, however, lack consideration of damping force dependence on both the factors. A model that can

accurately predict the nonlinear force-velocity property of the MR damper would be desirable to enhance design and implementation of real-time damping control and tracking performance. Therefore, a generalized formulation as well as integration of a nonlinear function describing the control current dependency of damping force, are proposed in the following sections. The prediction errors between the modified reported models and the measured data over a wide range of the excitation condition and applied current are further assessed.

3.3 MR-Damper Properties and Modeling Considerations

MR-fluids discovered by Rabinow [57] exhibit rapid, reversible and tunable transition from a free-flowing state to a semi-solid state upon the application of external magnetic field. As described in the previous chapter, a MR-damper is thoroughly characterized in the laboratory. Figure 3.1, as an example, illustrates the measured force-velocity characteristics of the MR damper under selected excitation conditions. The results show highly nonlinear force-velocity properties, which are further dependent upon the magnitudes of excitation and applied current. The measured f - v characteristics can be generally depicted as symmetric bi-nonlinear with significant hysteresis and nearly linear rise at lower velocities (pre-yield). This is followed by a transition to slightly increasing force at higher velocities (post-yield), while increase in the force could be considered nearly linear with the velocity. A force-limiting behavior is also evident in the high velocity response in the post-yield condition.

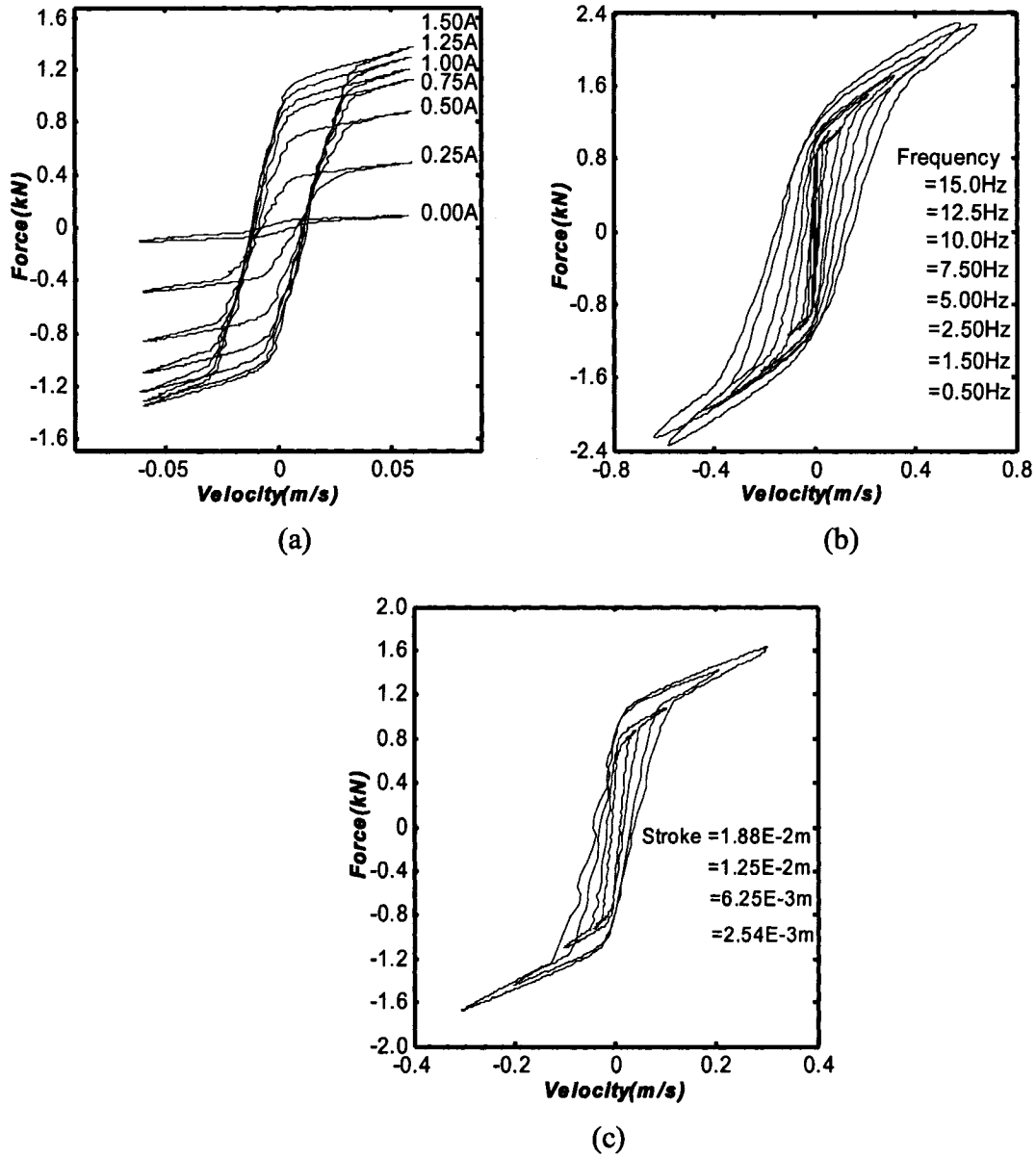


Figure 3.1: Measured $f-v$ characteristics of a MR-damper illustrating variations with: (a) applied current, $A_r = 6.35$ mm, $f_r = 1.5$ Hz; (b) excitation frequency, $A_r = 6.35$ mm, $i = 0.75$ A; (c) excitation amplitude, $f_r = 2.5$ Hz, $i = 0.75$ A.

Some of the characteristic properties of the MR-fluid damper, considered essential for modeling considerations, identified from the data are summarized below:

- The passive property of the damper, in the absence of the current, could be

characterized by nearly linear viscous damping.

- The damping force increases nearly linearly with velocity at low velocities, in a symmetric bilinear manner with significant hysteresis. The force and the hysteresis increase considerably with the magnitude of control current. An increase in current causes nearly parallel shift in the measured yield force, and approaches saturation when current exceeds 0.75 A.
- The damper hysteresis progresses along the counterclockwise path in time, and varies monotonically with the velocity. The upper and lower curves in the f - v characteristics reflect force variations under decreasing ($dv/dt < 0$) and increasing velocities ($dv/dt > 0$), respectively.
- A force-limiting behavior is also evident at high velocities in the post-yield, where the rate of change of force is relatively small but dependent upon the current.

The variations in the damping force not only depend on the control current, but also on the nature of excitation (frequency and stroke). The hysteretic force-velocity characteristics of a MR-damper may thus be expressed by a function in current, displacement, velocity and acceleration:

$$f_d = f(i, x, \dot{x}, \ddot{x}) \quad (3.1)$$

where f_d is the damping force, i is the applied current, x is the piston displacement and $\dot{x} = v$.

The above function may be synthesized to characterize the input-output force versus velocity relationship involving hysteresis and force-limiting nonlinearities. The following considerations are proposed for formulation and evaluations of the hysteresis damping force model for a MR-damper.

Basic feature: The model should fully describe the f - v characteristics with yield and post yield property of the MR-damper, i.e. a higher damping coefficient and nearly linear rise at lower velocities (pre-yield), and a considerably lower damping coefficient but nearly

linear increase in damping force at higher velocities (post-yield), irrespective of the applied current.

Operational feature: The model should adequately capture the evolution of hysteresis loop under a wide range of excitations, and the current dependence with incremental nonlinearity and current-induced damping force saturation.

Flexibility feature: The model should be sufficiently flexible such that it may be easily adapted to characterize the mean f - v characteristics for applications involving preliminary design and analyses. Moreover, the model flexibility should permit the characterization of asymmetric f - v characteristics for applications in vehicle suspension [106].

3.4 Current Dependent Hysteresis --- A Generalized Model Structure

The force-velocity (f - v) characteristics of a MR-damper, measured under a wide range of excitations and currents, clearly suggest nonlinear hysteretic behavior in the pre- and post-yield, post yield saturation, and strong dependence upon the excitation/response and the current. The variations in the current exhibit strong effect on the peak force, post-yield saturation and the magnitude of the hysteretic force. The effect of current on the width of the hysteresis loop, however, is relatively small. The damping force developed by a MR-damper could thus be expressed in a general form involving two independent functions in current control and the hysteretic force:

$$f_d = f_i(i)F_h(x, \dot{x}, \ddot{x}) \quad (3.2)$$

where f_i represents the current function and F_h is the hysteresis function describing the force variations with the piston displacement (x), velocity (\dot{x}) and acceleration (\ddot{x}).

The function f_i is a monotonous nonlinear incremental function with increasing i and could be considered as a gain function. The function must also exhibits post-yield limiting behavior of the damping force attributed to the rheological properties of the fluid.

The nonlinear incremental behavior of the current can be characterized by an asymmetric sigmoid function with a bias in the lateral axis [106], such that:

$$f_i(i) = 1 + \frac{k_2}{1 + e^{-a_2(i+I_0)}} - \frac{k_2}{1 + e^{-a_2I_0}}; \quad i \geq 0 \quad (3.3)$$

where k_2 and a_2 are positive constants, and I_0 is an arbitrary constant representing the bias, to be identified from the measured data.

The function F_h is formulated to describe the linear rise and force limiting behavior that are evident from the hysteretic f - v characteristics with yield and post yield properties of the MR-fluid. The function also characterizes the higher damping coefficient at lower velocities in the pre-yield and considerably lower damping coefficient at higher velocities in the post-yield condition [77]. The reported models of hysteretic systems have employed different techniques in formulating the function F_h , namely, the nonlinear hysteretic biviscous model, polynomial function model, extended Bouc-Wen model and generalized sigmoid model [73, 77, 78, 102].

3.5 Generalized Model Structure Implementation

The generalized model structure of MR-damper, expressed in Equation (3.2), involves two independent functions in current control f_i and the hysteretic force F_h . The current control function f_i is formulated in Equation (3.3) to describe the current nonlinear effects on the damping force, while the hysteretic force F_h is been expressed in the following sections by citing the four reported modeling techniques, that is, piecewise

function, polynomial function, Bouc-Wen hysteretic function and sigmoid function.

3.5.1 Nonlinear Hysteretic Biviscous Model [102]

A nonlinear biviscous model has been proposed to characterize the limiting and hysteresis nature of the damping force, as a function of the piston velocity. The model proposed by Werely et al. [102] utilizes a set of piecewise linear functions to construct the hysteresis loop on the basis of two different linear damping rates (c_{pr} and c_{po}) corresponding to pre- and post-yield behaviour of the MR fluid. The hysteresis loop described by the nonlinear biviscous model is illustrated in Figure 3.2 while the hysteresis force function is given by:

$$F_h = \begin{cases} c_{po}\dot{x} - f_y & \dot{x} \leq -\dot{x}_{b1} \quad \ddot{x} > 0 \\ c_{pr}(\dot{x} - v_h) & -\dot{x}_{b1} \leq \dot{x} \leq \dot{x}_{b2} \quad \ddot{x} > 0 \\ c_{po}\dot{x} + f_y & \dot{x}_{b2} \leq \dot{x} \quad \ddot{x} > 0 \\ c_{po}\dot{x} + f_y & \dot{x}_{b1} \leq \dot{x} \quad \ddot{x} < 0 \\ c_{pr}(\dot{x} + v_h) & -\dot{x}_{b2} \leq \dot{x} \leq \dot{x}_{b1} \quad \ddot{x} < 0 \\ c_{po}\dot{x} - f_y & \dot{x} \leq -\dot{x}_{b2} \quad \ddot{x} < 0 \end{cases} \quad (3.4)$$

where f_y is a constant derived upon projection of the post-yield curve at $\dot{x} = 0$, as shown in Figure 3.2, and v_h is the width of the hysteresis loop. \dot{x}_{b1} and \dot{x}_{b2} represent the velocities at the transition between pre- and post-yield curves corresponding to $\ddot{x} < 0$ and $\ddot{x} > 0$, respectively, such that:

$$\dot{x}_{b1} = \frac{f_y - c_{pr}v_h}{c_{pr} - c_{po}}, \quad \dot{x}_{b2} = \frac{f_y + c_{pr}v_h}{c_{pr} - c_{po}} \quad (3.5)$$

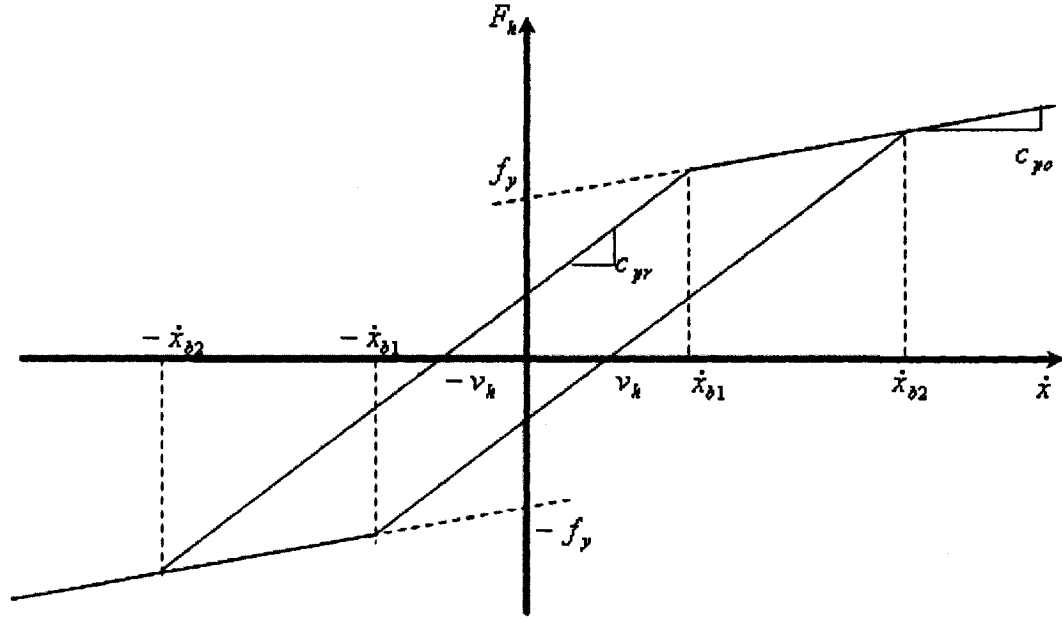


Figure 3.2: Nonlinear Hysteretic Biviscous Model [102].

The study showed that the nonlinear f - v characteristics could be adequately predicted using the piece-wise linear describing function F_h . The function however does not account for the dependency upon the current. Moreover, the model does not adequately account for variations in the excitation/response conditions, since the identified damping rates are applicable in the vicinity of a specific excitation and response. The model parameters thus need to be updated in time as the excitation conditions vary, which may limit the real-time tracking ability of the control algorithm.

The inherent limitations of the proposed model can be circumvented by integrating the current function in Equation (3.3) in conjunction with Equation (3.4). The measured data under a constant current suggests that the low velocity damping coefficient decreases with increasing frequency and magnitude of piston displacement, as observed in Figure

3.1 (b) and (c). The post-yield damping coefficient also decreases, although only slightly, with increasing excitation frequency and magnitude, and thus the velocity, but increases with the current [73]. The prediction ability of the model could be enhanced over a wide range of excitation conditions by introducing the peak velocity response v_m , in the model described in Equation (3.4). This model permits the definitions of damping rates, and hysteresis loop width as function of the velocity response, such that:

$$\begin{aligned} f_y &= f_{b0}(1 + e^{a_{b1}v_m}); \quad v_h = k_{b4}v_m; \\ c_{pr} &= a_{b0}/(1 + k_{b0}v_m); \quad c_{p0} = k_{b1}e^{-a_{b4}v_m}; \end{aligned} \quad (3.6)$$

where f_{b0} is a constant taken as the seal friction force measured under a very low speed. The model parameters $a_{b0}, a_{b1}, a_{b4}, k_{b0}, k_{b1}$ and k_{b4} are constants to be identified from the measured data.

The peak velocity v_m in the above formulations could be estimated from the instantaneous response measures. For a sinusoidal excitation, the peak velocity is estimated from:

$$v_m = \sqrt{(\dot{x})^2 - \ddot{x}x} \quad (3.7)$$

The above formulation is limited for harmonic excitations. Its general applications would necessitate measurements of instantaneous acceleration, velocity and displacement. The associated signal noise and the phase differences may also affect the accuracy of peak velocity estimation.

The vehicle suspension design invariably considers the mean f - v characteristics assuming small contributions due to damping hysteresis, particular in the open-loop mode

[99, 107]. The above model can be simplified to describe the mean force-velocity characteristic by letting $k_{b4} = 0$.

3.5.2 Polynomial Function Model [77]

Choi, et al. [77] proposed a model comprising two polynomial functions to describe the f - v relationship corresponding to $\ddot{x} > 0$ and $\ddot{x} < 0$, assuming linear dependency upon the control current. The model describes the damping force as:

$$F_h = \sum_{k=0}^n a_k \dot{x}(t)^k; \quad n = 6 \quad (3.8)$$

where F_h describes the hysteretic force. The coefficients a_k are defined as linear function of current, such that:

$$a_k = b_k + c_k i; \quad k = 0, 1, \dots, n \quad (3.9)$$

The model coefficients however are considered to be applicable in the vicinity of a pre-defined excitation, as in the case of the piece-wise linear biviscous model [102]. Furthermore, the current-induced rise in damping force may not be adequately characterized by the linear function in Equation (3.9). The applicability of this model could be enhanced by replacing the linear current coefficients, a_k ($k = 0, 1, 2, \dots, n$), by constants b_k ($k = 0, 1, 2, \dots, n$), and by introducing the nonlinear current function of Equation (3.3). The polynomial function model can thus be modified as:

$$f_d = f_i(i) \left(\sum_{k=0}^n b_k \dot{x}(t)^k \right); \quad n = 6 \quad (3.10)$$

where the constants b_k are identified from the hysteretic force-velocity curves

corresponding to $\ddot{x} > 0$ and $\ddot{x} < 0$, while $c_k = 0$.

The polynomial function model also exhibits another inherent limitation. The two curves correspond to $\ddot{x} > 0$ and $\ddot{x} < 0$ are known to be non-convergent at the extremities [77]. The deviations due to non-converging upper and lower curves could be eliminated by considering a model that ensures convergence near $\ddot{x} = 0$. The modified current dependent polynomial model is finally formulated as:

$$f_d(t) = \begin{cases} f_i(i) \left(\sum_{k=0}^6 b_{uk} \dot{x}(t)^k \right); & \ddot{x}(t) < 0 \\ f_i(i) \left(\sum_{k=0}^6 b_{dk} \dot{x}(t)^k \right); & \ddot{x}(t) > 0 \\ f_i(i) \left(\sum_{k=0}^6 \frac{1}{2} (b_{uk} + b_{dk}) \dot{x}(t)^k \right); & \ddot{x}(t) = 0 \end{cases} \quad (3.11)$$

where b_{uk} and b_{dk} ($k = 0, 1, \dots, 6$) are constants corresponding to upper and lower curves, respectively. Moreover, the model can be easily reduced to characterize the mean f - v characteristics, as:

$$f_d(t) = f_i(i) \left(\sum_{k=0}^n \frac{1}{2} (b_{uk} + b_{dk}) \dot{x}(t)^k \right), \quad n = 6 \quad (3.12)$$

3.5.3 Extended Bouc-Wen Hysteresis Model [73]

The Bouc-Wen hysteron is extremely general and has been widely used to adequately characterize the hysteresis behavior of various systems. For the MR-fluid damper, the Bouc-Wen hysteron has been applied in conjunction with an equivalent mechanical model to describe its hysteresis f - v characteristics, as illustrated in Figure 3.3 (a). The hysteresis damping force derived from the model can be expressed as:

$$F_h = c_0 \dot{x}(t) + k_{s0}(x - x_0) + \varepsilon z \quad (3.13)$$

where x_0 is the initial displacement of the piston due to compression of the gas, k_{s0} and c_0 are the stiffness and damping coefficient, respectively, ε is the pressure drop due to the MR effect (yield) stress, and z denotes a yield-force function derived from the hysteron expression as [22]:

$$\dot{z} = A\dot{x} - \beta\dot{x}|z|^n - \gamma|\dot{x}|z|^{n-1}z; \quad (3.14)$$

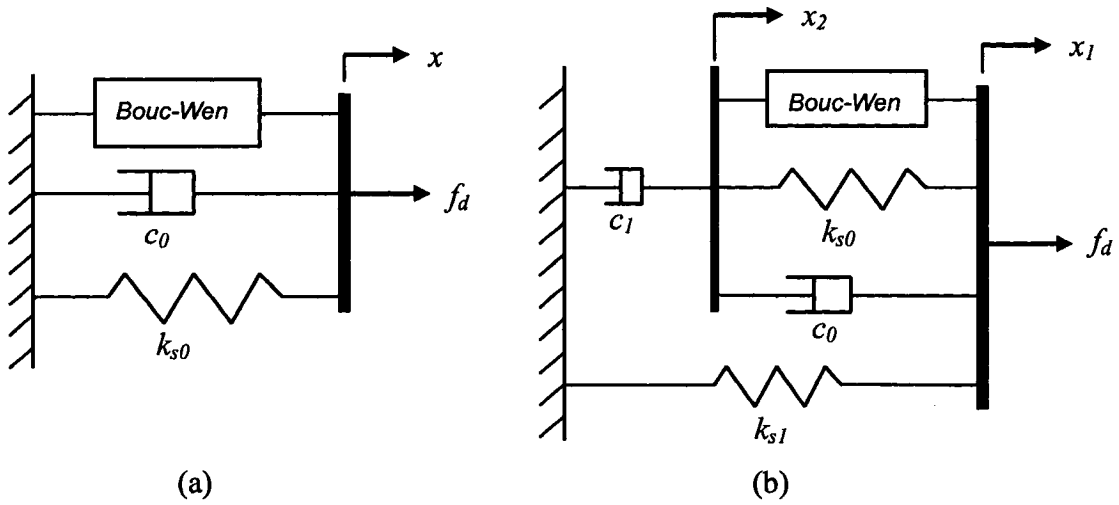


Figure 3.3: Bouc-Wen model [88] and extended Bouc-Wen model [73].

Owing to the inherent difficulties in predicting the model parameters and in realizing desired tracking performance, Spencer et al. [73] proposed an extended Bouc-Wen dynamic model, which considers linear dependency on the applied current. Figure 3.3 (b) illustrates the structure of the extended Bouc-Wen model. The proposed model has shown improved ability for predicting the behavior of the MR damper over a broad range of excitation and applied current. The constants ε , c_0 and c_1 are defined as linear functions of voltage applied to the current driver. The current-dependent damping force

predicted by this model is given by:

$$f_d = \varepsilon z + c_0 \dot{x} + (k_{s0} + k_{s1})x + k_{s1}x_2 \quad (3.15)$$

and

$$f_d = c_1 \dot{x}_2 + k_{s1}(x_1 - x_{10}) \quad (3.16)$$

where the evolutionary variable z is formulated in Equation (3.14). In this model, x represents the relative displacement ($x_1 - x_2$), the accumulator stiffness is represented by k_{s1} , and c_0 relates to damping coefficient observed at high velocities. A viscous damping element c_1 , is introduced in the model to account for the nonlinear roll-off that was observed in the experimental data at low velocities. The constant k_{s0} is related to the stiffness under higher displacement, and x_{10} is the initial displacement of spring k_{s1} associated with the accumulator. The shape of the hysteresis loops is mostly adjusted through the parameters γ, β and A . Assuming that the hysteretic damping force is linearly related to the applied current, Spencer et al. [73, 88] proposed following linear function in applied voltage for the extended model parameters.

$$\begin{aligned} \varepsilon(u) &= \varepsilon_a + \varepsilon_b u \\ c_1(u) &= c_{1a} + c_{1b} u \\ c_0(u) &= c_{0a} + c_{0b} u \end{aligned} \quad (3.17)$$

where u is the voltage applied to the current driver of the damper, and ε_a, c_{1a} and c_{0a} are constants coefficients. ε_b, c_{1b} and c_{0b} are constants describing the linear dependence on the applied voltage. The primary limitations of extended Bouc-Wen model arise from potential inaccuracies due to assumed linear current property and difficulties associated

with identification of a large number of parameters. The measured f - v data for the MR-damper presented in Figure 3.1 (a) suggests nonlinear dependence of the force on the applied current.

The extended Bouc-Wen model can be further modified by integrating the nonlinear current function $f_i(i)$ described in Equation (3.3), instead of the linear current functions. The Bouc-Wen damping force function, defined in Equation (3.15), would serve as the hysteresis function F_h in the generalized model of Equation (3.2) when the parameters ε , c_0 and c_1 are considered constants. The hysteretic damping force due to the MR-damper can thus be defined by the proposed generalized model in conjunction with the extended Bouc-Wen model.

3.5.4 Generalized Sigmoid Hysteretic Model

A generalized sigmoid hysteresis model has been proposed in Chapter 2 to describe the damping force developed by a MR-damper as a function of the applied current and the nature of excitation (frequency and magnitude) [78, 106]. The hysteresis force function is based upon the symmetric sigmoid function shown in Figure 2.5. The model parameters have been mostly related to the physical characteristics of the damper, such as linear low-velocity rise, high-velocity force saturation, transition velocity at the onset of the post-yield and the transition force. The model structure can be depicted as the general model proposed in Equation (3.2), such that:

$$f_d = f_i(i)F_h(x, \dot{x}, \ddot{x}) = f_i(i) \left(f_t \frac{1 - e^{-\alpha(\dot{x} + v_h)}}{1 + e^{-\alpha(\dot{x} + v_h)}} (1 + k_v |\dot{x}|) \right) \quad (3.18)$$

where the current dependent function $f_i(i)$ is described in Equation (3.3), f_t is the transition force at the onset of the post-yield, v_h defines the width of the hysteresis loop, α and k_v are model parameter. The parameters f_t , v_h , α , k_v are formulated as function of the peak velocity v_m to account for the damping force dependence on the excitation magnitude. The hysteresis loop width is also related to the applied current on the basis of observed measured data. These model parameters are expressed as:

$$\begin{aligned} f_t &= f_0(1 + e^{a_1 v_m}) \\ v_h &= \text{sign}(\ddot{x}) k_4 v_m \left(1 + \frac{k_3}{1 + e^{-a_3(i + I_1)}} - \frac{k_3}{1 + e^{-a_3 I_1}} \right) \\ \alpha &= \frac{a_0}{1 + k_0 v_m}; \quad k_v = k_1 e^{-a_4 v_m} \end{aligned} \quad (3.19)$$

where $f_0, I_1, a_0, a_1, a_3, a_4, k_0, k_1, k_3$ and k_4 are constants.

The model requires identification of a total of 13 parameters ($f_0, I_0, I_1, a_0, a_1, a_2, a_3, a_4, k_0, k_1, k_2, k_3$ and k_4) from the measured data. It should be noted that the above hysteretic model can be easily simplified to yield the mean f - v characteristics of the MR-damper by letting $k_4 = 0$. (i.e. $v_h = 0$), and the number of parameters to be identified can be reduced from 13 to 10.

3.6 Parameters Identification

The measured data acquired under a wide range of excitation conditions and control current has been thoroughly analyzed to identify parameters of the proposed modified

models to describe the current-dependent damping-force properties of the MR-damper. The model parameters are identified through minimization of the error sum function, given by:

$$J = \sum_{j=1}^{n_1} \sum_{k=1}^{n_2} \sum_{l=1}^{n_3} (f_d(i, x, \dot{x}, \ddot{x}) - f_{dm})^2 \quad (3.20)$$

where f_d is the damping force predicted from a model corresponding to a particular excitation and current condition, and f_{dm} is the measured damping force under the same conditions. The error function is formulation through summation of squared errors over a range of excitation and current conditions described by indices j , k and l . The indices j , k and l refer to n_1 levels of applied current, n_2 levels of excitation frequencies, n_3 coordinates chosen within a single hysteresis loop. In this study, a total of 7 current discrete levels (n_1) are considered in the 0 to 1.5 A range, while the excitation frequencies were chosen as 1.5, 2.5 and 5.0 Hz ($n_2 = 3$). A total of 360 coordinates (n_3) in the f - v loops are selected for each condition. The error minimization is performed using MATLAB constrained optimization toolbox, which function is “fmincon”, using the measured data under a wide range of conditions. The solutions are obtained for a fixed piston displacement amplitude of 6.25 mm. The variation in the excitation frequencies, however, permits for considerations of three different velocity magnitudes (v_m). Considering that the polynomial function model can predict the f - v behavior only under a particular excitation, the frequency levels in the minimization function must be limited to a single one ($n_2 = 1$). The parameter identification for this model is performed

for excitation frequency of 1.5Hz, while all other conditions (current and excitation amplitude) remain the same.

The model parameters identified through solution of the minimization problem are summarized in Tables 3.1 and 3.2. Owing to the minimization problem defined in Equation (3.20), the identified model parameters, with the exception of the polynomial function model, may be considered valid over a wide range of excitation and current conditions. It should be noted that the modified nonlinear biviscous, polynomial, Bouc-Wen and generalized sigmoid models require identification of a total of 10, 17, 12 and 13 parameters, respectively. The polynomial model involves largest number of parameters, since it tends to describe the hysteresis loop by two independent polynomial functions.

The results attained for the four models suggest comparable values of parameters associated with the current function, described in Equation (3.3). These include the constants a_2 , k_2 , and I_0 . This would suggest that the current dependence of the damping force due to a MR damper can be considered independent of the hysteresis force function F_h . The results further show that the constants f_{b0} and f_0 used in the nonlinear biviscous and the sigmoid function models converges to comparable values, in the 43 N, which has been related to the seal friction force.

Table 3.1: Identified parameters for hysteresis loop of all models.

Modified Models							
Biviscous		Polynomial		Bouc-Wen		Sigmoid	
Parameters	Values	Parameters	Values	Parameters	Values	Parameters	Values
a_{b0}	20	a_{u0}	0.0649	ε	20342.57	a_0	990.2431
a_{b1}	0.9986	a_{u1}	4.9674	β	232887	a_1	1.9012
a_{b4}	2.2015	a_{u2}	-71.2922	γ	9071.18	a_3	4.2882
k_{b0}	30	a_{u3}	-1461.82	c_0	380.61	a_4	-0.2907
k_{b1}	0.346	a_{u4}	23232.45	c_1	7951.32	k_0	110.3267
k_{b4}	0.15	a_{u5}	190972.68	k_{s0}	300	k_1	1.4116
f_{b0}	43.9828	a_{u6}	-2319223.8	k_{s1}	100	k_3	1.1465
		a_{d0}	-0.0674	n	2	k_4	-0.1163
		a_{d1}	5.0273	A	16.4366	f_0	43.9648
		a_{d2}	78.0024			I_1	-0.2455
		a_{d3}	-1549.09				
		a_{d4}	-27398.44				
		a_{d5}	210738.82				
		a_{d6}	3017864.4				

Table 3.2: Identified parameters for the current dependent function in all modified models.

Modified Models							
Biviscous		Polynomial		Bouc-Wen		Sigmoid	
Parameters	Values	Parameters	Values	Parameters	Values	Parameters	Values
a_2	3.0115	a_2	3.1042	a_2	2.9511	a_2	3.1895
k_2	20.7799	k_2	18.53	k_2	22.7928	k_2	19.2361
I_0	-0.1375	I_0	-0.150	I_0	-0.1252	I_0	-0.1425

3.7 Relative Assessments of Proposed Modified Models

The relative effectiveness of the proposed modified models in predicting the hysteretic and current-dependent damping force characteristics of a MR damper are

assessed. The nonlinear biviscous (Equations (3.3) to (3.7)), polynomial function (Equation (3.11)), modified extended Bouc-Wen (Equations (3.14) to (3.17)) and generalized sigmoid (Equations (3.18) and (3.19)) models are solved using the current function defined in Equation (3.3) together with the model parameter listed in Tables 3.1 and 3.2. The analyses are performed under harmonic excitations of different magnitude and frequency, and different levels of applied current. The results are compared with the measured data attained under same excitation and current condition to assess the prediction effectiveness of the models.

Figure 3.4 illustrates comparisons of results attained from the modified hysteretic biviscous model with the measured data under 6.35 mm displacement excitation at three different discrete frequencies (1.5, 2.5 and 5 Hz). The results are also compared for different levels of applied current in the 0 to 1.5A range. The comparisons show reasonably good agreements between the model and measured results, although considerable deviations are also evident, particularly in the post-yield. This can be mostly attributed to sharp transition between the piecewise linear function corresponding to pre- and post-yield. The results presented for different velocity magnitudes and currents suggest that the modified nonlinear biviscous model can predict the MR damping behavior reasonably well over the range of conditions considered. The proposed model can be easily applied to derive the mean f - v properties, when hysteresis is not of concern. This is achieved by letting $k_4=0$ in Equation (3.16).

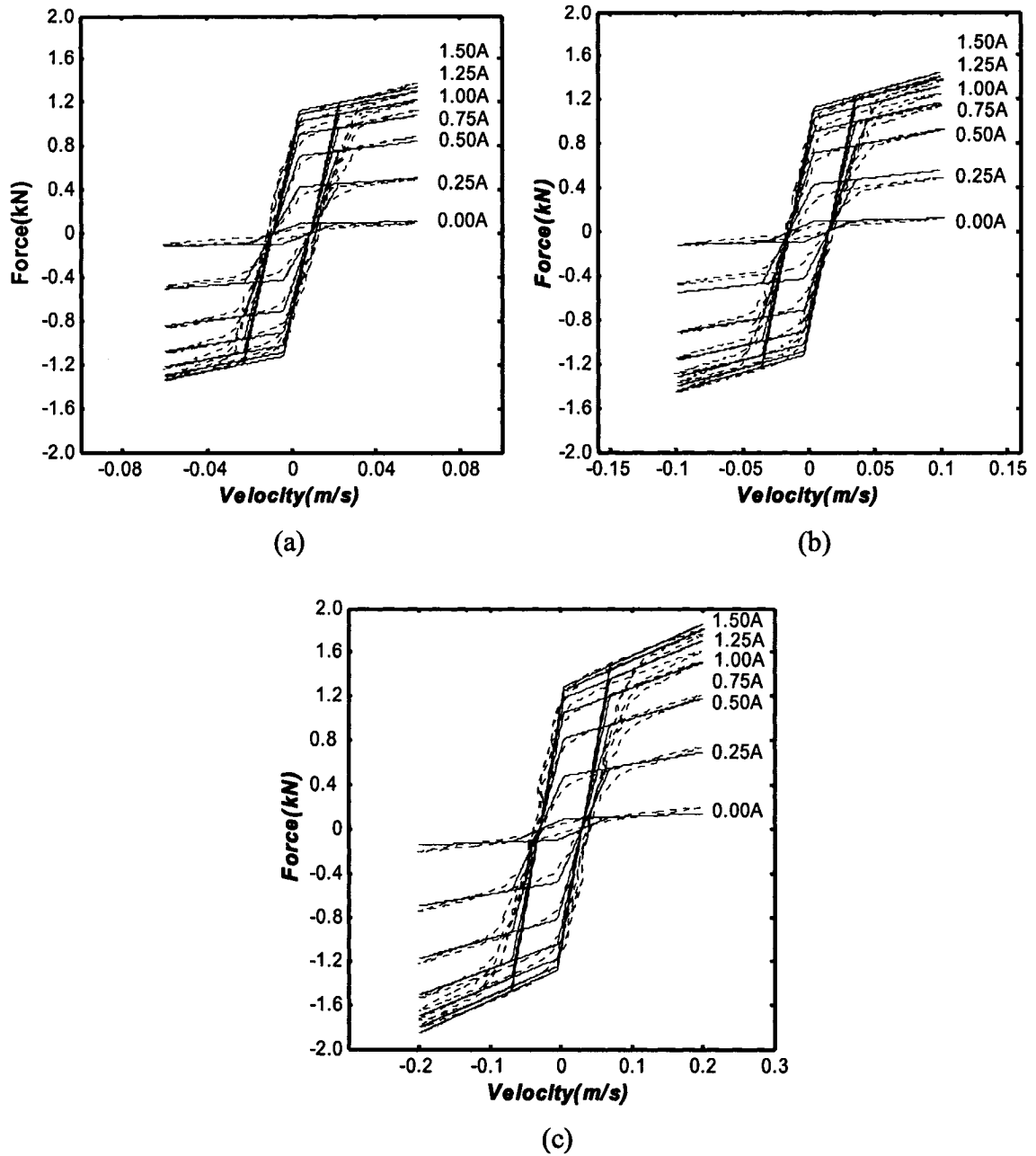
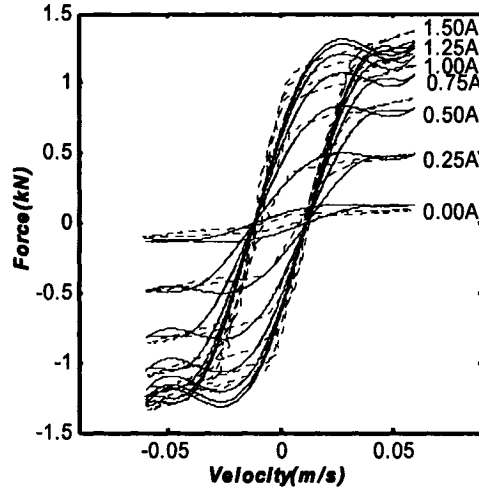


Figure 3.4: Comparisons of results from the modified piecewise linear biviscous model with the measured data under $A_r = 6.25$ mm at: (a) $f_r = 1.5$ Hz; (b) $f_r = 2.5$ Hz; (c) $f_r = 5.0$ Hz (..... Measured; ——— Simulation).

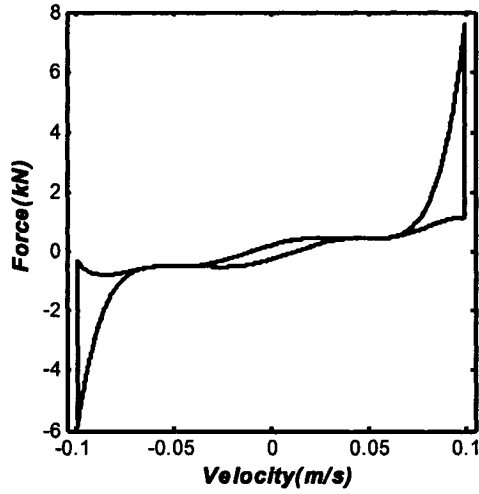
Figure 3.5 (a) illustrates comparisons of f - v responses of the modified polynomial function model with the measured data. The results are presented for 6.35 mm amplitude

excitation at 1.5 Hz, and applied current ranging from 0 to 1.5 A. The comparisons clearly suggest reasonable good agreements between the model results and the measured data for entire range of applied currents considered, while considerable deviations are evident in the post yield, particularly near the extreme velocity. Such deviations are most likely attributed to oscillations caused by the polynomial functions, particularly at higher velocities. The deviations may also be partly caused by poor convergence of the curves corresponding to $\ddot{x} > 0$ and $\ddot{x} < 0$ near the extreme velocity. It needs to be emphasized that the polynomial function model proposed by Choi and Lee [77], lacked convergence of the two curves. The results show that the modification proposed in Equation (3.11), in the vicinity of $\ddot{x} = 0$, can help improve the convergence.

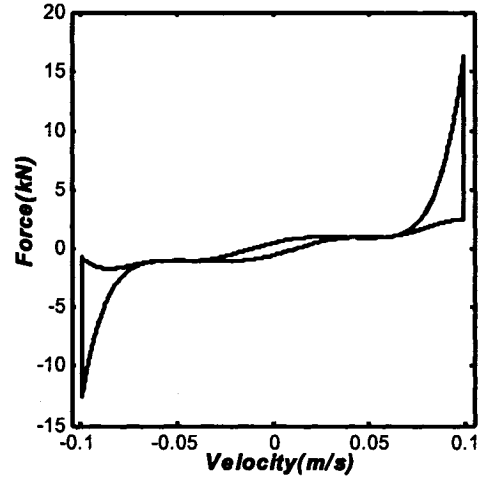
As it was stated earlier, the polynomial function model can be considered valid only in the vicinity of a particular excitation. The application of the model under a different excitation condition would be expected to yield considerable errors. As an example, Figure 3.5 (b) and (c) illustrate the model responses under an excitation amplitude of 6.35 mm at a frequency of 2.5 Hz, and different current. The results show extreme differences from the trends observed from the measured data under the same conditions.



(a) Measured; — Simulation



(b)



(c)

Figure 3.5: Comparisons of results from the modified polynomial model with the measured data under $A_r = 6.25$ mm at: (a) $f_r = 1.5$ Hz; (b) $f_r = 2.5$ Hz; $i = 0.25$ A; (c) $f_r = 2.5$ Hz; $i = 0.75$ A.

The results derived from the modified extended Bouc-Wen model under the same conditions compared with the corresponding measured data in Figure 3.6. The results show very good agreement between the model results and the measured data in the pre-yield, irrespective of the excitation frequency and the applied current. The model, however, yields considerable errors associated with force saturation in the post-yield. The

linear rise in the post-yield tends to increase considerably with increase in the excitation frequency. Such a trend is not evident from the measured force limiting behavior, which suggests only slight variation in the damping rate in the post yield, as seen in Figure 3.1(b).

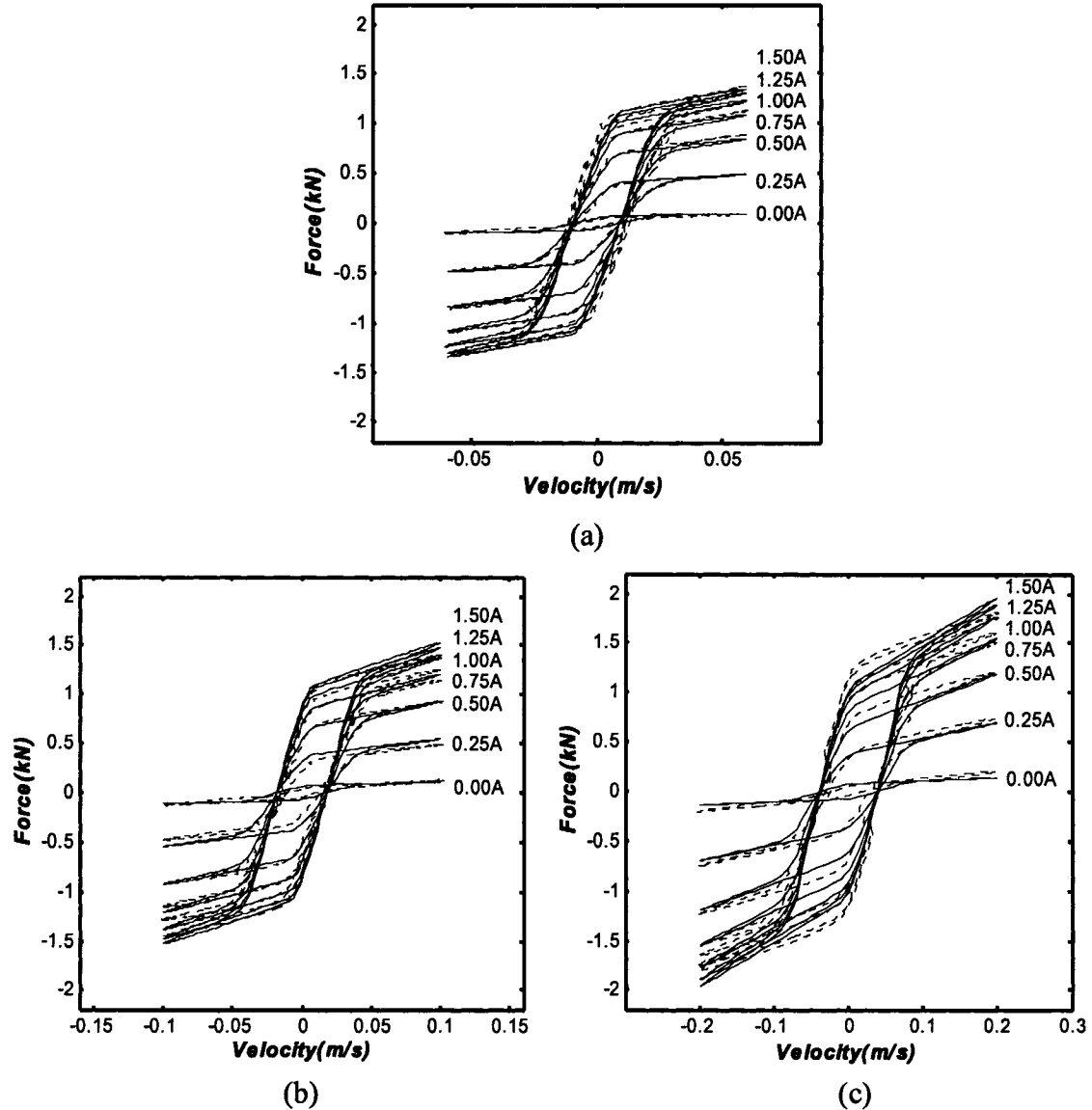
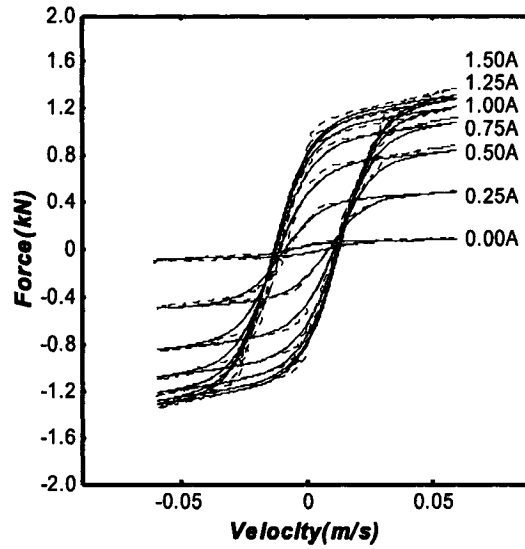


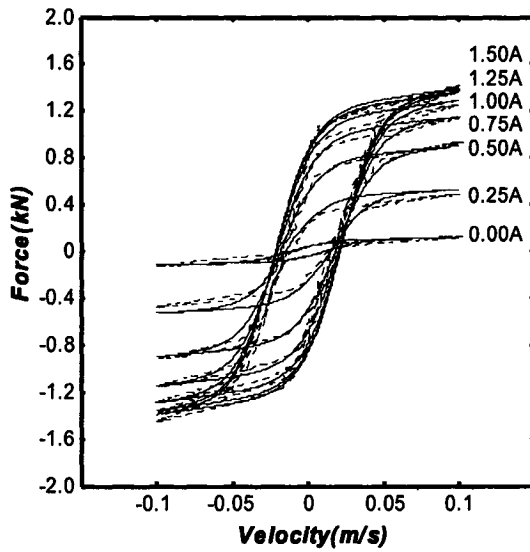
Figure 3.6: Comparisons of results from the modified extended Bouc-Wen model with the measured data under $A_r = 6.25$ mm at: (a) $f_r = 1.5$ Hz; (b) $f_r = 2.5$ Hz; (c) $f_r = 5.0$ Hz; (..... Measured; ——— Simulation).

The generalized sigmoid hysteretic model comprising the nonlinear current function has been shown to provide good estimate of the hysteresis f - v characteristics for the wide range of current and harmonic excitation [78, 106]. Figure 3.7 illustrates comparisons of the model results on the basis of parameters identified for the test damper considered in this study with the measured data. The results show very good agreements between the two for the entire range of excitation velocity and applied current. The model results exhibit excellent prediction ability in the pre- as well as post-yield, and force saturation, irrespective of the excitation and current condition considered.

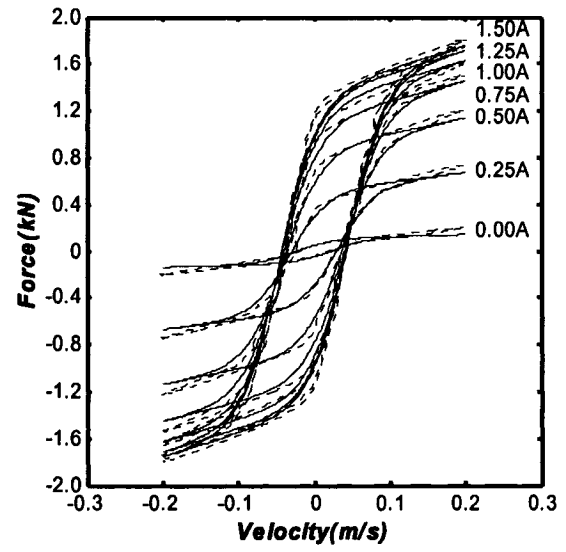
The reported nonlinear hysteretic biviscous, extended Bouc-Wen and polynomial function models are further analyzed, and the results are compared with the measured data to demonstrate their respective limitations and merits. It should be noted that the nonlinear hysteretic biviscous and polynomial function models require parameter identification for each excitation condition. The parameter identifications for the original models were performed on the basis of the data acquired under 6.35 mm displacement excitation at 1.5 Hz, while the applied current was varied in the 0-1.5 A range. The nonlinear hysteretic biviscous model involved second-order polynomial functions in i for $c_{pr}(i)$, $c_{po}(i)$ and $f_y(i)$, and a fourth-order function in i for $v_h(i)$, as suggested by Wereley et al.[102]. For the polynomial function model, the model coefficients were identified for each current.



(a)



(b)



(c)

Figure 3.7: Comparisons of results from the generalized hysteretic sigmoid model with the measured data under $A_r = 6.25$ mm at: (a) $f_r = 1.5$ Hz; (b) $f_r = 2.5$ Hz; (c) $f_r = 5.0$ Hz; (..... Measured; ——— Simulation).

The results attained from the original model under selected excitation and current are compared with the corresponding measured data in Figure 3.8. The results show that the nonlinear bi-viscous model can predict the damping behavior reasonably well for the

entire range, as evident in Figure 3.8 (a), except for the passive condition ($i = 0$. A). The identified model could be considered valid only in the vicinity of the selected excitation, and would yield considerable errors under different excitations. The originally proposed polynomial function model also yields reasonably good agreements with the measured data, as shown in Figure 3.8 (c). The results however clearly show lack of convergence of the two functions near the extremities, $\ddot{x} \approx 0$. The variations in the identified model coefficients a_k ($k = 0, 2, \dots, 6$) with the applied current were also examined. Figure 3.8 (d) illustrates variations in a_1 and a_3 for the upper curve with applied current, as an example, which show nonlinear dependency on the current. This model also can be considered valid only in the vicinity of the selected excitation and current conditions, and would yield considerable errors under different conditions, as observed from Figure 3.5, unless alternate sets of parameters are identified for different conditions.

Figure 3.8 (b) compares the results attained for the extended Bouc-Wen model with the measured data. The results show considerable errors with respect to the current dependency of the damping force. Such errors are significantly larger than those evident for the modified Bouc-Wen model in Figure 3.6. The results thus suggest that the current dependence of the hysteretic force cannot be adequately described by a linear function in current.

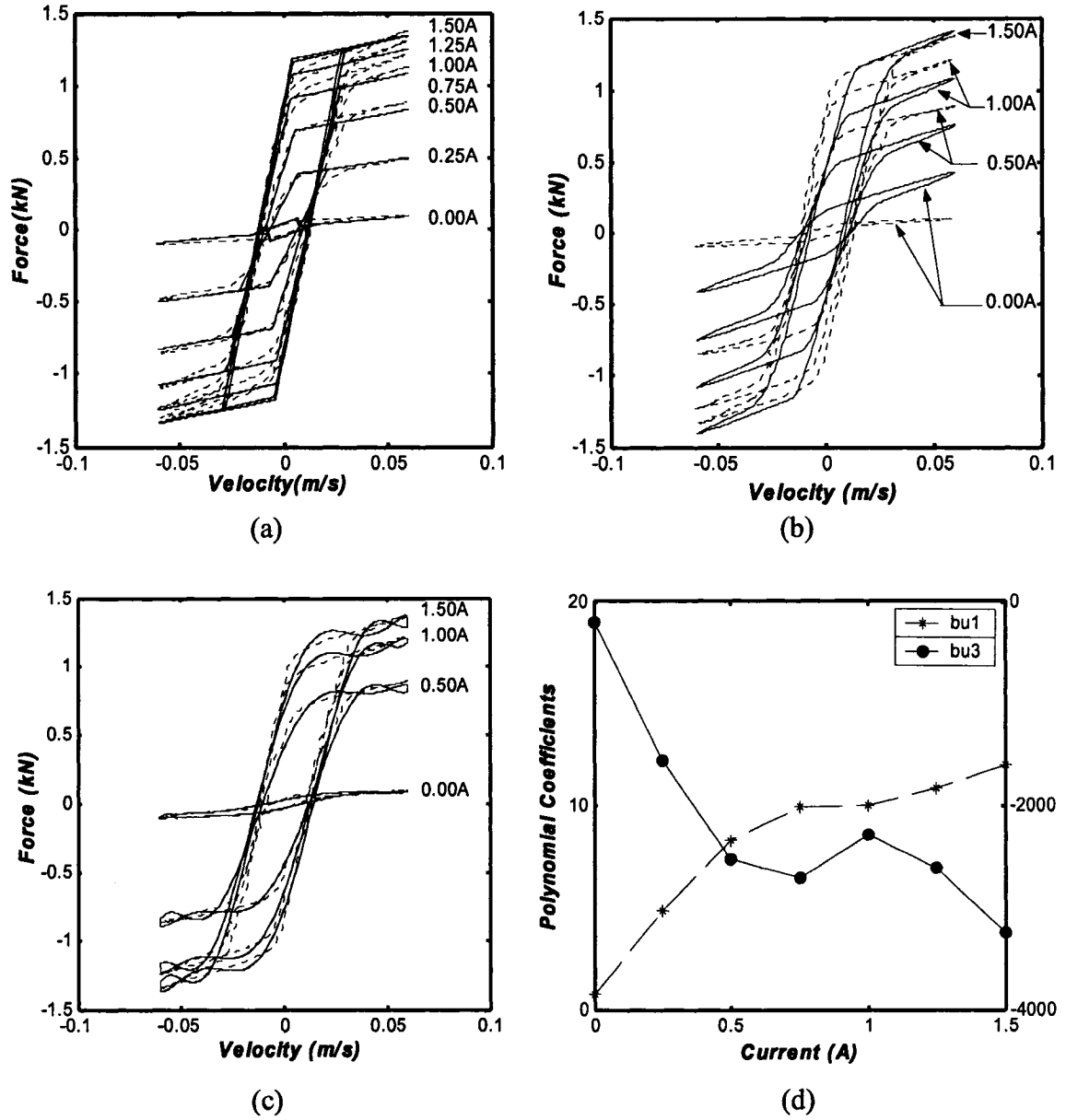


Figure 3.8: Comparisons of results attained from the original models with the measured data under 6.25 mm harmonic displacement excitation at 1.5 Hz: (a) nonlinear hysteretic biviscous model [102]; (b) extended Bouc-Wen model [73]; (c) polynomial function model [77]; (d) variations in selected polynomial function model coefficients with applied current (..... Measured; — Simulation).

3.8 Errors Analysis

The above results suggest that the reported models can be easily modified using the proposed current function to describe the nonlinear and hysteretic f - v characteristics of the MR dampers as a function of the applied current. The relative effectiveness of the modified models is further evaluated in terms of the damping force error under selected harmonic excitations of 6.25 mm amplitude at three different frequencies (1.5, 2.5 and 5.0 Hz) and four different applied currents (0, 0.5, 1.0 and 1.5 A). The computed and measured damping forces over a single steady-state period of oscillation, are considered to determine the prediction error, e . Owing to symmetry in the predicted force, the responses over half the cycle corresponding to $\ddot{x} \geq 0$ (lower curve) are considered to compute the error:

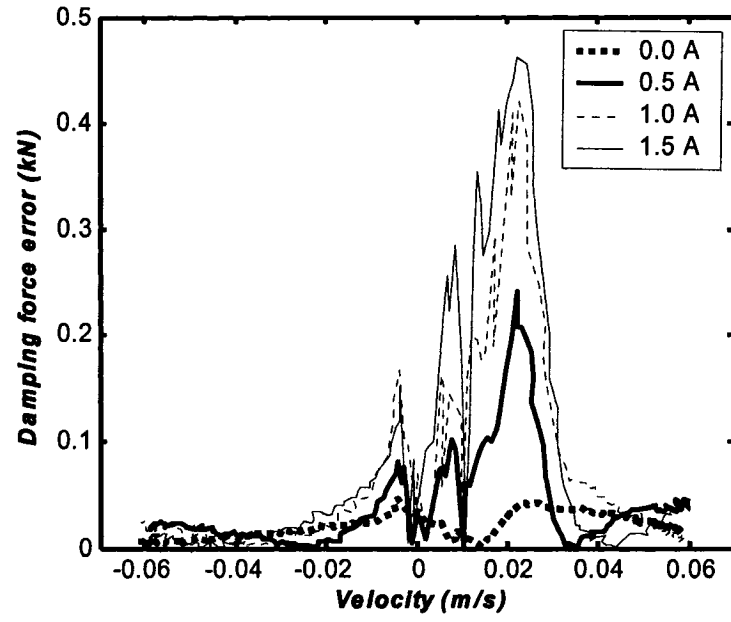
$$e = |f_d(t) - f_m(t)|; \quad t_0 \leq t \leq t_0 + T/2 \quad \text{and} \quad \ddot{x}(t) \geq 0 \quad (3.21)$$

where t_0 and T define the initial time and the period.

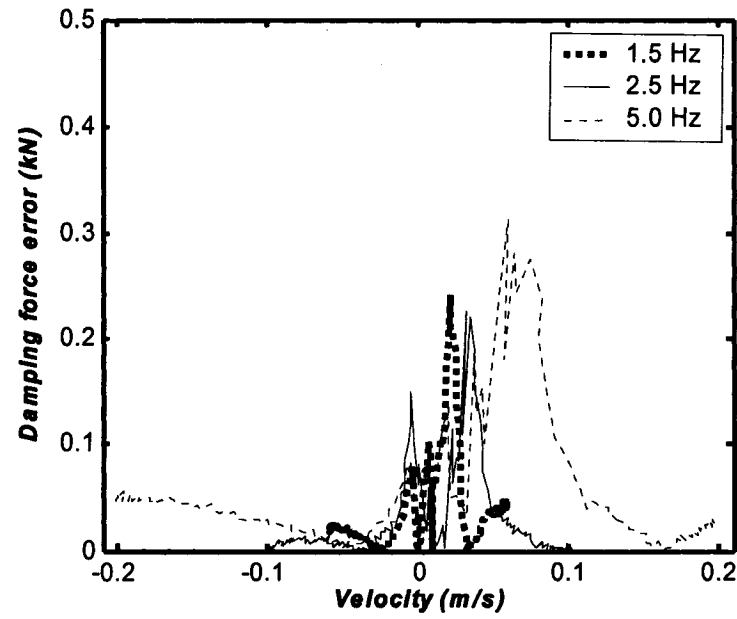
Figure 3.9 illustrates the damping force error of the modified piecewise linear biviscous model versus instantaneous velocity under selected levels of current, and excitation frequency, while the amplitude of excitation is held at 6.35 mm. Figure 3.9 (a) shows the error as a function of current under a constant excitation frequency of 1.5 Hz. The results show the peak error occurs near the transition velocity of 0.02 m/s between the pre- and post-yield conditions, irrespective of the applied current. This is attributed to the discontinuity in the piecewise linear force function defined by the model of the transition velocity. The magnitude of error tends to be larger at velocities within the width

of the hysteresis loop and diminishes at higher velocities. The magnitude of error increased with current due to higher associated peak force. Both the peak and the transition velocities increase with excitation frequency. Figure 3.9 (b) further shows that the peak error always occurs in the vicinity of the transition velocity, while the error magnitude increases with excitation frequency. The results suggest that the peak relative errors with respect to the corresponding damping force remain within 35% to 45% range for the excitation and current conditions considered.

The prediction error of the polynomial function model shown in Figure 3.10 is evaluated only for 1.5 Hz excitation frequency only, since the identified model parameters cannot be considered valid under other excitation conditions. While the peak damping force error is generally smaller than that obtained for the modified biviscous model, considerable error magnitudes are observed over the entire velocity range. The large errors generally occur in the vicinity of the transition velocity, and the oscillations inherent to the higher-order polynomial functions cause large magnitude errors, particularly when the force approaches saturation.



(a)



(b)

Figure 3.9: The damping force prediction error of the modified piecewise linear biviscous model as function of: (a) applied current, $A_r = 6.35$ mm, $f_r = 1.5$ Hz; and (b) excitation frequency, $A_r = 6.35$ mm, $i = 0.5$ A.

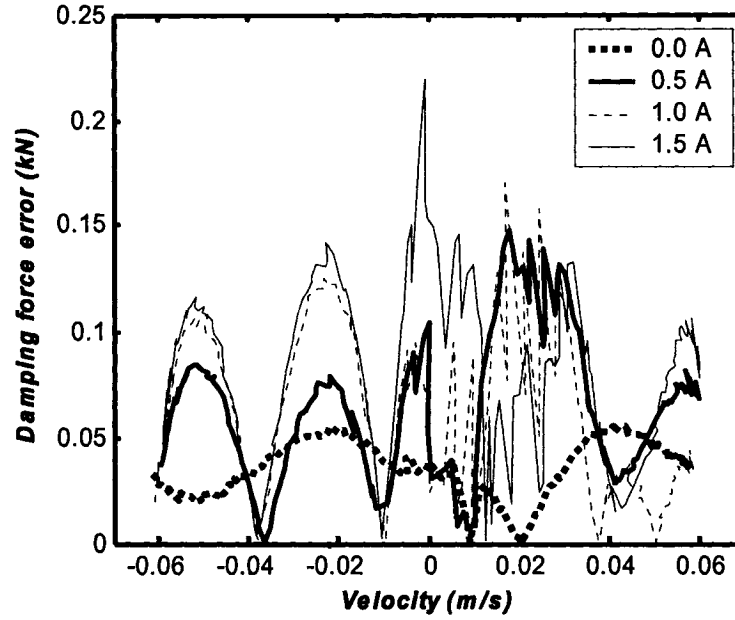
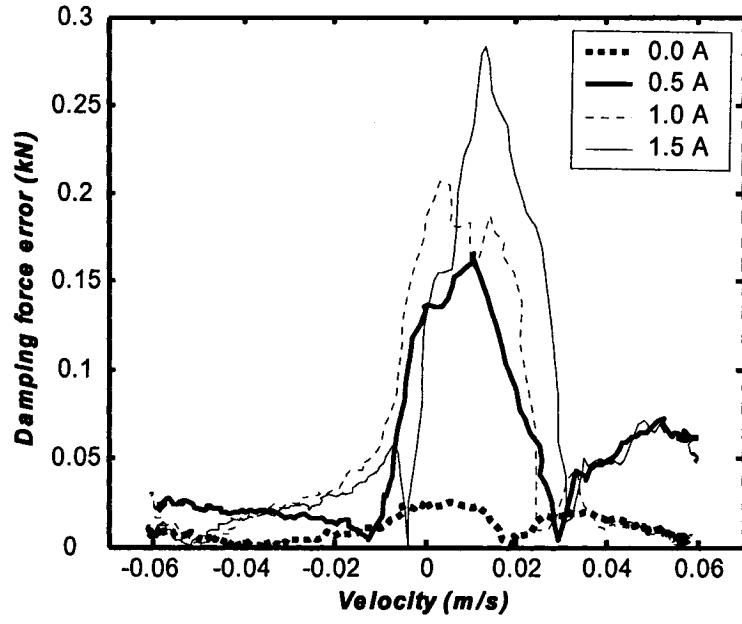
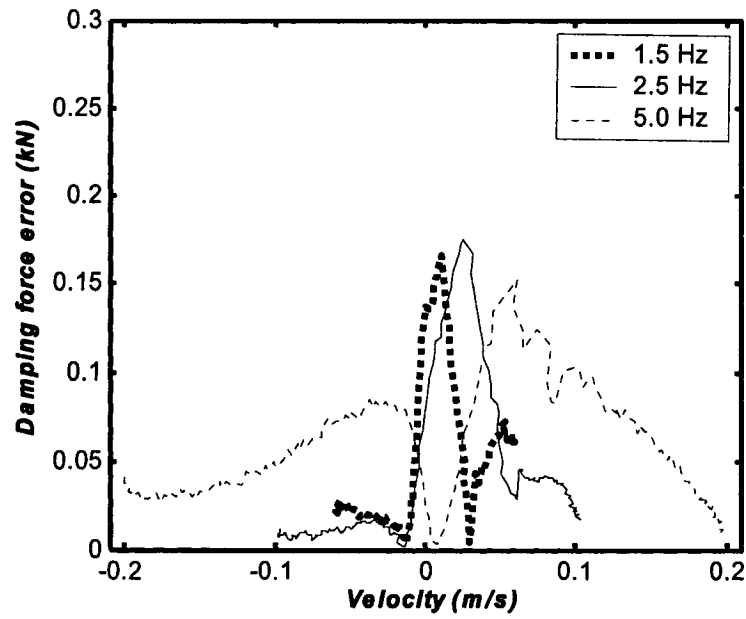


Figure 3.10: The damping force prediction error of the modified polynomial model as function of: applied current $A_r = 6.35$ mm, $f_r = 1.5$ Hz.

Figures 3.11 and 3.12 illustrate the damping force error due to modified extended Bouc-Wen and the sigmoid function models, respectively, as function of the applied current and excitation frequency. Both the models involve continuous and smooth transition between the pre- and post-yield behavior; the magnitudes of errors in the vicinity of the transition velocity are thus relatively small. Both the models show peak prediction errors at velocities lower than the transition velocity but within the width of the hysteresis loop, irrespective of the excitation frequency and applied current. While the sigmoid function model yields relatively smaller peak error, it causes considerable error near extreme velocities corresponding to force-limiting behavior of the damper.

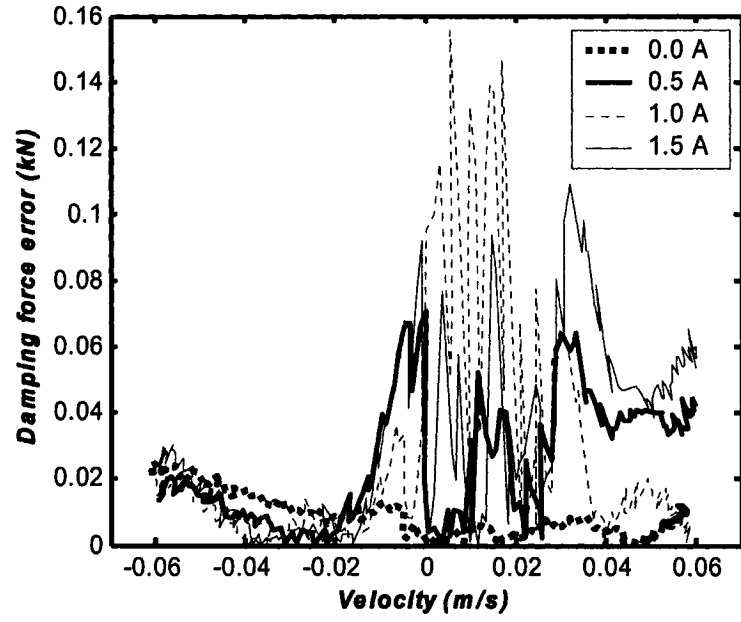


(a)

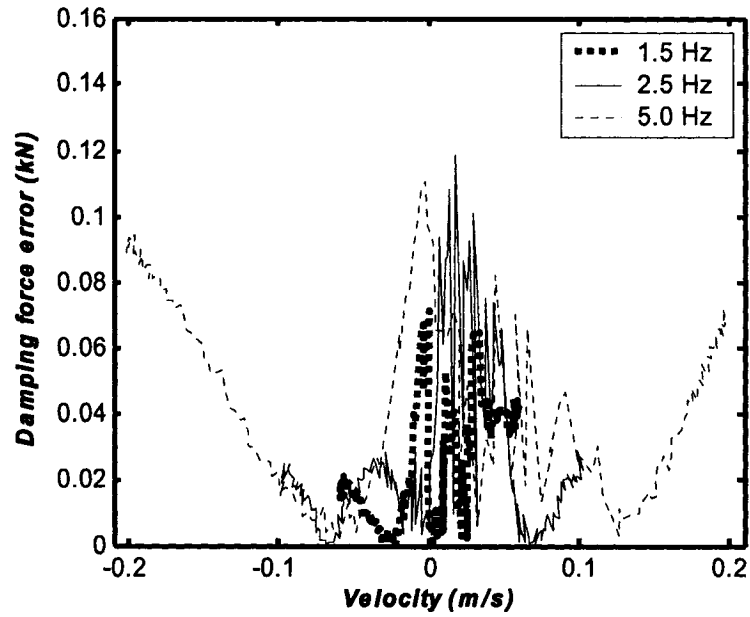


(b)

Figure 3.11: The damping force prediction error of the modified extended Bouc-Wen model as function of: (a) applied current, $A_r = 6.35$ mm, $f_r = 1.5$ Hz; and (b) excitation frequency, $A_r = 6.35$ mm, $i = 0.5$ A.



(a)



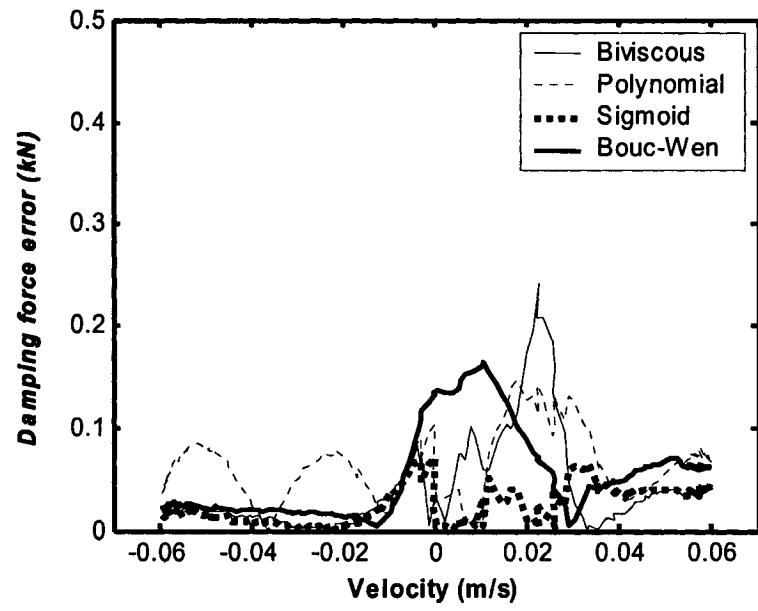
(b)

Figure 3.12: The damping force prediction error of the generalized hysteretic sigmoid model as function of: (a) applied current, $A_r = 6.35$ mm, $f_r = 1.5$ Hz; and (b) excitation frequency, $A_r = 6.35$ mm, $i = 0.5$ A.

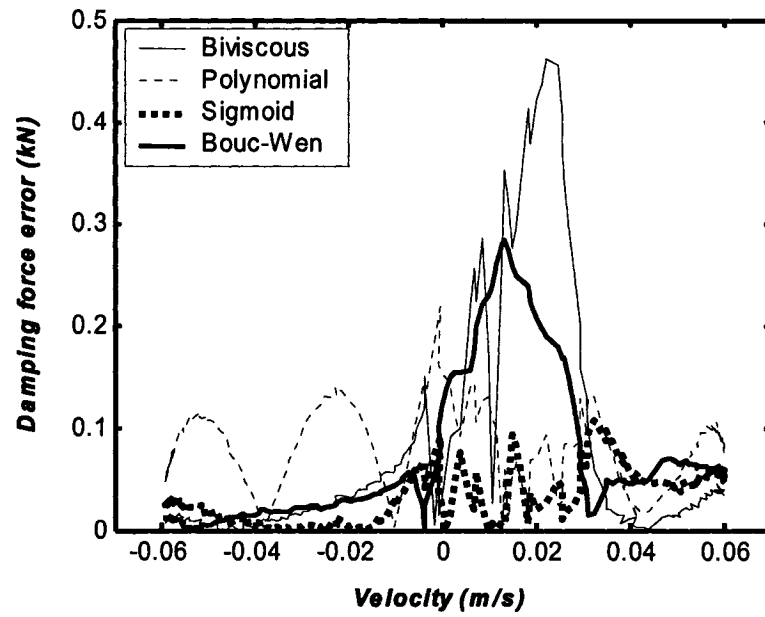
This error is significant under higher excitation frequency and thus the peak velocity,

as seen in Figure 3.12 (b). The extended Bouc-Wen model, on the other hand, yields significantly large error under higher frequency excitation, as seen in Figure 3.11 (b). It should be noted that the range of velocity excitation and thus the width of the hysteresis loop increase with the excitation frequency. The prediction error of the extended Bouc-Wen model could thus be reduced by identified the model parameters on the basis of data acquired at different discrete frequencies, although this would not be a practice approach.

Figure 3.13 further presents comparisons of the damping force prediction error of the four modified models under two different currents (0.5 and 1.5 A), and 6.35 mm excitation amplitude at a frequency of 1.5 Hz. The results show that the modified piecewise linear biviscous model yields highest error magnitude, while the generalized sigmoid models causes least error for both currents. Although the peak error due to the modified polynomial model is slightly smaller than that due to the extended Bouc-Wen model, the polynomial function model causes greater errors over the entire velocity range. With the exception of the modified biviscous model, the error peaks generally concentrate with the width of the hysteresis loop.

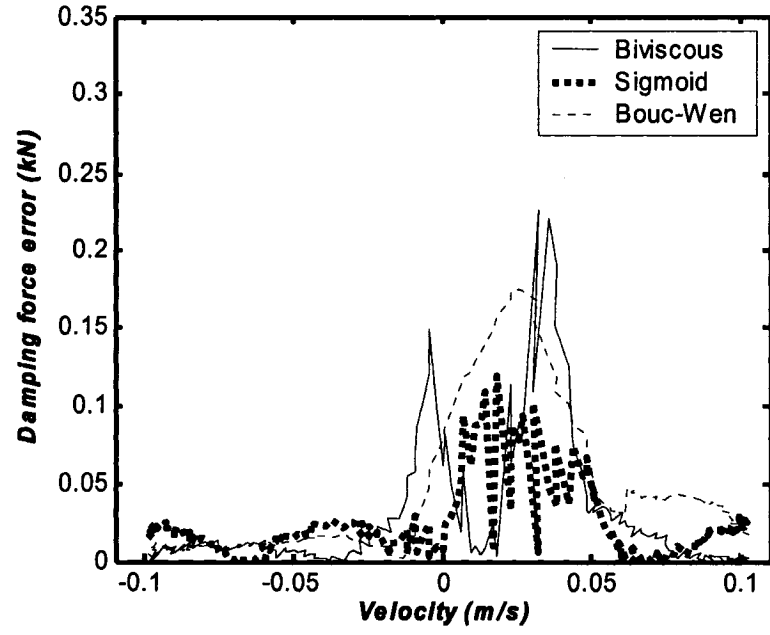


(a)

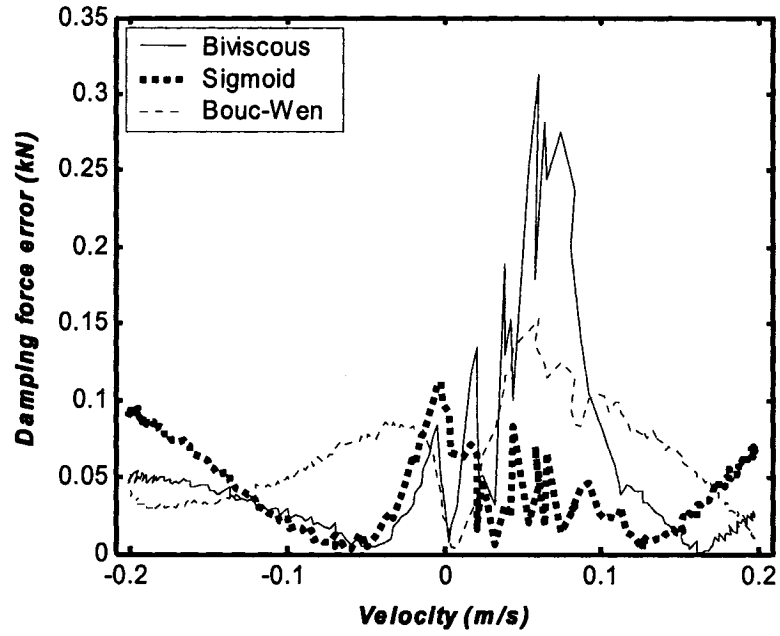


(b)

Figure 3.13: Comparisons of the damping force errors of modified models under $A_r = 6.35 \text{ mm}$, $f_r = 1.5 \text{ Hz}$: (a) $i = 0.5 \text{ A}$; and (b) $i = 1.5 \text{ A}$.



(a)



(b)

Figure 3.14: Comparisons of the damping force error of modified models under $A_r = 6.35$ mm, $i = 0.5$ A at: (a) 2.5 Hz; and (b) 5.0 Hz.

Figure 3.14 illustrates comparisons of the prediction errors of the models, with

exception of the modified polynomial function model under two different excitation frequencies (2.5 and 5.0 Hz) and 0.5 A applied current. The results further show that the generalized sigmoid model yields better prediction of the hysteretic damping force for both excitation frequencies. The relative error analyses suggest that both the extended Bouc-Wen and sigmoid function models can characterize the hysteretic damping force of the MR-damper reasonably well over the range of excitations. The application of the current function to the extended Bouc-Wen model could enhance its prediction ability over a wide range of currents.

3.9 Summary

The vast majority of the models formulated to characterize the hysteretic force-velocity properties of MR-dampers do not incorporate the nonlinear dependences upon the applied current, and the nature of excitation and response. A generalized model formulation comprising the hysteretic and current functions is proposed and applied to a number of reported models to account for variations in both the applied current and the excitation. From the comparisons of the results obtained from resulting modified models with the measured data, it is concluded that the quality of the models can be significantly enhanced using the proposed current function. The use of velocity-dependent slope functions could further enhance the prediction ability of the piecewise linear biviscous model. The presence of non-convergent behavior of the polynomial model can also be addressed by introducing a describing function corresponding to $\ddot{x} = 0$. The modified

linear biviscous model causes large error in the vicinity of the transition velocity due to the discontinuity, while the modified polynomial function exhibits cross-over of the upper and lower curves. The generalized sigmoid hysteretic model yields least error in the f - v hysteresis characteristics under varying currents and excitation conditions, while the modified extended Bouc-Wen model provides reasonably good estimations.

The MR-damper model validations in Chapter 2 and 3 show reasonably good agreements between the simulation results and the measured data, irrespective of the excitation conditions and control current. It is concluded that the proposed generalized sigmoid model as well as the independent current-dependent function can effectively describe the nonlinear steady state hysteretic dynamic and current dependent properties of the controllable MR damper. These models can thus be effectively used to design semi-active controller for implementation in the vehicle suspension, particularly in the suspension seat of off-road and heavy road vehicle. The modeling and analysis of a passive suspension seat are studied in the following chapter.

CHAPTER 4

MODELING AND ANALYSE OF A PASSIVE SUSPENSION SEAT

4.1 Introduction

The shock and vibration transmission performance characteristics of low natural frequency suspension seats, widely employed in off-road and heavy road vehicles, strongly depend upon the component properties and the nature of vertical vibration environment of the target vehicle. A suspension seat, however, is generally designed for particular classes of vehicles that may yield comparable magnitudes and frequencies of vibration [108]. A suspension seat may attenuate or amplify vibration depending upon the predominant frequencies of vehicle vibration, when the suspension movement is limited to its free travel. Exposure to higher magnitudes of vehicle vibration or shock may cause the suspension to impact against the elastic end-stops, and thereby transmit high intensity vibration and shock to the occupant [2, 27, 35]. The vibration environment of off-road vehicles may comprise continuous as well as intermittent vibration of different magnitudes arising from tire-terrain interactions. The vertical vibration environment of heavy road vehicles operating on city roads may also vary from low level continuous vibration to high intensity motions arising from interactions of tires with discontinuities in the road surface, such as drain covers and pot holes [9]. The design objective for a suspension seat should thus involve the consideration of low magnitude continuous vibration and high intensity intermittent shock motions.

The shock and vibration isolation performances of a suspension seat, however, pose conflicting design requirements. A soft and lightly-damped suspension would be adequate under low magnitudes of continuous vibration, while a relatively hard suspension with high damping would yield satisfactory attenuation of high intensity vibration of either continuous or intermittent nature [2]. The vibration isolation characteristics of suspension seats are mostly evaluated through measurements in either the laboratory or in the field. International Standard ISO-7096 [95] provides guidelines for a laboratory-based vibration assessment of suspension seats for different types of construction vehicles. The method involves measurement of frequency-weighted vibration transmission property of a seat under defined vehicular vibration spectra using human subjects of particular body masses, namely 55 and 98 kg. The standardized method thus allows for consideration of the effect of occupant (body) mass and dynamics on the vibration isolation behavior of the seat, while it does not address the performance under high intensity intermittent vibration. Moreover, laboratory assessments involving human exposure to high intensity vibration would raise many ethical concerns, apart from the high inter-subject variability.

Alternatively, a few studies have proposed linear and nonlinear analytical models of the suspension seat that may be employed to study the suspension performance under continuous and intermittent vibration of different intensities [2, 33, 27, 100, 108]. The reported models mostly consider the vertical suspension seat as a two-degrees-of-freedom (2-DOF) dynamic system with either linear or nonlinear component models. The human occupant in majority of these models is considered as a rigid mass [33, 27, 100]. It has

been suggested that human body absorbs considerable amount of vibration energy and may thus influence vibration performance of a seat [1, 32]. A few studies have also integrated multi-DOF biodynamic models of the seated body, derived from the measured apparent mass responses, to the suspension seat model to derive analytical models of the coupled human seat system [2, 32, 108]. A recent study has established that contributions due to the seated occupant are very small for low natural frequency suspension seats but quite substantial for automotive seats with relatively higher natural frequency [97]. This is further supported by the driving-point mechanical impedance response of seated occupants exposed to vertical vibration, which resembles that of a rigid mass at frequencies up to 2 Hz [101]. The shock and vibration isolation analyses of low natural frequency suspension seats may thus be effectively carried out using an equivalent mass representation of the seated occupant.

The applicability of many of the reported component models, may be limited to only low magnitudes of excitations. A recent study has proposed nonlinear component models to study the vibration isolation performance of suspension seats under high magnitudes of vibration [100]. The majority of these employ linear visco-elastic cushion and spring models [2, 27, 32]. A seat cushion exhibits linear properties under low magnitudes of deformation but highly nonlinear force-deflection characteristics under higher deflections [109, 110], which under extreme conditions may cause intermittent loss of body-seat contact [108]. A few studies have proposed regression functions to characterize the cushion behavior as functions of the excitation frequency, magnitude of relative

deformation and the preload [100, 108, 110]. Such models require prior knowledge of excitation frequency and magnitude of relative deflection of the cushion, and thus limit their general applicability. The suspension system comprising either a mechanical or an air spring and a hydraulic damper, within the guiding linkages, also exhibits highly nonlinear force-deflection and force-velocity properties under high magnitudes of excitation. In a recent study, the Bouc-Wen model has been applied to characterize the hysteretic force-deflection ($f-d$) and force-velocity ($f-v$) properties of the overall suspension system, while the contribution due to cushion is ignored [12]. This model can not be considered to be generally applicable as the Bouc-Wen parameters are identified for a particular body mass and suspension type. A few studies have also introduced linear or nonlinear models of the elastic end-stops to study the frequency and severity of end-stop impacts, and the shock isolation performance [27, 35, 111].

In this chapter, the role of suspension design parameters on the shock and vibration performance characteristics of suspension seats are investigated through development and analysis of a nonlinear model under different types of excitations. A polynomial based cushion model is proposed and integrated to the suspension model. The resulting model is validated using the laboratory-measured data, and analyzed under a wide range of excitations including high magnitude excitations that cause impacts against the end-stops. The influences of variations in design parameters on the shock as well as vibration isolation performances are assessed in terms of different measures, namely the seat effective amplitude transmissibility ($SEAT$), and vibration dose value (VDV) ratio. The

results are used to identify desirable suspension damping parameters for realizing improved shock and vibration isolation for the selected vehicles.

4.2 Model Development

Assuming a rigid mass representation of the seated human occupant, a suspension seat can be described by a 2-degrees-of-freedom (DOF) nonlinear dynamic system model constrained along the vertical direction, as shown in Figure 4.1 [27, 100, 109, 111]. In the model, m_o and m_s represent the driver body mass and mass due to seat suspension. The suspension system is characterized by: (i) friction force F_f due to the guiding linkage and joints, and damper seal; (ii) spring force F_s ; (iii) nonlinear damping force F_d due to an inclined hydraulic damper; (iv) F_b due to elastic end-stops considered as a clearance spring; and (v) a visco-elastic cushion force F_c . The differential equations of motion of the two-DOF suspension seat system can be written as:

$$\begin{cases} m_o \ddot{x}_o = -F_c + m_o g \\ m_s \ddot{x}_s = -F_s - F_f - F_d - F_b + F_c + m_s g \end{cases} \quad (4.1)$$

The suspension seat considered in this study comprises a relatively soft poly-urethane foam (PUF) cushion supported on the suspension platform. The platform is supported by a cross-linkage mechanism to ensure nearly vertical motion. A pneumatic spring and a hydraulic damper are installed between the platform and the suspension base. The rebound (top) and compression (bottom) elastic end-stops are installed to limit the free travel to approximately 140 mm. The rebound end-stop, installed within the roller

guide, could be adjusted to achieve different suspension travel, while the height adjustment is achieved by controlling the air volume and pressure within the pneumatic spring. The natural frequency of the suspension seat was measured as 1.25 Hz [100]. The suspension may thus be employed in a wide range of heavy highway and off-highway vehicles. The static and dynamic characteristics of suspension components were measured in the laboratory in terms of instantaneous force, displacement and velocity responses under different preloads and excitation levels [100].

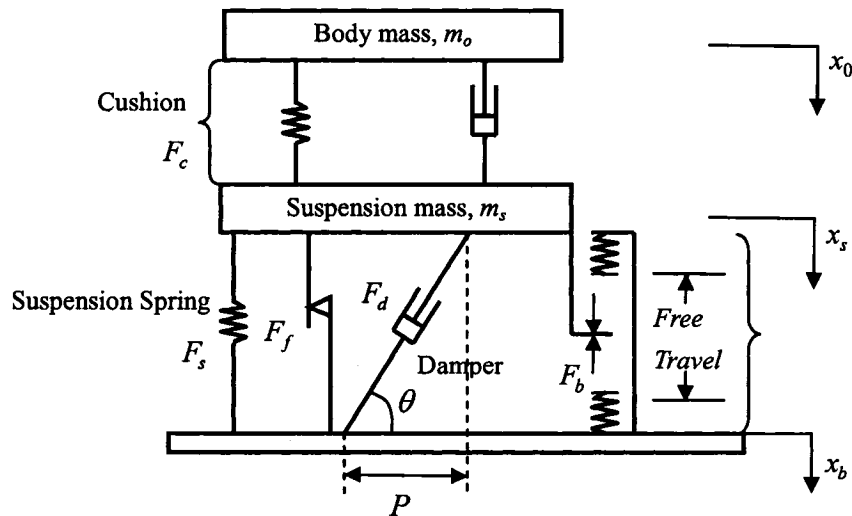


Figure 4.1: Two-DOF combined human-suspension seat model.

4.2.1 Nonlinear Cushion Model

The static force-deflection characteristics of seat cushions generally reveal progressively hardening and hysteretic properties, as illustrated in Figure 4.2 [100, 110]. The mean force-deflection (f - d) characteristics are often used to identify the stiffness

coefficients at different preloads. In order to characterize the dynamic properties of the seat cushion, experiments were performed to measure the force-deflection characteristics under sinusoidal excitations of different amplitudes at different discrete frequencies in the 0.5 to 10 Hz range. The experiments were also performed under three different preloads (40, 55 and 66 kg) representing different body masses supported by the seat.

The dynamic force developed by the seat cushion can be characterized in three different categories depending upon the magnitude of cushion deformation. Under continuous motion, the dynamic force varies nonlinearly with the deflection, and is directly related to the seated mass, such that:

$$f_{cm}(t, x_{os}) = \sigma m_o \begin{cases} k_{l0}x_{os}(t) + k_{nl}x_{os}(t)^2 + c_{l0}\dot{x}_{os}(t); & \dot{x}_{os}(t) \geq 0 \\ k_{l0}x_{os}(t) + k_{nl}x_{os}(t)^2 + c_{rl}\dot{x}_{os}(t); & \dot{x}_{os}(t) < 0 \end{cases} \quad (4.2)$$

where $f_{cm}(t)$ is the cushion force under continuous deformation of the PUF material alone, σ is a coefficient describing the dependence on the seated mass m_o , k_{l0} and k_{nl} are the linear and nonlinear stiffness coefficients, and $x_{os}(t) = x_o(t) - x_s(t)$ is the instantaneous cushion deformation. The measured data, acquired under harmonic excitations, generally revealed asymmetric energy dissipation properties of the PUF cushion in compression and rebound, which are presented in Figure 4.3 (dotted line) under different excitation frequencies. The viscous damping coefficients in compression and rebound are thus described by constants c_{l0} and c_{rl} , respectively.

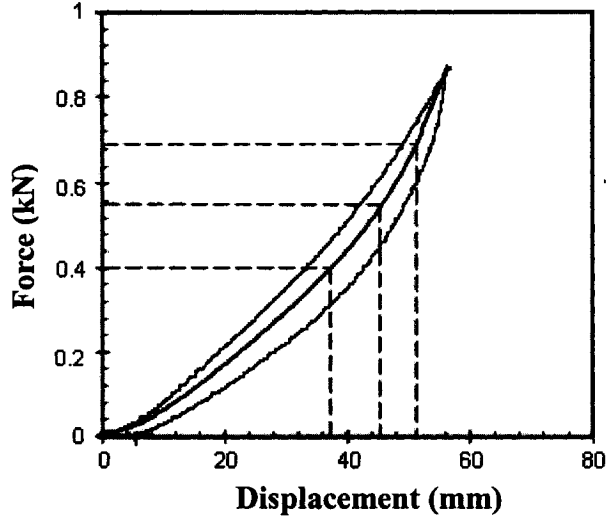


Figure 4.2: Measured static force-deflection characteristics of a typical seat cushion.

Under high magnitudes of excitation, the PUF may collapse and induce bending of the pan, which would yield extremely high stiffness of the cushion. For the candidate seat considered in the study, the free thickness (T_c) of the cushion was measured as 79 mm. On the basis of the measured data, it was established that the pan bending initiates, when cushion deformation approaches 91% of its free thickness. Furthermore, a large magnitude of the resulting force could cause loss of contact between the body and the seat, which constitutes the third category for the cushion model. The force developed by a seat cushion could thus be generally expressed as:

$$F_c(t) = \begin{cases} f_{cm}(t, x_{os}) & \text{for } 0 < x_{os}(t) \leq \eta T_c \\ 0 & \text{for } x_{os}(t) \leq 0 \\ f_{cm}(t, \eta T_c) + k_b(x_{os}(t) - \eta T_c) & \text{for } x_{os}(t) > \eta T_c \end{cases} \quad (4.3)$$

where η defines the proportion of the free thickness T_c , when pan bending initiates, and k_b is the effective stiffness of the pan. The force due to PUF, $f_{cm}(t, \eta T_c)$, is assumed to

saturate when pan bending initiates.

The parameters of the proposed cushion model are identified from the measured data acquired under a broad range of excitations. A minimization function of error between the model and measured forces is formulated as:

$$J = \sum_{j=1}^3 \sum_{k=1}^3 \sum_{l=1}^3 \sum_{m=1}^{360} (f_{ce(j,k,l,m)} - f_{cm(j,k,l,m)})^2 \quad (4.4)$$

where f_{ce} and f_{cm} are the magnitudes of dynamic forces derived from the measured data and the model, respectively, corresponding to j^{th} , k^{th} and l^{th} test condition involving three different deformation magnitudes (6.35, 12.7, 19.05 mm), frequencies (1.5, 2.0, 2.5 Hz), and preloads (431.2, 539, 646.8 N). Index m refers to the number of coordinates considered in a single f - d hysteresis loop. Considering that the low natural frequency suspension seat yields considerable attenuation of vibration at frequencies above 2.5 Hz, the minimization function employs measured data corresponding to three discrete excitation frequencies (1.5, 2.0 and 2.5 Hz). The error minimization problem is solved using the '*fmincon*' function available within the MATLAB optimization toolbox [84], while subject to inequality constraints: $\sigma > 0$, $k_{t0} > 0$, $c_{t0} > 0$ and $c_{t1} > 0$. The solution resulted in model parameters summarized in Table 4.1.

The validity of the proposed model is examined under different preloads and excitation conditions. As an example, Figure 4.3 (a, b, c) illustrates comparisons of measured and computed dynamic cushion forces under different excitation frequencies (1.5, 2.0 and 2.5 Hz), deformation magnitudes (6.35, 12.7 and 19.05 mm) and 40 kg

preload. Comparisons show reasonably good agreement between the model results and the measured data under low to medium levels of deformations (6.35 and 12.7 mm). The model responses under high magnitude of deformation, however, deviate from the corresponding measured data, during the rebound cycle ($\dot{x}_{os} < 0$), irrespective of the excitation frequency. This suggests nonlinear energy dissipation property of the PUF cushion during rebound under high magnitude of excitation, which may be attributed to limited rate of air intake by the PUF at higher frequencies.

Table 4.1: The model parameters.

Component	Parameters	
Cushion	$k_{i0} = 20.6 \text{ N/mm}$	$c_{i0} = 0.34 \text{ Ns/mm}$
	$k_{i1} = 0.26 \text{ N/mm}^2$	$c_{i1} = 0.46 \text{ Ns/mm}$
	$\sigma = 0.018$	$T_c = 79 \text{ mm}$
	$k_b = 80 \text{ N/mm}$	$\eta = 0.91$
Damper	$C_{c1} = 2 \text{ kNs/m}$	$p = 0.79$
	$\gamma_c = 0.4$	$v_c = 0.115 \text{ m/s}$
	$\gamma_e = 1$	$F_{sb} = 65.0 \text{ N}$
	$\theta_0 = 40^\circ$	
Linkage with Spring	$k_s = 7.7 \text{ m}^{-1}$	$d_e + d_c = 140 \text{ mm}$
	$a_{f0} = 0.16$	$a_{f1} = -0.76$
	$a_{f2} = 4.81$	
Elastic end Stops	$k_{c1} = 12.5 \text{ kN/m}$	$k_{e1} = 10.8 \text{ kN/m}$
	$k_{c2} = 93.8 \text{ kN/m}$	$k_{e2} = 60.0 \text{ kN/m}$
	$h_{c1} = 86.5 \text{ mm}$	$h_{e1} = 80.6 \text{ mm}$
	$d_m^{(c)} = 89.4 \text{ mm}$	$d_m^{(e)} = 83.0 \text{ mm}$

The dependence of the measured and computed cushion forces on the preload is illustrated in Figure 4.3 (d) under 6.35 mm peak deformation at 2 Hz. The figure shows the magnitude of the dynamic component of the force, which is derived upon removing

the static force from the total force. The results show comparable trends and further validate the consideration of body mass dependence coefficient σ in the model.

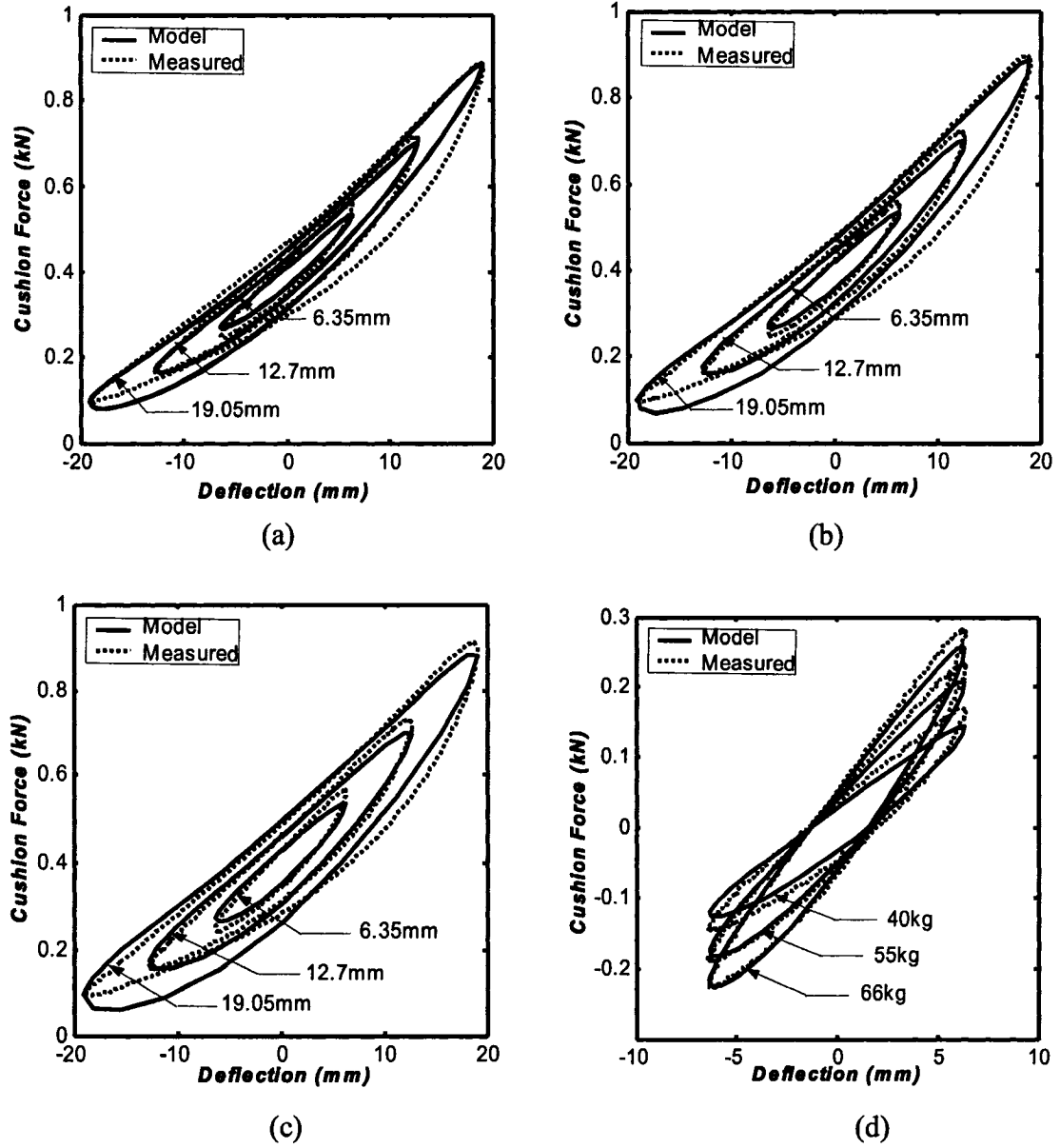


Figure 4.3: Comparisons of cushion model responses with the measured data under different excitation frequencies and preloads: (a) 1.5 Hz, 40 kg preload; (b) 2.0 Hz, 40 kg preload; (c) 2.5 Hz, 40 kg preload; (d) 40, 55, 66 kg preloads.

4.2.2 Suspension Forces

The suspension force is characterized by three components due to damper, spring and end-stops. Assuming negligible force due to the gas charge in a hydraulic damper, the damper force measured at extremely low speeds is generally considered to represent the seal friction force. The hydraulic or viscous forces attributed to pressure drop across the bleed and blow-off valves of the damper vary with the relative velocity in a nonlinear manner [107]. Hydraulic dampers are generally designed to yield asymmetric damping force in compression and rebound. The mean force-velocity characteristics of a two-stage damper can be characterized in terms of low and high speed damping coefficients in a piecewise linear manner, as shown in Figure 4.4:

$$F_d = \begin{cases} C_{c1}\dot{x} & 0 \leq \dot{x} \leq v_c \\ C_{c1}[v_c + \gamma_c(\dot{x} - v_c)] & \dot{x} \geq v_c \\ pC_{c1}\dot{x} & v_e \leq \dot{x} \leq 0 \\ pC_{c1}[v_e + \gamma_e(\dot{x} - v_e)] & \dot{x} \leq v_e \end{cases} \quad (4.5)$$

where \dot{x} is damper piston velocity along the axis of the damper, F_d is damping force along the axis of the damper installation, C_{c1} is the low-speed compression mode damping coefficient, $\gamma_c = C_{c2}/C_{c1}$ is the compression damping reduction factor, and v_c is the transition velocity. The damping asymmetry in rebound and compression is described by the asymmetry factor $p = C_{e1}/C_{c1}$ and $\gamma_e = C_{e2}/C_{e1}$ is the rebound damping reduction factor and v_e is the corresponding transition velocity. The model parameters for the suspension seat damper were derived from the measured data, and summarized in Table 4.1.

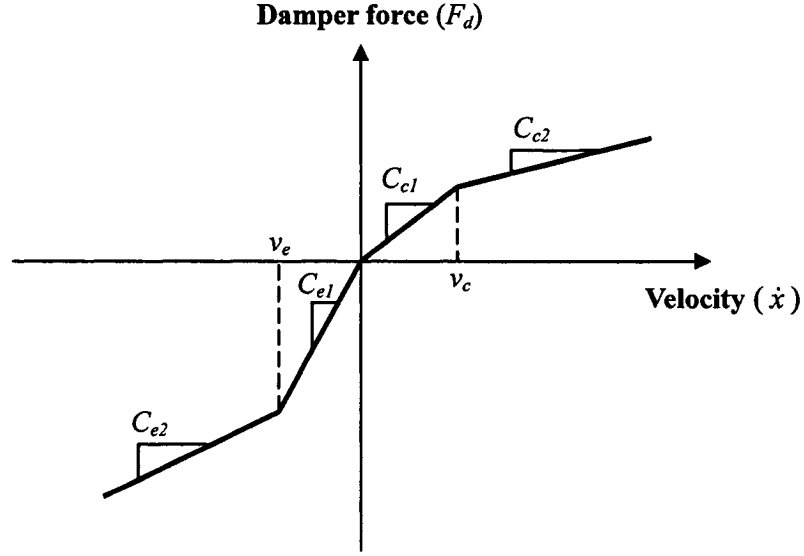


Figure 4.4: Force-velocity characteristics of a typical hydraulic damper.

The vertical damping force due to the inclined damper F_{dv} can be derived from:

$$F_{dv} = \begin{cases} C_{c1} \dot{x}_{sb} \sin^2 \theta & 0 \leq \dot{x}_{sb} \sin \theta \leq v_c \\ C_{c1} [v_c + \gamma_c (\dot{x}_{sb} \sin \theta - v_c)] \sin \theta & \dot{x}_{sb} \sin \theta \geq v_c \\ p C_{c1} \dot{x}_{sb} \sin^2 \theta & v_e \leq \dot{x}_{sb} \sin \theta \leq 0 \\ p C_{c1} [v_e + \gamma_e (\dot{x}_{sb} \sin \theta - v_e)] & \dot{x}_{sb} \sin \theta \leq v_e \end{cases} \quad (4.6)$$

where $\dot{x}_{sb} = \dot{x}_s - \dot{x}_b$ is the vertical relative velocity between the suspension mass and the base, θ is the instantaneous inclination angle of the damper (Figure 4.1), which can be derived from initial inclination angle θ_0 , relative displacement x_{sb} , and horizontal projection of the attachment points of the damper P , such that:

$$\alpha = \tan^{-1} \left[\tan(\theta_0) - \frac{x_{sb}}{P} \right] \quad (4.7)$$

The restoring force due to a suspension seat can be conveniently derived from the static force-deflection properties of the suspension system in the absence of the hydraulic damper. Such properties would not only yield the restoring force due to the air spring, but

also the friction force due to linkage and the end stop forces. Figure 4.5 (a) illustrates typical force-deflection characteristics of the suspension-seat mechanism including the air spring [32]. Linear variations in the force within the free travel ($d_e \leq x_{sb} \leq d_c$) suggest linear stiffness properties of the air spring, while the difference in the forces during loading and unloading characterize the static friction. The nonlinear variations at the extremities represent the force-deflection characteristics of the end-stop buffers, and $d_m^{(e)}$ and $d_m^{(c)}$ represent the total effective travel in rebound and compression, respectively. The suspension adjustment to the mid-ride height would yield $d_e = d_c$.

The static stiffness due to the spring tends to increase with increasing preload due to higher charge pressure [100]. The restoring force due to air spring is thus expressed as a function of normalized stiffness (k_s , ratio of spring rate to the preload), such that:

$$F_s = F_{preload} k_s x_{sb} \quad (4.8)$$

The friction force due to the suspension mechanism was also found to vary with the preload and the deflection, as shown in Figure 4.6 [100]. A regression function in x_{sb} was proposed to describe the variations in the friction force F_f , such that:

$$F_f = F_{preload} [a_{f0} + a_{f1} x_{sb} + a_{f2} x_{sb}^2] + F_{sb} \quad (4.9)$$

where F_{sb} is the damper seal friction lumped with the suspension friction force, and a_{f0} , a_{f1} and a_{f2} are constant coefficients, identified from the measured data.

Suspension seats are designed with elastic end-stops to limit the excessive relative motion of the soft suspension that may occur under high levels of excitations. The end stops are generally of conical geometry, which yield relatively soft impact as the travel

exceeds the free travel. The stiffness, however, gradually increases with the deflection of elastic buffer. The force-deflection characteristics of elastic end-stops can be characterized by a two-stage piece-wise linear clearance spring model (Figure 4.5 b), such that:

$$F_b = \begin{cases} 0 & -d_e \leq x_{sb} \leq d_c \\ k_{c1}(x_{sb} - d_c) & d_c < x_{sb} \leq h_{c1} \\ k_{c1}(h_{c1} - d_c) + k_{c2}(x_{sb} - h_{c1}) & h_{c1} < x_{sb} \leq (d_m^{(c)}) \\ k_{e1}(x_{sb} + d_e) & -h_{e1} < x_{sb} \leq -d_e \\ -k_{e1}(h_{e1} - d_e) + k_{e2}(x_{sb} + h_{e1}) & (-d_m^{(e)}) < x_{sb} \leq -h_{e1} \end{cases} \quad (4.10)$$

where F_b is the restoring force, and k_{c1} , k_{c2} , k_{e1} and k_{e2} are the piece-wise linear stiffness constants in compression and rebound, respectively. These parameters, identified from the measured data, are summarized in Table 4.1.

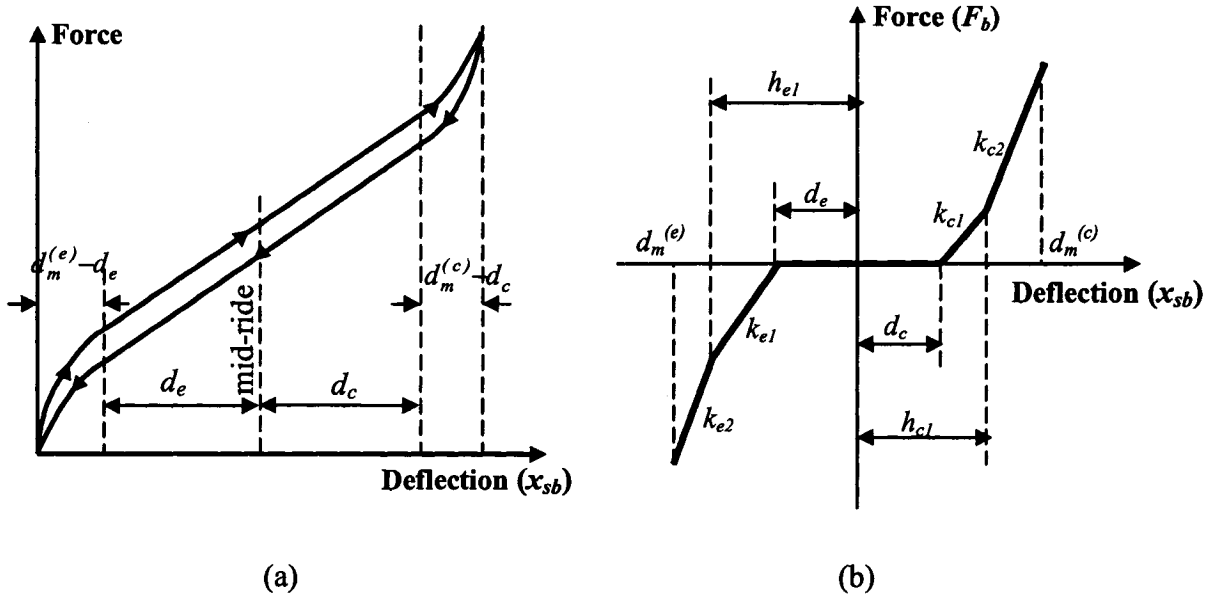


Figure 4.5: Force-deflection characteristics of the: (a) elastic element of suspension mechanism; and (b) end-stops.

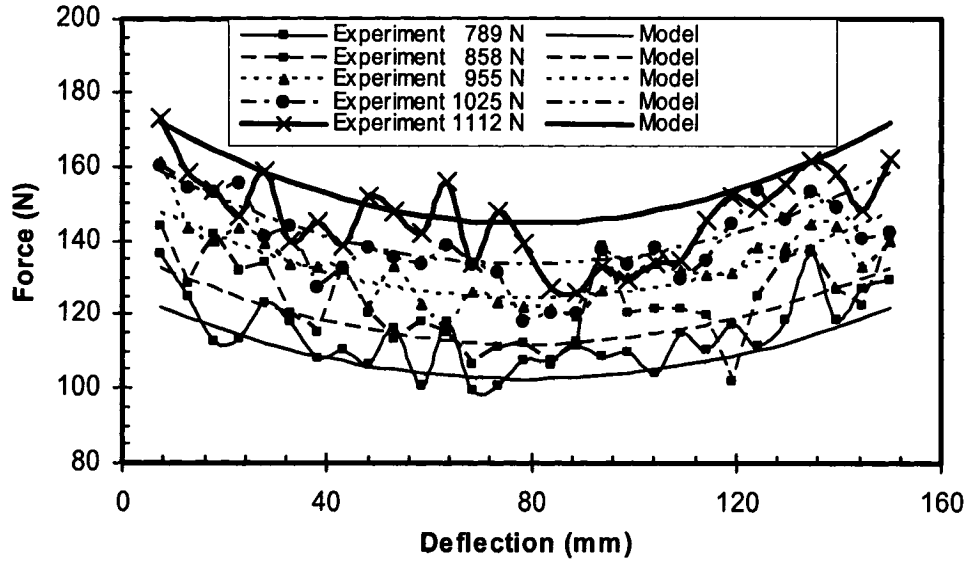


Figure 4.6: Comparisons of measured friction force with the model results as function of preload and deflection.

4.3 Excitation Signals

Laboratory experiments were performed to study the shock as well as vibration transmission characteristics of the suspension seat using a whole-body vehicular vibration simulator (WBVVS), which comprises a seat platform supported on two servo-hydraulic actuators. The experiments were designed to evaluate the suspension performance under different excitations representing continuous as well as high intensity deterministic and random vibration. These included: (i) harmonic vibration in the 0.625 to 10 Hz frequency range, swept at a rate of 1 octave/min (constant peak displacement of 25 mm in the 0.625 to 2 Hz range, and constant peak acceleration of 3.95 m/s^2 at frequencies above 2 Hz); (ii) harmonic excitation in the vicinity of suspension resonant frequency; (iii) a transient excitation representing the vehicle response to an abrupt input, as shown in Figure 4.7;

and (iv) random vertical vibration due to different vehicles, which are described below. The transient excitations caused by abrupt discontinuities in the road profile comprise oscillating motions in the vicinity of the vertical mode natural frequency of the vehicle spring mass.

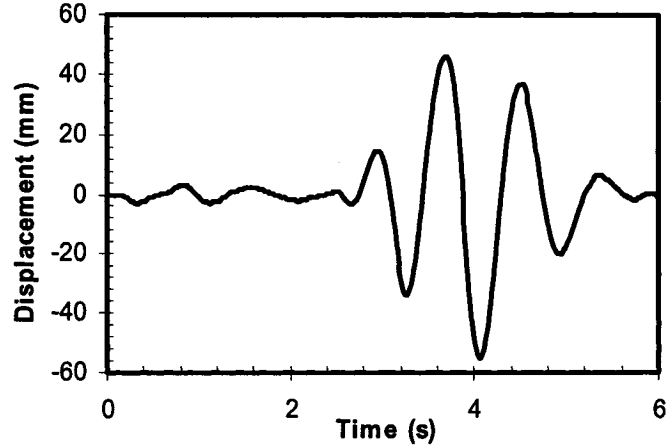


Figure 4.7: Time history of transient excitation.

4.3.1 Vehicular Vertical Vibration

The vertical vibration spectra of three different vehicles (an urban bus, a sidewalk snowplow, and a class I construction vehicle defined in ISO-7096 [95]) are considered to study the suitability of the seat suspension system for different vehicles. The vertical vibration environment of an urban bus, referred to as “Bus”, is synthesized from the power spectral density (PSD) function defined in [9]:

$$H(s) = K_m \frac{s(s^2 + A_{m1}s + B_{m1})}{\prod_{i=1}^2 (s^2 + C_{mi}s + D_{mi})} \quad (4.11)$$

where $H(s)$ is the transfer function proposed to describe the PSD of vertical

acceleration measured beneath the driver seat of an urban bus, $s = j\omega$, and A_{m1} , B_{m1} , and C_{mi} , D_{mi} ($i=1, 2$) are the constant coefficients. This transfer function Equation (4.11) could also be applied to characterize the vertical vibration spectrum of a sidewalk snowplow [9], referred to as “Snow”. The convolution of the transfer function with a white noise random signal (PSD magnitude ≈ 1.0) yields the acceleration time history due to vehicle vibration.

ISO 7096 [95] defines the vertical vibration spectra of tractor-scrapers with either front axle suspension or vibration absorber hitch, referred to as “EM1”. The PSD of vertical acceleration of this vehicle vibration is defined in terms of a low- and a high-pass filter with 24 dB/octave attenuation. The transfer function for synthesizing the vehicle vibration is given by:

$$H(s) = K_m \frac{s^4}{\prod_{i=1}^2 (s^4 + A_{mi}s^3 + B_{mi}s^2 + C_{mi}s + D_{mi})} \quad (4.12)$$

The constant coefficients, A_{mi} , B_{mi} , C_{mi} and D_{mi} ($i=1, 2$) for the three vehicular spectra are summarized in Table 4.2. The analyses are also performed under above excitations amplified by 150% to study the seat performance under high intensity vibration. Figure 4.8 illustrates the PSD of vertical vibration of selected vehicles (“Bus”, “Snow” and “EM1”) and the corresponding amplified vibration (“BusA”, “SnowA” and “EM1A”). The predominant frequencies of vertical vibration of the bus and construction vehicle occur around 1.5 Hz and 2.1 Hz, respectively, while that for the snowplow occur near 2 Hz and in the 4-6 Hz bands. The peak acceleration PSD magnitude is the highest for the

EM1 vehicle, and the lowest for the urban bus. The relative magnitudes of selected vertical vibration are further assessed in terms of frequency-weighted and un-weighted *rms* acceleration and vibration dose (*VDV*) values, using the W_k -weighting function described in ISO-2631 [94], which are presented in the following sections.

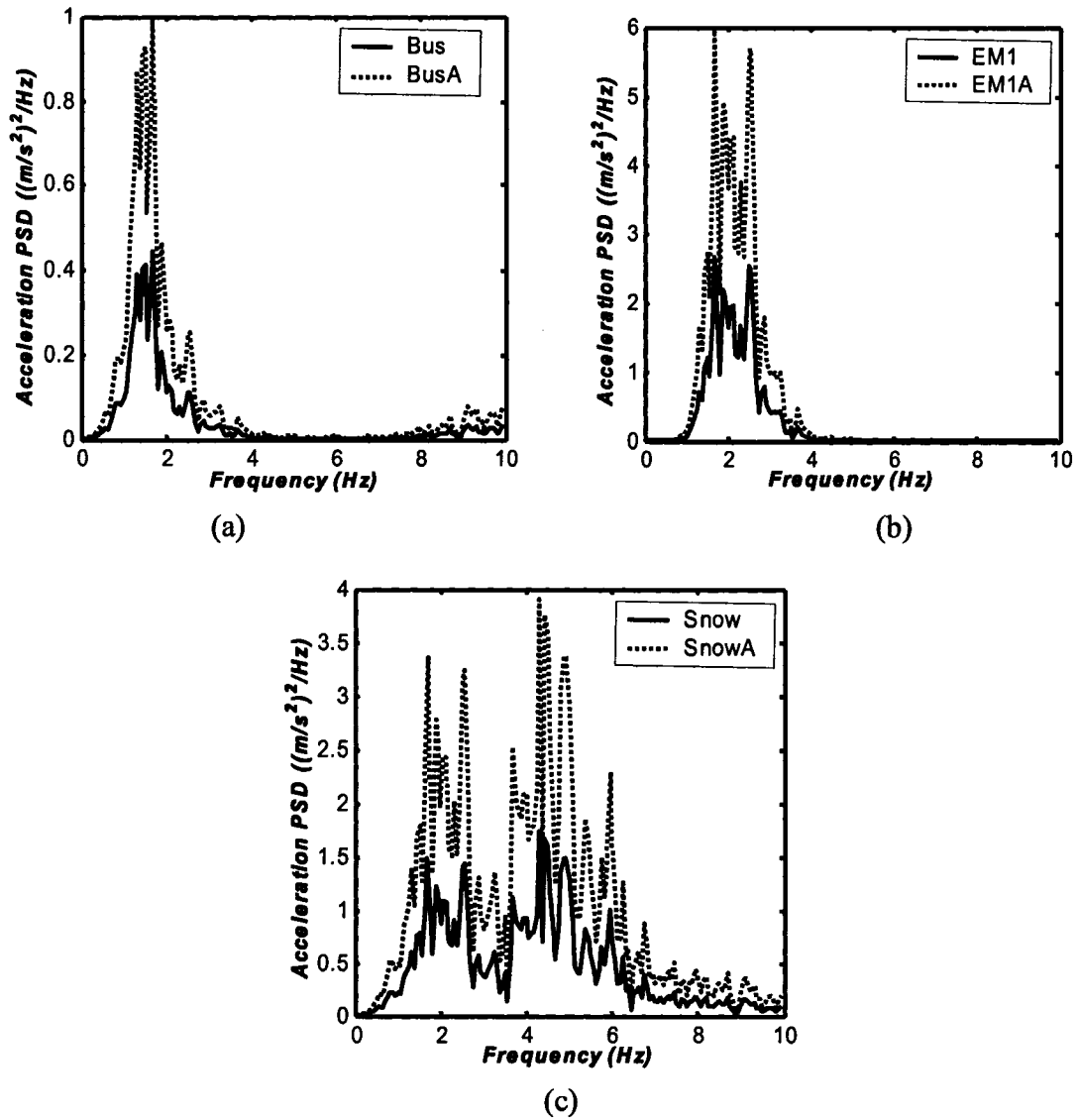


Figure 4.8: PSD of vertical acceleration of selected vehicles and the corresponding amplified signals: (a) Bus & BusA; (b) EM1 & EM1A; (c) Snow & SnowA.

Table 4.2: The coefficients of the vertical acceleration transfer functions describing the vertical vibration characteristic of an urban bus (Bus), a sidewalk snowplow (Snow) and a class I construction vehicle (EM1).

Vehicle	Coefficients								
	K_m	A_{m1}	B_{m1}	C_{m1}	D_{m1}	A_{m2}	B_{m2}	C_{m2}	D_{m2}
Bus	9.99	13.13	1405.83	31.98	4352.5	-	-	4.62	82.9
Snow	18.6	8.48	476.11	7.29	712.98	-	-	10.12	157.91
EM1	1.02e5	24.8	303.25	2.2e3	7.89e3	41.33	842.37	1.02e4	6.09e4

4.4 Suspension Seat Model Validation

The model validity was examined under different excitations, while the human occupant is considered as a rigid mass of 77 kg. The equations of motion for the suspension model together with the component relations are solved under selected vibration excitations. The responses under harmonic excitations were evaluated in terms of *rms* acceleration transmissibility of the seat, while those under random excitations were expressed in terms of PSD of acceleration. The responses under transient and resonant harmonic excitations were also evaluated in terms of time-histories of acceleration. The experimental data acquired by the CONCAVE group [100] were further analyzed to derive the same responses. The model validity under different excitation is examined by comparing the model results with the measured data.

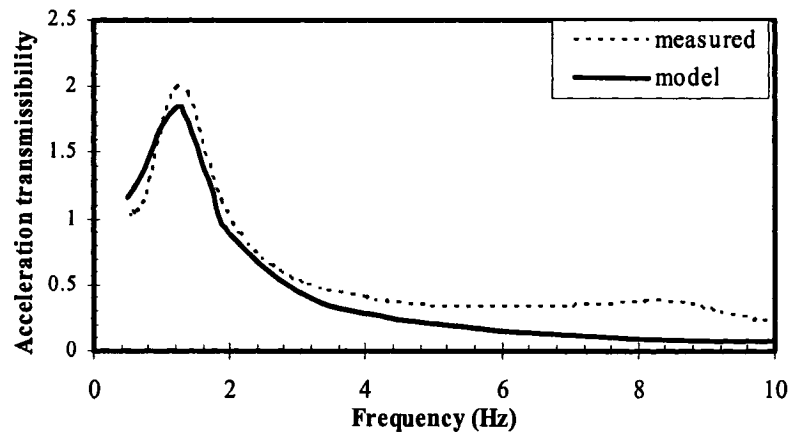
4.4.1 Deterministic Excitations

The acceleration transmissibility characteristics of the seat suspension model are compared with the measured response acquired under the swept harmonic excitation, as

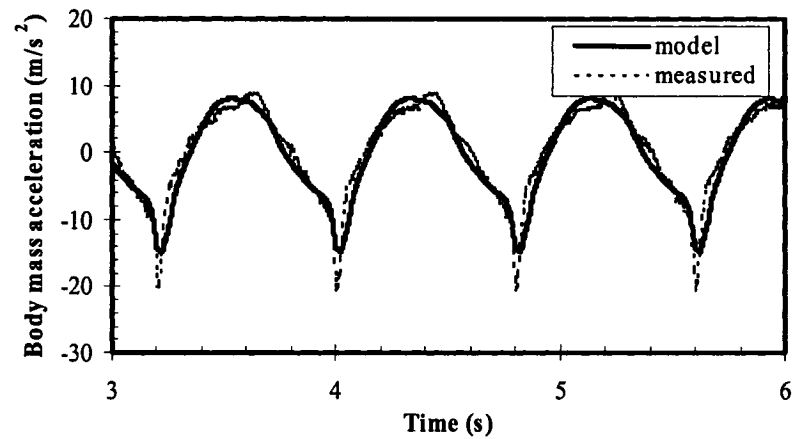
shown in Figure 4.9 (a). The figure suggests reasonably good agreements between the model results and the measured data over the entire frequency range, although considerable deviations are evident near resonant and at higher frequencies. The peak acceleration transmissibility magnitude of the suspension seat approaches nearly 2 around the natural frequency of 1.25 Hz. The model response tends to be higher than the measured response at low frequencies up to 1 Hz, which is most likely attributed to deficiencies in modeling the suspension friction. At higher frequencies the model tends to underestimate the magnitude of acceleration transmissibility, which is believed to be caused by the movement of the unrestrained rigid mass on the seat.

The resonant response of the model is further validated by comparing the body mass response under a harmonic excitation at 1.25 Hz with the measured data. Figure 4.9 (b) illustrates comparison of the time-history of acceleration response of the body mass in the model subject to a 55 mm harmonic displacement excitation at 1.25 Hz, with the corresponding measured data. The responses illustrate the resonant behavior of the suspension, contribution due to impacts against end-stop buffers, and loss of contact between the mass and the seat. The results show reasonably good agreement between the model and measured responses. The peak acceleration approaches 9.81 m/s^2 in the upward direction suggesting loss of contact between the mass and the cushion, and exceeds 20 m/s^2 in compression due to impact with relatively stiff end-stops. The results in Figure 4.9 demonstrate reasonably good validity of the model under low and high intensity continuous vibration.

Figure 4.10 further illustrates a comparison of the model response in terms of mass acceleration with the measured data under the transient excitation of peak displacement magnitude of 55 mm and predominant frequency of 1.5 Hz. The model results in terms of the body mass acceleration again show trends that are very similar to the measured data in the presence of end-stop impacts and momentary loss of mass-cushion contact.



(a)



(b)

Figure 4.9: Comparisons of measured and computed responses: (a) acceleration transmissibility of the suspension seat; and (b) time histories of mass acceleration under a harmonic displacement excitation ($A_r = 55$ mm and $f_r = 1.25$ Hz).

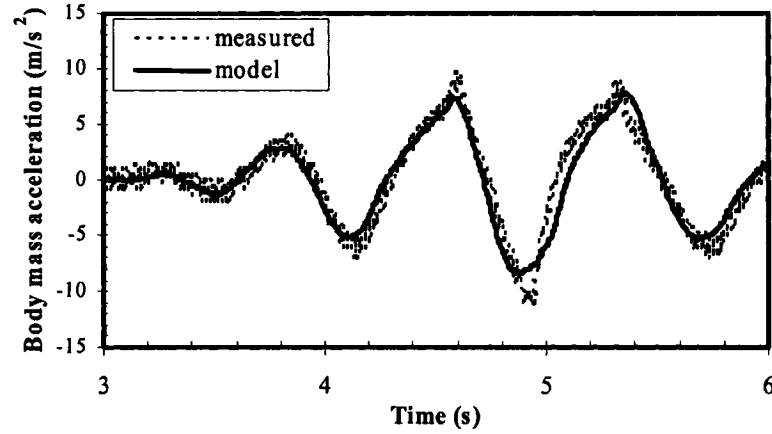
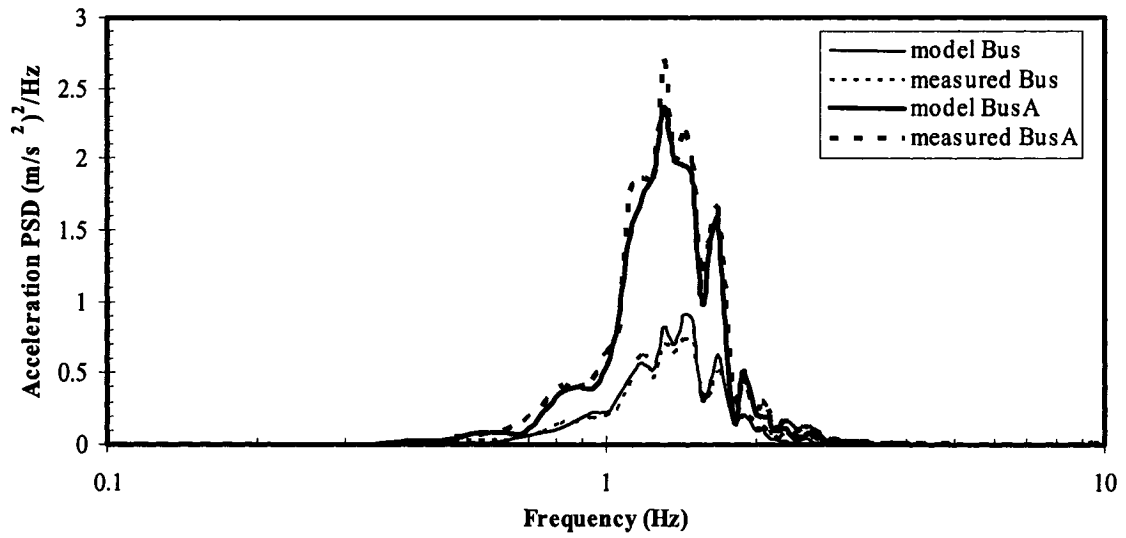


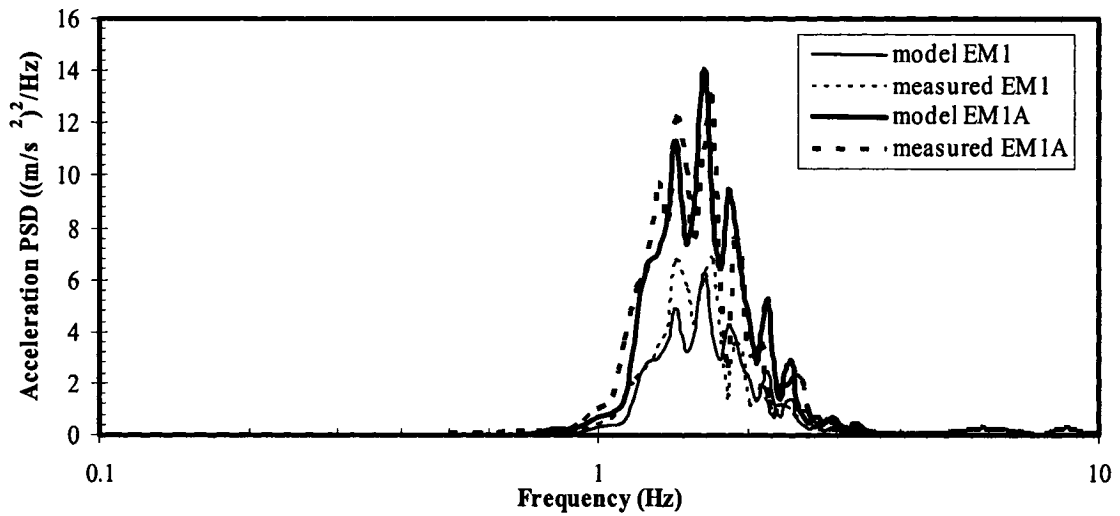
Figure 4.10: Comparison of the mass acceleration response of the model with the experimental data under transient excitation.

4.4.2 Random Vehicular Excitations

The model responses to excitations due to Bus, BusA, EM1 and EM1A are evaluated in terms of PSD of the mass acceleration and compared with those derived from the experimental data, as shown in Figure 4.11. The figures in general show reasonably good agreement between the PSD of the body mass acceleration response of the model with the measured responses under both vehicular excitations and the corresponding amplified excitations. The peak acceleration PSD responses of the mass under BusA and EM1A excitations are nearly 2.3 times the corresponding values under the nominal Bus and EM1 excitations, which is almost in proportion with the excitation amplification of 1.5. Moreover, the relatively high intensity of EM1A excitation revealed light impacts against the end-stops, which was not apparent under the BusA excitation.



(a)



(b)

Figure 4.11: Comparisons of measured and computed acceleration PSD responses of the seat-suspension subject to: (a) Bus and BusA; and (b) EM1 and EM1A excitations.

4.5 Performance Criteria

The shock and vibration attenuation performance of a suspension seat and the occupant exposure to vibration are mostly assessed on the basis of frequency-weighted

acceleration of the seated body mass or the occupant. For exposure to vertical vibration, ISO-2631 [94] recommends the use of W_k - weighting filter, and suggests for assessment of exposure to continuous vibration in terms of frequency-weighted *rms* acceleration, while that to intermittent or shock motion in terms of vibration dose value (*VDV*). The frequency-weighted *rms* values of excitation and response accelerations are computed from:

$$a_{wb} = \sqrt{\frac{1}{T} \int_0^T \ddot{x}_{bw}^2 dt}; \quad a_{wo} = \sqrt{\frac{1}{T} \int_0^T \ddot{x}_{ow}^2 dt}; \quad (4.13)$$

where a_{wb} and a_{wo} are frequency-weighted *rms* accelerations due to base excitation and response of the seated mass m_o , respectively, $\ddot{x}_{bw}(t)$ and $\ddot{x}_{ow}(t)$ are the corresponding frequency-weighted accelerations, and T is the integration period.

The *VDV* due to base (VDV_b) and mass (VDV_o) accelerations are computed in a similar manner from:

$$VDV_{wo} = \left[\int_0^T \ddot{x}_{ow}^4 dt \right]^{1/4}; \quad VDV_{wb} = \left[\int_0^T \ddot{x}_{bw}^4 dt \right]^{1/4} \quad (4.14)$$

The vibration and shock transmission performance characteristics of a suspension seat are evaluated in terms of seat effective amplitude transmissibility ($SEAT_w$) and the *VDV* ratio ($VDVR_w$), respectively defined as [94]:

$$SEAT_w = \frac{a_{wo}}{a_{wb}}; \quad VDVR_w = \frac{VDV_{wo}}{VDV_{wb}} \quad (4.15)$$

The performance measure in terms of *VDV* ratio is considered to be more appropriate for assessment of suspension seats under high magnitude excitations, as it tends to

emphasize the contributions due to short duration high acceleration events that may arise from impacts with the end-stops. The *SEAT* measure is used to assess the vibration attenuation capability of a suspension seat under continuous vibration.

The frequency-weighted and unweighted *rms* acceleration and vibration dose (*VDV*) values of selected vertical vehicular excitations as well as their amplified signals ('Bus', 'BusA', 'EM1', 'EM1A', 'Snow' and 'SnowA') are computed and summarized in Table 4.3. The values show that the 'Bus' signal is the lowest intensity excitation while the 'SnowA' is the highest. The *VDV* values of all selected vehicular excitations are considerably higher than the *rms* acceleration values of the corresponding excitations. The frequency-weighted *VDV* and *rms* acceleration values of all excitations decreased, while compared with those unweighted values.

Table 4.3: Frequency-weighted and unweighted *VDV* and *rms* acceleration values of excitations.

<i>Excitation</i>	<i>Bus</i>	<i>EM1</i>	<i>Snow</i>	<i>BusA</i>	<i>EM1A</i>	<i>SnowA</i>
<i>rms</i> acceleration	0.9960	1.9137	2.4475	1.4947	2.8706	3.6712
<i>VDV</i>	3.9159	7.2604	8.8948	5.8484	10.8906	13.3422
<i>rms</i> acceleration – weighted	0.6937	1.1264	2.0884	1.0656	1.6896	3.1325
<i>VDV</i> - weighted	2.6811	4.2499	7.6013	4.0407	6.3748	11.4019

4.6 Damping Requirements of Suspension Seats

The vibration attenuation performance of a suspension seat could be enhanced by reducing its natural frequency to a frequency well below the predominant frequency of

vehicle vibration, together with light damping. Considering that the vast majority of heavy road and wheeled off-road vehicles exhibit predominant vibration in the 1.25-2.5 Hz range, suspension seats with natural frequency well below 1.25 Hz would be desirable. Such a suspension, however, would cause excessive relative motion, and more frequent and severe impacts against the elastic end-stops. Alternatively, the enhancement of shock and vibration performance could be realized through selection of appropriate damping.

On the basis of symmetric damping in compression and rebound, it has been suggested that shock and vibration performance of a suspension seat impose conflicting requirements for the suspension damping [1]. This study concerns with a comprehensive parametric study on the influences of asymmetric suspension damping properties to identify desirable damping requirements for suspension seats under vehicular vibration with predominantly low and medium frequency excitations. The parameters include the low speed compression damping coefficient (C_{cl}), asymmetry factor (p), compression and extension reduction factors (γ_c and γ_e), and transition velocities (v_c and v_e) as described in Equation (4.5). The suspension responses to variations in the damping parameters are evaluated in terms of the performance measures presented in the previous section. The responses are examined to identify limitations of the fixed damping parameters and desirable damping properties. The variations in the damping parameter are limited to $\pm 25\%$, except for p , which is varied by $\pm 50\%$ of the nominal value. It should be noted that the nominal damping properties exhibit two-stage compression

damping and a single-stage rebound damping ($\gamma_e=1$), as evident from the data reported in Table 4.1, while the asymmetry factor of 0.79 suggests lower damping force in rebound than in compression. Owing to only minimal effects of variations in the transition velocities, v_c and v_e , in the ranges considered, the results are limited to illustrate the effects of C_{cl} , p , γ_c and γ_e .

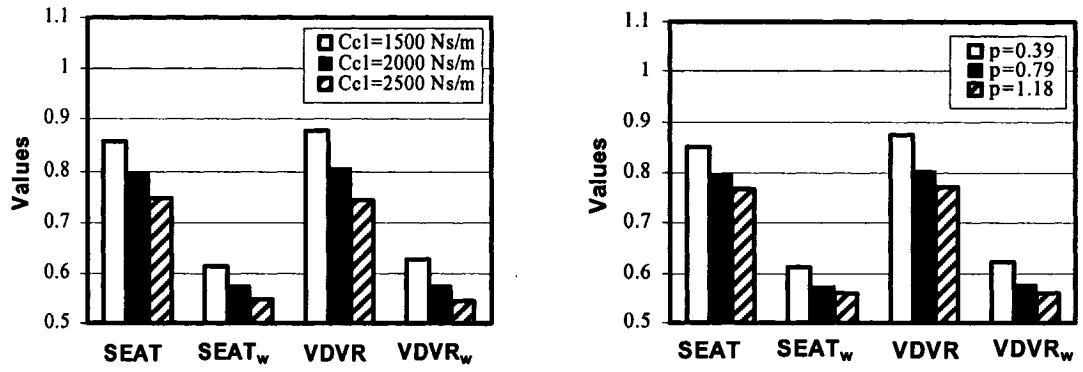
4.6.1 Low Frequency Vehicular Vibration

The effects of variations in the damping parameters are investigated under continuous and high magnitude random vibrations that predominate at low frequencies (Bus, EM1 and the corresponding amplified vibration, predominant near 1.5 and 2.1 Hz, respectively). Figure 4.12 illustrates the effects of variations in C_{cl} and p on the suspension performance in terms of W_k -weighted and unweighted *SEAT* and *VDVR* values under Bus and BusA excitations, while Figure 4.13 illustrates those on the peak acceleration response of the body mass (m_o). It should be noted that a variation in C_{cl} would also yield proportional variations in C_{c2} , C_{e1} and C_{e2} , which is evident from the definitions of the reduction and asymmetry factors described in section 4.2.2.

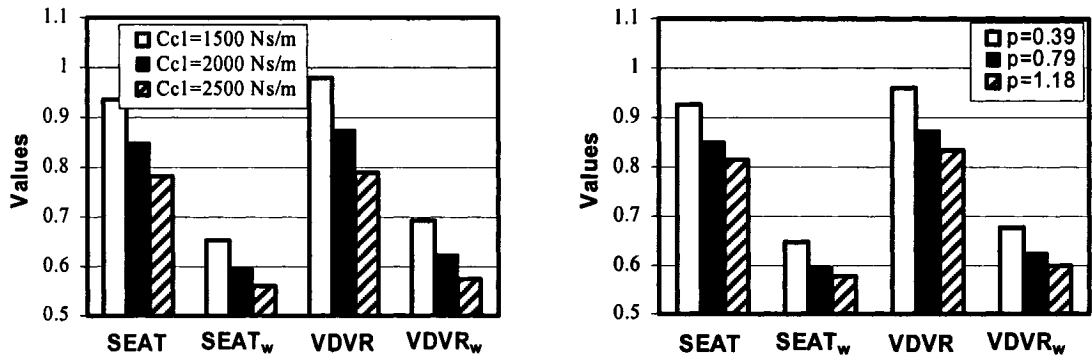
The results clearly show the most significant effects of variations in C_{cl} on the performance measures under both the nominal and amplified excitations. A decrease in C_{cl} yields comparable increases in both the *SEAT* and *VDVR* measures, whether unweighted or weighted. Both the measures tend to be slightly higher under BusA excitation, when compared to those under the nominal Bus excitation. The *VDVR* and

SEAT values are somewhat comparable, which suggests absence of end-stop impacts under BusA excitation. The end-stop impacts, however, occur when the magnitude of excitation is amplified by 200% (refers to as “BusA2”), as observed in Figure 4.12 (c). The results show relatively higher values of *VDVR* due to repetitive impacts against the end-stops, while the *SEAT* values remain comparable with those in Figure 4.12 (a) and (b). Figure 4.13 (a) further shows the influence of variations in C_{c1} on the peak acceleration responses of the body mass (m_o). The results clearly show significantly higher peak acceleration under ‘BusA2’ excitation, particularly under lower value of C_{c1} . The differences in the values of peak accelerations under ‘BusA2’ excitation, are more apparent when compared with those under Bus or BusA.

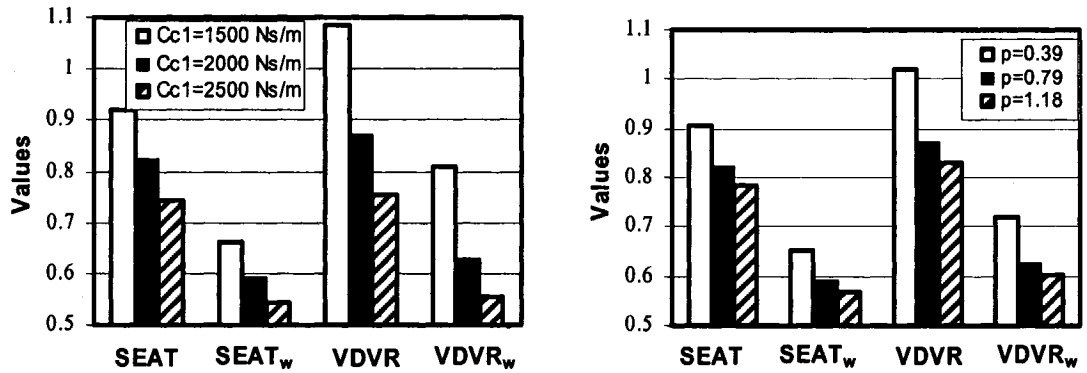
Variations in the rebound damping, represented by the asymmetry factor p , also yield similar effects on the performance measures, while the relative changes in the *SEAT* and *VDVR* measures are less than those observed for variations in C_{c1} . An increase in p from the nominal value of 0.79 to 1.18 could yield improved attenuation of continuous and high intensity vibration, as evident in Figure 4.12. Figure 4.13 (b) shows that the influence of variation in the asymmetric factor p on the peak acceleration response of the body mass is relatively less than that of the variation in the damping coefficient C_{c1} .



(a)



(b)



(c)

Figure 4.12: Influences of variation in damping parameters (C_{c1} and p) on the SEAT and VDVR responses under: (a) Bus; (b) BusA; and (c) BusA2.

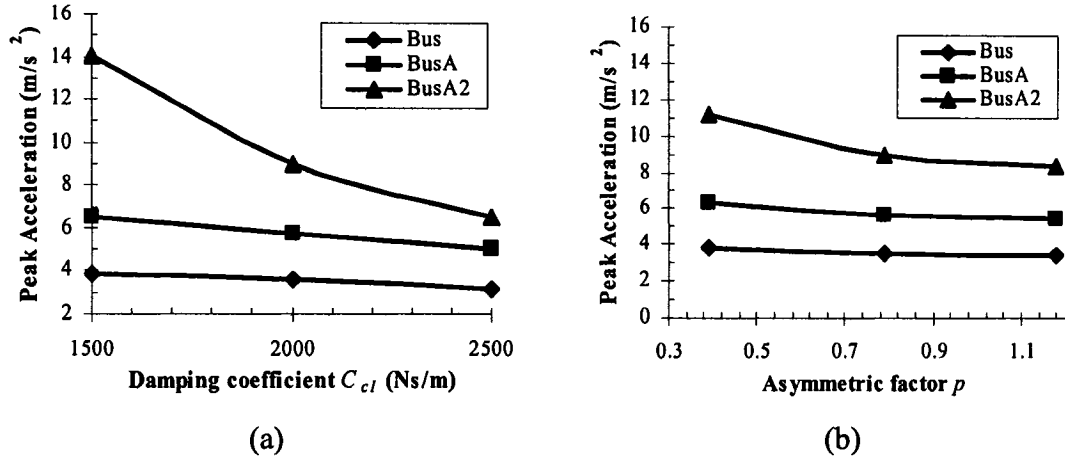


Figure 4.13: Comparison of the peak acceleration under Bus, BusA and BusA2 excitations, influenced by variations in damping parameters of: (a) C_{cl} ; and (b) p .

The variations in the high-speed compression and rebound damping reduction factors (γ_c and γ_e) revealed only slightly lower values of both the measures under Bus and BusA excitations, as shown in Figure 4.14. These slight effects are attributed to the relatively lower intensity vibration of both Bus and BusA excitations. These lower intensity excitations yield lower motion velocity of the piston of hydraulic damper. The high-speed compression and rebound damping reduction factors thus contribute little to the damping force of the suspension seat.

The above results suggest that higher suspension damping in compression and rebound is desirable to increase the vibration isolation efficiency, particularly for mitigating the effects of end-stop impacts, of the suspension under Bus excitation, irrespective of its amplification. This is mostly attributed to the predominance of Bus vibration near the suspension resonance.

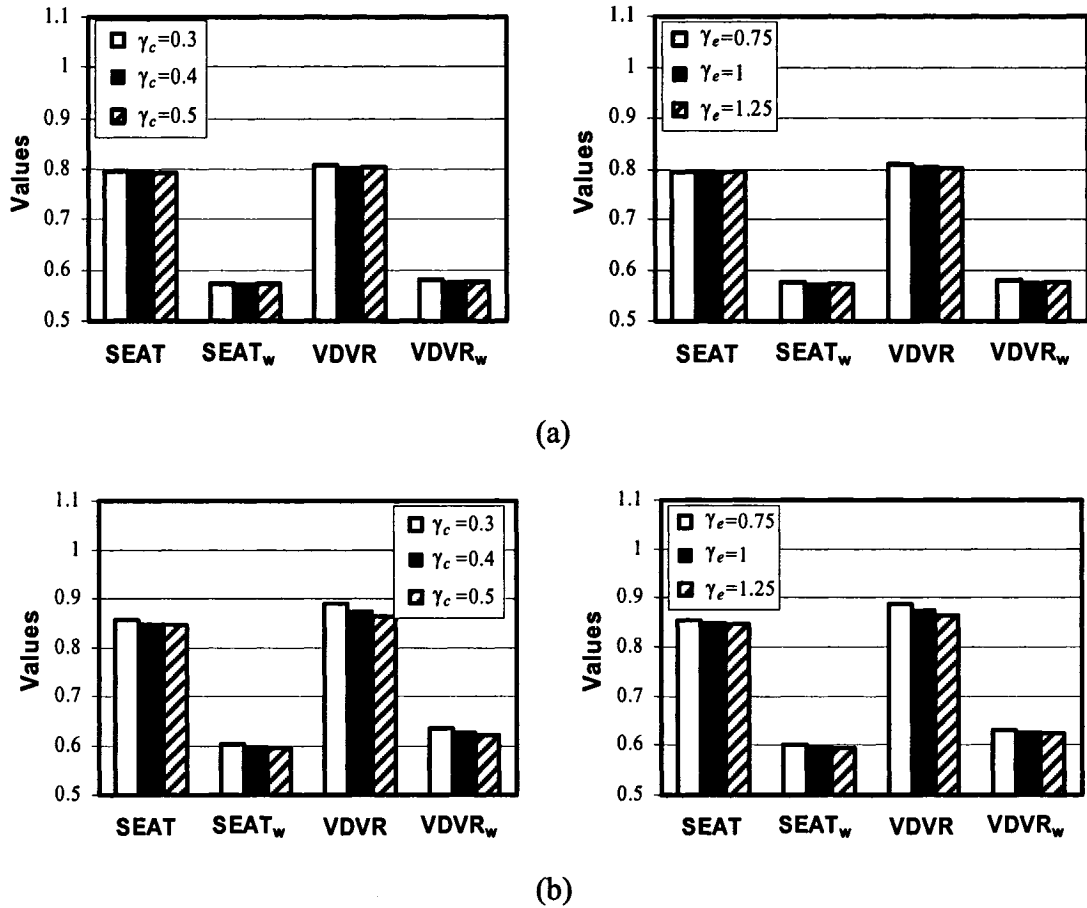


Figure 4.14: Influences of variation in damping parameters (γ_c and γ_e) on the *SEAT* and *VDVR* responses under: (a) Bus; and (b) BusA.

The influences of variations in the damping parameters on the defined performance measures and the body peak acceleration of the suspension seat subject to EM1 and EM1A excitations are shown in Figures 4.15 and 4.16. A 25% decrease in C_{cl} could yield 25% increase in VDVR and only 6% increase in SEAT measures under EM1 excitation. The VDVR value of the suspension under nominal EM1 excitation is in the order of 1.03. This however increases to 1.7 when the suspension is subject to EM1A

excitation. The corresponding increase in the SEAT value is very small. These results suggest the occurrence of end-stop impacts under EM1A excitation. A reduction in C_{c1} by 25% yields excessively higher peak acceleration, irrespective of the excitations, as evident in Figure 4.15. These results suggest higher frequency and severity of end-stop impacts under this excitation, while a lower damping would yield more severe impacts. A higher value of C_{c1} helps to reduce the severity of end-stop impacts, while the performance under continuous nominal vibration deteriorates slightly as observed from higher SEAT responses under higher damping. Both the W_k -weighted measures, however, show consistent effects of suspension damping under higher EM1A excitation.

A reduction in the rebound damping coefficient, the asymmetric factor p , also yields higher values of both the measures. An increase in the asymmetry factor, however, deteriorates the seat isolation effectiveness and does not offer any benefits in terms of end-stop impact performance. This is most likely attributed to higher frequency of end-stop impacts during the compression stroke. This could also be observed from the variations in the peak acceleration illustrated in Figure 4.16 (b), where magnitudes of peak acceleration vary only slightly with varying asymmetric factor p . The Figure 4.17 also illustrate the effects of variations in the high-speed compression and rebound damping reduction factors, γ_c and γ_e , on the performance measures under EM1 and EM1A excitations. The results suggest that an increase in the low-speed compression damping coefficient would be desirable ($\gamma_c > 1$) for realizing improved shock as well as vibration isolation performance.

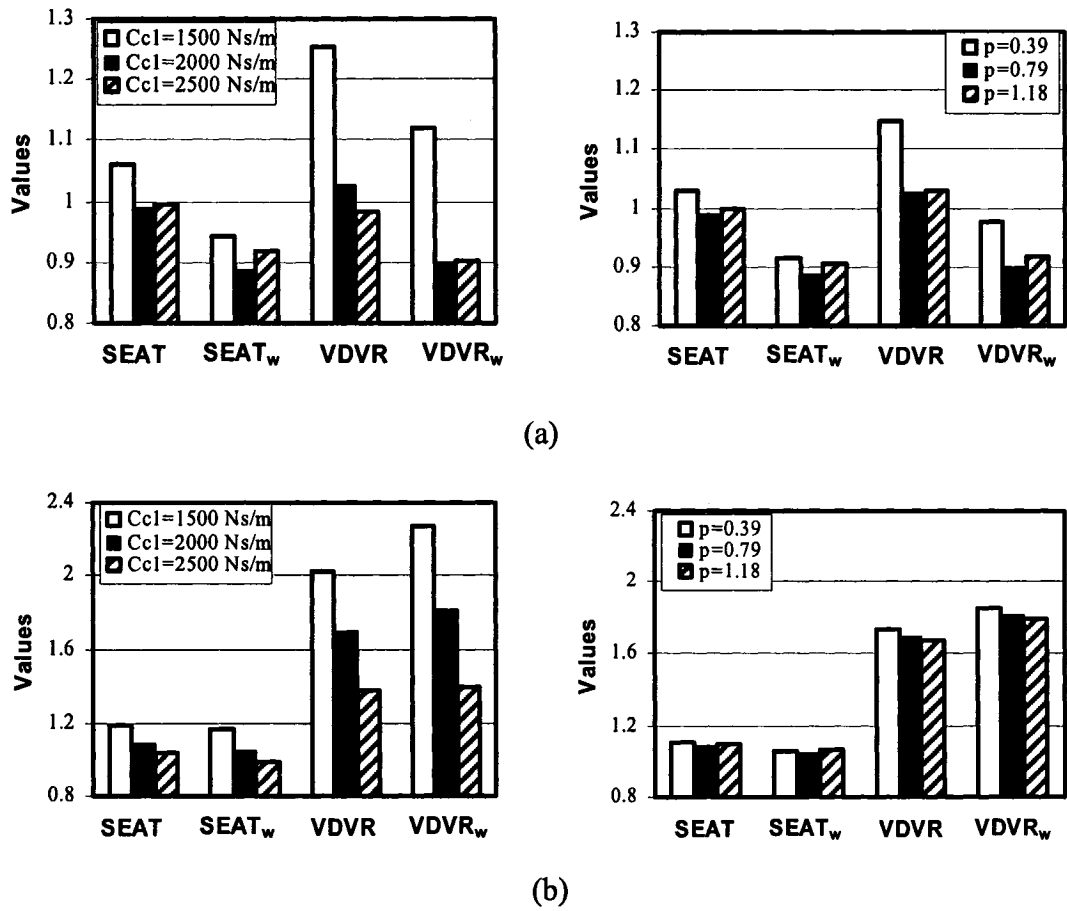


Figure 4.15: Influence of variation in damping parameters (C_{cl} and p) on the SEAT and VDV ratio responses of suspension seat under: (a) EM1; and (b) EM1A.

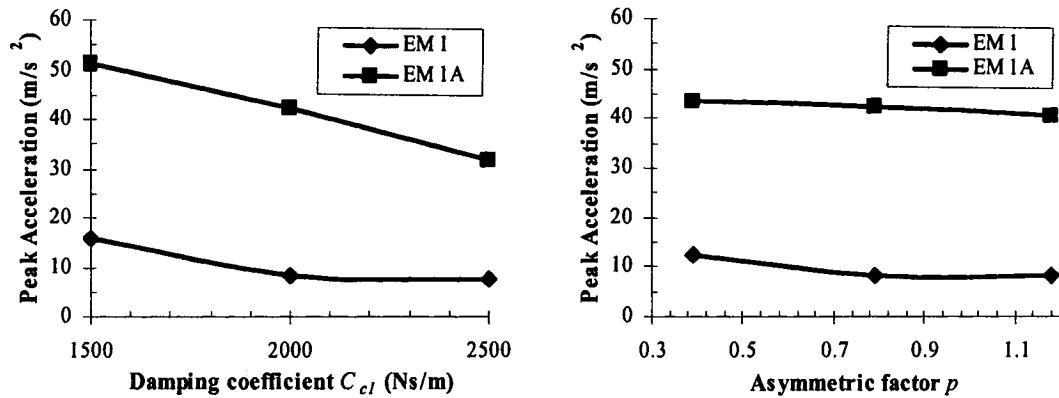


Figure 4.16: Comparison of the peak acceleration under EM1 and EM1A excitations, influenced by variations in damping parameters of: (a) C_{cl} ; and (b) p .

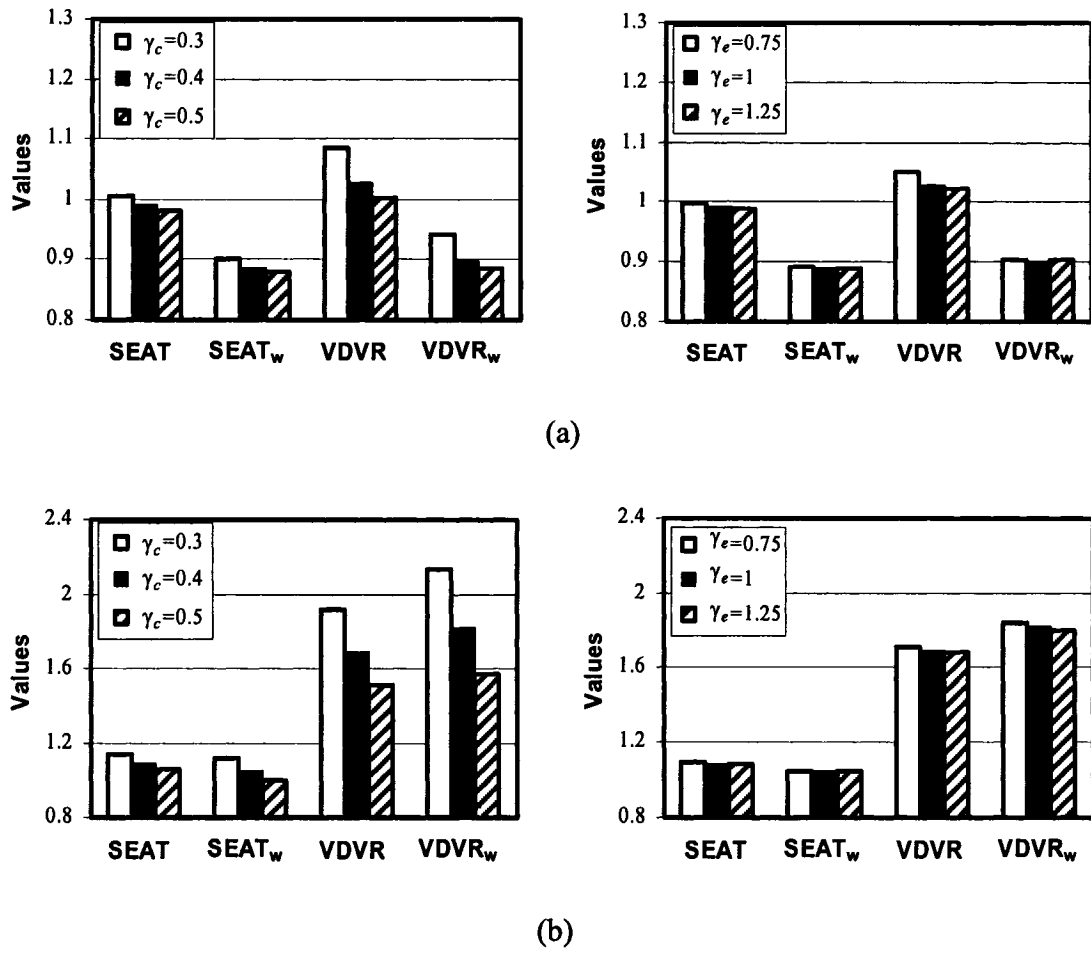


Figure 4.17: Influence of variation in damping parameters (γ_c and γ_e) on the SEAT and VDVR ratio responses of suspension seat under: (a) EM1; (b) EM1A.

4.6.2 High Frequency Vehicular Vibration

The role of damping parameters on the suspension performance under excitations at relatively higher frequencies are investigated for the ‘Snow’ as well as ‘SnowA’ excitations, which predominate around 4.5 Hz. The candidate low frequency suspension would thus be expected to yield superior vibration isolation. Figure 4.18 illustrates the influences of variations in C_{el} and p on the two performance measures under these excitations. The results clearly show significantly lower *SEAT* and *VDVR* values (<0.71)

under Snow and SnowA excitations, when compared to those observed under Bus and EM1 excitations. Both the W_k -weighted measures tend to be even lower due to effective attenuation of dominant ride vibration near 4.5 Hz. The results suggest that the variations in the damping parameters (C_{cl} and p) in the range considered would alter the SEAT and VDVR measures only slightly, while a lower damping would yield only slightly lower weighted measures under the nominal excitation. The responses under amplified excitations also exhibit only slight influences of variations in the damping parameters.

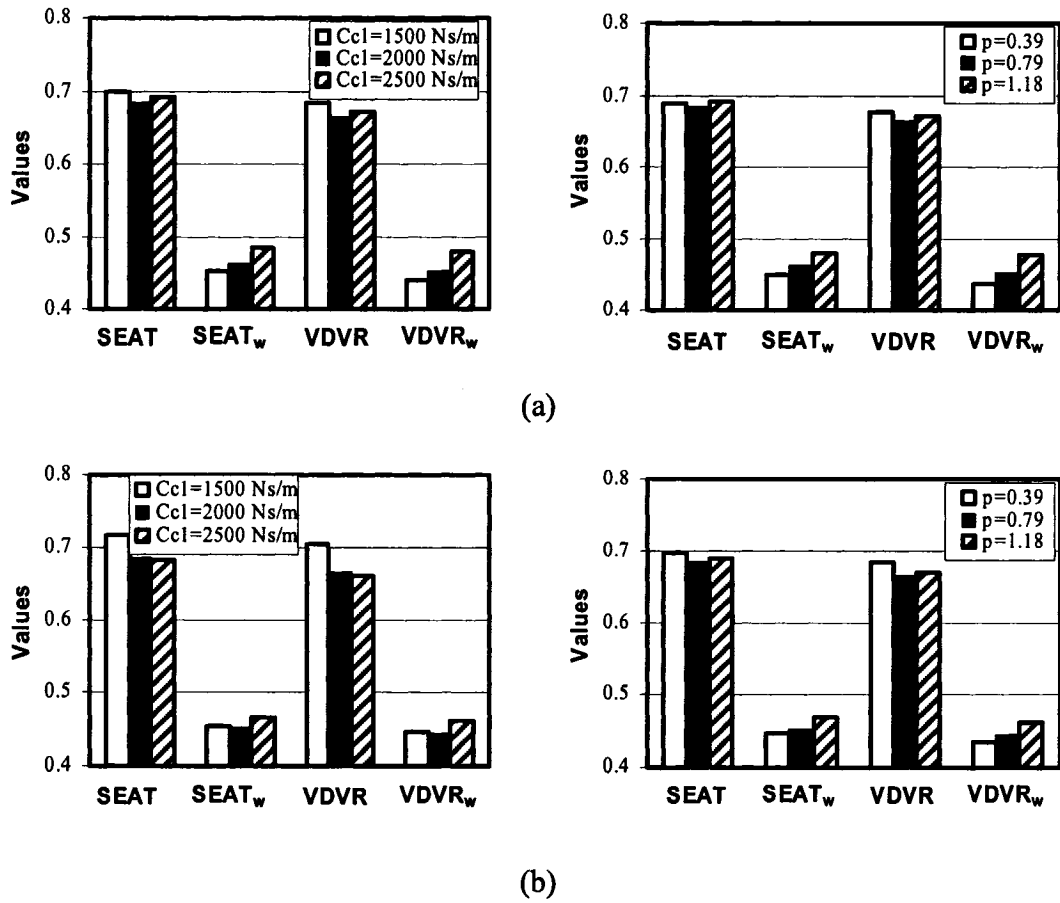


Figure 4.18: Influence of variation in damping parameters (C_{cl} and p) on the *SEAT* and *VDV* ratio responses of suspension seat subject to excitation signals: (a) Snow; and (b) SnowA.

From the results, it is concluded that a suspension design with higher compression as well as rebound damping could yield enhanced performance under low frequency excitations, while it would not deteriorate the performance very much under higher frequency excitations.

4.6.3 Acceleration Transmissibility

The influences of variations in C_{cl} and p are further illustrated in terms of acceleration transmissibility response of the suspension seat under swept harmonic excitations in the 0.5-10 Hz range. The results presented in Figure 4.19 clearly show that higher damping and asymmetry factor help to limit the resonant acceleration response considerably, while the response in the 2 to 6 Hz range tends to be only slightly higher. A higher suspension damping is thus vital for enhancing the shock as well as vibration attenuation performance of the suspension seat for target vehicles with predominant vibration near the seat suspension resonance, as it was observed under Bus and EM1 excitations. The higher damping yields only slight degradation of the acceleration transmission performance at higher frequencies. High damping design would thus be equally acceptable for vehicles with relatively higher frequency vibration, as observed for the Snow excitations.

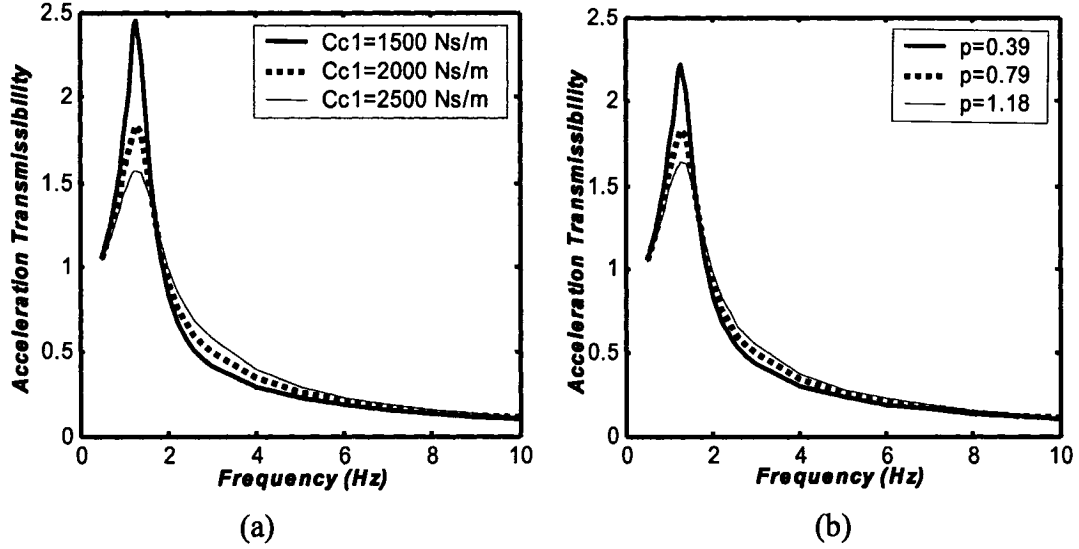


Figure 4.19: Influence of variation in damping parameters (C_{c1} and p) on the acceleration transmissibility response of the suspension seat.

4.6.4 Transient Excitation

The role of damping on the suspension performance under high intensity intermittent excitations is further evaluated under transient excitations in the vicinity of 1.5 Hz and peak displacement (A_p) of 55 mm. Figures 4.20 and 4.21 illustrate the influences of variations in C_{c1} and p , respectively on the suspension performance, presented in terms of time-histories of mass acceleration \ddot{x}_0 , vertical damping force F_{dv} , suspension deflection x_{sb} and end-stop force F_b . The results show that a reduction in C_{c1} causes suspension deflection to exceed its permissible travel resulting in more severe impacts against the end-stops. This is evident from the variations in the end-stop force. The seated mass acceleration thus increases considerably, as seen in Figure 4.20. The frequency and severity of end-stop impacts and thus the mass acceleration can be reduced by

increasing C_{cl} .

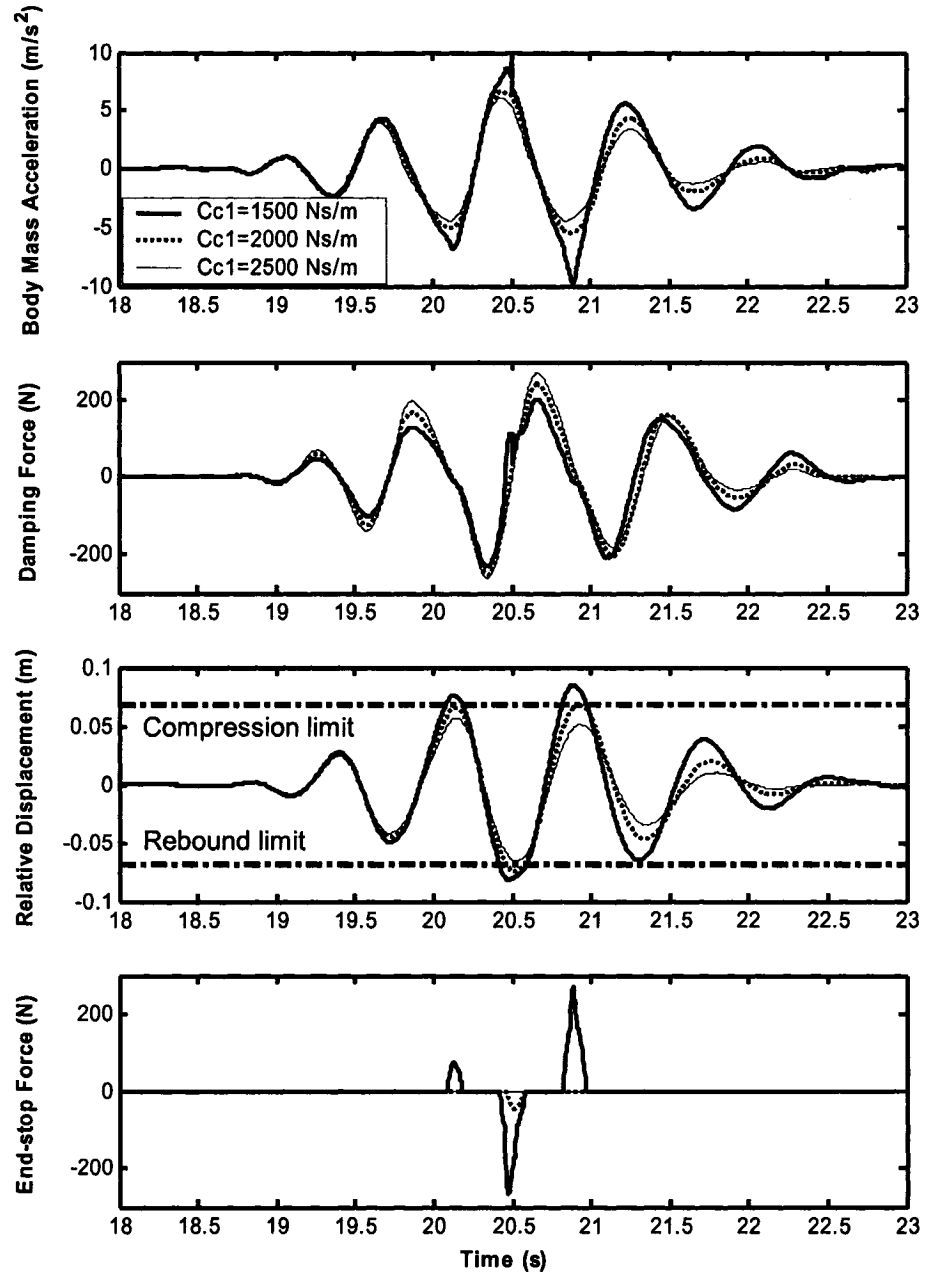


Figure 4.20: Influence of variations in damping coefficient C_{cl} on the suspension seat responses under transient excitation ($A_p = 55$ mm).

The influences of variations in the asymmetry factor p on the responses to transient excitations are also quite similar to those observed for C_{cl} , as seen in Figure 4.21. A

lower value of p yields considerably lower rebound damping force and thus far more severe end-stop impact in the rebound stroke. A higher asymmetry factor, on the other hand, tends to eliminate the impacts under the selected excitation.

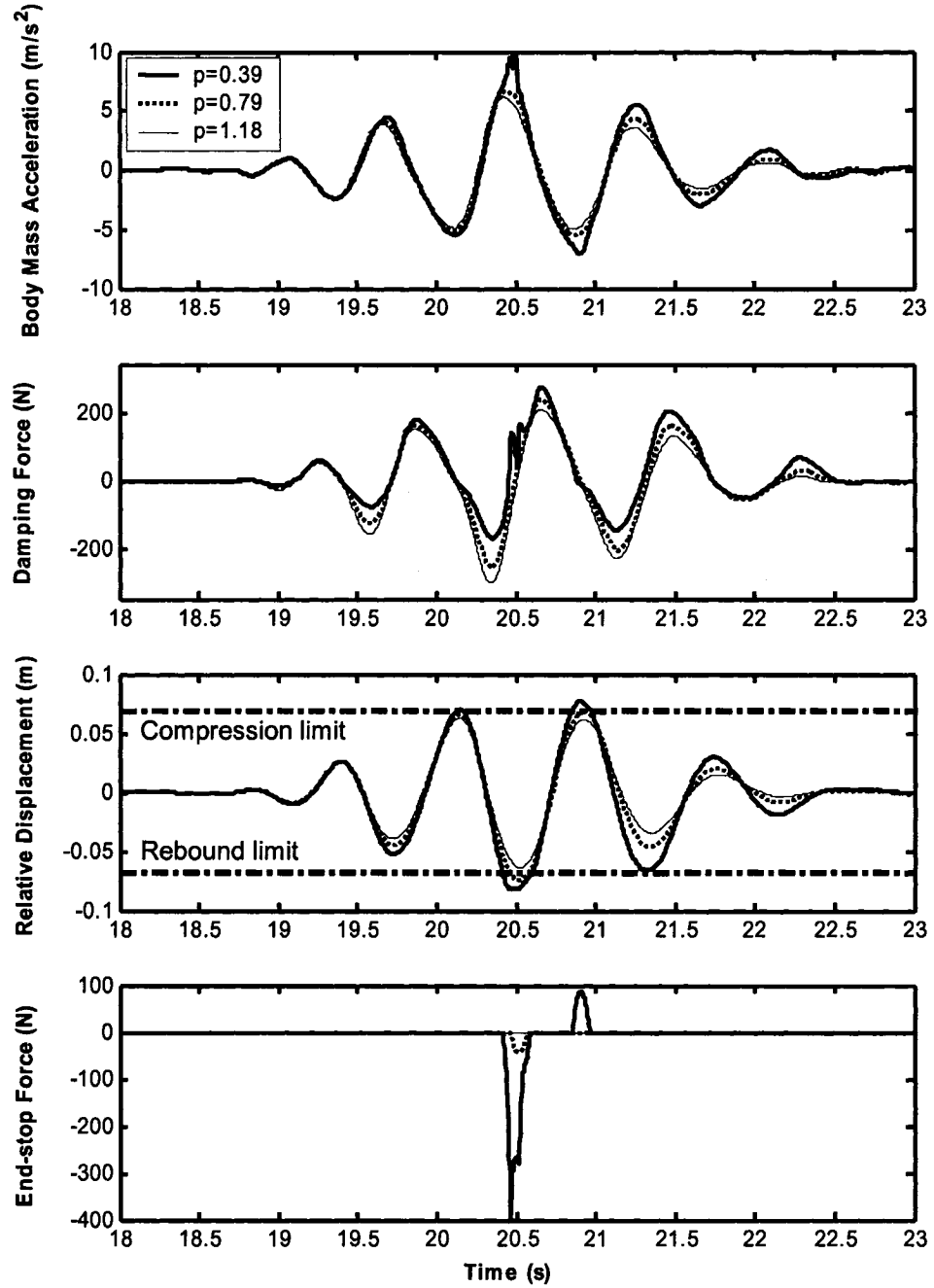


Figure 4.21: Influence of selected asymmetric factor p of damping coefficient on the weighted and unweighted of the *SEAT* and *VDV* ratio of the suspension seat subject to transient excitation.

4.7 Discussions

Occupational drivers of heavy road as well as off-road vehicles are exposed to comprehensive levels of continuous vibration and intermittent shock motions. A suspension seat is mostly designed to achieve attenuation of continuous vibration of a class of vehicles in accordance with the methods outlined in ISO-7096. The suspension performance under high intensity intermittent excitations is either ignored or is believed to impose conflicting design requirements. Considering that the exposure to high intensity shock motions could pose far greater health risks among the drivers than the continuous vibration of lower magnitude, the attenuation of high intensity vibration and shock should also form the essential design goal. The suspension seats are mostly designed with low natural frequency and limited travel, which permit their implementations in a wide range of road as well as off-road vehicles. Exposure to high intensity vibration and shocks thus yields high magnitude suspension deflection and repetitive impacts against the elastic end-stops. It is vital to limit the suspension travel to a reasonable level to provide a stable sitting platform for the drivers to perform the needed tasks in a safe and efficient manner. A further reduction in the natural frequency would thus not be feasible. Alternatively, the shock and vibration isolation performance could be enhanced through selection of appropriate low-and high-speed compression as well as rebound mode suspension damping.

The vibration and shock attenuation performances of a suspension seat could be effectively evaluated in terms of unweighted and frequency-weighted seat effective

amplitude transmissibility (*SEAT*) and vibration dose value ratio (*VDVR*), respectively. The results of this study suggest that higher suspension damping is desirable for improved attenuation of high intensity vibration and intermittent shock motions, particularly for vehicles with predominantly low frequency vibration. This would be generally applicable for road vehicles operating on relatively rough urban roads and a wide range of wheeled off-road vehicles employed in construction, forestry and service sectors. Such a suspension design could considerably reduce the severity and frequency of end-stop impacts and thereby limit the high intensity vibration and shock exposure of the operators. Moreover, such a design approach would offer improved vibration isolation effectiveness of the suspension seats. For applications in vehicles with relatively higher frequency vibration, such as industrial vehicles and off-road tracked vehicles, this design approach would also be acceptable as it would limit the frequency and severity of end-stop impacts, while the performance under lower levels of continuous vibration would deteriorate only slightly.

Therefore, a higher suspension damping is desirable for improved attenuation of high intensity vibration and intermittent shock motions, particularly for vehicles with predominantly low frequency vibration. A light damping, however, is desirable for realizing enhanced isolation of continuous vibration of low to medium intensity. The attenuation of shock as well as vibration imposes difficulties design compromise of the passive damper. On the other hand, the magneto-rheological fluid (MR) damper could provide the variable damping force modulated by varying the command current. Owing

to the strongly nonlinear properties of the suspension-seat and the MR-damper, synthesizing an effective control algorithm will become a challenging task and derived in the following chapter.

CHAPTER 5

SYNTHESIS AND ANALYSES OF THE SEMI-ACTIVE SUSPENSION SEAT CONTROLLERS

5.1 Introduction

A vast number of semi-active and active suspension systems have been explored for vehicular applications to generate variable forces in response to varying excitations and to achieve better compromise among the various conflicting performance requirements. Some of these concepts have also been applied for suspension seats to achieve improved shock and vibration isolation performance [18, 36, 52, 54]. A few studies on variable damping concepts using conventional hydraulic dampers have established that such dampers can effectively track the desired force that could be generated by a fully active force generator when the force is of a dissipative nature [53, 54]. Considering the potential advantages of magneto-rheological (MR) damper, such as variable damping coefficient, low power rapid response, low cost and simple hardware, a few recent studies have explored different control methods to improve the performance of suspension seat equipped with a MR-damper [49, 55, 56]. As evident in the results presented in Chapter 2, the MR dampers offer high viscous damping corresponding to low velocities in the pre-yield condition, while the post-yield saturation at the higher velocities can be characterized lower damping coefficient, such properties are considered to be well suited for suspension seat applications as demonstrated by the results presented in the previous chapter. The development of an effective controller for realizing desirable variations in

the damping force, however, remains a challenging task and requires not only an accurate characterization of the hysteretic f - v properties in the pre-yield and force saturation in the post-yield, but also effective control algorithms.

The well-known skyhook control algorithm that has been widely employed in wheel suspensions could also be applied for semi-active suspension seats [49, 56]. This control algorithm effectively utilizes the damping variations in the pre- and post-yield as a function of the applied current. While a few studies have attempted the implementation of this control methodology for enhancement of shock and vibration attenuation performance, the contributions due to hysteresis are invariably ignored. It has been reported that the presence of hysteresis could deteriorate the force tracking performance of the controller [80, 81, 90]. Moreover, the repeated semi-active control methods mostly employ on-off modulation of the damping force or the current, which tend to cause considerably transient motions associated with discontinuous mode of operation. A recent study on assessment of a suspension seat with controlled MR-damping, has demonstrated the suspension effectiveness in limiting the shock motions by eliminating end-stop impacts [55]. The measured results did not show improvement in vibration attenuation performance over the fixed damping suspension. Another study has shown improved vibration isolation, while the end-stop impact performance was not considered [49]. The reported studies, however, did not consider the contributions due to hysteresis and the switching discontinuities.

In this chapter, the generalized sigmoid model for the MR-damper, formulated in

Chapters 2 and 3, is employed to the suspension seat model described in Chapter 4, in order to synthesize and evaluate the skyhook and the integrated control algorithms. A set of performance measures is also defined to carry out relative evaluations of the controllers under harmonic, transient and random excitations due to a class I construction machinery (EM1) and a city bus (Bus).

5.2 Development of the Suspension Seat with MR Damper

Figure 5.1 illustrates the two-DOF model of the load-seat-suspension system, assuming a rigid mass human body model, as described in Chapter 4. The passive hydraulic damper in the model is replaced by the model of the MR-fluid damper, described in Chapter 2 and 3. The differential equations of motion for the model can be rewritten as:

$$\begin{cases} m_o \ddot{x}_o = -F_c + m_o g \\ m_s \ddot{x}_s = -F_s - F_f - f_d - F_b + F_c + m_s g \end{cases} \quad (5.1)$$

where F_b , F_s and F_f are suspension force components due to end-stop buffer, suspension spring, Coulomb friction, and are defined in Equations (4.10), (4.8) and (4.9), respectively. The force F_c , due to seat cushion, is defined in Equations (4.2) and (4.3), while the damping force f_d due to the MR-damper is defined in Equations (2.16) and (2.17), as a function of applied current, and excitation and response.

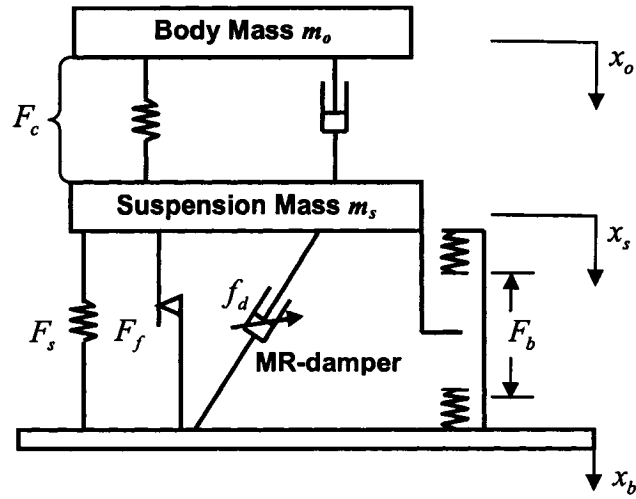


Figure 5.1: Combined rigid human-suspension seat model equipped with MR-damper.

5.3 Responses of MR Suspension Seat under Constant Currents

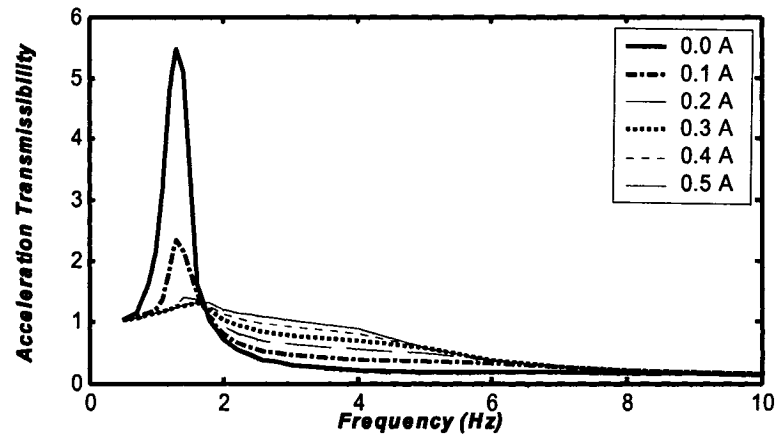
The above equations are initially solved for an open-loop MR-damper subject to different levels of constant current. The results attained under selected excitation are reviewed to qualify the applicability of the damper model, and contributions due to damper nonlinearities. These are expected to aid in formulation of control algorithms. The responses are compared with those of the suspension seat model with the hydraulic passive damper. The hysteresis effects will further be analyzed in this open-loop uncontrolled system of a suspension seat. The responses under harmonic excitations are evaluated in terms of *rms* acceleration transmissibility of the body mass, while those under random excitations are expressed in terms of PSD of acceleration. The responses under transient excitations are assessed in terms of time-histories of acceleration, damping force and end-stop force, under different magnitudes of excitations.

5.3.1 Harmonic Excitations

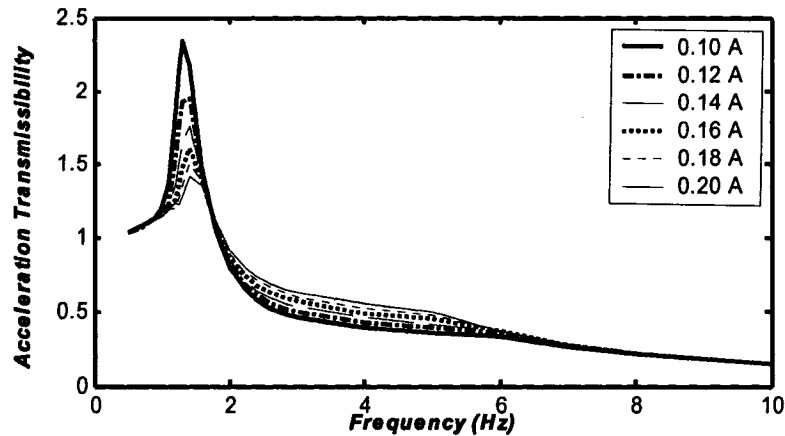
Figure 5.2 illustrates the acceleration transmissibility characteristics of the MR suspension seat model subject to swept harmonic excitations in the 0.5 to 10 Hz frequency range, as described in the previous chapter. The results are obtained under different levels of constant currents in the 0 to 0.5 A range with increments of 0.1 A, as shown in Figure 5.2 (a). Figure 5.2 (b) further shows the influence of applied current in a smaller range of 0.1 to 0.2 A with increments of only 0.02 A. The results show that the peak acceleration transmissibility occurs near the frequency of 1.20 Hz and approaches a magnitude of 5.5 under light damping produced by zero current. The magnitude peak tends to shift towards right to slightly higher frequencies with the increasing of applied current, while the resonant acceleration transmissibility magnitude decreases significantly. The transmissibility magnitude, however, increases in the higher isolation frequency range, as it would be expected for fixed damping properties. The results, however, show a trend that differs from those observed in systems with passive/fixed damping. The frequency corresponding to the peak magnitude increases slightly with increasing current and thus the damping, which is opposite to behavior expected for a passive/fixed damped system. This difference is most likely attributed to nonlinear and hysteretic force-velocity characteristics of the MR-damper.

Figure 5.2 (b) further illustrates the acceleration transmissibility responses in the 0.1 to 0.2 A current range. The peak transmissibility magnitude approaches near 2 under 0.12 A, which is comparable with that attained from the model with the passive hydraulic

damper. The results show that only a slight change in the applied current could significantly reduce the peak resonant transmissibility.



(a)



(b)

Figure 5.2: Influence of applied current on the occupant mass acceleration transmissibility response of the MR-damped suspension seat model.

Figure 5.3 further presents the comparisons of the acceleration transmissibility responses of the suspension seat with the hydraulic and the MR-damper under 0.12 A applied constant current with the measured data acquired for the suspension seat with hydraulic damper. The response characteristics of the MR suspension seat model

generally agree with the measured response of the hydraulic suspension seat. The MR-damped seat model yields somewhat lower magnitudes at lower frequencies, which is attributed to relatively higher damping coefficient of the MR-damper at low velocities.

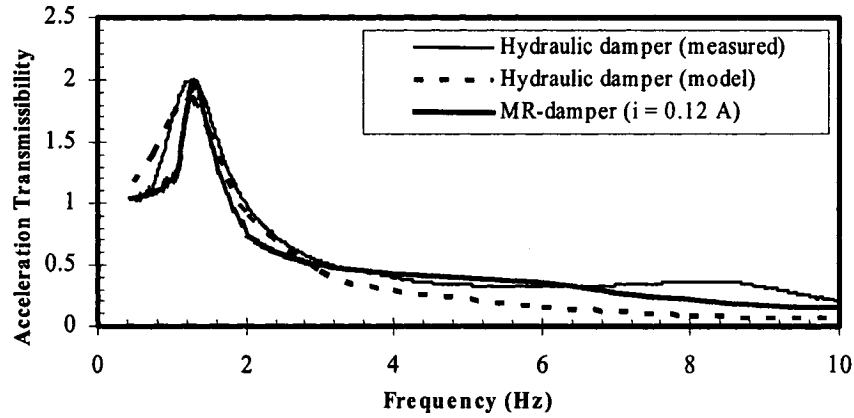


Figure 5.3: Comparison of acceleration transmissibility responses of the model with hydraulic and MR-damper with the measured data of the hydraulic suspension seat.

5.3.2 Transient Excitations

The influence of excitation magnitude on the response is also evaluated by varying the magnitude of peak displacement by $\pm 20\%$ about the nominal value of 55 mm, as shown in Figure 5.4. Figure 5.5 illustrates a comparison of the responses of the model, in terms of body acceleration \ddot{x}_c as a function of the applied current together with variations in the damping force f_d and the end-stop force f_b , under the transient excitation (peak displacement $A_p = 55$ mm and predominant frequency = 1.5 Hz), as described earlier in Figure 4.7. The results show that an increase in the applied constant current could limit peak acceleration magnitude and thus decrease the frequency and severity of end-stop impacts. The presence of end-stop impacts under applied current equal to or below 0.12 A

are evident from the high acceleration peaks and the bump stop forces. The application of a low current also yields loss of contact between the occupant mass and the seat, as observed from peak acceleration of 9.81 m/s^2 in the upward direction. The results further reveal that the MR damper seat with applied current of 0.12 A yields the responses similar to those of the seat with the hydraulic damper presented in the previous chapter.

Figure 5.6 illustrates comparisons of the responses of the suspension seat model with a MR-damper and applied current of 0.12 A under the three transient excitations (peak displacement magnitudes of 44, 55 and 66 mm). The presence of a relatively less severe end-stop impact is evident under the 55 mm transient excitation, while the severity increases considerably under 66 mm excitation. The results also show that the interactions with the top buffer occur first, which is followed by a more severe impact with the compression end-stop near $t = 20.5 \text{ s}$. The most severe impact, however, occurs near $t = 21 \text{ s}$ due to impact with the top buffer.

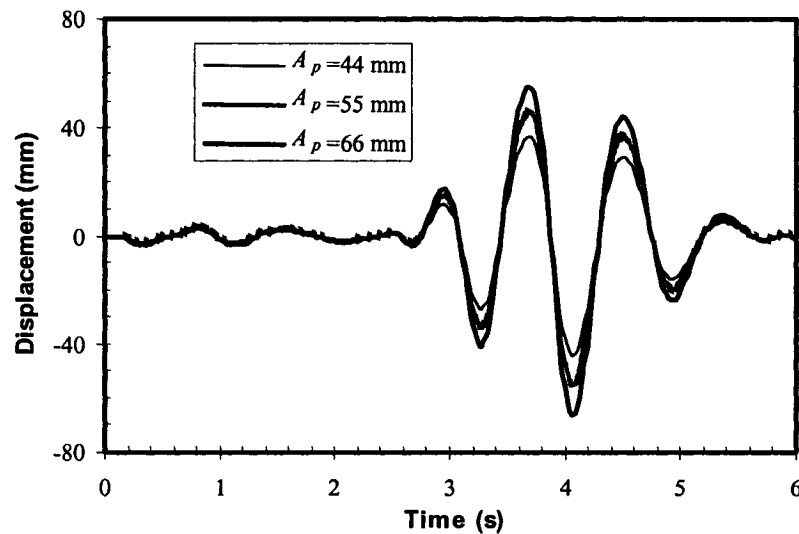


Figure 5.4: Time history of transient excitations of different peak magnitudes (1.5 Hz).

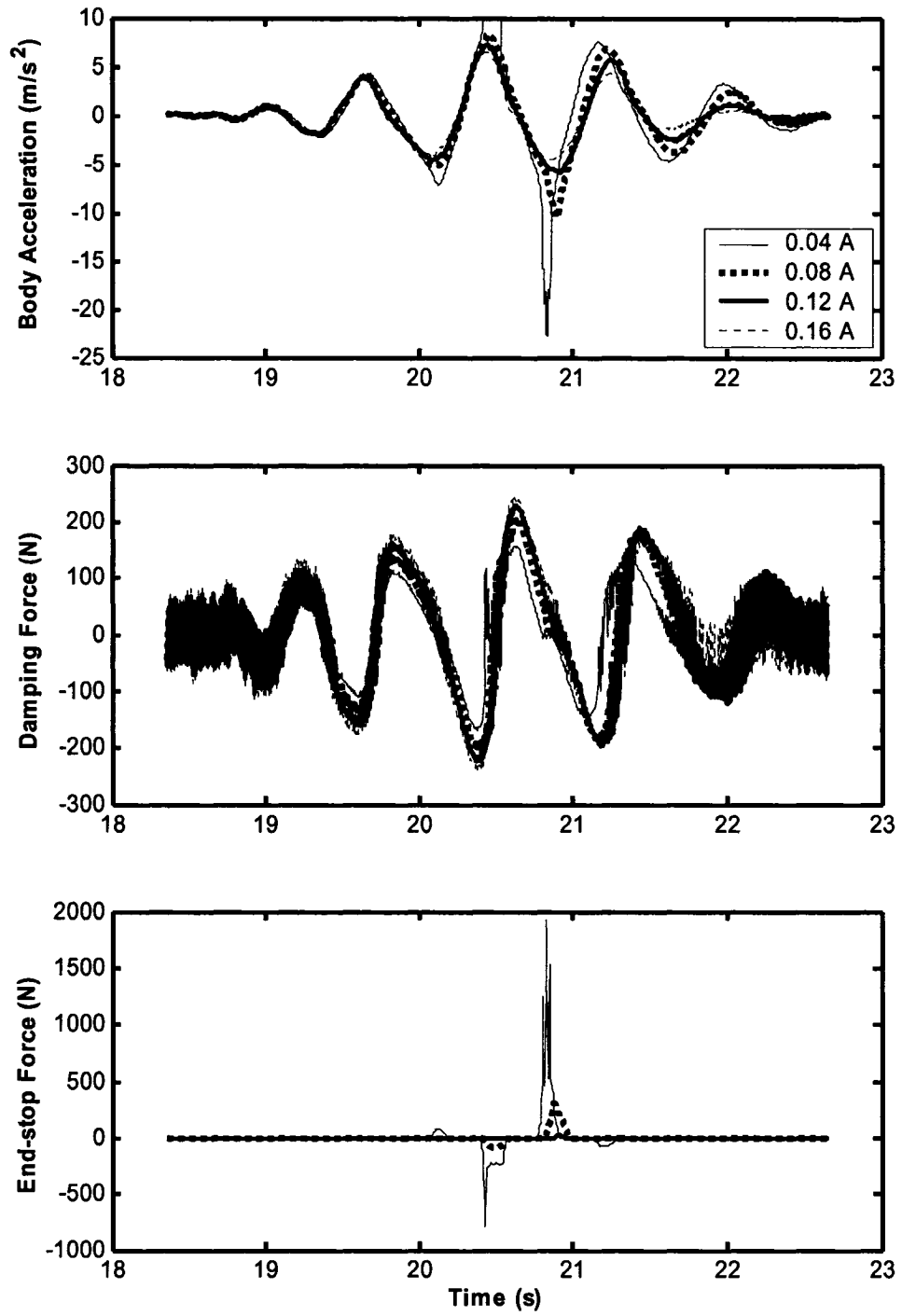


Figure 5.5: Influence of applied current on the body mass acceleration \ddot{x}_o , damping force f_d and end-stop force F_b , of the MR-damper suspension seat model subject to a 55 mm peak transient excitation.

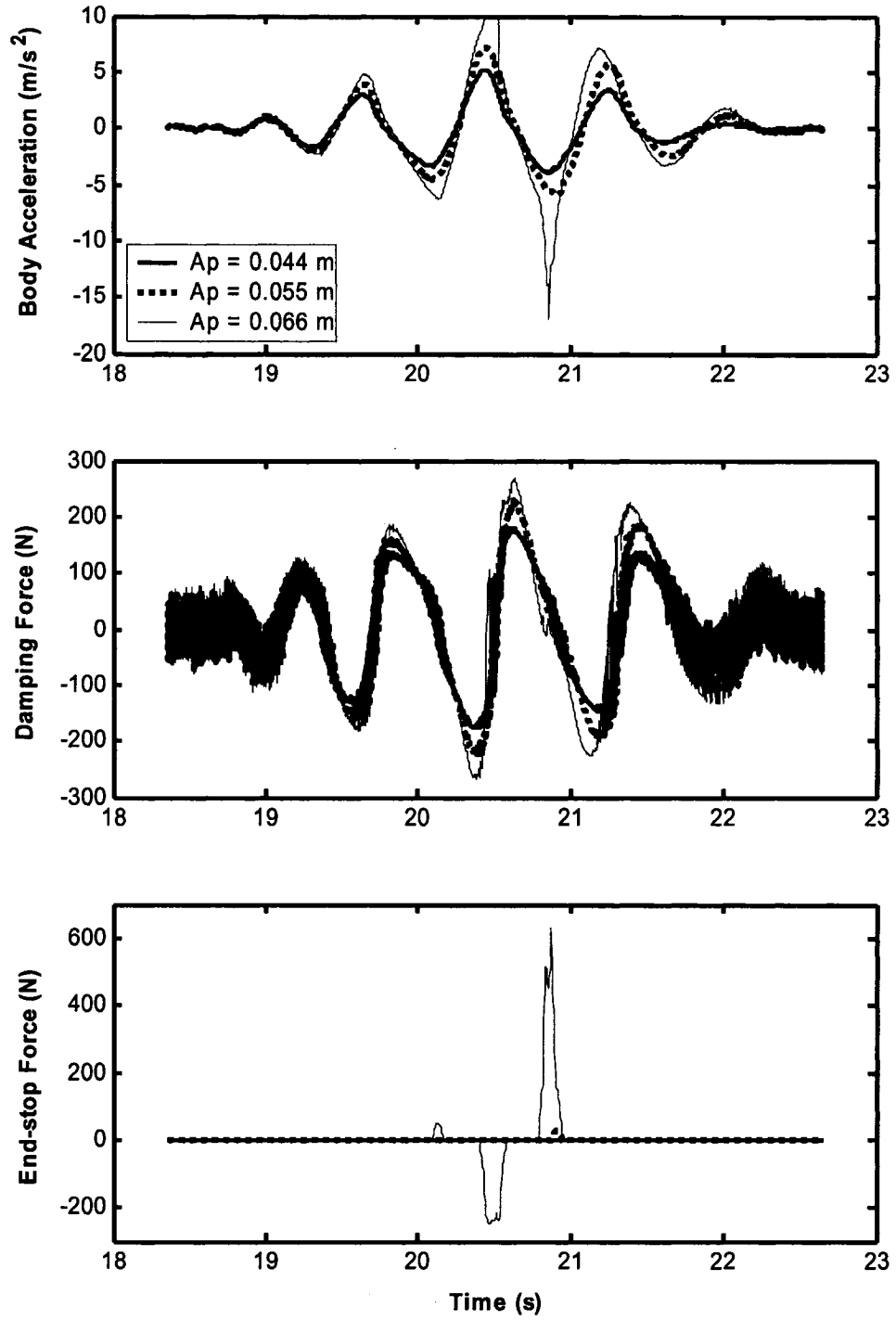


Figure 5.6: Comparison of responses, body acceleration \ddot{x}_o , damping force f_d and end-stop force F_b , of MR-damper suspension seat model under three different peak magnitude of transient excitations (applied constant current $i = 0.12\text{A}$).

5.3.3 Vehicular Excitations

The acceleration responses of the suspension seat models with the hydraulic and MR-dampers (0.12 A) are also evaluated under vehicular excitations (Bus, BusA, EM1 and EM1A) to further examine the validity of the MR-damper model. The responses are evaluated in terms of PSD of the mass acceleration and presented in Figures 5.7 and 5.8 for the Bus and EM1 excitations, respectively. The results in general show reasonably good agreements with the measured responses of the seat with the conventional hydraulic damper under both vehicular excitations and the corresponding amplified excitations, although considerably deviations exist under EM1A excitation. The relatively high intensity of EM1A excitation causes stronger impacts against the end-stops, when compared with those observed from the measured responses. Figure 5.8 reveals considerable differences between the response of seat model with the MR-damper and the model with the hydraulic damper under EM1A excitation. Such differences were not evident under harmonic, transient, Bus, BusA and EM1 excitations. These deviations are attributed to saturation of MR-damping force under extreme high velocities caused by the EM1A excitation, which predominates near 2 Hz.

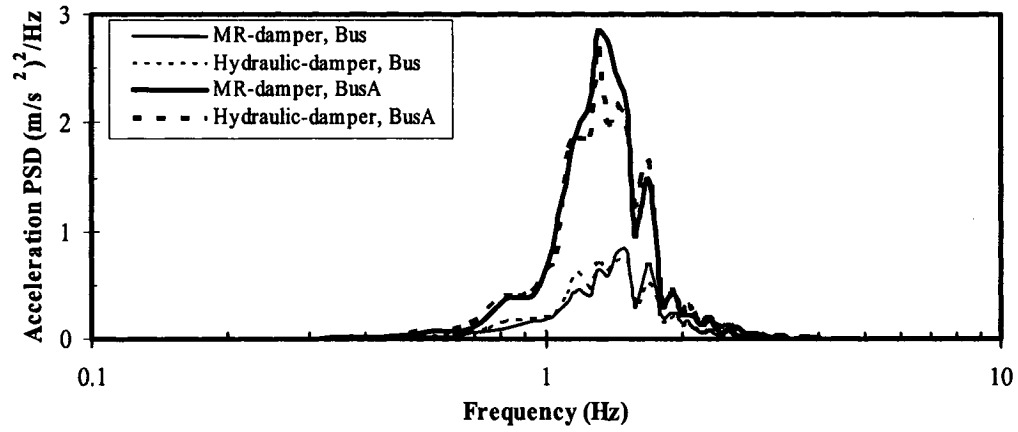


Figure 5.7: Comparison of acceleration PSD responses of suspension seat models with the MR-damper (0.12 A) and the hydraulic passive damper under Bus and BusA excitations.

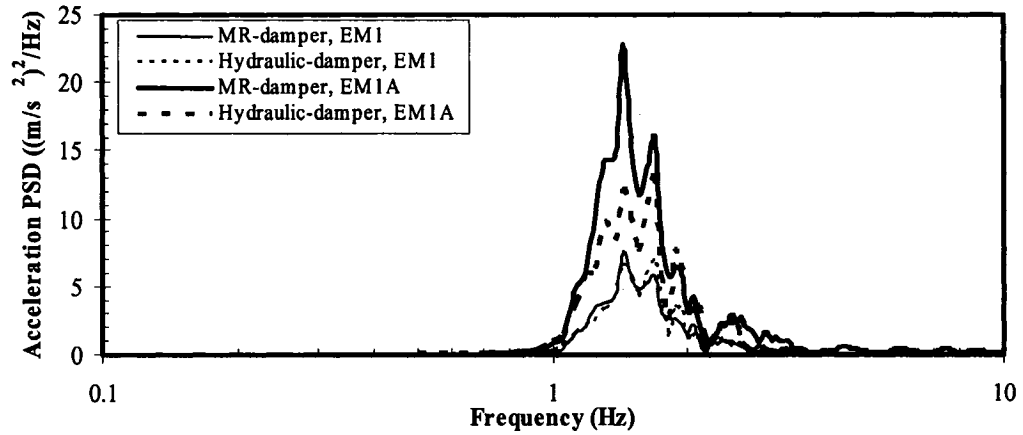


Figure 5.8: Comparison of acceleration PSD responses of suspension seat models with the MR-damper (0.12 A) and the hydraulic passive damper under EM1 and EM1A excitations.

5.3.4 Influences of MR-damper Hysteresis

The strong hysteresis nonlinearities of the MR-damper, as observed from the measured force-velocity characteristics, may cause undesirable effects on the dynamic performance of the suspension system, particularly in the closed-loop mode. These may

include limit cycle behaviour and a relatively larger steady-state error [81]. Moreover, such nonlinearities may cause large magnitudes of transient responses near zero velocity.

The effect of damping force hysteresis on the responses could be conveniently assessed using the suspension seat employing MR-damper models based on mean as well as hysteretic f - v characteristics. Figure 5.9 illustrates comparisons of body mass acceleration transmissibility responses of the suspension seat model employing mean and hysteretic damping force models, while the drive current is held as 0.12 A. The results suggest negligible effects of hysteresis under harmonic excitations when the damper is operated in an open-loop manner.

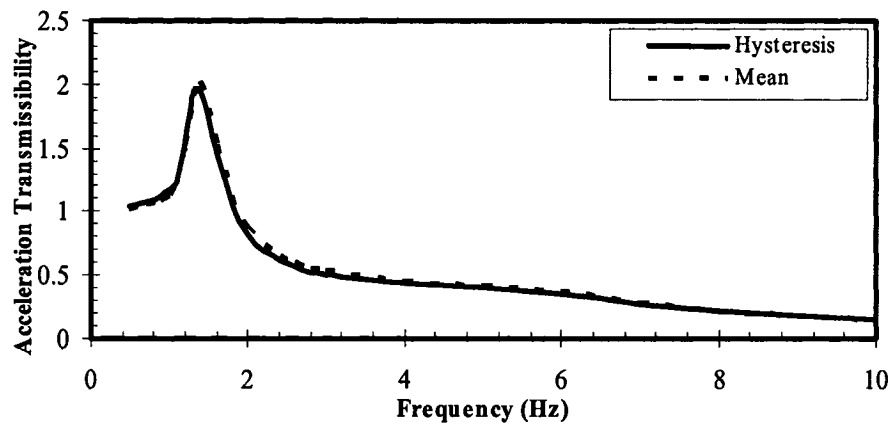


Figure 5.9: Comparison of acceleration transmissibility of the body mass of the suspension seat model employing hysteresis and mean damping force model (0.12 A).

The relatively small contribution of the hysteresis to the acceleration response can be observed from the steady-state time history of the response shown in Figure 5.10 (a) under excitation at 1.25 Hz. The damping forces developed by the mean and hysteretic

models during the cycle are also compared in Figure 5.10 (b). The results reveal relatively small effects of hysteresis on the body mass acceleration in the vicinity of zero relative velocity.

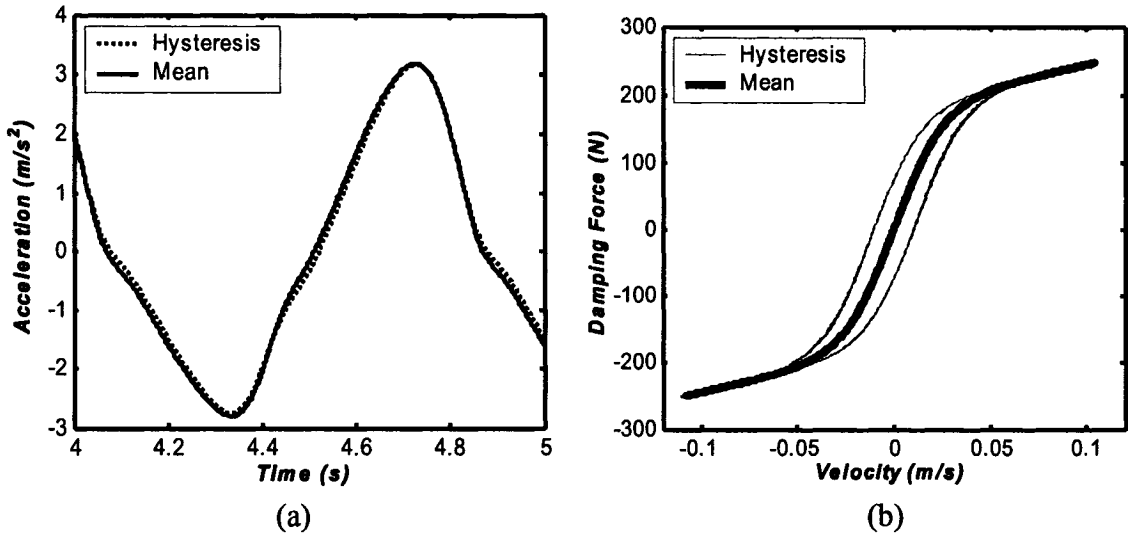


Figure 5.10: Comparison of responses of the suspension seat model with mean and hysteresis damper models under a harmonic excitation ($A_r = 25 \text{ mm}$; $f_r = 1.25 \text{ Hz}$; $i = 0.12$ A): (a) body acceleration \ddot{x}_o ; (b) f_v characteristics of the MR-dampers.

The effect of hysteresis is more clearly evident from the response obtained under a transient excitation, as shown in Figure 5.11. The results show that the hysteresis nonlinearity of the MR-damper causes high frequency variations in the damping force and thus the body mass acceleration near zero relative velocity. Furthermore, the comparisons of acceleration response of the mean and hysteretic damping show the presence of high magnitude oscillations in the acceleration responses due to hysteresis.

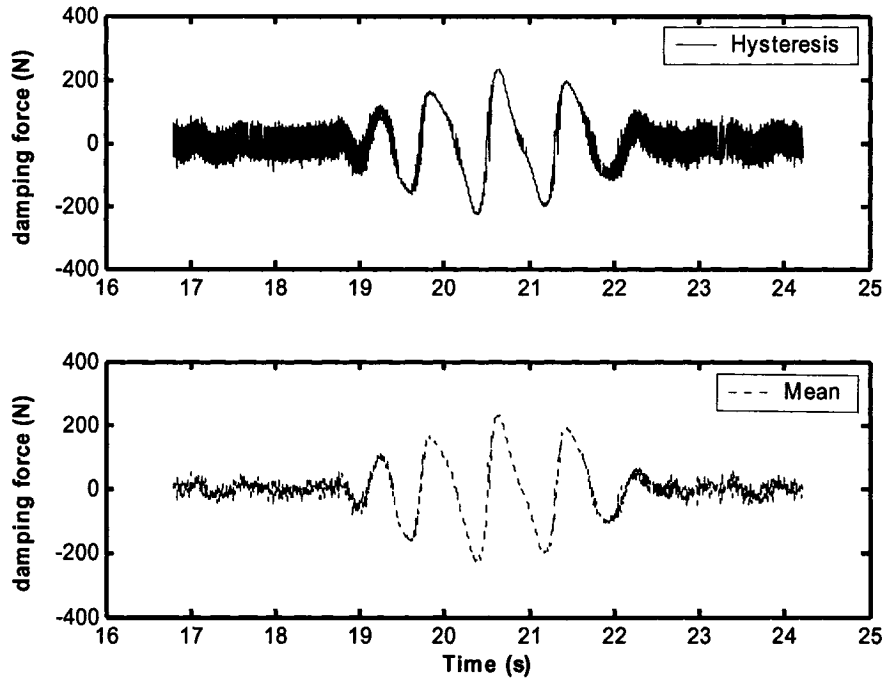


Figure 5.11: Comparison of acceleration responses of the suspension seat model with mean and hysteresis f - v damper models under transient excitation (peak displacement amplitude = 55 mm).

5.4 Formulation of Controller Synthesis

The above results demonstrate the validity of the MR-damper model in conjunction with the generalized two-DOF suspension seat model. The results also show the limitations due to saturation property of the MR-dampers, which can be overcome through variations in the current through synthesis and design of a controller. Controller synthesis for the MR-damper suspension seat under varying excitations could be realized by formulating target functions on the basis of a reference model. A reference model based upon the well-known “skyhook” damping concept, proposed by Karnopp *et al.* [86], is developed to realize variable damping. The skyhook control concept proposes that the

magnitude of mass acceleration could be reduced by reducing the damping force, when the suspension mass velocity (\dot{x}_s) is out of phase with the damper force or relative velocity ($\dot{x}_s - \dot{x}_b$) across the suspension spring. A number of studies have thus employed on-off damping mechanisms for vehicle suspensions, where the damping force is suppressed to zero, when mass velocity is in phase with the damping force or relative velocity [46, 49]. Such an approach yields significant magnitudes of transient oscillations associated with switching from ‘on’ to the ‘off’ state or vice versa. The MR-damper, however, continues to provide light damping force even in the absence of an applied current. The ‘off’ state is thus limited to the light damping, referred to as the ‘lo’ state, which can help reduce the magnitudes of switching transients. In this study, a skyhook concept-based control synthesis is formulated to realize ‘hi-lo’ variations in damping force through modulation of the current.

5.4.1 Control Algorithm

The ‘hi-lo’ damping mode can be realized by modulating the controller current i_c on the basis of a condition function comprising the responses of the suspension mass and the base excitation. Karnopp et al. [86] proposed the following condition function for realizing on-off damping:

$$F_d = \begin{cases} c\dot{x}_s; & \text{if } \dot{x}_s(\dot{x}_s - \dot{x}_b) > 0 \\ 0; & \text{if } \dot{x}_s(\dot{x}_s - \dot{x}_b) \leq 0 \end{cases} \quad (5.2)$$

where F_d is the variable damping force, which is dependent upon the body mass velocity

and viscous damping coefficient c .

For most automotive dampers, it would be quite difficult to derive a generally applicable viscous damping coefficient. The constant c may thus be considered as a controller gain. For a MR-damper, the modulation of the damping force is achieved through modulation of the current, while the ‘off’ state is replaced by the ‘lo’ state. A skyhook-based control algorithm (SC) is thus formulated as:

$$i_c = \begin{cases} i_z; & \text{if } \dot{x}_s(\dot{x}_s - \dot{x}_b) > 0 \\ 0; & \text{if } \dot{x}_s(\dot{x}_s - \dot{x}_b) \leq 0 \end{cases} \quad (5.3)$$

In the above formulation, i_c represents the command current, and i_z refers to the current corresponding to the ‘hi’ state and is limited to a maximum current of i_H ($0 < i_z \leq i_H$). A higher current and thus the damping force is realized when the absolute suspension mass velocity (\dot{x}_s) is in phase with the relative velocity ($\dot{x}_s - \dot{x}_b$). Unlike the originally proposed “skyhook” control concept, this scheme would yield non-zero damping force, when $\dot{x}_s(\dot{x}_s - \dot{x}_b) \leq 0$. The ‘hi’ state current i_z however is varied in proportional with the relative velocity ($\dot{x}_s - \dot{x}_b$), such that:

$$i_z = G|\dot{x}_s - \dot{x}_b| \quad (5.4)$$

where G represents the control gain of the ‘hi-lo’ semi-active control scheme.

The condition function in Equation (5.3) represents a discontinuity in current and thus the damping force, when either $\dot{x}_s = 0$ or $\dot{x}_s - \dot{x}_b = 0$. Such a discontinuity in the controller synthesis is known to cause transient oscillations in the system responses. A smoothing algorithm is consequently formulated to reduce the contributions due to

current discontinuity. This function is formulated to achieve continuous modulation of the current as a function of a condition function z_c , and allows for varying degree of smoothness in the control current, such that:

$$M_c(p_c, \xi_c, z_c) = \frac{1+p_c}{2} + \left[\frac{p_c-1}{\pi} (z_c \geq 0) \cup \frac{1-p_c}{\pi} (z_c < 0) \right] \left| \tan^{-1}(\xi_c z_c) \right| \quad (5.5)$$

where $M_c(p_c, \xi_c, z_c)$ refers to the continuous modulation (CM) multiplier, and the condition function z_c may be either positive or negative as it is evident from:

$$z_c = -\dot{x}_s (\dot{x}_s - \dot{x}_b) \quad (5.6)$$

The smoothing function is applied as a multiplier of the command current i_c to achieve continuously modulated desired control current, i_d , such that:

$$i_d = M_c(p_c, \xi_c, z_c) i_c ; \quad 0 \leq i_d \leq i_H \quad (5.7)$$

The second term within the parenthesis of Equation (5.5) defines the logic function that depends upon the sign of z_c . The factor p_c can assume a value equal to or greater than 0 but less than 1 ($0 \leq p_c < 1$) and describes the ratio of currents corresponding to ‘lo’ and ‘hi’ states. A unity value of p_c yields a unity value of the multiplier and thereby the idealized ‘hi-lo’ switching without a smoothing. For the idealized skyhook-based control Equation (5.3) involving the zero ‘lo’ state, the factor p_c remains zero. The modulation function may thus be simplified to:

$$M_c(0, \xi_c, z_c) = \frac{1}{2} + \left[-\frac{1}{\pi} (z_c \geq 0) \cup \frac{1}{\pi} (z_c < 0) \right] \left| \tan^{-1}(\xi_c z_c) \right| \quad (5.8)$$

The target function in the above equation together with the smoothing factor $\xi_c > 0$ yields a smooth transition between the ‘hi’ and ‘lo’ states. As an example, Figure 5.12

illustrates variations in the command current i_c for different values of the smoothing factor ξ_c , range from 0 to 10, while assuming that $-1 \leq z_c \leq 1$. The results show that a lower value of ξ_c yields more continuous and smooth variation in i_c , and may cause greater error in the desired control current i_d . An increase in ξ_c yields rapid transition of the command current from the ‘hi’ to the ‘lo’ state. For a non-zero ‘lo’ state, the factor p_c assumes a non-zero value, which relates to the proportionality of the ‘lo’ and ‘hi’ currents. The continuous variations in the command current of a ‘hi-lo’ control algorithm with non-zero ‘lo’ state is illustrated in Figure 5.13 for different values of p_c , ranging from 0 to 0.5. The results are presented for a constant value of $\xi_c = 10$, and show that the increase in the proportionality factor yields a higher ‘lo’ limit, while the ‘hi’ state current remains unchanged.

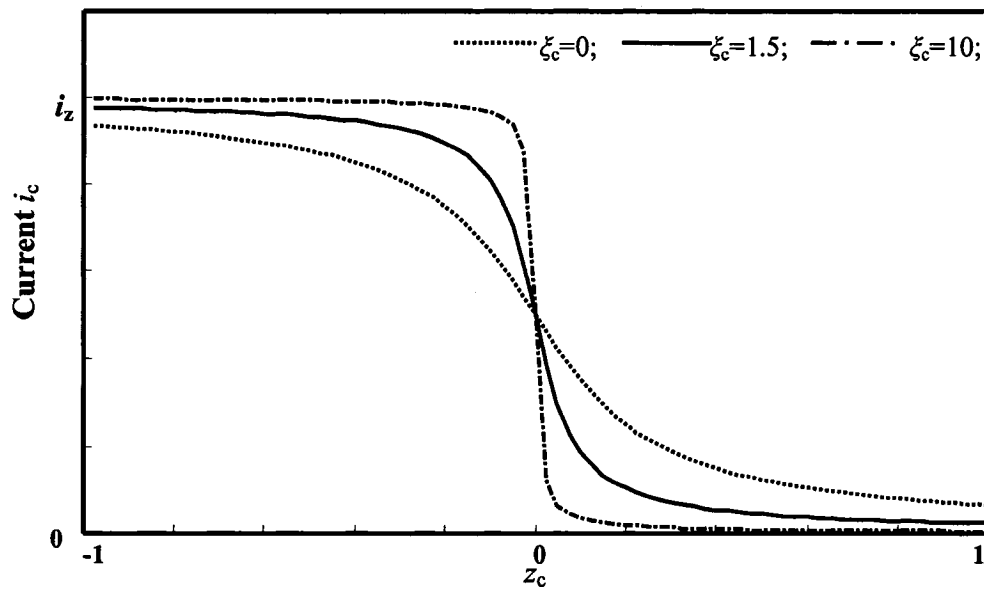


Figure 5.12: Continuous variations in the command current i_c of a ‘hi-lo’ control algorithm and the effects of smoothing.

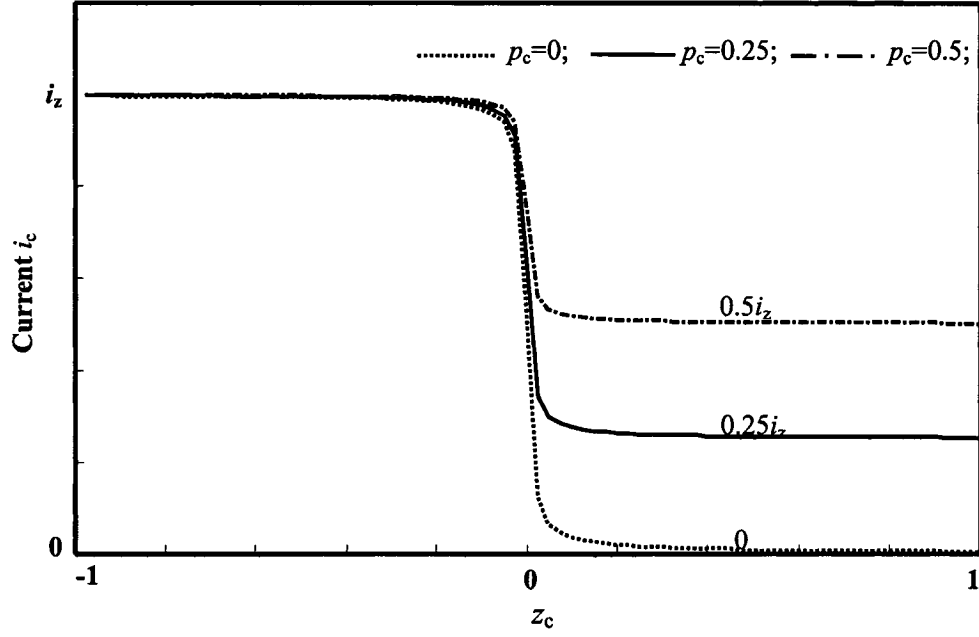


Figure 5.13: Continuous variations in the control current i_c of a 'hi-lo' control algorithm and the effects of the proportionality factor p_c ($\xi_c = 10$).

Figure 5.14 illustrates a general structure of the semi-active MR-damping control scheme based on the skyhook control and modulation of the current. The suspension mass velocity (\dot{x}_s) and the relative velocity ($\dot{x}_s - \dot{x}_b$) responses of the plant to an excitation $x_b(t)$ are applied to derive the command current i_c , the continuous modulation function CM and the desired control current i_d , using the formulations in Equations (5.3), (5.5) and (5.7), respectively.

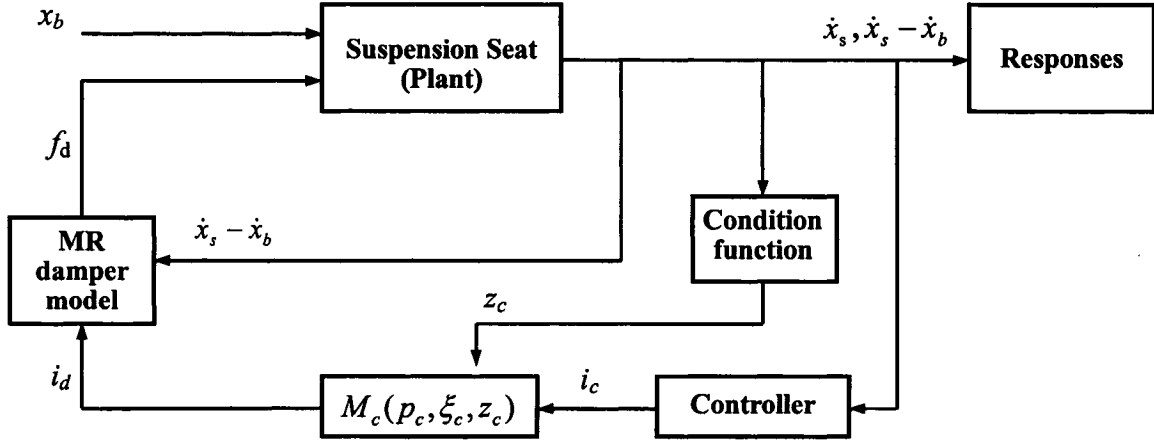


Figure 5.14: Schematic of the general structure of the semi-active MR-damping control scheme based on skyhook and continuous modulation algorithm.

5.5 Response Characteristics of Suspension Seat with ‘hi-lo’ Control

The response characteristics of the two-DOF suspension seat model employing semi-active controlled MR-damper on the basis of the skyhook control are evaluated under different excitations described in section 4.3. The controller involved zero ‘lo’ state is applied in conjunction with the CM function, where a constant value of ξ_c ($\xi_c = 40$). The results attained are also compared with the responses obtained under constant currents, as described in section 5.3.

5.5.1 Harmonic Excitations

The responses under harmonic excitations in the 0.625 to 10 Hz frequency range are evaluated in terms of *rms* acceleration transmissibility of the suspension seat. The acceleration transmissibility characteristics of the semi-active suspension seat are illustrated in Figure 5.15 for different selected value of the controller gain G , ranging

from 1 to 9. The results show that peak transmissibility magnitude decreases considerably when the control gain is increased from 1 to 3. A further increase in the control gain however yields relatively smaller reduction in the peak magnitude, which is attributed to the saturation of the MR damper. The higher damping associated with a higher gain yields only slightly higher acceleration transmissibility in the isolation range ($f_r > 2$ Hz). Unlike the response of the semi-active suspension, the constant current or passive mode operation yields considerably higher magnitude of acceleration transmissibility in the isolation range, as observed in Figure 5.16. The figure illustrates comparison of the semi-active suspension responses with those of the passive suspension with fixed currents (0.12 or 0.20 A). The results clearly show that the proposed control algorithm can help achieve reduced resonant response with only minimal influence on the response in the isolation frequency range.

The results presented in Figure 5.15 are attained using the continuous modulation function, which tends to suppress the transient responses due to discontinuous ideal control. The contributions of the CM function are demonstrated by comparing the desired control current (i_d) responses of the controller with and without the CM algorithm. As an example, Figure 5.17 illustrates the comparisons of time-histories of i_d responses of the controller with and without the CM algorithm, while subject to harmonic excitation in the vicinity of the resonant frequency and $G = 1$. The results clearly show the presence of transient oscillations of considerable magnitudes in the applied current in the absence of the smoothing algorithm, when the controller switches from the 'hi' to 'lo' state. The use

of the CM algorithm effectively suppresses the transient oscillations leading to smooth transition of current from the 'hi' to the 'lo' state.

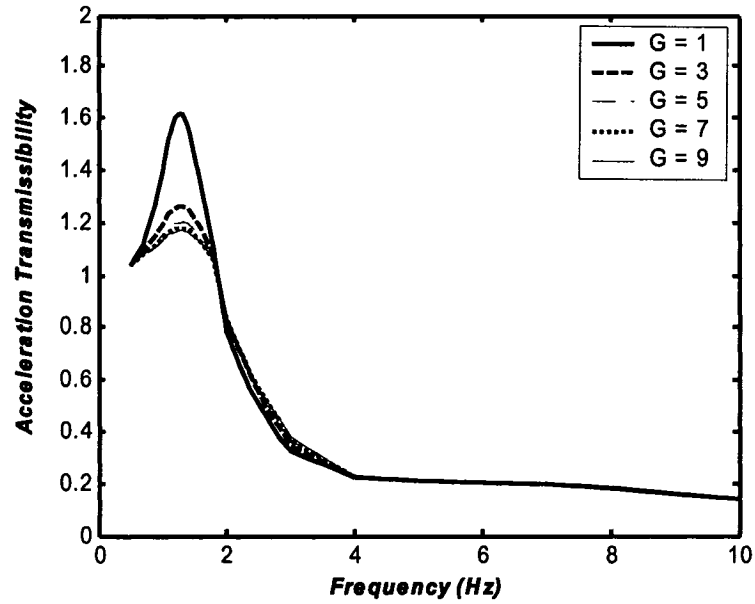


Figure 5.15: Comparison of acceleration transmissibility characteristics of semi-active suspension seat with different value of control gain G .

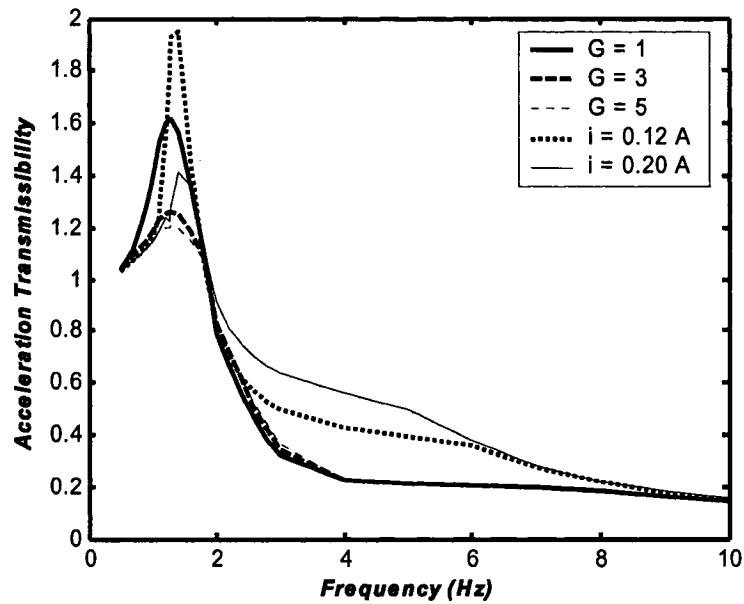


Figure 5.16: Comparison of acceleration transmissibility characteristics of the semi-active suspension seat with selected control gain with those attained under constant currents.

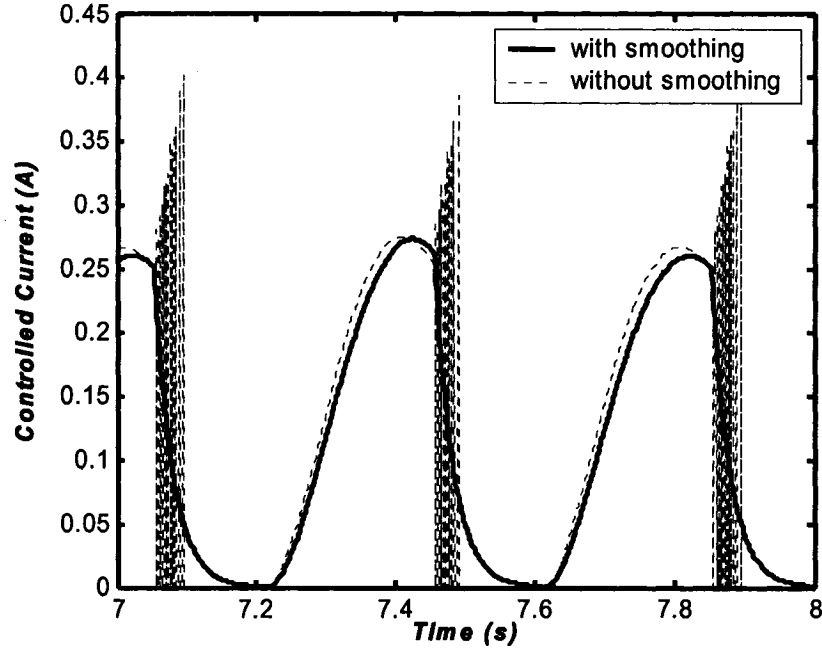


Figure 5.17: Comparison of the control current with smoothing and without smoothing while semi-active skyhook-based controller applied ($A_r=25\text{mm}$; $f_r=1.25\text{Hz}$; $G=1$).

5.5.2 Transient Excitations

Figure 5.18 illustrates the semi-active suspension responses to transient excitations in terms of body mass acceleration (\ddot{x}_o), damping force (f_d), end-stop force (F_b) and control current (i_d), for different controller gain. The results are obtained under transient excitation occurring at a frequency of 1.5 Hz with peak displacement of 55 mm, as described earlier in section 4.3. The results show that the peak damping force and acceleration responses decrease with increasing gain value, which is attributed to higher peak values of the control current. The results do not suggest the presence of an end-stop impact, irrespective of the controller gain. A comparison of the damping force response with that attained in the passive mode (Figure 5.5) further suggests that the closed-loop

control helps to suppress the oscillations caused by damper hysteresis in the vicinity of zero velocity.

Suspension seats generally exhibit end-stop impacts under high magnitude excitations in the vicinity of the resonant frequency, as it was evident for the passive (Figure 4.20) as well as constant current MR (Figure 5.6) damper suspensions. Figures 5.19 and 5.20 illustrate the responses of the semi-active suspension for $G = 1$ and $G = 3$, respectively, to transient excitations of significantly higher displacement amplitude ranging from 55 to 126 mm. The results clearly show that the end-stop impacts initiate under transient excitation of peak displacements near 0.077 m and 0.115 m, respectively for the controller with $G = 1$ and $G = 3$. The effectiveness of the suspension under high intensity excitations could be further enhanced by increasing the damping force bandwidth of the MR damper. From Figure 5.20, it is clearly evident that the damping force approaches its saturation limit under 0.115 and 0.126 m excitation, as the control current approach the upper limit of 1.5 A. The results also suggest that the impacts initially occur with the top end-stop, while a loss of contact between the body mass and the seat is also observed under 0.077 and 0.088 m excitations for $G = 1$, and 0.115 and 0.126 m excitation for $G = 3$.

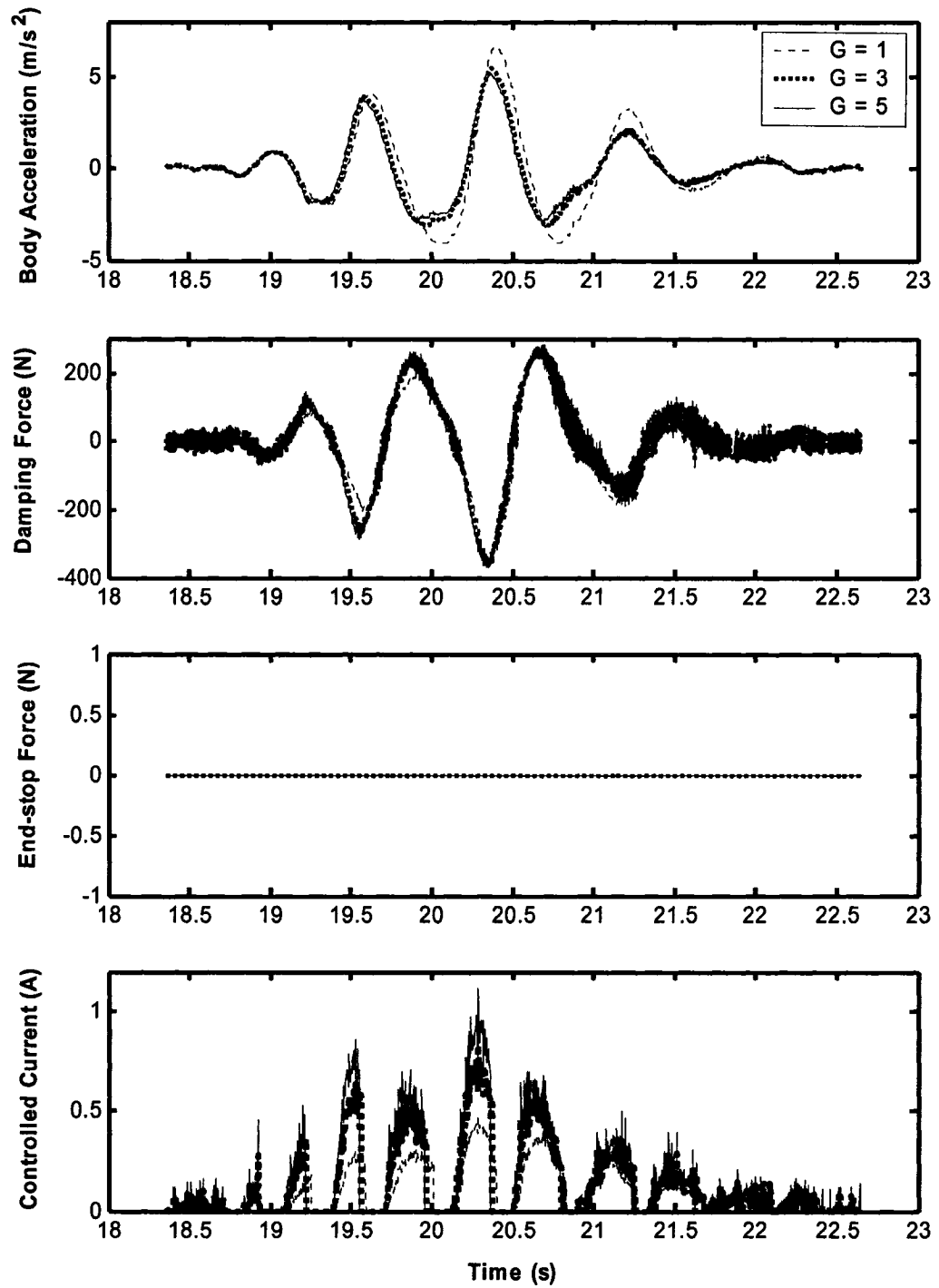


Figure 5.18: Influence of controller gain on the response characteristics of the semi-active suspension seat to a transient excitation (peak displacement = 55 mm).

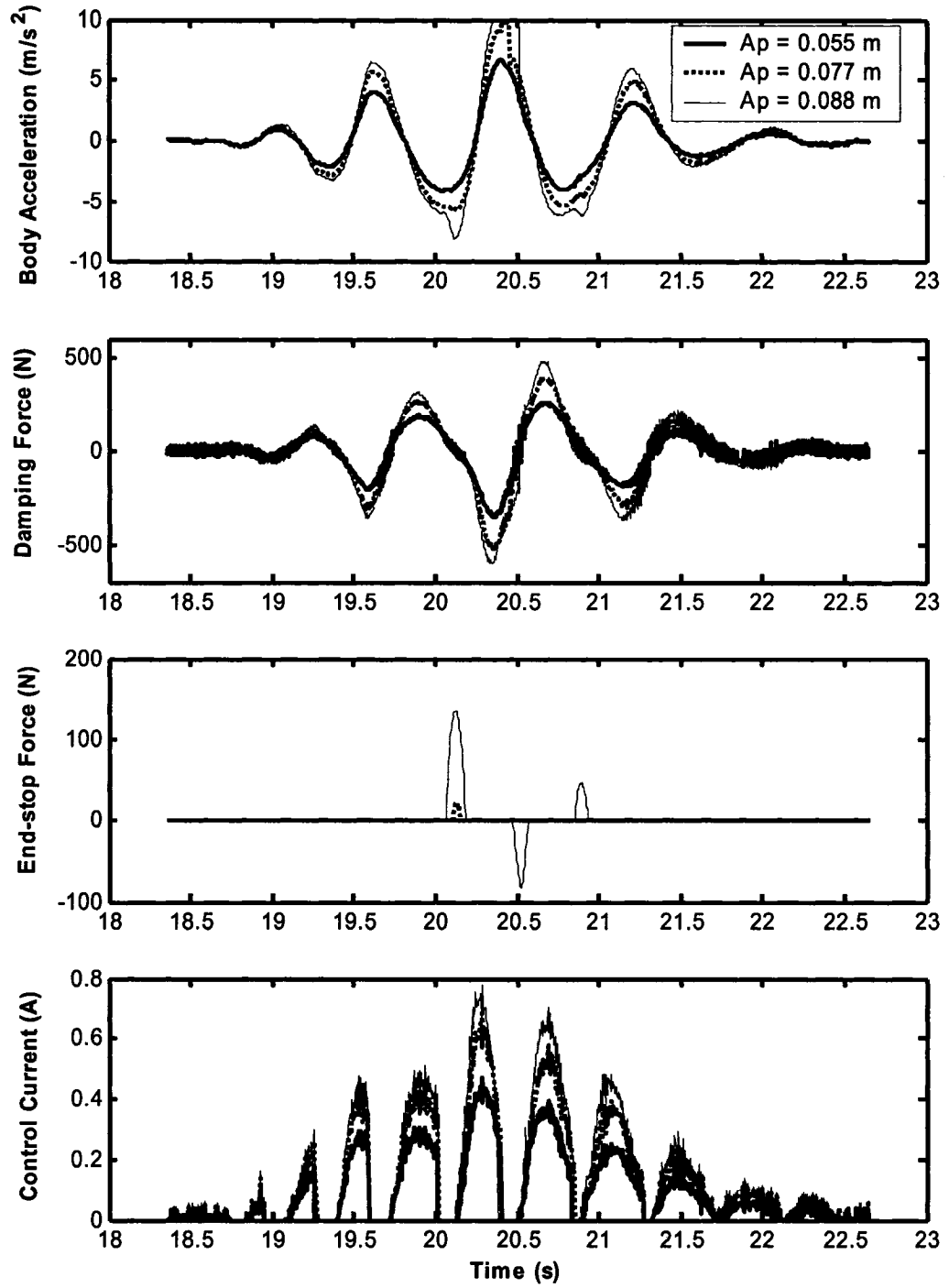


Figure 5.19: Influence of peak displacement amplitudes of the transient excitation on the semi-actively suspension responses ($G=1$).

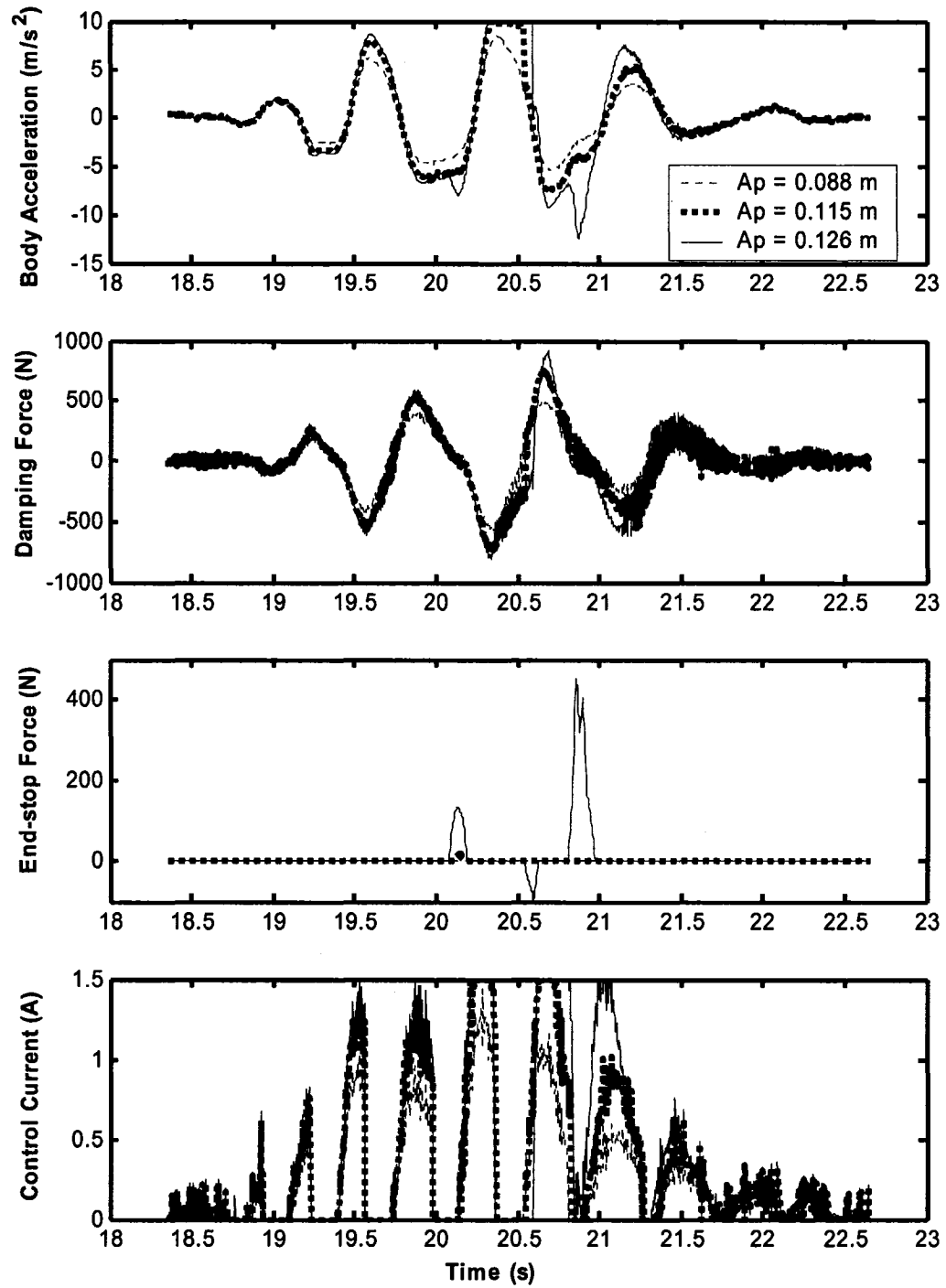
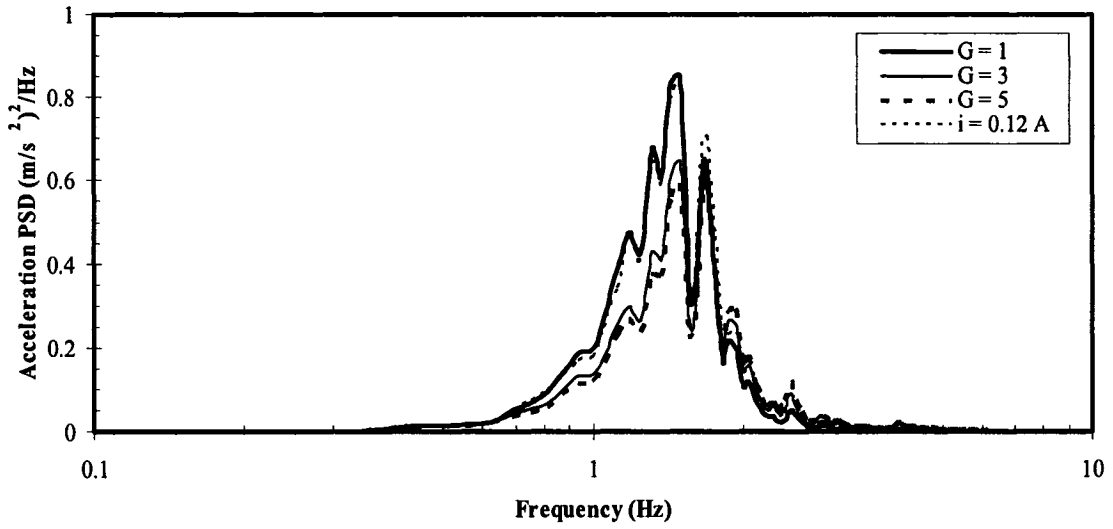


Figure 5.20: Influence of peak displacement amplitudes of the transient excitation on the semi-actively suspension responses ($G=3$).

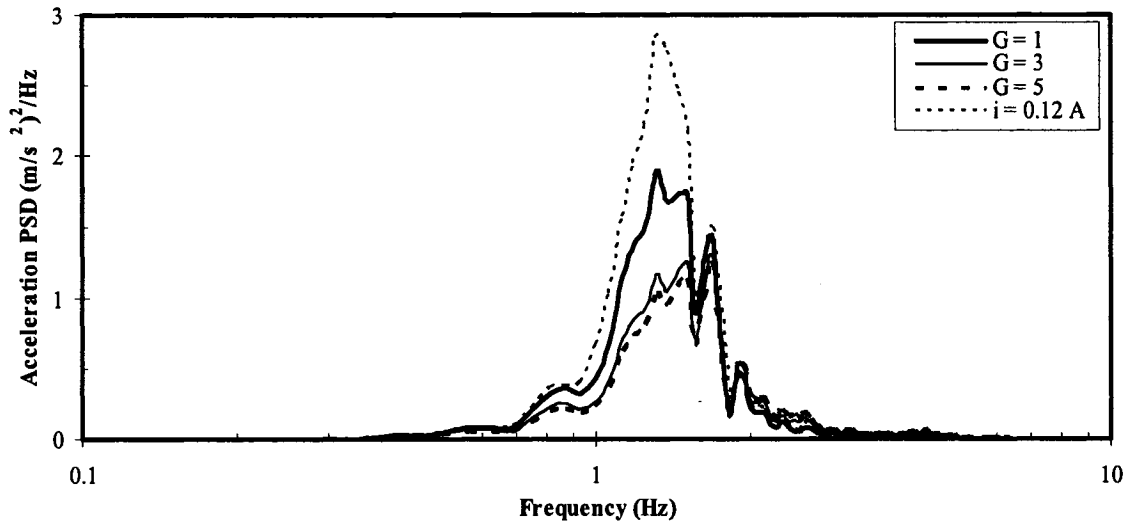
5.5.3 Vehicular Excitations

The response characteristics of the semi-actively controlled MR-damper suspension seat are further evaluated under vehicular excitations, namely Bus and EM1, nominal as well as amplified. The corresponding weighted and un-weighted seat effective amplitude transmissibility (*SEAT*) and the ratio of vibration dose values (*VDVR*), are also computed and presented in section 5.7.

Figure 5.21 illustrate the body mass acceleration PSD responses of the MR semi-active suspension subject to the excitation 'Bus' and 'BusA' excitations, respectively. The figures presented the acceleration responses corresponding to different controller gains and constant current of 0.12 A. The results show that the response characteristics corresponding to $G = 1$ are comparable with those of the constant current suspension under the 'Bus' excitation. The effectiveness of the semi-active control become evident for higher gain and amplified excitations. The results also show significant effect of the control gain, irrespective of the excitations, while the effect is far more significant under the amplified excitation. The peak magnitude of the acceleration PSD response reduce from 0.9 to 0.7 $(\text{m/s}^2)^2/\text{Hz}$ under 'Bus' excitation as the controller gain is increased from 1 to 3. The corresponding reduction under 'BusA' excitation occurs from 2.8 to 1.5 $(\text{m/s}^2)^2/\text{Hz}$, as evident in Figure 5.21 (b).



(a)



(b)

Figure 5.21: Comparisons of the PSD of body mass acceleration responses of the semi-active and constant current suspension seats under a bus excitation for different gains: (a) Bus; and (b) BusA.

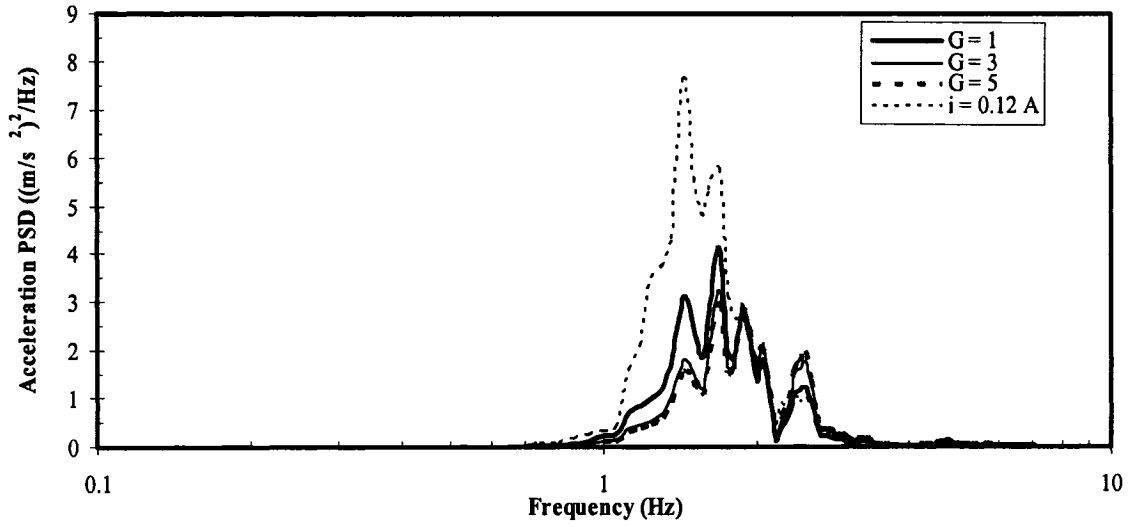
It is evident that constant current suspension yields significantly high peak acceleration PSD and thus the *rms* value. The results suggest that the proposed controller

is more effective under high intensity excitation, where the excitation occur in the vicinity of the resonant frequency. This is attributed to the fact that the MR suspension damping is strongly dependent upon the relative velocity apart from the applied current. The control effects under 'Bus' excitation appear to be less than those observed under 'BusA' excitation. The results also show that the overall *rms* values of the acceleration response would also decrease considerably with a high controller gain, particularly under the 'BusA' excitation.

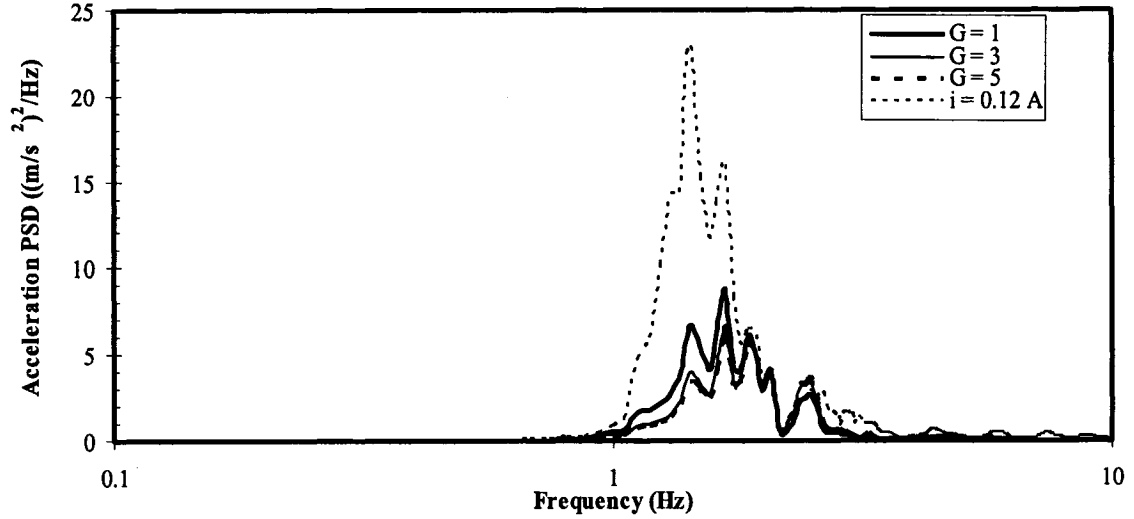
Figure 5.22 illustrate the acceleration PSD responses of the semi-active as well as constant current suspension seats subject to 'EM1' and 'EM1A' excitations, respectively, for different control gain ($G = 1, 3$ and 5). Unlike the Bus excitation, the results clearly show the superior performance of the semi-actively controlled suspension seat under the nominal as well as amplified EM1 excitations. This is attributed to the relatively higher predominant frequency of the EM1 excitation (≈ 2.1 Hz).

The peak acceleration PSD responses of the constant current suspension under the EM1 and EM1A excitations approach approximately 8.2 and $2.3 \text{ (m/s}^2\text{)}^2/\text{Hz}$, respectively. These peak values reduce to nearly 3.5 and $7 \text{ (m/s}^2\text{)}^2/\text{Hz}$ for the semi-active suspension with $G = 3$. The extremely high magnitude response of the constant current suspension is partly attributed to the end-stop impacts, as discussed in section 5.3.3. The implementation of the proposed controller could eliminate such impacts. The results clearly show superior vibration attenuation and end-stop impact performance of the semi-actively suspension seat for both the nominal as well as amplified EM1 excitations.

The results further show only minimal benefits of higher control gain due to saturation and current limitation properties of the MR-damper.



(a)



(b)

Figure 5.22: Comparisons of the PSD of body mass acceleration responses of the semi-active and constant current suspension seats under class I construction vehicle excitation for different gains: (a) EM1; (b) EM1A.

5.6 Integrated End-stop Impact Control (IC)

The suspension seats with limited travel yield frequent impacts against compression and extension end-stops. Such impacts cause transmission of severe vibration and shock to the seated occupants, particularly under high intensity and transient excitations [1, 24, 26]. Considerable efforts have thus been made to limit the frequency and severity of the end-stop impacts. A few recent studies have employed ER and MR-dampers using a simple relative displacement control [36]. Such a control methodology yields definite benefits in limiting the end-stop impacts, while the enhancement of vibration attenuation performance under continuous vibrations is entirely ignored. Owing to the vehicle operations on terrains of varying roughness, it is vital to enhance both the vibration attenuation and the end-stop performance characteristics.

The skyhook-based controller proposed in the previous section is thus further enhanced by integrating the end-stop impact control. The primary goal of this integrated controller is to attain improved shock as well as vibration isolation of the suspension seat under continuous as well as transient or intermittent excitations of varying intensity. The integrated control algorithm is formulated by introducing a position control to the proposed skyhook-based control. The important prerequisite for the integrated controller is the ability to adapt rapidly to sudden changes in the suspension position caused by high intensity transient or continuous excitations. The transient oscillations attributed to the switching would be expected to be far more significant for such a control. The integrated control, therefore, must incorporate an adequate smoothing function to ensure continuous

transitions between the different states.

5.6.1 Formulation of the Control Algorithm

The design of passive suspensions invariably involves difficult compromise between the resonant response and the vibration attenuation response in the isolation frequency range. This was clearly demonstrated for the passive suspension seat in the previous chapter. The results obtained for the semi-active MR-damping suspension seat reveal that the proposed suspension control could achieve suspension resonance control and vibration isolation. The shock and vibration attenuation performance of a suspension seat also impose conflicting requirement on the suspension damping [111]. This was also demonstrated through the results presented in Chapter 4. The proposed control algorithm could be further enhanced to limit the suspension travel within the permissible ranges by applying the maximum current i_H as the suspension approaches its travel limits. An integrated control algorithm is thus formulated as:

$$i_c = \begin{cases} i_H; & \text{if } |x_s - x_b| > \delta_s d \\ G|\dot{x}_s - \dot{x}_b|; & \text{if } (|x_s - x_b| \leq \delta_s d) \cap (\dot{x}_s(\dot{x}_s - \dot{x}_b) > 0) \\ 0; & \text{if } (|x_s - x_b| \leq \delta_s d) \cap (\dot{x}_s(\dot{x}_s - \dot{x}_b) \leq 0) \end{cases} \quad (5.9)$$

where G is the control gain related to the proposed skyhook-based controller, $d = d_c = d_e$ is the suspension free travel, and δ_s is the switching margin related to relative position control. The constant δ_s defines the margin between the instantaneous suspension deflection and the permissible travel, when the control current switches to its limiting value i_H .

The above control algorithm involves switching in the command current in addition to those associated with switching between ‘hi’ and ‘lo’ states, as described in the previous section. The command current is thus expected to exhibit far more discontinuous modulations. In order to minimize the effects of such discontinuities in the control current, two different continuous modulation (CM) multipliers, M_c and M_{ce} , are formulated and introduced within integrated control. The CM function M_c ensures smooth transition between the ‘hi’ and ‘lo’ states, as demonstrated in the previous section. The function M_{ce} is formulated to provide smooth transition to the limiting current as the relative position exceeds the margin value. The M_{ce} function is formulated similar to the M_c , where the proportionality constant is considered as non-zero, such that:

$$M_{ce}(p_{ce}, \xi_{ce}, z_{ce}) = \frac{1+p_{ce}}{2} + \left[\frac{p_{ce}-1}{\pi} (z_{ce} \geq 0) \cup \frac{1-p_{ce}}{\pi} (z_{ce} < 0) \right] \left| \tan^{-1}(\xi_{ce} z_{ce}) \right| \quad (5.10)$$

where p_{ce} is the proportion of the ‘hi’ state command current i_c to the limiting value of the current, given by:

$$p_{ce} = \frac{G|\dot{x}_s - \dot{x}_b|}{i_H} \quad (5.11)$$

z_{ce} is the condition function formulated to control the end-stop impacts, given by:

$$z_{ce} = \delta_s d - |x_s - x_b| \quad (5.12)$$

ξ_{ce} is the smoothing factor used to vary the degree of the smoothness in the current modulation, identical to ξ_c .

5.7 Response Characteristics of MR-suspension Seat with Integrated Control

The response characteristics of the two-DOF suspension seat model employing the integrated end-stop impacts controller are assessed under different excitations described in the previous sections. The effectiveness of the integrated end-stop impacts control algorithm could only be evaluated while the suspension seat is subject to higher intensity excitations. In other words, this integrated control algorithm reduces to the semi-active skyhook-based control scheme, when the suspension seat is subject to a lower intensity excitation. The integrated controller involves non-zero 'lo' state in the position control in conjunction with two CM functions, M_c and M_{ce} , while a relatively value of the smoothing factor ξ_{ce} ($\xi_{ce} \approx 450$) is desirable to ensure least transients associated with the relative position switching algorithm. For vehicular excitations, the weighted and un-weighted seat effective amplitude transmissibility (*SEAT*) and the ratio of the vibration dose values (*VDVR*) of the suspension seat, are also computed and compared with those obtained for the seat employing a passive hydraulic damper, constant current MR-damper and under semi-active 'hi-lo' damping.

5.7.1 Harmonic Excitations

The *rms* acceleration transmissibility of the suspension seat with integrated control under a lower intensity harmonic excitation in the 0.625 to 10 Hz frequency would be identical to that of the seat with 'hi-lo' skyhook-based control, as described in section 5.5.1. This is attributed to the fact that the suspension travel under such excitation does

not exceed the position margin ($\delta_s d$). The influence of the relative position control on the suspension responses, however, can be observed from the resonant response, as evident in Figure 5.23. The figure illustrates the time-histories of body mass acceleration (\ddot{x}_o), damping force (f_d), suspension relative displacement ($x_s - x_b$) and the control current (i_d), when the suspension with the proposed integrated controller is subject to sinusoid excitations of two different amplitudes ($A_r = 0.06$ and 0.07 m) at a frequency of 1.25 Hz. The results show that the suspension travel response under lower amplitude excitation ($A_r = 0.06$ m) remains within the selected margin of $0.6d$, which yields negligible contribution due to position control. A slight increase in the excitation magnitude to 0.07 m, however, causes the peak travel to exceed the selected margin during extension, which results in considerably higher control current (approaching $i_H = 1.5$ A) and thus the damping force. The corresponding change in the acceleration response, however, is nearly negligible due to absence of an end-stop impact.

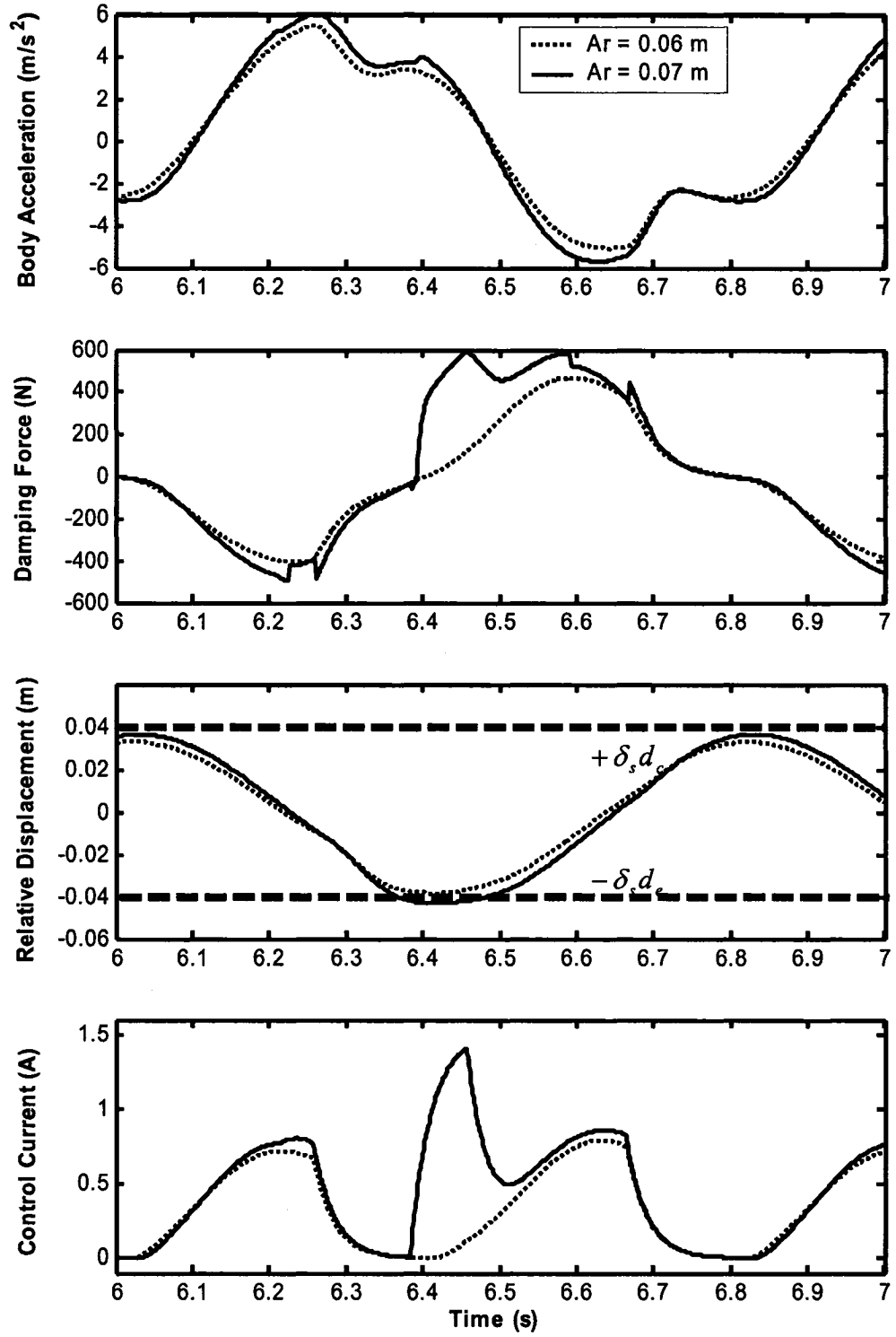


Figure 5.23: Influence of relative position control on the responses of the suspension with integrated controller under different magnitudes of harmonic excitations ($f_r = 1.25$ Hz; $G = 3$; $\delta_s = 0.6$).

Figure 5.24 illustrates the some responses under a higher amplitude excitation ($A_r = 0.112$ m) that causes the end-stop impacts to occur. The results show that the i_d assumes a value of i_H for most of the cycle, since the relative displacement exceeds the selected position margin. While the damping force tends to be higher under high excitation, the magnitude of the maximum damping force (corresponding to $i_H = 1.5$ A) is insufficient to limit the occurrence of the end-stop impact. Moreover, the suspension behaves as a fixed damping suspension with high damping for majority of the cycle. This tends to nullify the semi-active control and thus yields significantly higher magnitude of body mass acceleration and loss of contact between the mass and the seat as evident in Figure 5.24.

The nearly passive behaviour of the suspension system with the integrated control is mostly caused by relatively smaller position margin ($\delta_s = 0.6$). An increase in this margin could allow the damping variation following the semi-active algorithm and thus limit the body mass acceleration. The figure also illustrates the responses, when the margin is relaxed to 0.8. This allows more continuous modulation of the control current, which tends to eliminate the end-stop impacts and the loss of body mass contact with the seat by limiting the magnitude of the body mass acceleration.

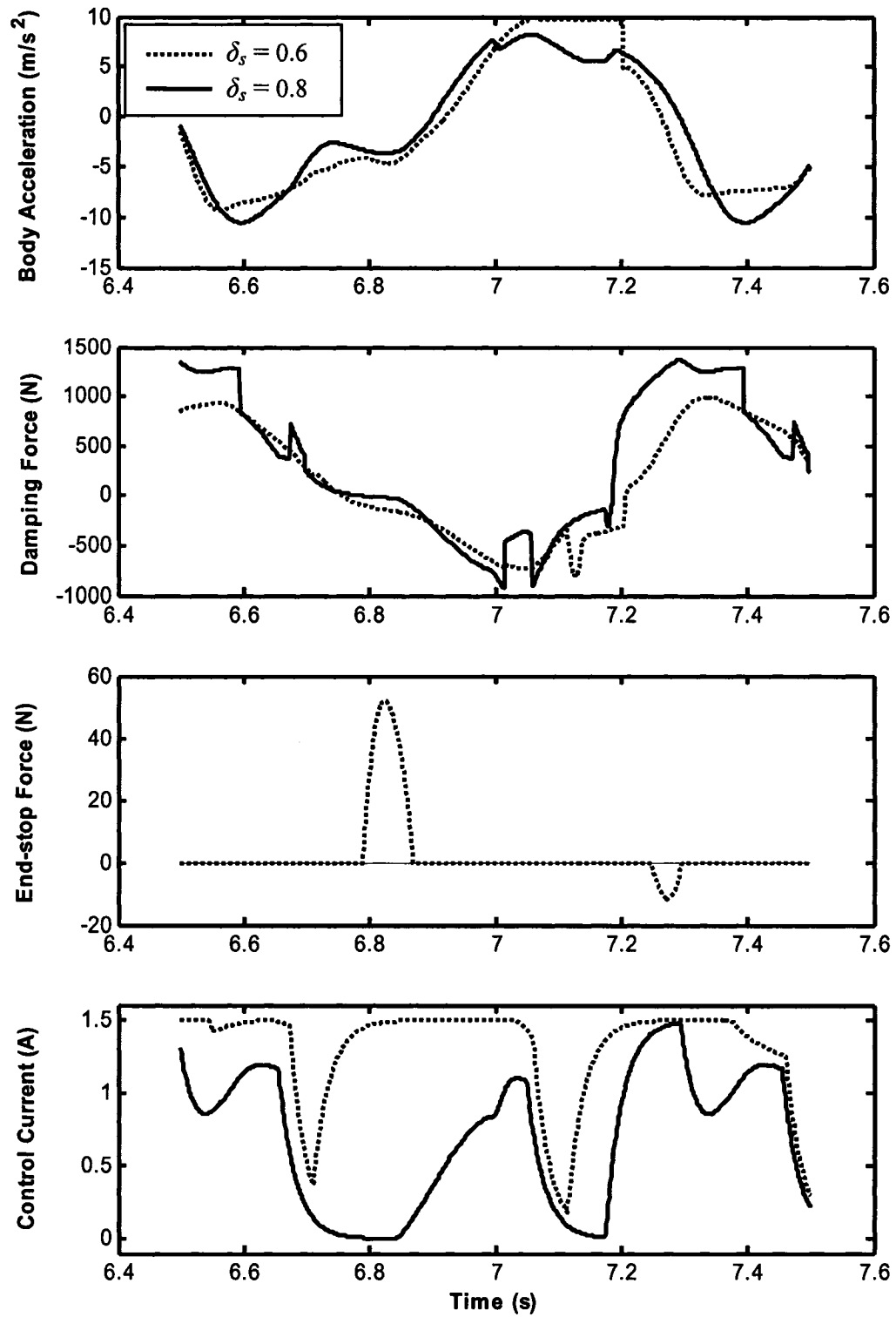


Figure 5.24: Influence of position margin on the responses of the suspension with integrated control under a relatively higher excitation magnitude ($f_r = 1.25$ Hz; $G = 3$; $A_r = 0.112$ m).

5.7.2 Transient Excitations

Figure 5.25 illustrates the responses of the suspension seat with integrated control to transient excitation of different peak magnitudes, while the predominant frequency is 1.5 Hz. The results show time-histories of body mass acceleration (\ddot{x}_o), damping force (f_d), end-stop force (F_b) and the control current (i_d), while a unity control gain ($G = 1$) and position margin of 0.6 are used. The results show absence of end-stop impacts under 0.099 m peak displacement excitation, while the impacts are considered to initiate under 0.115 m excitation. This excitation level is significantly higher than that initiated the impacts with the skyhook control alone (0.077 m; Figure 5.19), and thus suggests effectiveness of the integrated control. Both the excitations, however, reveal loss of contact between the mass and the seat, which was also observed for the skyhook control under 0.077 m excitation. The magnitude of the impact force tends to increase under higher magnitude excitation ($A_p = 0.132$ m). The results further show that the control current approach the limiting value for a relatively larger segment of vibration cycle and thus yields relatively higher values of peak acceleration.

The magnitude and frequency of the end-stop impact and thus the mass acceleration could be limited by relaxing the position margin, which allows for damper operation in the skyhook control mode for a relatively larger position of the vibration cycle. This is evident from the results presented in Figures 5.26 and 5.27, respectively, for $\delta_s = 0.7$ and 0.8, while the peak magnitude of excitation is held at 0.115 m. Comparisons of Figures 5.25 to 5.27 show that the peak impact force decreases with increasing position margin,

while the control current approaches i_H less frequently for a higher value of δ_s . The results suggest that a margin value of 0.8 would yield less frequent and less severe end-stop impacts under high intensity transient excitations.

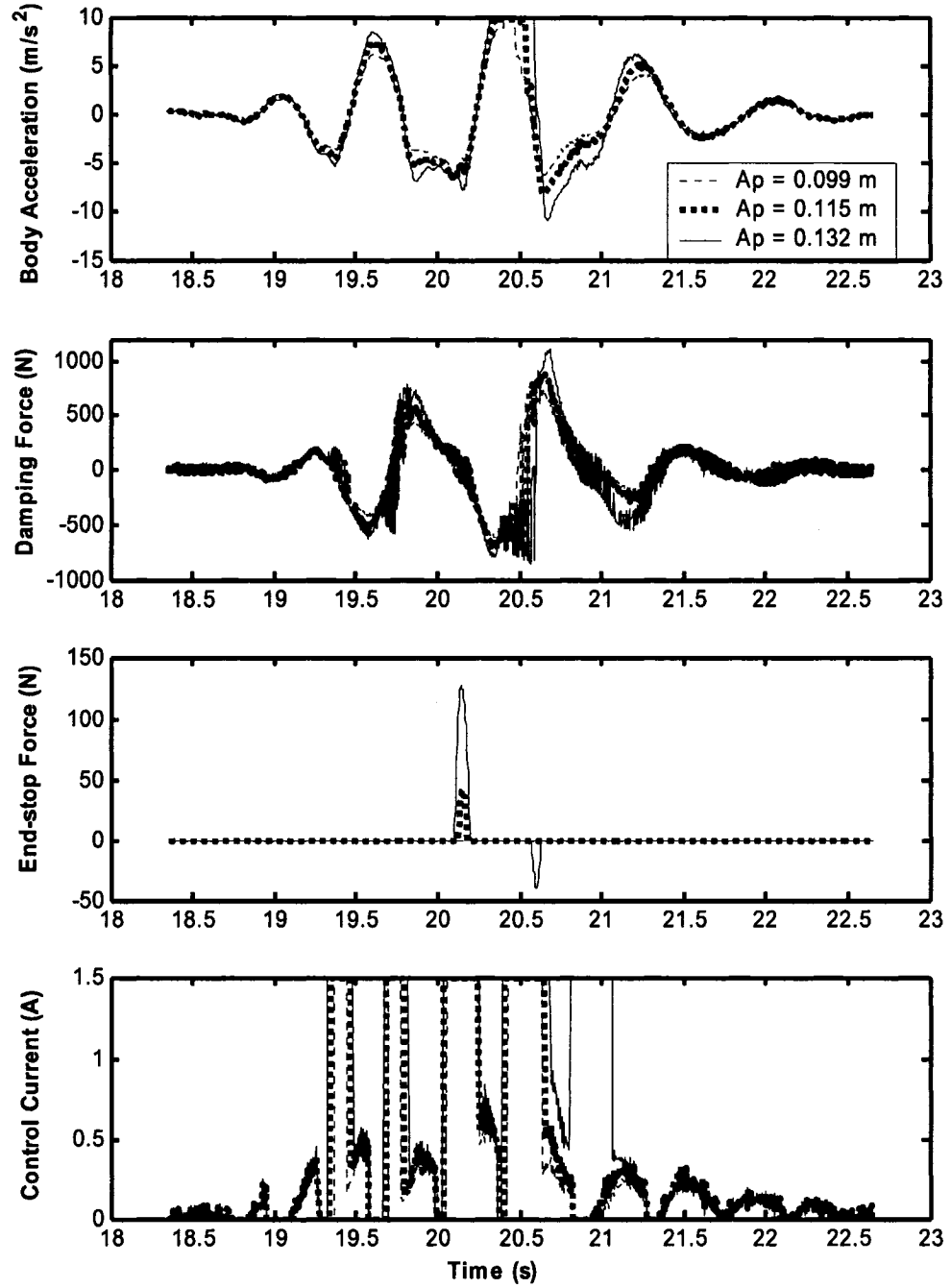


Figure 5.25: Transient response characteristics of the suspension with integrated control under different magnitudes of transient excitations ($G = 1$; $\delta_s = 0.6$).

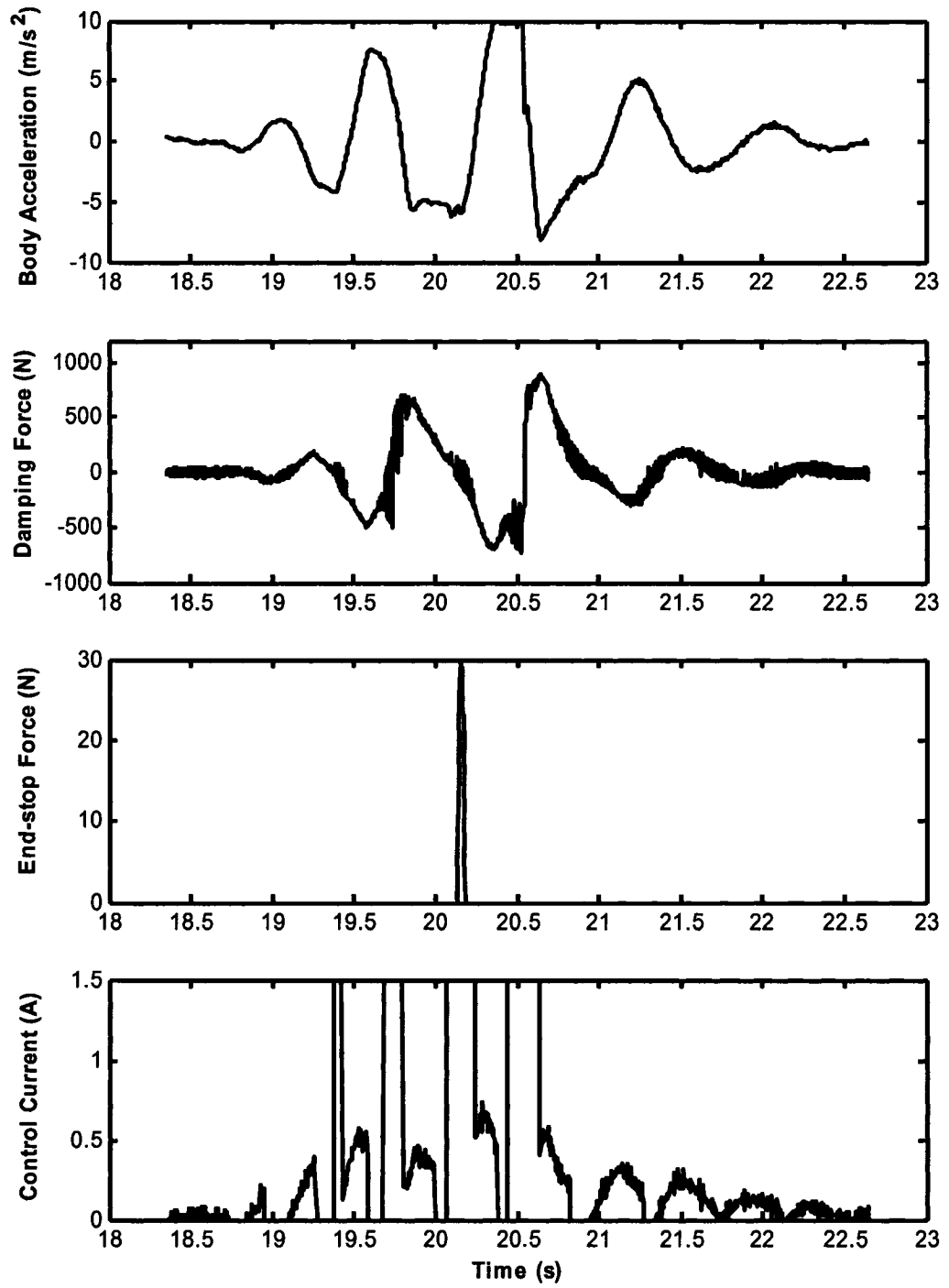


Figure 5.26: Transient response characteristics of the suspension with integrated control ($A_p = 0.115$ m; $G = 1$; and $\delta_s = 0.7$).

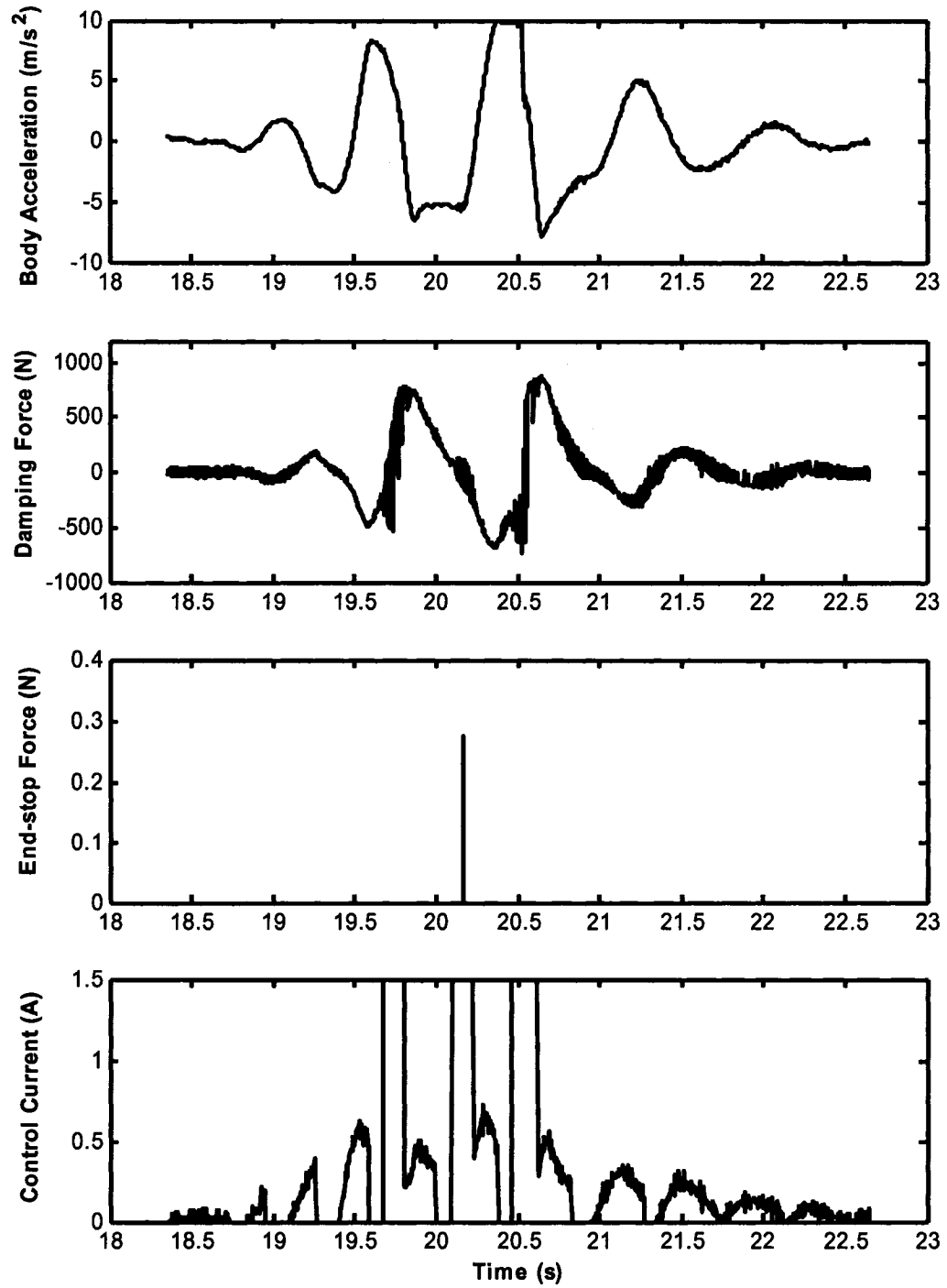


Figure 5.27: Transient response characteristics of the suspension with integrated control ($A_p = 0.115$ m; $G = 1$; and $\delta_s = 0.8$).

The likelihood of an end-stop impact could also be reduced by selecting a higher skyhook control gain. Figures 5.28 and 5.29, respectively, illustrate the influences of peak displacement magnitude (A_p) of the transient excitation and the position margin (δ_s), on the suspension seat responses with integrated controller, while the skyhook control gain is increased to 3. It is evident that the end-stop impacts occurring under 0.115 m are entirely eliminated due to the higher control gain. It should be noted that the controller with skyhook control also resulted in impact under this excitation (Figure 5.20). The results in Figure 5.28 show that the end-stop impact initiates under a considerably higher excitation ($A_p = 0.132$ m) when the margin is chosen as 0.7. An increase in the margin to 0.8 together with $G = 3$, however, tends to increase the severity of the end-stop impact, as observed in Figure 5.29. This is mostly caused by the smoothing function M_{ce} , which tends to limit the control bandwidth. The results presented in Figures 5.25 to 5.29 suggest that position margin for limiting the shock response must be selected with appropriate consideration of the skyhook control gain chosen for enhancement of the vibration attenuation performance.

As described in Chapter 2, the damping force due to a MR-damper strongly depends on the nature of excitation and the applied current. The damping force could be increased by increasing the applied current limits through appropriate design of coils. A higher limiting value of i_H from 1.5 to 2.5 A, and thus the corresponding force, would help limit end-stop impacts under high intensity excitations. Furthermore, such a damper design would yield relatively higher damping force bandwidth for the skyhook control. Figure

5.30 illustrates the responses of the suspension seat with the integrated controller under a transient excitation with peak displacement magnitude of 0.132 m, while the control gain G and the current limit i_H are increased to 7 and 2.5 A, respectively. The results show that increasing the damper current limits could reduce the occurrence of the end-stop impacts and yield improved shock attenuation performance.

The effectiveness of the integrated control in limiting the frequency and severity of end-stop impacts can be demonstrated by comparing the peak magnitudes of transient excitation that either cause or initiate interaction with the end stops. Table 5.1 summarizes the peak displacement excitations that are considered to initiate end-stop impacts of different suspension dampers including passive hydraulic, constant current MR, skyhook control and integrated control. The table also lists the corresponding control gains and the position margins. The results clearly show that the vibration energy required to initiate end-stop impacts increases most significantly, when either the skyhook or integrated controller is employed. Both the passive hydraulic and constant current MR damper suspension revealed impacts under 0.055 m transient excitation, while the skyhook-based control yields impacts only under 0.077 and 0.115 m excitations for $G = 1$ and $G = 3$, respectively. These limits increase to 0.115 and 0.132 m, respectively, with the integrated control.

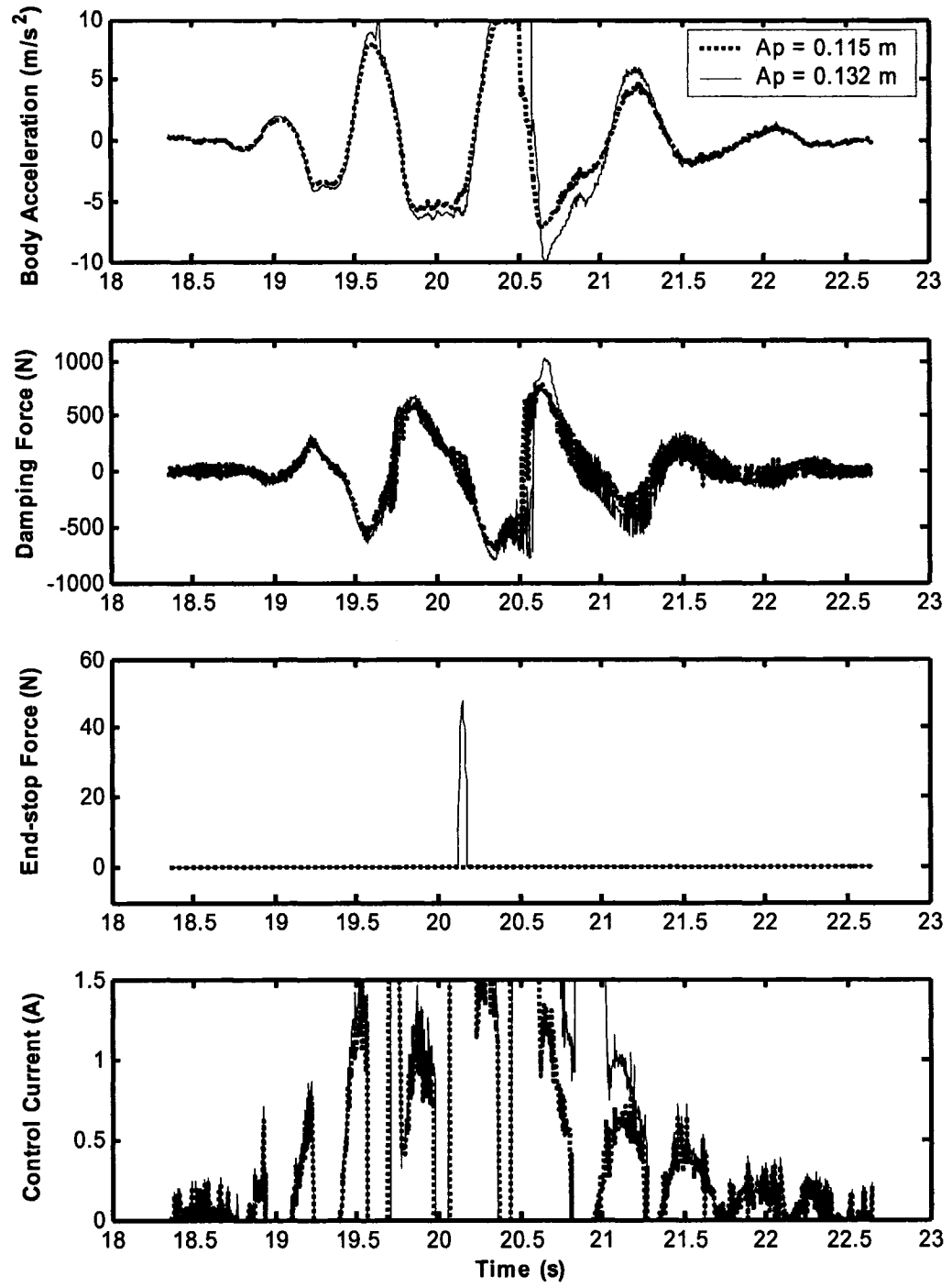


Figure 5.28: Influence of peak transient excitation amplitude (A_p) on the response characteristics of the suspension with integrated control ($G = 3$; $\delta_s = 0.7$).

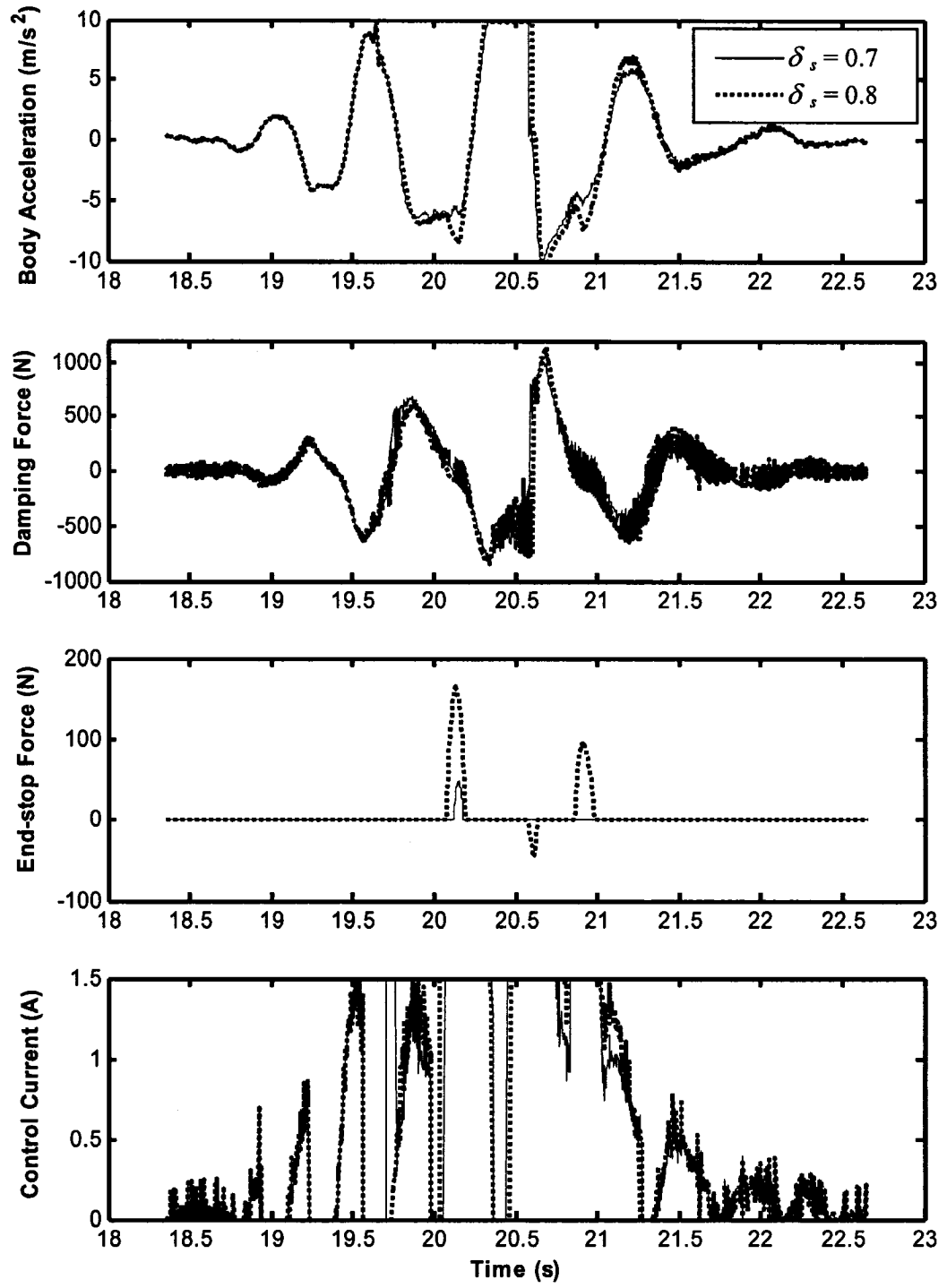


Figure 5.29: Influence of position margin (δ_s) on the response characteristics of the suspension with integrated control under a transient excitation ($A_p = 0.132$ m; $G = 3$).

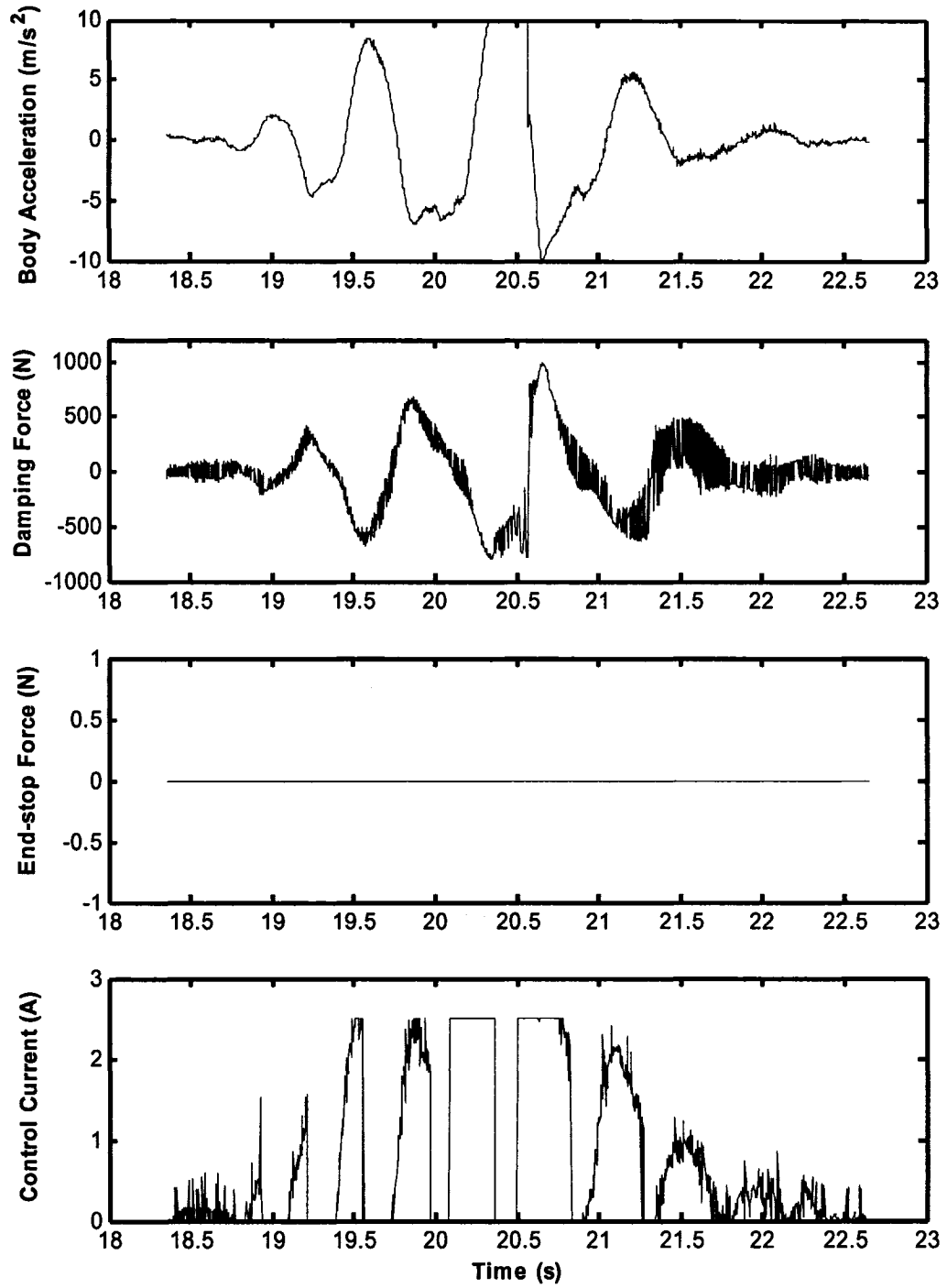


Figure 5.30: The response characteristics of the suspension seat with integrated control and higher limiting current (Transient excitation: $A_p = 0.132$ m; $G = 7$; $i_H = 2.5$ A; $\delta_s = 0.7$).

Table 5.1: The peak displacement magnitudes of transient excitations that initiate end-stop impacts of different suspensions.

Passive suspension seat equipped with hydraulic damper	0.055 m
MR suspension seat with constant current $i = 0.12$ A	0.055 m
MR suspension seat under ‘hi-lo’ skyhook-based control with $G = 1$	0.077 m
MR suspension seat under ‘hi-lo’ skyhook-based control with $G = 3$	0.115 m
MR suspension seat under integrated control with $G = 1$ and $\delta_s = 0.8$	0.115 m
MR suspension seat under integrated control with $G = 3$ and $\delta_s = 0.7$	0.132 m

5.7.3 Vehicular Excitations

The response characteristics of the MR suspension seat with the integrated suspension control (IC) are further evaluated under two different vehicular excitations and their amplified levels, namely, ‘Bus’, ‘BusA’, ‘BusA2’, ‘EM1’ and ‘EM1A’. The responses are evaluated in terms of $SEAT$, $SEAT_w$, $VDVR$ and $VDVR_w$, and compared with those derived for the suspension seats equipped with a hydraulic damper, a constant current ($i = 0.12$ A) MR-damper and with a semi-active skyhook-based damping control (SC). The results are attained for different values of skyhook control gains, while the position margin for the IC controller is chosen as 0.8.

Figure 5.31 illustrates comparisons of the $SEAT$ and $VDVR$ measures of different suspension seats under the ‘Bus’ excitation. The results show that both the SC and IC controller yield lower values of $SEAT$ and $VDVR$, when compared to those of the passive and constant current MR dampers. Moreover, both the controllers yield nearly identical responses, which can be attributed to absence of end-stop impacts under this excitation, as it was observed for the passive suspension seat in section 4.4.1. The results show that a

higher controller gain would be desirable in limiting the transmission of continuous random vibration. Too high a gain value, however, deteriorates the suspension performance, which is particularly evident from the weighted measures. The results suggest gain value, $G = 3$, would yield a *SEAT* and *VDVR* values of 0.67, compared to 0.8 for the passive suspension.

The relative performance characteristics of the suspension are further evaluated under amplified Bus excitation, 'BusA' and 'BusA2'. Figures 5.32 and 5.33 present comparisons of the *SEAT* and *VDVR* measures of different suspension under 'BusA' and 'BusA2' excitations, respectively. An increase in the excitation level yields only marginal increase in *SEAT* and *VDVR* measures of the passive suspension, suggesting negligible contributions due to end-stop impacts. The relatively lighter damping of the constant current MR-damper, however, causes end-stop impacts under amplified excitations. The *VDVR* values thus tend to considerably higher than two *SEAT* measures for both excitations. The skyhook and integrated damping controls, on the other hand, continue to provide comparable values of *SEAT* and *VDVR*, irrespective of the amplification, which also demonstrates robustness of the control algorithm. These results further suggest absence of the end-stop impacts and $G = 3$ as the desirable controller gain.

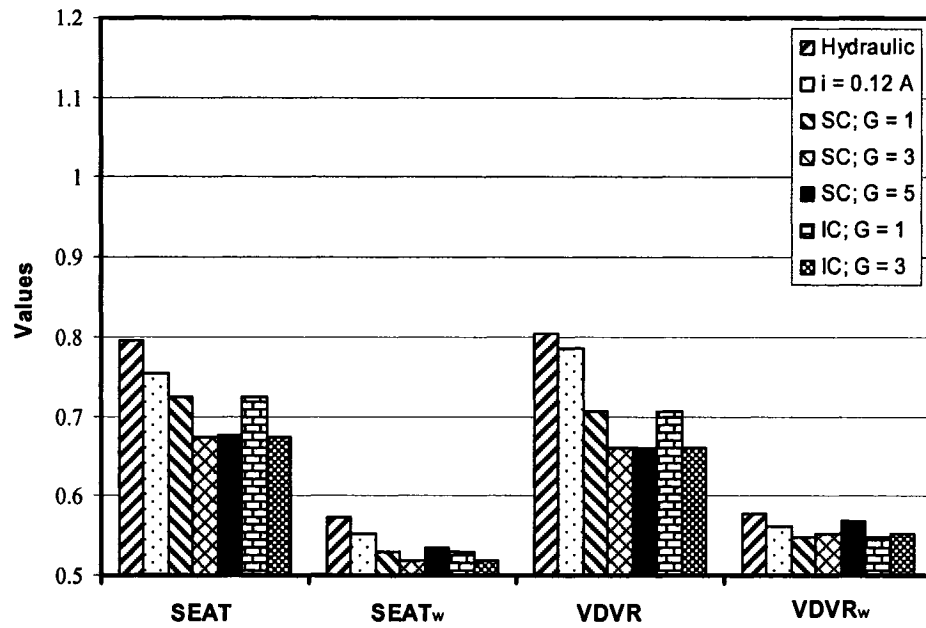


Figure 5.31: Comparisons of the weighted and unweighted SEAT and VDVR measures of different suspension seats subject to 'Bus' excitation.

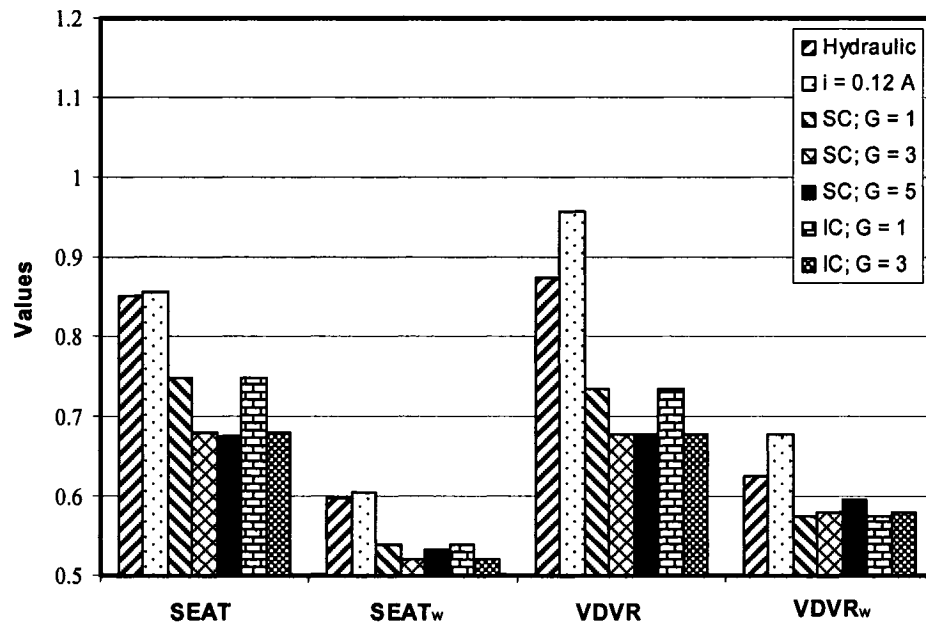


Figure 5.32: Comparisons of the weighted and unweighted SEAT and VDVR measures of different suspension seats subject to 'BusA' excitation.

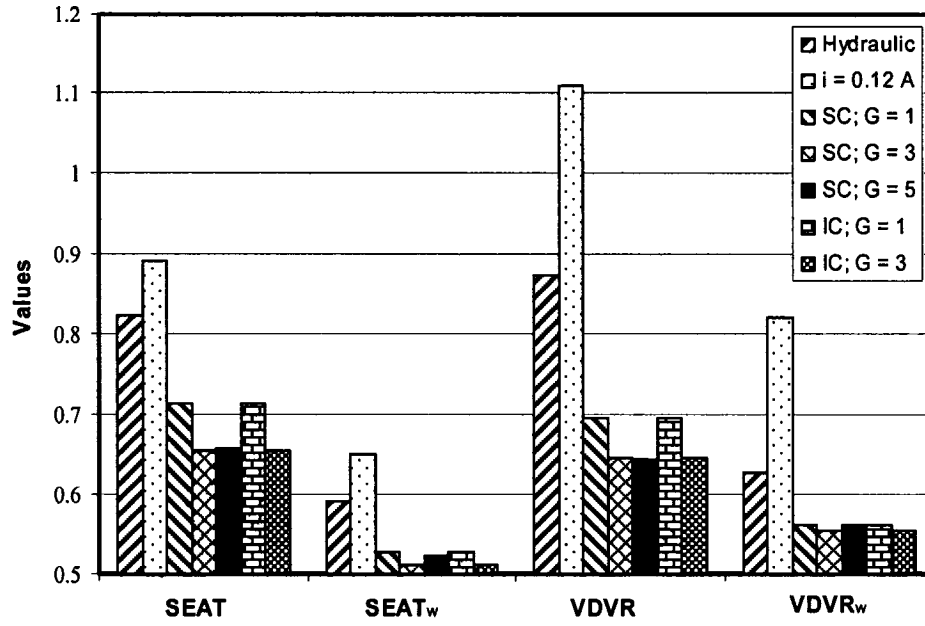


Figure 5.33: Comparisons of the weighted and unweighted SEAT and VDVR measures of different suspension seats subject to 'BusA2' excitation.

Figures 5.34 and 5.35 illustrate comparisons of the $SEAT$, $VDVR$, $SEAT_w$ and $VDVR_w$ measures of different suspension seats under 'EM1' and 'EM1A' excitations, respectively, which predominate at a relatively higher frequency of 2.1 Hz. The position margin (δ_s) for the IC suspension is chosen as 0.8, while the gain values are varied. The passive suspension seat exhibits end-stop impacts only under EM1A excitation, where the $VDVR$ values are considerably larger than the $SEAT$ values. The suspension seat with constant current ($i = 0.12$ A) MR-damping, on the other hand, yields relatively higher $SEAT$ values due to its light damping. The corresponding $VDVR$ values are significantly higher under both 'EM1' and 'EM1A' excitations, suggesting the presence of end-stop impacts. The suspension seats with SC and IC damping yield comparable but

considerably lower values of *SEAT* and *VDVR* under ‘EM1’ excitation, when compared with those attained for the passive and constant current MR damping suspension. These values tend to be ever lower under ‘EM1A’ excitation, suggesting superior performance of the SC damping suspension in limiting both the vibration transmission and the end-stop impacts. The results also suggest that the integrated control (IC) is not required since the SC damping control effectively limits the suspension travel within the specified margin.

The results further show that a lower controller gain would be desirable when the assessments are performed on the basis of weighted measures. It can be established that a higher gain yields higher vibration transmission in the isolation frequency range, where the magnitude of the weighting filter tends to be higher [94]. A lower gain, on the other hand, would cause higher resonant vibration under transient excitation or excitation in the vicinity of the suspension natural frequency, such as ‘Bus’. A control gain of 3 is thus considered to provide an adequate compromise among the measures under different excitations. This is also evident from the comparisons of the performance measures evaluated under different values of the position margin, ranging from 0.6 to 0.8, presented in Figure 5.36.

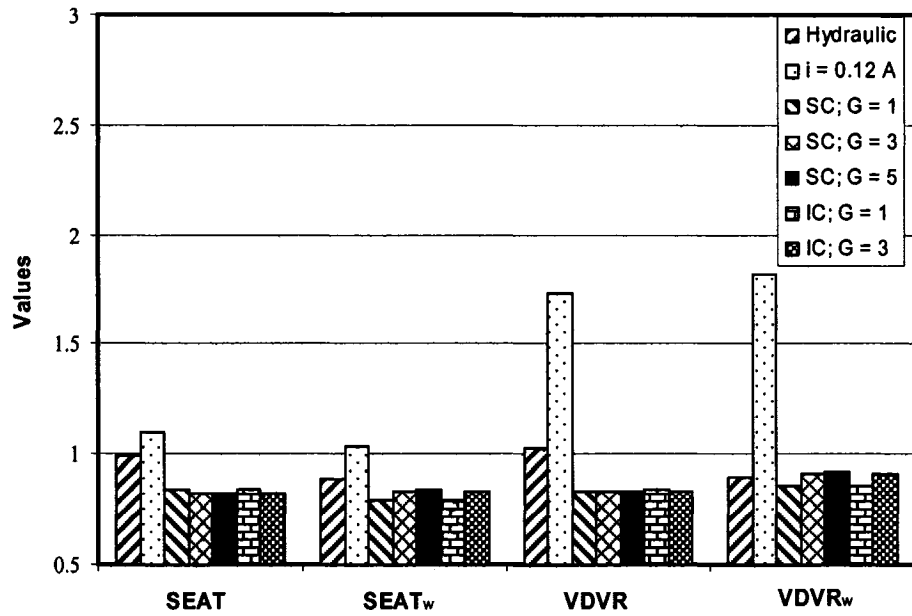


Figure 5.34: Comparisons of the weighted and unweighted SEAT and VDVR measures of different suspension seats subject to 'EM1' excitation.

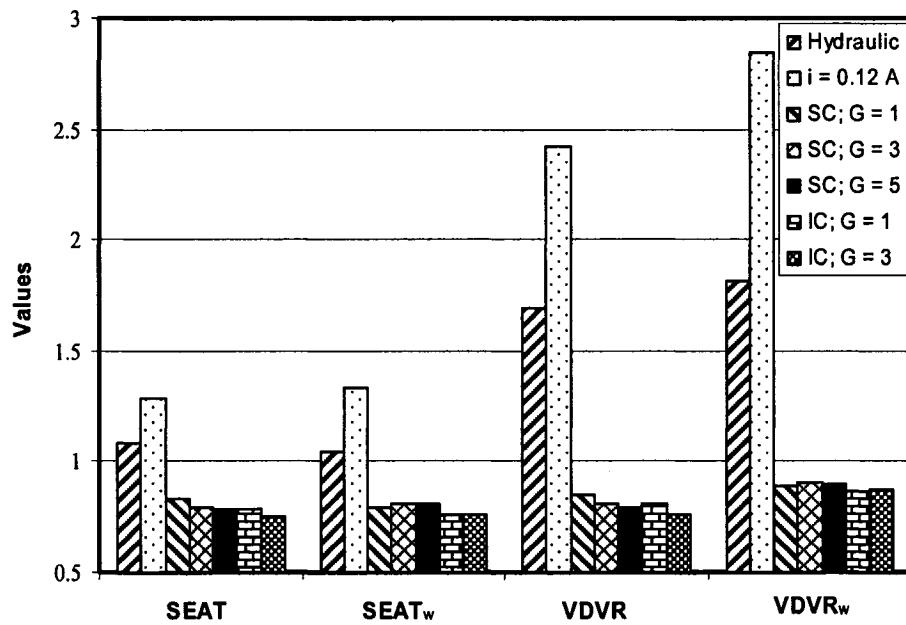


Figure 5.35: Comparisons of the weighted and unweighted SEAT and VDVR measures of different suspension seats subject to 'EM1A' excitation.

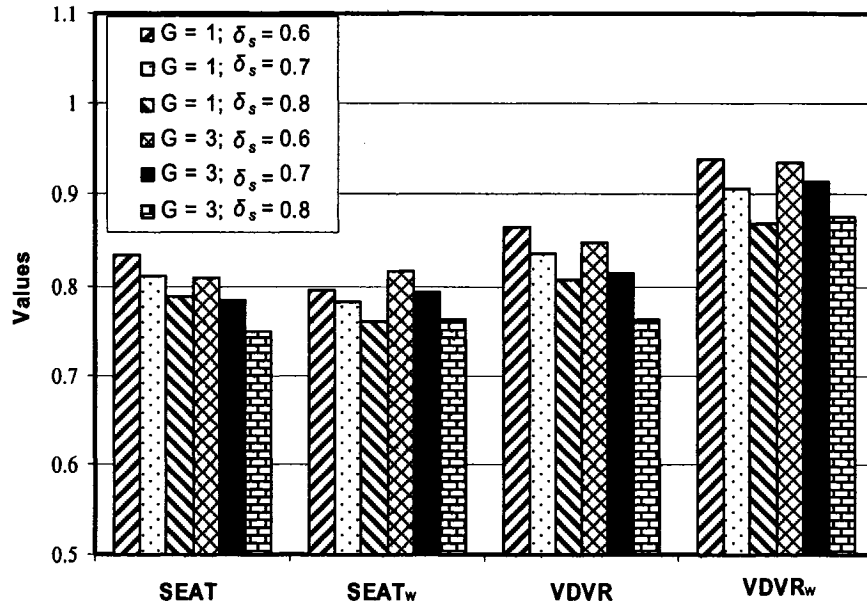


Figure 5.36: Influences of controller gain (G) and position margin (δ_s) on the *SEAT* and *VDVR* responses of the suspension seats with integrated control subject to ‘EM1A’ excitation.

5.8 Summary

The MR-damper model, derived in Chapter 2, is integrated to the validated passive suspension seat model to formulate and investigate the performance potentials of controllable MR damper. The analysis of the model with the constant current MR damper revealed that the response characteristics of the seat with an uncontrolled MR damper are similar to those of the passive suspension seat, under different continuous and transient excitations considered. A ‘hi-lo’ semi-active control algorithm (SC) is formulated on the basis of well-known skyhook control to modulate the control current from ‘zero’ state to the ‘hi’ state, which is proportional to instantaneous relative velocity response of the

suspension. The contributions due to current switch and damper hysteresis to the suspension responses are also presented. Owing to the significant transient oscillations caused by current switching, a continuous modulation (CM) algorithm is proposed to achieve smoother transition from the 'hi' to 'lo' state. The results attained under deterministic and random excitations of continuous and transient nature revealed the effectiveness of the smoothing function in limiting the switching oscillations. Furthermore, the SC damping suspension resulted in superior performances under harmonic, transient and random vehicular excitations. It is concluded that a gain value of 3 would yield adequate compromise between the vibration attenuation and end-stop impact performance of the suspension.

In order to further improve the shock attenuation performance, an integrated control scheme (IC) is synthesized by introducing a relative position control to the semi-active skyhook-based control algorithm. The results show that the integrated control scheme could improve the shock attenuation performance of seat under high intensity excitations by limiting the frequency and severity of end-stop impacts. The proposed IC algorithm does not affect the suspension performance under lower intensity excitations. The proposed controller thus yields improved shock as well as vibration attenuation performance of the suspension seat, which are known to pose conflicting design requirements for passive suspension seats.

CHAPTER 6

HARDWARE-IN-THE-LOOP TEST AND ANALYSES

6.1 Introduction

A mathematical model of the nonlinear MR damper suspension seats has been developed and systematically analyzed in Chapters 2 and 3, upon considerations of the hysteretic properties. Such hysteretic characteristics of the MR damper are strongly dependent on both the excitations and the control currents, which pose significant difficulty and challenges in modeling, analysis and controller design. The effectiveness of the proposed skyhook-based and integrated controllers has been demonstrated for different continuous and transient excitations of varying intensities, in the previous chapters. The simulation results attained show superior potential of the proposed controllers in limiting the shock and vibration transmission of the suspension seat. Further studies on experimental validations and practical implementation of the controller would thus be highly desirable.

The implementation and the performance analyses of the hardware would involve fabrication of a suspension seat with a MR damper, integration of sensors to acquire the suspension mass velocity, as well as relative displacement and relative velocity across the suspension, and assessments under different excitations. Alternatively, Hardware-in-the-loop (HIL) test methodology may be applied to examine the validity of the suspension and controller models, and to further tune the controller hardware for

prototype development. Hardware-in-the-loop (HIL) test and simulation methodologies have been widely used for efficient analysis of various controllers and systems [18, 46, 112, 113]. Such methodologies have been effectively applied for tuning and assessments of vehicle suspensions [18, 46, 114]. A recent study has also applied the HIL technique for assessing the performance potential of a semi-active MR damping suspension seat coupled with a “full-vehicle” model based upon a PID controller synthesis [49]. The study, however, did not explore the shock responses induced by the seat suspension end-stop impacts, which might be more detrimental for driver’s ride comfort and health to some extent. The reported studies have invariably demonstrated superior potential of the HIL methods for tuning of the controller parameters and system design variables, and for assessments under varying operating conditions. Hansselmann [112] has summarized the HIL test techniques together with the hardware requirements and various capabilities of the HIL real-time simulation.

The HIL technique could provide a real time simulation environment, under which the objective component can be conveniently evaluated while interacting with other components within the total system considered. In this study, a hardware-in-the-loop test and simulation platform is developed for synthesis, tuning and evaluations of different control algorithms in a real-time environment. The tests and simulations are performed under different excitations, while the magnitudes of excitation are limited to ensure safety of the damper hardware and the system. The results attained are used to demonstrate the validity of the analytical models of the MR-damper, the integrated seat suspension system

and the controllers.

6.2 Development of the Hardware-in-the-loop Test and Simulation Platform

A HIL test platform was developed in the laboratory for efficient assessments of the MR damper suspension seat and the controller. The platform integrates the damper hardware with the MATLAB/SIMULINK model of the suspension seat and the controller through the dSPACE communication hardware and software in a real-time manner. While the SIMULINK model provides “mode-switching” including both continuous and discrete time representations, the dSPACE offers a modular real-time simulation environment with configurable I/O capability to realize data communications between software and hardware. A power supply is further designed to provide the control current for the MR-damper using the digital command signal generated by the controller within the SIMULINK model. The platform consisted of a primary interface window that permitted the user to select model parameters, control algorithm, controller gain and excitation. This window was developed using the ControlDesk module of the dSPACE. The structure and design of the platform is described in the following subsection.

6.2.1 Description of HIL Test System

Figures 6.1 and 6.2 illustrate the schematic diagrams of the HIL test system developed for design and assessment of a semi-active seat suspension involving a MR damper. The figures show the interface between the hardware and the software. The HIL

platform can be divided into three major components: software, hardware and interface part between the software and the hardware. The software part consists of the control algorithm and the nonlinear analytical model of the suspension seat system, as described in Chapter 4, with the exception of the damper model. The hardware portion comprises the MR damper, a servo-hydraulic vibration test system, a power supply for the damper (DPS), a force sensor for acquiring the damper force signal, and a thermometer for monitoring the damper body temperature.

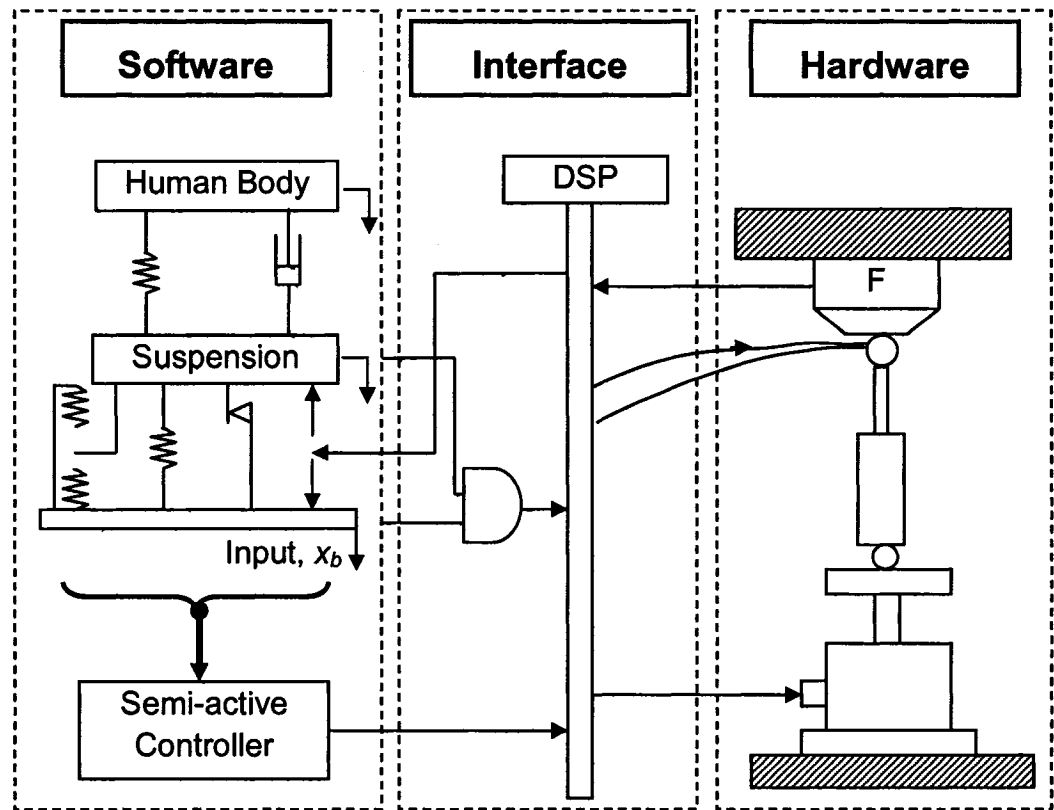


Figure 6.1: Schematic diagram of the HIL test system comprising the MR-damper hardware, the suspension seat model and the interface.

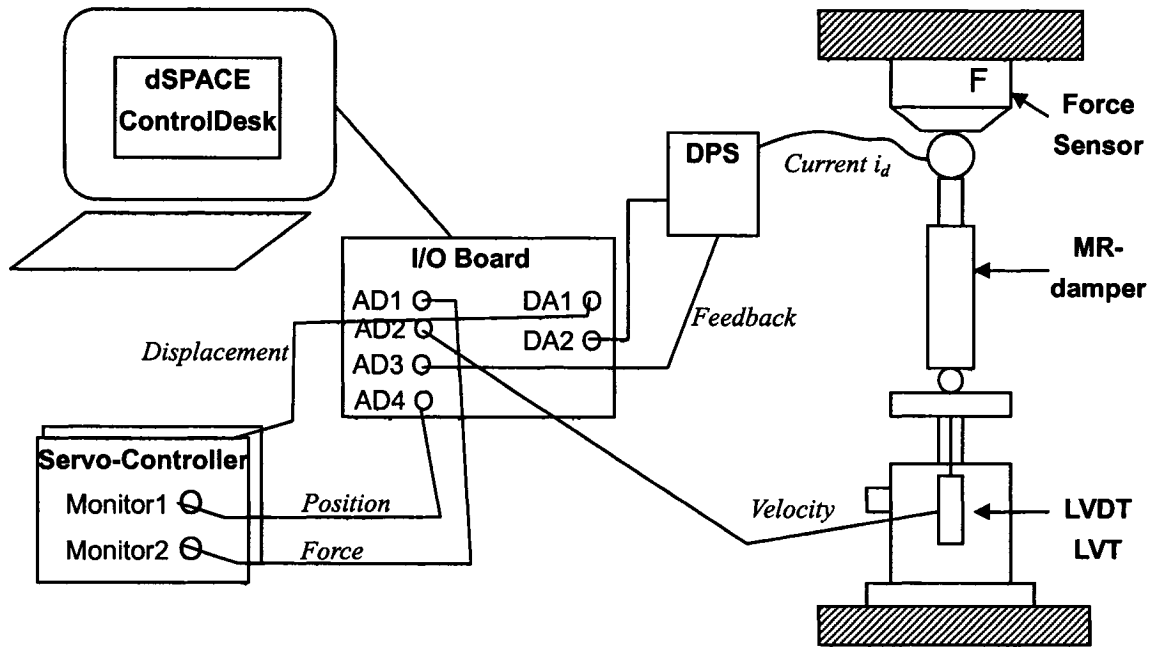


Figure 6.2: Schematic diagram of the interface between the hardware and the software.

The servo-hydraulic test system (MTS) used in the HIL test system was described in Chapter 2 (Figure 2.1), which includes the hydraulic power unit, a servo-hydraulic actuator, the controller and an AD board for acquiring the instantaneous force, velocity and displacement signals. The interface component provides communications between the software and the hardware through DSP processor and I/O boards. Figure 6.3 illustrates a pictorial view of the HIL test system.

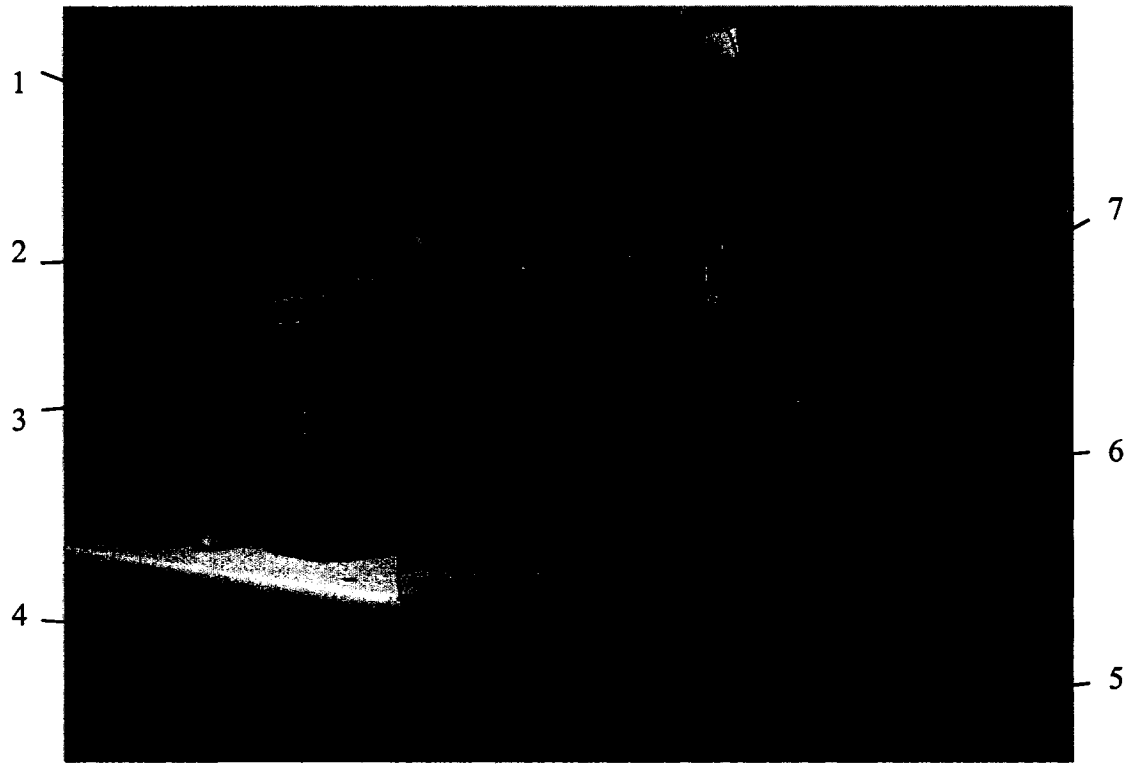


Figure 6.3: A pictorial view of HILS for the proposed suspension seat (1- DPS; 2- I/O board ; 3- Temperature monitor; 4- Hydraulic actuator; 5-LVDT & LVT; 6- MR-damper; 7- Force sensor).

The HIL test and simulation is initiated by selecting an excitation signal $x_b(t)$ from the primary interface window. The real-time simulation of the suspension seat model is then performed within the SIMULINK environment and the resulting suspension relative displacement response $(x_s - x_b)$ is supplied to the servo-controller through the DSP and I/O board. The servo controller generates the necessary command to create actuator and thus the damper motion of $(x_s - x_b)$, while the resulting damping force measured from the force sensor is supplied to the SIMULINK model to close the hardware-in-the-loop. The SIMULINK model also provides the velocity and position signals for the damper

controller. A digital command signal is further generated from the SIMULINK program, which is interfaced with the damper power supply (DPS) through the I/O board. The platform thus allows real-time communications between the suspension seat software and damping force hardware, and controller command current and the DPS. A PID controller is also developed and integrated to ensure stable current supply for the damper. While the HIL platform serves as an efficient real-time test and simulation tool, its applications are limited within a bandwidth of 25 Hz, attributed the dynamics of the servo-valve and the hydraulic actuator [23].

6.2.2 Design of the Digital Damper Power Supply (DPS)

A digital damper power supply is designed and fabricated to provide a direct current for driving the MR-damper coils. The control algorithms, described in Equations (5.3) and (5.9), are defined within the SIMULINK environment in conjunction with suspension seat model. This algorithm yields the command signal for the damper, while maximum current and voltage outputs of the I/O board are limited 25 mA and 10 V, respectively. A digital damper power supply is thus design to amplify and stabilize the control current using the signal from the I/O board and a DC power supply. It needs to be noted that the inductive coils within the damper piston may induce some time delay and steady-state error, which was attenuated through a PID controller. Figure 6.4 illustrates the damper power supply, where a simple $1\ \Omega$ resistance was used to form a feedback loop for the PID controller. This resistance value cannot be too low in order to limit the current level.

The ± 5 mV voltage offset of the A/D converter would also cause a corresponding offset in the current. Maximizing the resistance could therefore minimize the current offset. A thermocouple (Channel #1) was further utilized to monitor the DPS temperature and the experiments were conducted at the temperatures below 60°C .

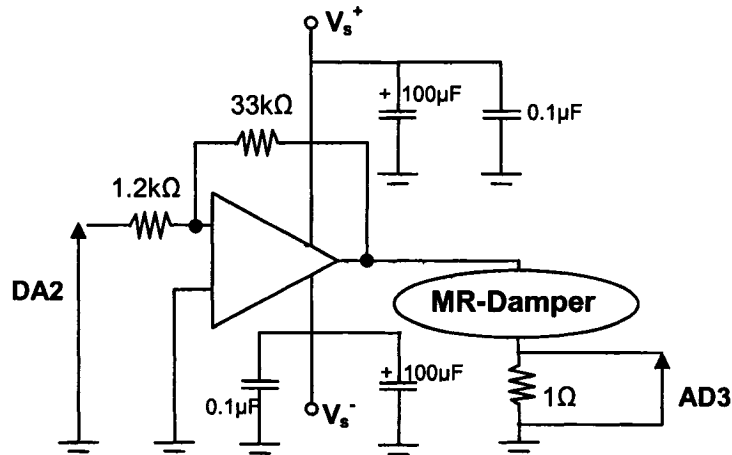


Figure 6.4: The damper power supply circuit (DA2- Command signal from I/O board; AD3- Feedback for the PID controller).

6.2.3 dSPACE Communication and Interface Window Design

The dSPACE communication and the interface window were designed to provide efficient environment for the experimenter in selecting the test and simulation parameters. The HIL test and simulation of configured suspension seat model and the damper controller is launched within the ControlDesk module by loading the compiled files and the software under the ds1104 operating environment.

The interface window was developed to include parameter selection, signal monitoring and data recording, as shown in Figure 6.5. The instrumentation of the

ControlDesk was used to provide a number of virtual instruments for monitoring the different response variables. System parameters, such as the amplitude and frequency of the excitation signals, the controller gain and the constant current values, could be easily configured on the input panel, as seen in Figure 6.5. The input panels, “A” and “B”, were designed with menus on the excitation signals and the controller option, respectively. The excitations could be selected from a variety of signals, such as harmonic, white noise, EM1, Bus and transient signals, as described in Chapter 4. The control algorithm options included zero current (‘lo’ state), constant current, skyhook control and integrated control.

The signal monitoring panels on the left- and right-sides were built for displaying the displacement, velocity and acceleration due to the excitation, suspension mass and the body mass together with the control current. The platform also permitted for monitoring and measurement of component forces, such as spring force, fiction force, damping force, buffer force and the cushion force. The ControlDesk further allowed the experimenter to save the captured data from real-time applications or simulations, using the capture settings window displayed under the panel B of the interface window in Figure 6.5. For the proposed HIL system, the capture settings window was chosen for the data recording. The reference data manager could further be used to generate and save the data, while two file formats were supported: the comma-separated values file format (CSV) and the MATLAB binary file format (MAT file).

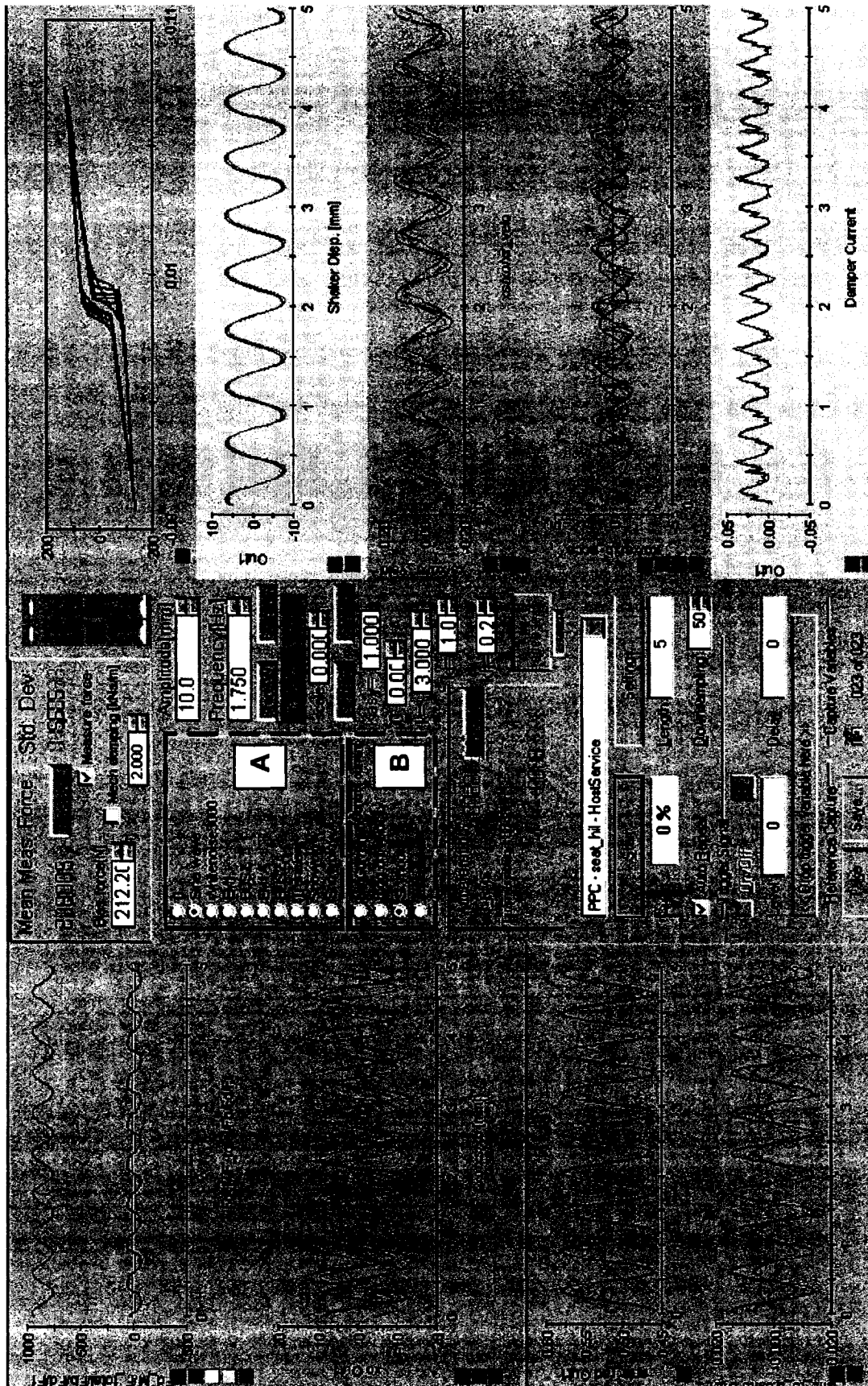


Figure 6.5: The designed layout of the interface window of the HIL test and simulation platform.

6.3 Experiment Methodology

It was established that the damping characteristics of a MR damper are strongly dependent upon the excitation and the control current. The proposed HIL tests and simulations were therefore conducted under a variety of excitations, as described in section 4.3, and the proposed ‘hi-lo’ semi-active controller with different control gains (G). The results were analyzed and compared to those derived from the analyses of the corresponding model, so as to assess the validity of the proposed analytical formulations and the effectiveness of the controller. The results derived for the proposed suspension seat models (software), involving MR damper (hardware) with constant current are also evaluated and discussed in the following sections. Owing to the limited stroke of the candidate MR-damper and its vertical orientation in the test system, the free travel ($d_c + d_e$) of the suspension seat had to be limited to 60 mm instead of 140 mm used in the simulation model to ensure safety of the damper and the test system.

6.3.1 Excitation Signals and Control Methods

The excitation signals to the proposed HIL test system were selected to be identical to those used in the simulation of the analytical models, as described in section 4.3. Constant displacement excitations of 15 and 25 mm amplitude at frequencies of 0.5, 0.75, 1.0, 1.25, 1.5, 1.75 and 2.0 Hz were initially applied to study the low frequency characteristics of the suspension seat with a MR-damper. The high frequency responses were evaluated under constant acceleration harmonic excitations of 2.37 and 3.95 m/s²

amplitude at frequencies of 2.5, 3.0, 4.0, 5.0, 6.0, 8.0, 10.0 Hz.

The responses to transient excitation were evaluated under the transient signal, described in section 4.3, with peak displacement magnitudes of 27.5, 42.5 and 66 mm at a frequency of 1.5 Hz. It should be noted that the magnitude of the transient excitation could be easily tuned within the HIL test platform. The response characteristics of the suspension software and hardware were also evaluated under selected vehicular excitations. For this purpose, the excitations due to the urban bus (Bus) and an earthmoving machine (EM1) were applied together with the amplified excitation (BusA and EM1A).

Four different experiments were designed to study the effects of control current inputs. The first experiment involved zero control current, which permitted for validation of the MR-damper and passive suspension models. The second series of experiments were performed under a constant current ($i = 0.1$ A), which further provided an opportunity to further examine the validity of the models. The last two experiments involved the skyhook based ‘hi-lo’ control with gains of 1 and 3, respectively. The results attained from the latter experiment were used to demonstrate the validity and effectiveness of the proposed semi-active suspension seat. The experiments for the integrated controller were also attempted, which provided poor results due to the travel limit constraint of ± 30 mm imposed on the control together with the position margin of 0.8 (effective travel = 24 mm). This limit caused the damper to operate in the ‘hi’ mode for majority of the time and thus resulted in deteriorated performance. The results

attained from this experiment are thus not presented.

6.4 Responses to Harmonic Excitations

The responses to low frequency constant displacement and high-frequency constant acceleration harmonic excitation were measured under four different current inputs. The results attained in each experiment are compared with those derived from the models, described in Chapter 5.

6.4.1 Constant Current Inputs

Figure 6.6 presents the comparisons of the measured and computed time domain responses of the suspension seat model with the passive MR damper hardware ($i = 0.1$ A), subject to a 25 mm harmonic displacement excitation at the frequency of 1.5 Hz. The comparisons are presented in terms of a few selected measures, namely applied current (i), vertical damping force (f_{dv}), body mass acceleration (\ddot{x}_o) and suspension mass acceleration (\ddot{x}_s). The results suggest reasonably good agreements between the measured and model responses, except for the high frequency oscillation in the measured suspension mass acceleration response. This deviation was attributed to the noise induced by the tracking error in the drive circuit employing the PID control, as described in Figure 6.4. The oscillations in the drive current are clearly evident in Figure 6.6.

The damping force and the suspension velocity data are further analyzed to derive the hysteretic f - v characteristics of the MR-damper. The results are compared with those

derived from the mathematic model of the damper described in Chapter 2 (Figure 6.7). The measured data exhibits trends similar to those observed in the model response, although some deviations are evident. The measured data reveals relatively higher hysteresis in the damping force at higher velocities than that evident from the model results. Such a deviation was also observed in the results presented in Chapter 2 at very low currents.

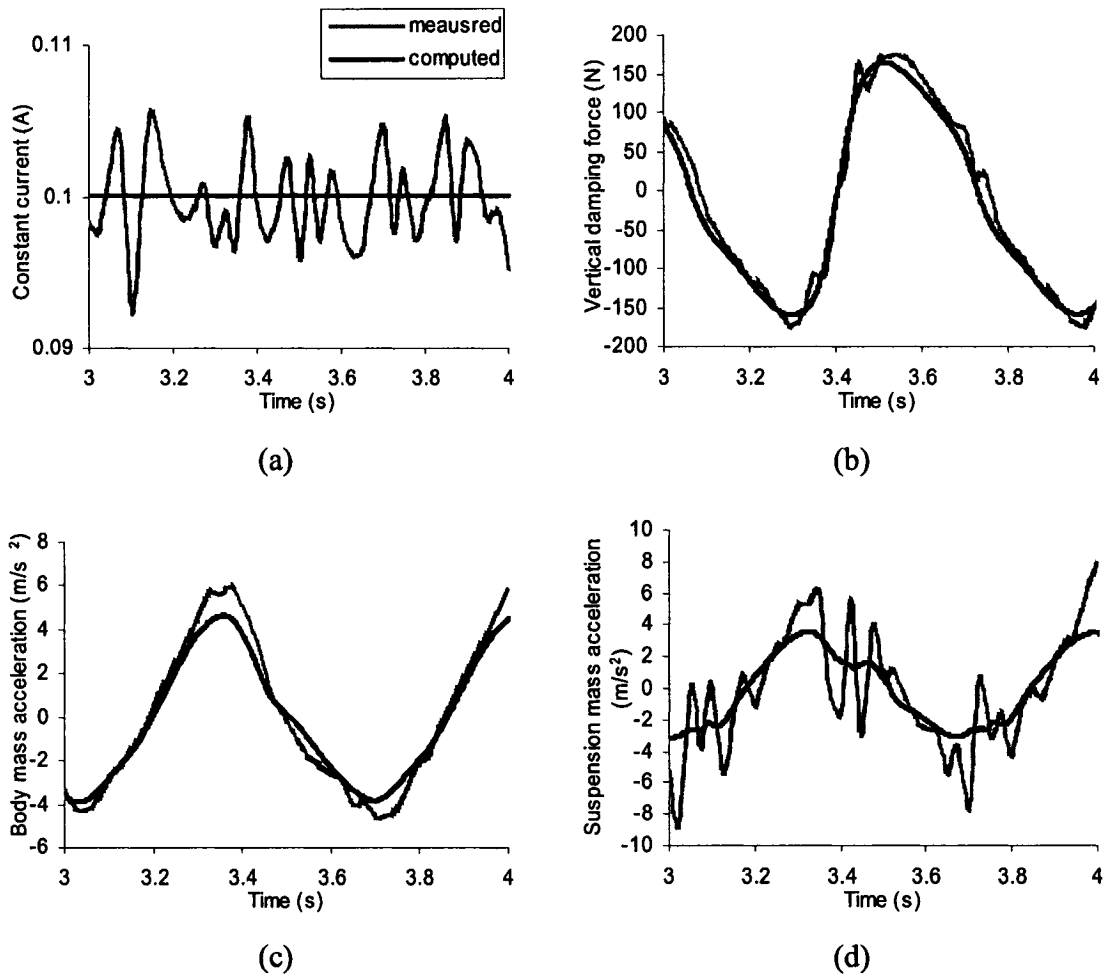


Figure 6.6: Comparisons of model and measured responses of the suspension seat with the MR damper hardware subject to 0.1 A constant current and a harmonic excitation ($f_r = 1.5$ Hz and $A_r = 25$ mm).

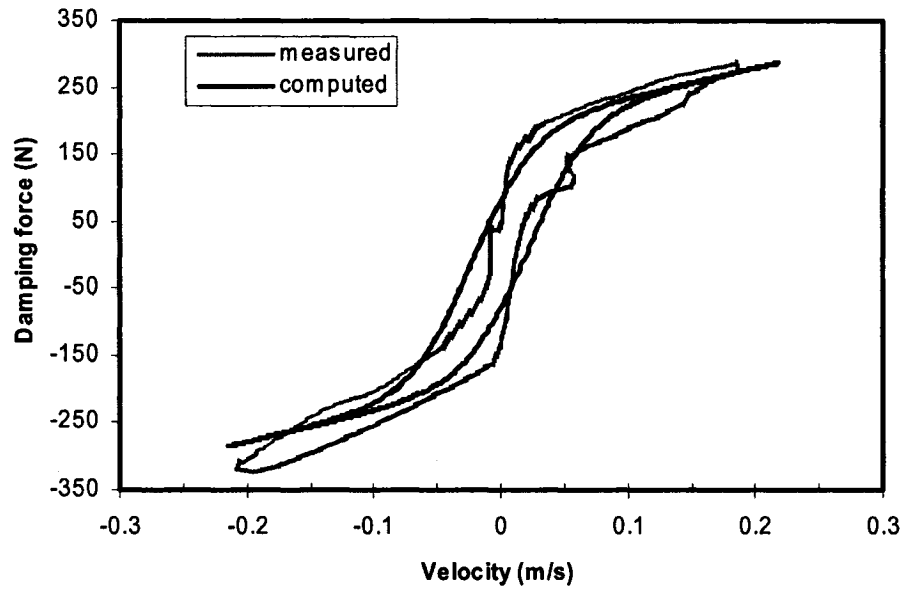


Figure 6.7: Comparison of the computed and measured f - v characteristics of the MR-damper in the damper installing direction under a harmonic excitation ($i=0.1$ A, $f_r=1.5$ Hz, $A_r=25$ mm).

The body mass acceleration responses under the selected excitations at discrete frequencies were analyzed to derive the *rms* acceleration transmissibility ratio. Figure 6.8 shows comparisons of the measured and computed acceleration transmissibility responses of the suspension seat model with the MR dampers subject to 0 and 0.1 A constant current and the harmonic excitations in the 0.5 to 10 Hz frequency range, as described in Section 6.3.1. For the zero-current set up, the peak displacement and acceleration amplitudes in the low and high frequency ranges were limited to 15 mm and 2.37 m/s^2 , respectively, in order to limit the resonant response. For the 0.1 A excitations, these limits relaxed to 3.95 m/s^2 , respectively. The result suggests reasonably good agreements between the measured and model results over the entire frequency range, irrespective of

the applied currents. Some deviations, however, are evident in the 3-6 Hz frequency range. The zero-current damper operation yields excessive resonant transmissibility, which decreases most significantly with the application of only small current (0.1 A). The peak transmissibility reduces to less than 50%, even though the excitation amplitude is considerably higher.

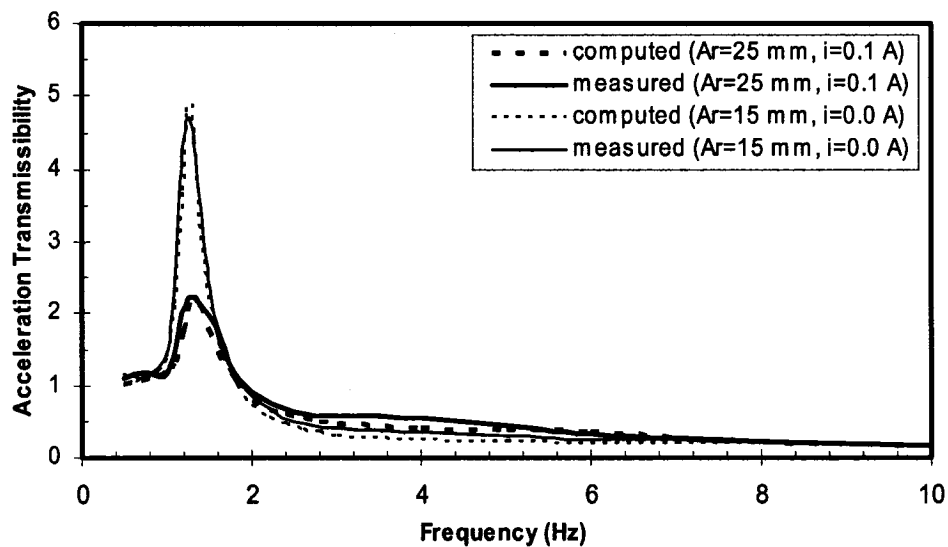


Figure 6.8: Comparisons of the body mass acceleration transmissibility responses derived from the measured data and the model of the MR suspension seat with MR-damper ($i = 0$ and 0.1 A).

6.4.2 Semi-active Damping

The experiments performed with the suspension seat with semi-actively controlled MR damper revealed excessive high frequency noise in the acceleration and damping force responses, irrespective of the controller gain. This was partly attributed to the tracking error caused by the PID controller for the drive circuit and partly to the travel limit constant, as discussed earlier. A reduction in the harmonic excitation magnitude

from 25 mm to 20 mm helped to suppress this noise. The experiments were thus performed under different discrete frequencies in the 0.5-10 Hz range, where the displacement amplitude was held as 20 mm up to 2 Hz, and acceleration amplitude as 3.16 m/s^2 at frequencies above 2 Hz. The results attained under this excitation are analyzed and compared with those derived from the model described in Chapter 5. The measured data acquired under two different controller gains ($G = 1$ and 3) were analyzed to derive the body mass acceleration transmissibility responses. The results are compared with the corresponding model results in Figure 6.9.

The results suggest reasonably good agreements between the computed and measured responses for both controller gains, except for some deviations in the 3-6 Hz frequency range. A comparison with the acceleration transmissibility response of the seat with constant MR damping, shown in Figure 6.8, suggests that the proposed semi-active “skyhook”-based control algorithm could considerably reduce the resonant transmissibility and provide superior vibration attenuation in the isolation frequency range, irrespective of control gains. The results also show that an increase in the gain from 1 to 3 yields lower resonant transmissibility, while the response in the 3 to 6 Hz range remains unaffected. A higher controller gain is thus desirable for limiting the shock as well as vibration transmission to the body mass. The experiments were performed using control gains of 5 and 7. The results did not show noticeable improvement or variation in the response due to saturation of the candidate damper, which was also observed from the model results presented in section 5.5.1.

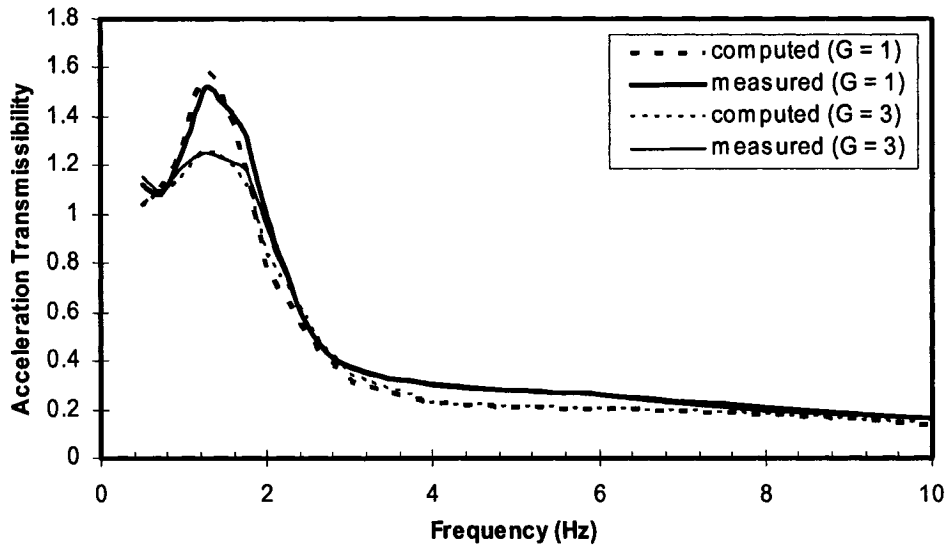


Figure 6.9: Comparisons of measured and computed acceleration transmissibility responses of the suspension seat employing the proposed skyhook-based semi-active damping control with two different control gains.

Figure 6.10 further compares the computed and measured responses of the seat model employing the proposed semi-active skyhook-based MR damping control under 20 mm harmonic displacement excitation at 1.5 Hz. The comparisons are presented in terms of measured and computed control current (i_d), vertical damping force (f_{dv}), body mass acceleration (\ddot{x}_o) and suspension mass acceleration (\ddot{x}_s). The reasonably good agreements between the measured and computed responses can be observed. Considerable deviations, however, are also evident in the suspension mass acceleration response, which shows large magnitude transient peaks, which were attributed to the logic and condition functions used in the continuous modulation algorithm together with the tracking error in the drive circuit. The results show smooth transition in the current

from its 'lo' to 'hi'; and 'hi' to 'lo' states, while a sudden change in current occurs after the 'hi' to 'lo' state transition. This switching causes oscillations in the damping force near zero velocity, as observed in the figure.

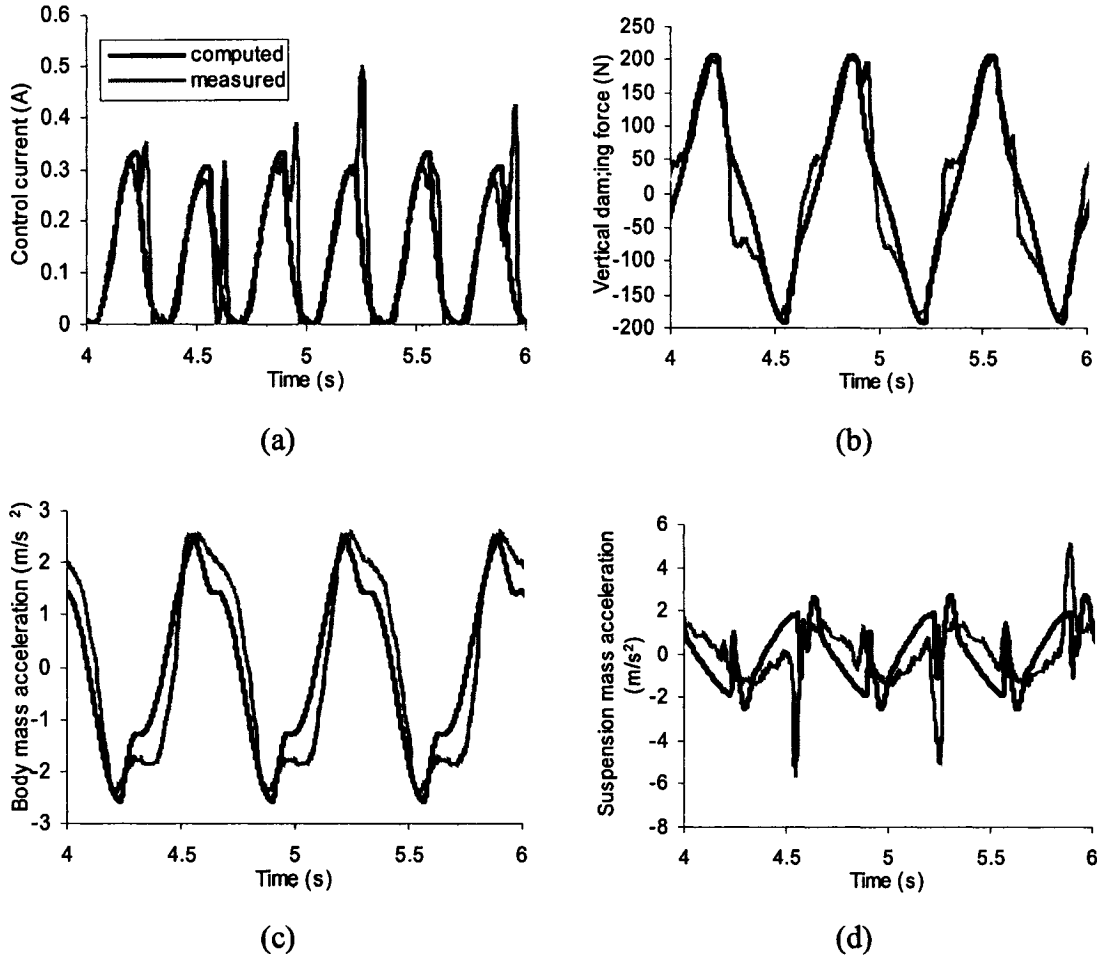


Figure 6.10: Comparisons of the computed and measured responses of the suspension seat model employing the proposed semi-active skyhook-based MR-damping under a harmonic excitation ($f_r=1.5$ Hz, $A_r=20$ mm and $G=3$).

The results presented in Figures 6.6 to 6.10 clearly demonstrate the validity of the MR-damper and suspension seat models with and without the controller under harmonic excitations, although the test methodology utilizes only the damper hardware. The results

further show effectiveness of the proposed controller in limiting the resonant transmissibility and enhancing the vibration isolation performance.

6.5 Responses to Transient Excitations

The experiments under transient excitation were performed under different magnitudes of peak displacements, while the dominant frequency was limited to 1.5 Hz. For constant applied current (0.1 A), the peak magnitude were limited to 27.5 and 42.5 mm, while the experiments under zero-current were discontinued due to severe end-stop impacts. Higher excitation magnitudes (42.5 and 66 mm), however, were applied to assess the performance of the semi-active suspension controller.

6.5.1 Constant Current Inputs

Figures 6.11 and 6.12 illustrate the responses of the suspension seat with a constant current MR damping ($i = 0.1$ A) under 27.5 and 42.5 mm transient excitations, respectively. The results are presented in terms of vertical damping force (f_{dv}), end-stop force (F_b), body mass acceleration (\ddot{x}_o) and body mass displacement (x_o), and compared with those attained from the analytical model. The results show very good agreements between the model and measured data under both excitations. The results show high frequency oscillations in the damping force of considerable magnitude, irrespective of the peak displacement magnitude. This contributed to the damper hysteresis, which tends to introduce high frequency oscillations near zero velocity. The end-stop impacts seem to

occur under 42.5 mm excitation, while the results show some deviations in the peak end-stop forces desired from the HIL test and the model. It should be noted that the end-stop impacts occur at a relatively lower excitation since the suspension travel is limited to only ± 30 mm. Both the measured body mass acceleration and displacement agree very well with the simulation results.

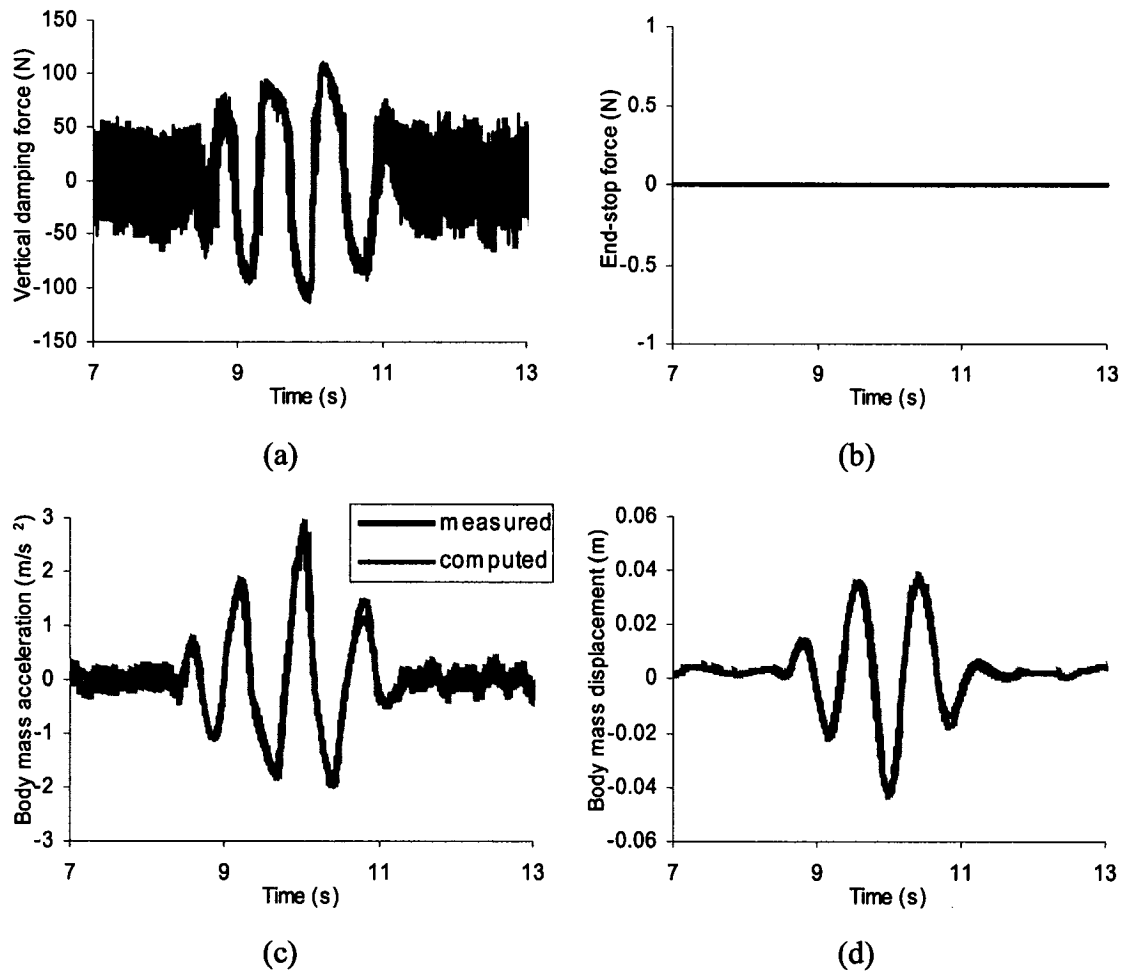


Figure 6.11: Comparisons of model and measured responses of the suspension seat with a constant current MR damping under transient excitations ($i = 0.1$ A; $A_p = 27.5$ mm).

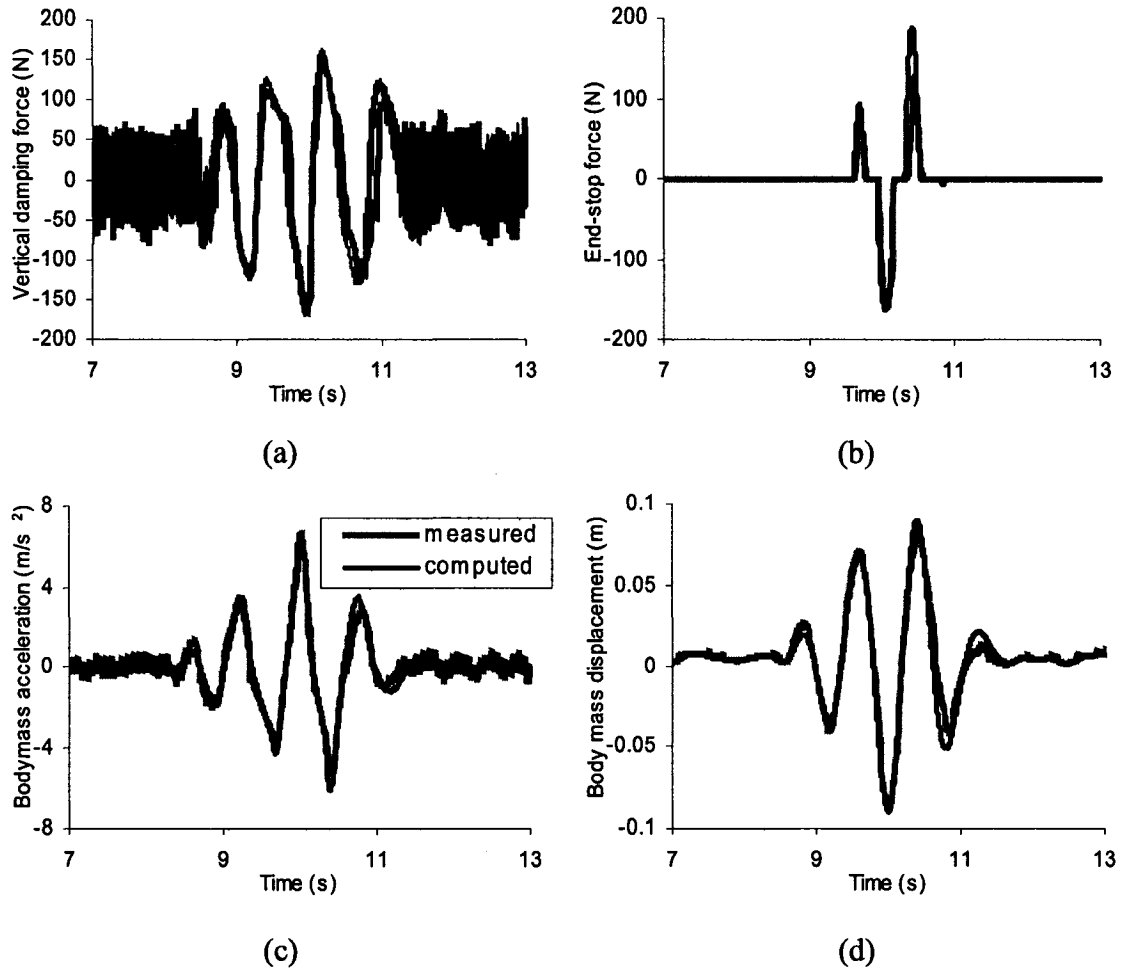


Figure 6.12: Comparisons of model and measured responses of the suspension seat with a constant current MR damping under transient excitations ($i = 0.1$ A; $A_p = 42.5$ mm).

6.5.2 Semi-active Damping

The transient response characteristics of the proposed semi-active “skyhook”-based controller are also measured under excitations of different magnitudes (42.5 and 66 mm) and different control gains ($G = 1$ and 3). Figures 6.13 and 6.14 present the comparisons of computed and measured responses of the suspension seat employing semi-active skyhook-based damping control, subject to 42.5 mm transient excitation and control gains of 1 and 3, respectively. The measured and computed responses of the

controlled suspension model agree reasonably well, while some deviations in the peak acceleration responses are evident. The results show high oscillation in the control current near $t = 8$ s, which induces oscillations in the damping force and the acceleration responses. Such oscillations are most likely caused by the current-drive circuit instability.

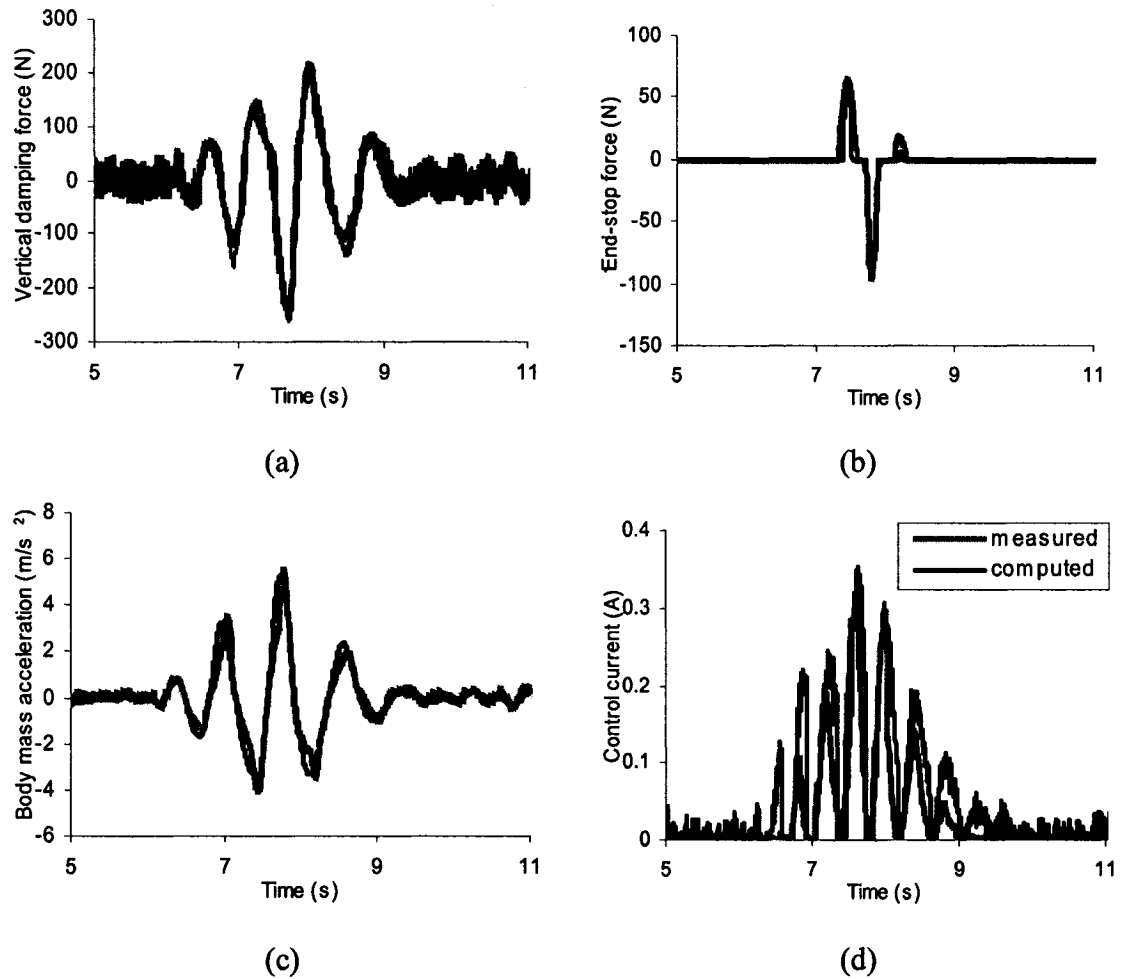


Figure 6.13: Comparisons of computed and measured responses of the suspension seat employing the proposed semi-active damping control under 42.5 mm transient excitation ($G = 1$).

The results further indicate that the proposed semi-active skyhook-based controller with a unity control gain ($G = 1$) yields end-stop impacts, while the magnitude of the

end-stop force is significantly smaller than that attained with the constant current damper (Figure 6.12). The results thus suggest that the proposed controller could yield improved shock isolation performance. The occurrence of the end-stop impact, however, could be eliminated by increasing the control gain to 3, as seen in Figure 6.14.

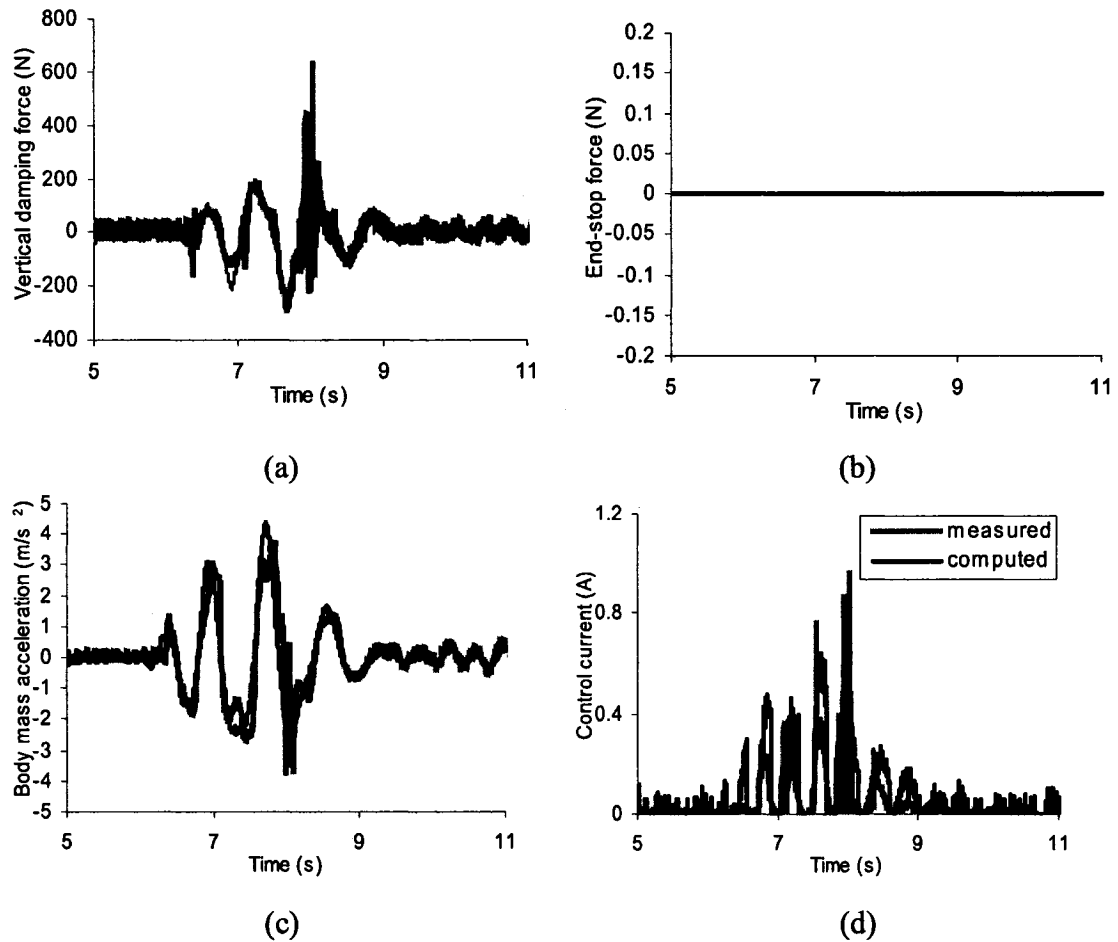


Figure 6.14: Comparisons of computed and measured responses of the suspension seat employing the proposed semi-active damping control under 42.5 mm transient excitation ($G=3$).

Figure 6.15 further illustrates the comparison of measured and model responses, when the peak excitation magnitude is increased to 66 mm. The results again show reasonably good agreements between the measured and computed responses, while the

measured peak end-stop forces are slightly higher than the corresponding computed values. The results do not show the oscillations in the control current that were observed in Figure 6.14 corresponding to 42.5 mm excitation. Such oscillations were thus believed to be caused by misalignment in the damper mounting used in the experiment under 42.5 mm excitation. A comparison of the results with those attained for the constant current damper (Figures 6.11 and 6.12) also shows that the high frequency oscillations in the damping force, attained to the hysteresis, are effectively suppressed by the proposed controller.

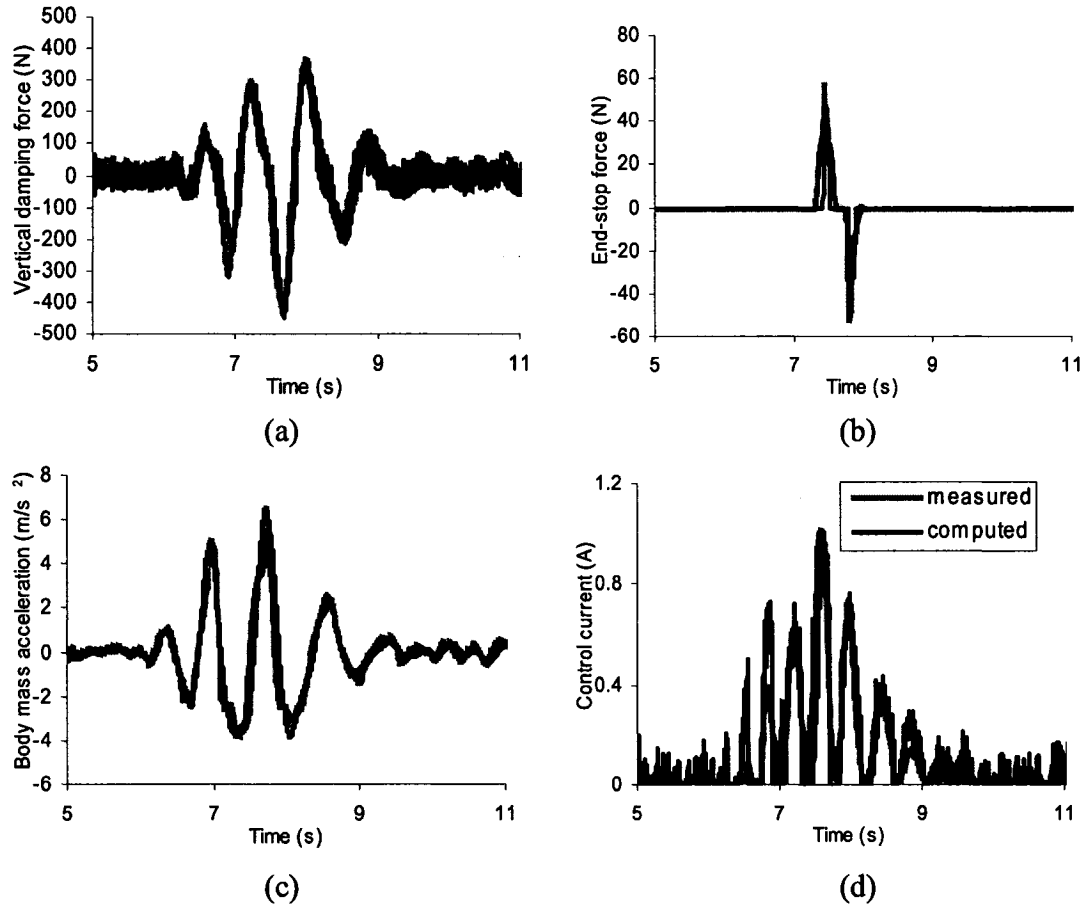


Figure 6.15: Comparisons of computed and measured responses of the suspension seat employing the proposed semi-active damping control under 66 mm transient excitation ($G=3$).

6.6 Responses to Vehicular Excitations

The response characteristics of the suspension software and hardware were also evaluated under selected vehicular excitations. Therefore, the vehicular excitations, such as Bus, EM1, BusA and EM1A were applied to assess the performance of the suspension seat with a fixed current and the semi-active controller.

6.6.1 Constant Current Inputs

The experiments were performed under the selected vehicular vertical vibrations, 'Bus' and 'EM1', together with the corresponding amplified signals, 'BusA' and 'EM1A', respectively, as illustrated in Figure 4.8. Figure 6.16 illustrates comparison of PSD's of the measured and computed body mass acceleration responses of the suspension seat with a constant current MR-damping ($i = 0.1$ A). The figure shows the comparisons under all four excitations (Bus, BusA, EM1 and EM1A). Very good agreements between the measured and computed responses are obtained under all the excitations, although some deviations in 2-6 Hz frequency range can be observed, as was in case of the harmonic excitations. The peak acceleration PSD responses of the mass under BusA and EM1A excitations are nearly 3.8 times larger than those under Bus and EM1 excitations. This is attributed to the effects of the end-stop impacts encountered under relatively high intensity of the BusA and EM1A excitations. The end-stop impacts also occur under EM1 excitation due to limited suspension travel.

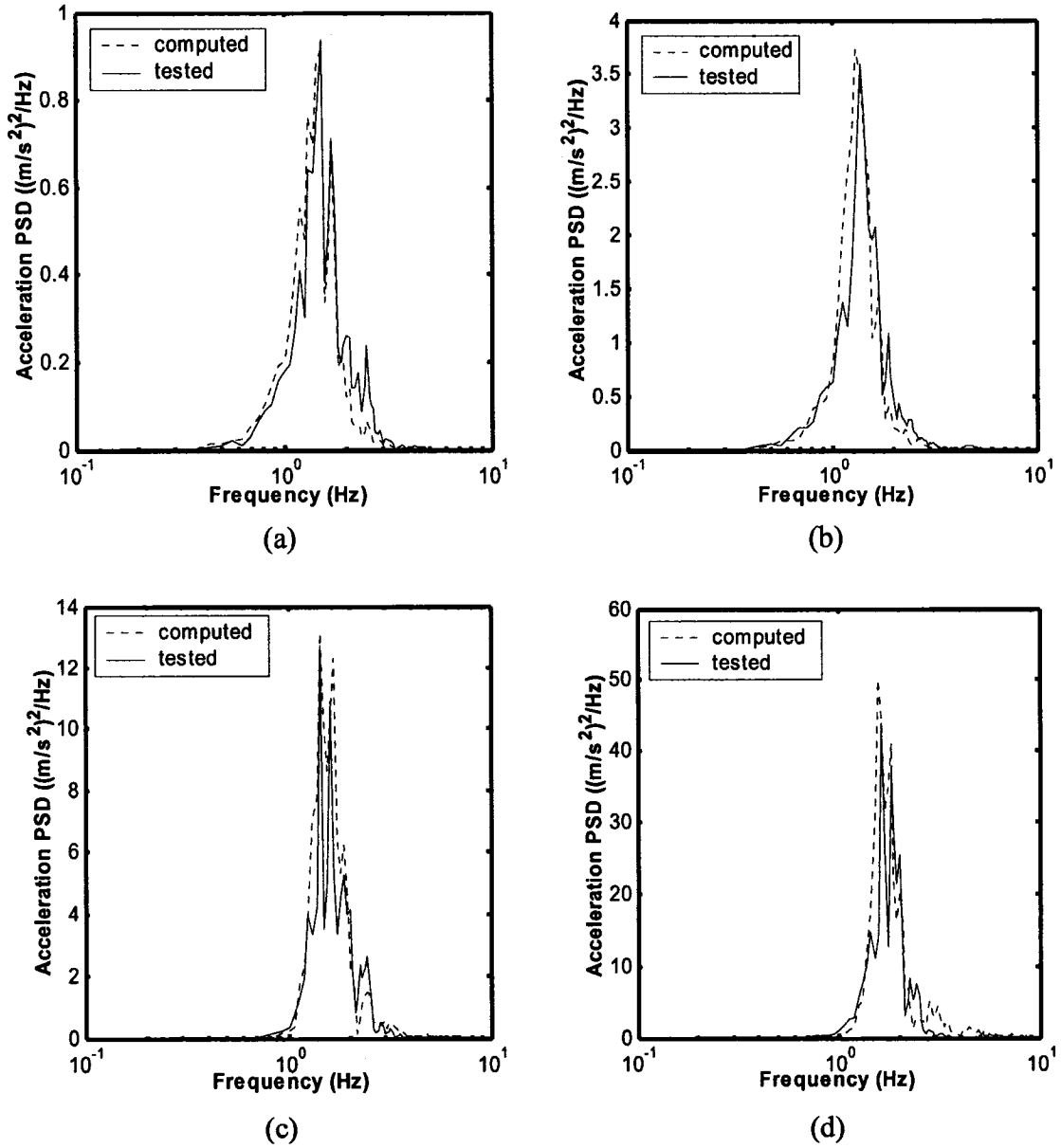


Figure 6.16: Comparisons of PSD of the measured and computed body mass acceleration of the suspension seat with a constant current MR damping ($i = 0.1$ A) subject to vehicular vertical vibration: (a) Bus; (b) BusA; (c) EM1; (d) EM1A.

6.6.2 Semi-active Damping

The assessment and effectiveness of the proposed semi-active skyhook-based control algorithms, described in Equations (5.3) to (5.7), are performed through HIL

measurements under the selected vehicular excitations. Two different values of the control gain ($G = 1$ and $G = 3$) were applied to study the shock and vibration transmission performance of the suspension seat. Figures 6.17 and 6.18 illustrate comparisons of the PSD's of measured and computed body mass acceleration responses of the semi-active suspension for two different control gains ($G = 1$ and $G = 3$) under 'Bus' and 'BusA' excitations, respectively. The results show very good agreements between the measured and computed responses, irrespective of the excitations and the control gains. The results further reveal that increasing the control gain G could decrease the peak body mass acceleration PSD considerably, particularly under the amplified excitation. A comparison of the results with those attained under a constant current (Figure 6.16) suggests the proposed controller helps to limit the occurrence of the end-stop impacts. The results suggest that the vibration and shock isolation performance characteristics of a suspension seat could be considerably enhanced by increasing the control gain. It should be noted that the peak body mass acceleration PSD response of the fixed damping suspension is comparable with that of the semi-active suspension under the 'Bus' excitation. The peak response of the semi-active suspension under the 'BusA' excitation, however, is significantly smaller suggesting elimination of the end-stop impacts. Moreover, the control gain of 3 would be desirable to achieve adequate attenuation of vibration and elimination of the end-stop impacts.

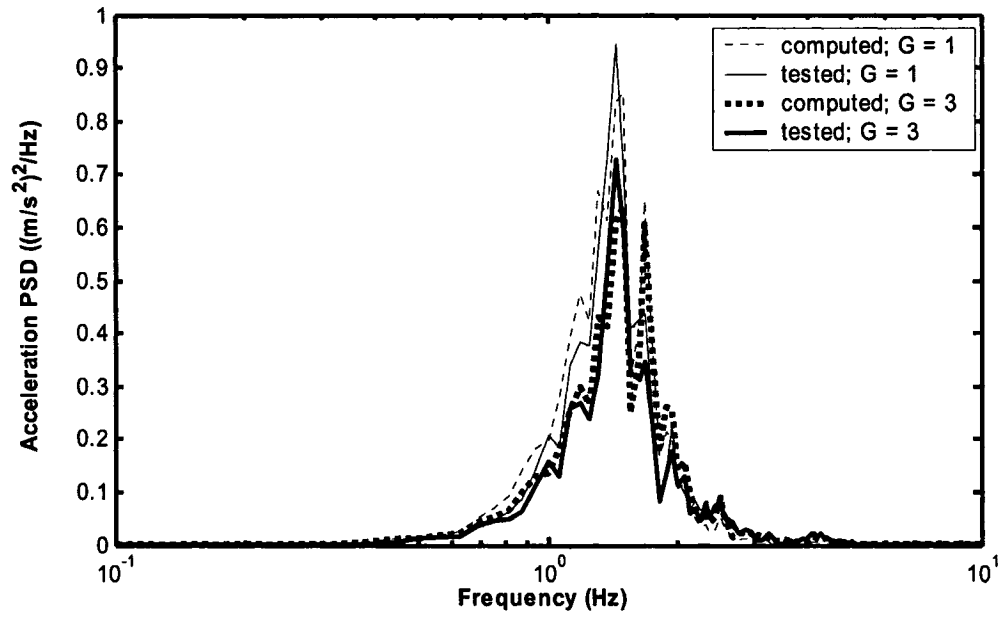


Figure 6.17: Comparisons of PSD of the measured and computed body acceleration of the suspension seat employing semi-active damping control with different control gains (excitation: Bus).

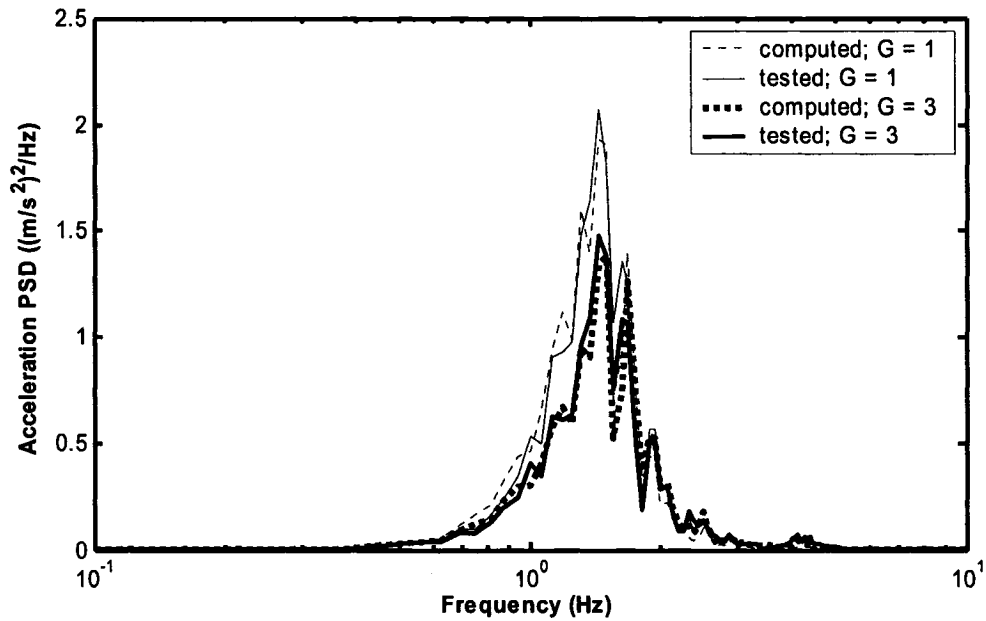


Figure 6.18: Comparisons of PSD of the measured and computed body acceleration of the suspension seat employing semi-active damping control with different control gains (excitation: BusA).

Figures 6.19 and 6.20 illustrate comparisons of the PSD of the measured and

computed body mass acceleration of responses of the semi-active suspension with two different control gains and subject to “EM1” and “EM1A” excitations, respectively. The results not only show reasonably good agreements between the measured and computed acceleration PSD responses, but also confirm that a gain value of 3 is desirable. The results also show the absence of end-stop impacts under the EM1 excitation, which were observed for the constant current suspension. A comparison of the results with the attained under constant current reveals that the peak acceleration PSD values decrease from nearly 13 to $3.2 \text{ (m/s}^2\text{)}^2/\text{Hz}$ under the EM1A excitation, when the semi-active control with gain of 3 is employed. The end-stop impacts, however, continue to occur under EM1A excitation, which is mostly caused by limited suspension travel ($\pm 30 \text{ mm}$).

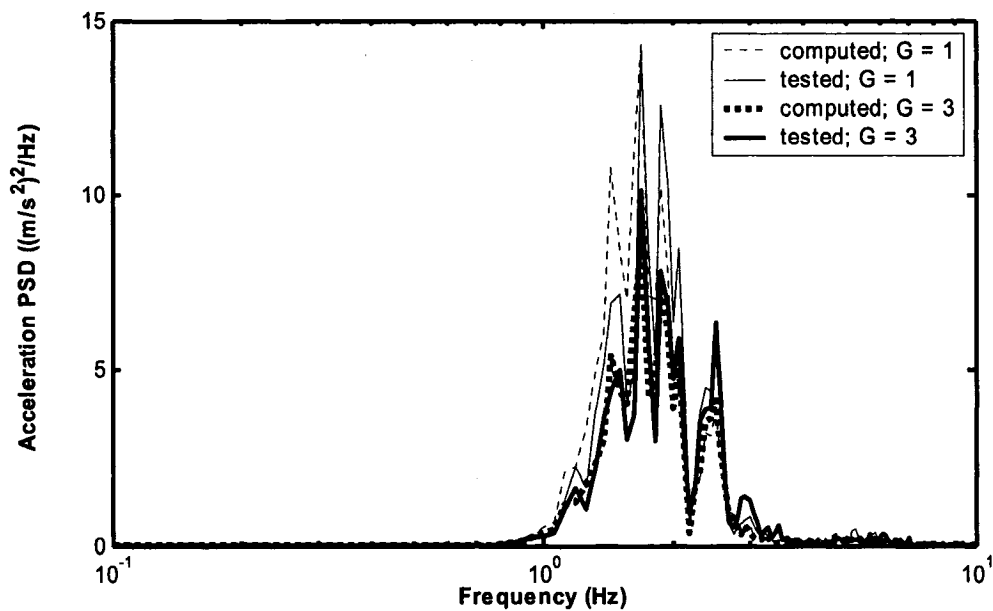


Figure 6.19: Comparisons of PSD of the measured and computed body acceleration of the suspension seat employing semi-active damping control with different control gains (excitation: EM1).

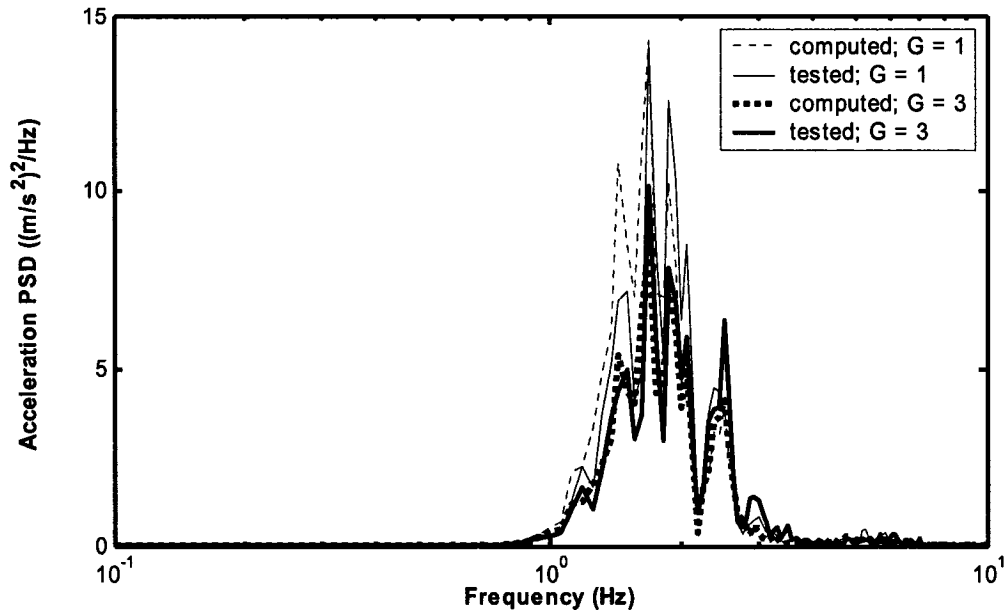


Figure 6.20: Comparisons of PSD of the measured and computed body acceleration of the suspension seat employing semi-active damping control with different control gains (excitation: EM1A).

6.7 Summary

A hardware-in-the-loop (HIL) test platform was developed in the laboratory to evaluate the performance characteristics of the proposed controller and examine the validity of the analytical models of the MR-damper and the suspension system with the control algorithms. Experiments were conducted to achieve the measured responses of the suspension seat with a constant current MR-damper and the proposed semi-active skyhook-based damping control. The measured data were acquired under harmonic, transient and random vehicular excitations of different magnitudes. The measured responses were compared with those obtained from the model simulation to examine the validity and effectiveness of the proposed analytical models and the controller. The

results generally revealed good agreements between the computed and measured results, while high frequency oscillations were observed in the control current, particularly under transient excitation, which were attributed to the tracking error of the PID controlled employed for the drive current circuit. The results clearly revealed validity of the analytical models, although the experiments involved only damper and drive-current hardware. The results also confirmed the findings from the simulation results, namely the role of the controller gain and the effectiveness of the semi-active control in enhancing both the shock and vibration isolation performance.

CHAPTER 7

CONCLUSIONS AND RECOMMENDATIONS FOR FUTURE WORK

Occupational drivers are frequently exposed to severe vibration and shocks caused by the vehicle interactions with the road irregularities. The severity of such shock and vibration transmitted to the seated driver tends to be considerably more in off-road and heavy road vehicles. The design of an effective suspension at the seat involves complex compromises in attenuating the vibration and shock transmitted to the seated human body. A number of low natural frequency suspension seats have been widely adopted in the off-road and heavy road vehicles. Such seats yield effective attenuation of vehicular vertical vibration but cause transmission of excessive shock motions under high intensity or transient excitations due to impacts against the end stops. The MR-fluid dampers offer excellent potential to achieve variable damping with a wide bandwidth, which could help achieve better compromise between the shock and vibration isolation performances under continuous and transient vibration of varying intensities. The design and synthesis of a MR-suspension seat, however, requires formulation of an effective controller with appropriate considerations of the current-dependent hysteresis and saturation nonlinearities of the MR-damper.

7.1 Highlights and Major Contributions of the Study

The highlights and major contributions of this investigation on the MR-fluid dampers

and the semi-actively controlled suspension seat could be summarized under five different topics that also describe the scope of the work: (a) characterization and modeling the hysteretic properties of a MR-fluid damper; (b) development and relative assessments of a generalized current-dependent function for describing the hysteresis properties of a MR-fluid damper; (c) modeling and analyses of a passive suspension seat with hydraulic damper and identification of performance limits; (d) controller synthesis and performance evaluations of a semi-active suspension seat under a wide-range of excitations; and (e) hardware-in-the-loop tests and simulations of the semi-active MR-damper suspensions. The major contributions of the thesis research are summarized below:

- Laboratory experiments are performed to characterize the f - v properties of a MR damper over a wide range of motion and current excitations. The measured force-displacement, force-velocity and seal friction properties of a MR damper attained under a wide range of excitation conditions, are thoroughly analyzed to derive essential and generally applicable features that could facilitate the model synthesis.
- A generalized model synthesis is proposed to characterize the hysteretic force-velocity characteristics of a controllable MR damper under a wide range of sinusoidal excitation conditions and magnitudes of control current. A sigmoid model synthesis is realized by integrating the components describing the excitation and current dependent hysteretic linear rise in the pre-yield condition, force limiting in the post-yield condition, zero-force velocity intercept, zero-velocity force intercept and yield force corresponding to onset of saturation. Simulations are performed to assess the effectiveness of the proposed model synthesis and results obtained under wide range of simulation conditions are compared with those obtained from the measured data. The results show reasonably good agreements between the simulation results and the measured data, irrespective of the excitation conditions and control current.
- The vast majority of the models formulated to characterize the hysteretic

force-velocity properties of MR-dampers do not incorporate the nonlinear dependencies upon the applied current, and the nature of excitation and response. A generalized model formulation comprising the hysteretic and current functions is proposed and applied to a number of reported models to account for variations in both the applied current and the excitation. From the comparisons of the results obtained from resulting modified models with the measured data, it is concluded that the quality of the models can be significantly enhanced using the proposed current function.

- The reported nonlinear hysteretic biviscous, extended Bouc-Wen and polynomial function models are further analyzed, and the results are compared with the measured data to demonstrate their respective limitations and merits. The relative effectiveness of the modified models based on the reported models is further evaluated in terms of time history of the damping force error under selected harmonic excitations. As a result, the generalized sigmoid hysteretic model yields least error in the f - v hysteresis characteristics under varying currents and excitation conditions, while the modified extended Bouc-Wen model provides reasonably good estimations.
- A nonlinear analytical model of a typical air suspension seat comprising of nonlinear component models is developed to investigate its performance under continuous and transient excitations of varying intensities. A polynomial based cushion model is formulated to describe the force-displacement properties as a function of the preload and deflection, and integrated to the suspension model. The resulting model is validated using the laboratory-measured data, and analyzed under a wide range of excitations including high magnitude excitations that cause impacts against the end-stops.
- The parameters of the MR-damper and cushion models are identified through minimization of an error sum function based upon the measured data under several excitation conditions.
- The role of the suspension design parameters on the shock and vibration performance characteristics of suspension seats are investigated on the basis of the validated nonlinear model under different types of excitations. The effects of variations in damping parameters on the seat performance are evaluated in terms of seat effective amplitude transmissibility ($SEAT_w$) and the VDV ratio ($VDVR_w$) under continuous and high magnitude random vibration that predominate at low and higher frequencies. The performance limits of the passively damped suspension are identified on the basis of the shock and vibration attenuation measures.

- A MR-damper suspension seat model is formulated and analyzed under constant current applications. It is shown that the open-loop MR-damper seat can provide performance comparable to that of a passive suspension seat.
- A ‘hi-lo’ semi-active control algorithm (SC) is formulated on the basis of well-known skyhook control. Unlike the skyhook control algorithm, the modulation from the ‘hi’ to ‘lo’ states or vice versa is based on the current control. Moreover, the ‘off’ state is replaced by the ‘lo’ state corresponding to zero current, while the ‘hi’ state is synthesized to yield damping force proportional to the instantaneous relative velocity response. The contributions due to the current switching and damper hysteresis to the suspension responses are also presented.
- Owing to the significant transient oscillations caused by current switching, a continuous modulation (CM) algorithm is proposed to achieve smoother transition from the ‘hi’ to the ‘lo’ state. The results attained under deterministic and random excitations of continuous and transient nature revealed the effectiveness of the smoothing function in limiting the switching oscillations.
- In order to further improve the shock attenuation performance, an integrated control scheme (IC) is synthesized by introducing a relative position control to the semi-active skyhook-based control algorithm. The results show that the integrated control scheme could improve the shock attenuation performance of seat under high intensity excitations by limiting the frequency and severity of end-stop impacts, while retaining superior vibration isolation under lower magnitude and higher frequency excitations.
- In order to set up a hardware-in-the-loop test platform, a digital damper power supply (DPS) is designed to amplify and stabilize the command signal based on the I/O Board and a DC power supply. A PID controller was designed and integrated within the current drive circuit to compensate for the time delays and steady-state error caused by the inductive coils within the damper piston.
- The hardware-in-the-loop (HIL) test platform is developed in the laboratory to evaluate the performance characteristics of the proposed controller and examine the validity of the MR-damper model and the control scheme. Experiments are performed to measure the responses of the seat model with constant current MR-damper, and employing the proposed semi-active “skyhook”-based controller. The measured data, acquired under harmonic, transient and vehicular excitations, are compared with the corresponding model results to demonstrate the model and controller validity.

7.2 Major Conclusions

On the basis of the studies conducted in this dissertation, the following major conclusions are drawn:

- The laboratory-measured properties of a MR-damper revealed highly nonlinear force-velocity characteristics, which included: (a) symmetric bi-nonlinear behavior with significant hysteresis at lower velocities (pre-yield), followed by linearly increasing force at higher velocities (post-yield); (b) force-limiting behaviour under higher velocities; (c) passive property as evident from the nearly elliptical force-displacement and nonlinear force-velocity curves with relatively small hysteresis under a zero control current; (d) the damping force nonlinearly increasing with magnitude of control current; (e) the damping force strongly dependent on the intensity of the applied magnetic field, and magnitudes of excitation and response.
- The generalized model of the MR-damper, derived on the basis of symmetric and asymmetric sigmoid functions, could accurately characterize the force-velocity properties over a wide range of current and excitation conditions. The results showed reasonably good agreements with the measured data, irrespective of the excitation conditions and the control current. It is thus concluded that the proposed model can effectively describe the nonlinear steady state hysteretic dynamic properties of the controllable MR damper and can be effectively used to design semi-active or model-based controllers.
- The strong current dependence of the MR-fluid damper behaviour could be characterized by an independent function in current. It is concluded that the prediction abilities of various hysteresis models could be significantly enhanced upon integration of the proposed current function.
- It is further concluded that the use of velocity-dependent slope functions could further enhance the prediction ability of the piecewise linear biviscous model.
- The non-convergent behavior of the polynomial function model can be eliminated by introducing a describing function corresponding to $\ddot{x} = 0$. The modified extended Bouc-Wen and the generalized sigmoid hysteretic models can ideally characterize the hysteretic and current-dependent force-velocity properties of the MR-damper.
- The preload and deformation-dependent force-deflection properties of a polyurethane foam seat cushion can be adequately described by a polynomial

function in normal static load and instantaneous deflection. This model also allows for consideration of the pan bending under high intensity excitations.

- A passive suspension seat can be adequately modeled as a two-DOF dynamic system, provided that the component properties are accurately described. Moreover, the human operator can be represented by a rigid mass when the suspension natural frequency and excitations lie in the low frequency range.
- The results suggest that a higher suspension damping is desirable for improved attenuation of high intensity vibration and intermittent shock motions, particularly for vehicles with predominantly low frequency vibration. For applications in vehicles with relatively higher frequency vibration, such as industrial and tracked vehicles, this design approach would also be acceptable as it would limit the frequency and severity of end-stop impacts, while the performance under lower levels of continuous vibration would deteriorate only slightly. A light damping, however, is desirable for realizing enhanced isolation of continuous vibration of low to medium intensity.
- Replacing the 'off' state of the skyhook control by the 'lo' ($i = 0$) state of the damper helps to reduce the undesirable contributions due to switching. The 'hi' current state permits for deriving damping force proportional to the relative velocity response.
- The transient oscillations in the control current and thus the damping force can be effectively suppressed by integrating the proposed continuous modulation function that permits smooth transition from 'hi' to the 'lo' state.
- A relative position control integrated to the 'hi-lo' control can enhance the suspension performance significantly by limiting the frequency and severity of end-stop impacts under high intensity vibration.
- The proposed semi-active "skyhook" based damping control yields a better compromise between the shock and vibration isolation responses, thereby reduced frequency and severity of repeated end-stop impacts. This yields lower seat effective amplitude transmissibility (*SEAT*) and the ratio of vibration dose value (*VDVR*) under random excitations of varying intensity.
- The 'hi-lo' semi-active control algorithm (SC) resulted in superior performances under harmonic, transient and random vehicular excitations. It is concluded that a gain value of 3 would yield adequate compromise between the vibration attenuation and end-stop impact performance of the suspension. A higher gain value is not beneficial due to saturation of the damping force.

- An alternate MR-damper with larger damping force bandwidth is desirable for eliminating end-stop impacts.
- The integrated control scheme (IC) could further improve the shock attenuation performance of seat under high intensity excitations by limiting the frequency and severity of end-stop impacts. The proposed IC algorithm does not affect the suspension performance under lower intensity excitations. The proposed controller thus yields improved shock as well as vibration attenuation performance of the suspension seat.
- The controller synthesis can be conveniently realized and assessed in a hardware-in-the-loop (HIL) test and simulation environment, which offers added flexibility for tuning of the controller.
- The measured data acquired from the HIL experiments in the passive as well as semi-active damping modes showed generally good agreements with the computed responses, except for the oscillations in the control current caused by the drive circuit.

7.3 Recommendations for Further Studies

This dissertation research represents preliminary efforts in realizing effective model of a MR-damper and control syntheses for applications in suspension seats. Owing to the strong potential of the MR-damper and the proposed controller, further efforts are highly recommended to conceive the design of a high performance suspension seat. Following are some of the suggested further studies that should be undertaken:

- The development of a prototype semi-active suspension with integrated controller should be undertaken for laboratory and field assessments of the shock as well as vibration isolation performance benefits.
- Alternate control algorithms that reduce the hardware requirements, particularly the acquisition of the absolute velocity signal, should be explored.
- Owing the superior performance of the semi-active “skyhook” based algorithm, it is vital to explore methods for measurement of the suspension mass velocity.

Signal filter functions may be explored to derive the suspension mass velocity signal from the directly measurable acceleration, although the phase response would need to be examined.

- The stability and robustness of the semi-active “skyhook” based control algorithm and its complementary algorithm (integrated control scheme) should be further verified from the simulation or experimental results.
- An alternate damper design with relatively larger stroke and damping force bandwidth is desirable for realizing improved suspension performance and assessments using HIL test techniques.
- An alternate drive current circuit is highly desirable for ensuring stable control current supply for the damper. It is recommended that alternate control algorithms be explored to accurately track the command current.
- Development of an effective phase compensator is vital to enhance the bandwidth of the servo-control system within the HIL test platform.
- Owing to the availability of only limited space, it is suggested that optimal damper size and inclination be desired to achieve improved suspension performance.

REFERENCES

1. Griffin, M. J. (1990), "Handbook of Human Vibration", Academic Press Limited, London.
2. Boileau, P. -E., Rakheja, S. and Liu, P. J. (1997), "A combined seat suspension-vehicle driver model for estimating the exposure to whole-body vehicular vibration and shock", *International J. of Vehicle Design, Heavy Vehicle Systems*, 4(2-4): 244-265.
3. Corbridge, C. (1987), "Vertical vibration transmission through a seat: effects of vibration input, subjects' postures and subjects' physical characteristics", *The UK informal Group Meeting on Human Response to Vibration*, Royal Military College of Science, Shrivenham, England, 21-22 September.
4. Thakurta, K., Koester, D., Bush N. and Bachle, S. (1995), "Evaluating short and long term seating comfort", *International Congress and Exposition*, Detroit, Michigan, February 27-March 2, SAE Paper No. 950144.
5. Eger, T., Grenier, S. and Salmoni, A. (2004), "Whole-body vibration exposure experienced by mining equipment operators", *Proceedings of Fifth Canadian Rural Health Research Society Conference and the Fourth international Rural Nurses Congress*, Sudbury, ON, Canada.
6. Ahmadian, M. and Marjoram, R. H. (1998), "Effects of passive and semi-active suspensions on body and wheel hop control", *Journal of Commercial Vehicles*, 98: 596-604.
7. Rakheja, S., Ahmed, A. K. W., Yang, X. and Guerette, C. (1999), "Optimal suspension damping for improved driver- and road-friendliness of urban buses", *Proc. of the SAE Int. Truck & Bus Meeting*, Detroit, USA, November.
8. Cebon, D. (1999), "Handbook of Vehicle-Road Interaction", ISBN 9026515545, Copyright © 1999 Swets & Zeitlinger B. V., Lisse, the Netherlands.
9. Boileau, P. -É and Rakheja, S. (2000), "Caractérisation de l'environnement vibratoire dans différentes catégories de véhicules : industriels, utilitaires et de transport urbain", *Institut de recherche en santé et en sécurité du travail (IRSST) Report*, R-242, 162.
10. Tchernychouk, V. (1999), "Objective assessment of static and dynamics seats under

vehicular vibration”, Master’s Thesis, Concordia University, Montreal.

11. Suggs, C. W., Abrams, C. F. and Stikeleather, L. F. (1969), “Application of a damped spring-mass human vibration simulator in vibration testing of vehicle seats”, *Ergonomics*, 12: 79-90.
12. Gunston, T. P., Rebelle, J. and Griffin, M. J. (2004), “A comparison of two methods of simulating seat suspension dynamic performance”, *Journal of Sound and Vibration*, 278(1-2): 117-134.
13. Lewis, C. H. and Griffin, M. J. (2002), “Evaluating the vibration isolation of soft seat cushions using an active anthropodynamic dummy”, *J. of Sound and Vibration*, 253(1): 295-311.
14. Perisse, J. and Jezequel, L. (2000), “An original feedback control with a reversible eletromechanical actuator used as an active isolation system for a seat suspension. Part I: theoretical study”, *Vehicle System Dynamics*, 34: 305-331.
15. Perisse, J. and Jezequel, L. (2000), “An original feedback control with a reversible eletromechanical actuator used as an active isolation system for a seat suspension. Part II: experimental study”, *Vehicle System Dynamics*, 34: 381-399.
16. Thompson, A. G. (1984), “Optimal and suboptimal linear active suspensions for road vehicles”, *Vehicle System Dynamics*, 13: 61-72.
17. Margolis, D. L. (1983), “Procedure for comparing passive, active and semi-active approaches to vibration isolation”, *J. of the Franklin Institute*, 315(4): 225-238.
18. Choi, S. -B., Lee, B. -K., Nam, M. -H. and Cheong, C. -C. (2000), “Control and response characteristics of a magneto-rheological fluid damper for passenger vehicles”, *Smart Materials and Structures 2000, Proceedings of SPIE*, 3985: 438-443.
19. Yokoyama, M., Hedrick, J. K. and Toyama, S. (2001), “A model following sliding mode controller for semi-active suspension systems with MR dampers”, *Proc. of the American Control Conference*, 4: 2652-2657.
20. Liao, W. H. and Wang, D. H. (2003), “Semi-active vibration control of train suspension systems via magneto-rheological dampers”, *J. of Intelligent Material Systems and structures*, 14(3):161-172.
21. Guo, D. L., Hu, H. Y. and Yi, J. Q. (2004), “Neural network control for a semi-active vehicle suspension with a magneto-rheological damper”, *J. of vibration and control*, 10(3):461-471.

22. Wen, Y. –K. (1976), “Method for random vibration of hysteresis systems”, *Journal of the Engineering Mechanics Division*, pp. 249-263.
23. Balike, M., Rakheja, S. and Hoa, S. V. (1998), “Study of an energy dissipating under-ride guard using hardware-in-the-loop”, *Proc. of the Symposium on Recent Advances in Vehicle Systems and Technologies, CSME Forum 98*, Toronto, Canada.
24. Allen, G. R. (1979), “A critical look at biodynamic modeling in relation to specifications for human tolerance of vibration and shock”, *AGARD Conference Proceedings*, Paris, France, 6-10 November, No. 253, Paper A25-5, pp. 519.
25. International Organization for Standardization (2001), “Mechanical vibration and shock-range of idealized values to characterize seated-body biodynamic response under vertical vibration”, ISO 5982
26. Renae, B. C., Carnahan, T., Rachel, T. –C., Crump, R. and et al. (1995), “User perspectives on seat design”, *International Truck and Bus Meeting and Exposition*, Winston-Salem, North Carolina, 13-15 November, SAE No. 952679.
27. Rebelle, J. (2000), “Development of a numerical model of seat suspension to optimize the end-stop buffers”, *Proc. of the 35th UK Group Meeting on Human Responses to Vibration*, Southampton, England, September, pp. 221-238.
28. Rakheja, S. (1983), “Computer-aided dynamic analysis and optimal design of suspension systems for off-road tractors”, Ph. D, Thesis, Concordia University, Montreal, Canada.
29. Pare, C. A (1998), “Experimental evaluation of semi-active magneto-rheological suspensions for passenger vehicles”, M. Sc. Thesis, Virginia Polytechnic Institute and State University, Blacksburg, Virginia.
30. Wu, X. (1998), “Study of drive-seat interactions and enhancement of vehicular ride vibration environment”, Ph. D thesis, Concordia University, Montreal, Canada.
31. Boileau, P. –E. (1995), “A study of secondary suspension and human driver response to whole-body vehicular vibration and shock”, Ph. D., Thesis, Concordia University, Montreal, Canada.
32. Rakheja, S., Afework, Y. and Sankar, S. (1994), “An analytical and experimental investigation of the driver-seat-suspension system”, *Vehicle System Dynamics*, 23: 501-524.
33. Gunston, T. (2000), “An investigation of suspension seat damping using a theoretical model”, *Proc. of the 35th UK Group Meeting on Human Responses to*

Vibration, Southampton, England, September, pp. 207-219.

34. Ebe, K. (1993), "Effect of composition of polyurethane foam on the vibration transmissibility of automotive seat", *The UK informal Group Meeting on Human Response to Vibration*, Ministry of Defense, Farnborough, Hampshire, England, 20-22 September.
35. Wu, X. and Griffin, M. J. (1998), "The influence of end-stop buffer characteristic on the severity of suspension seat end-stop impacts", *Journal of Sound and Vibration*, 215(4): 989-996.
36. Wu, X. and Griffin, M. J. (1997), "A semi-active control policy to reduce the occurrence and severity of end-stop impacts in a suspension seat with an electrorheological fluid damper", *Journal of Sound and Vibration*, 203: 781-793.
37. Ng, D., Cassar, T. and Gross, C. M. (1995), "Evaluation of an intelligent seat system", *Applied Ergonomics*, 26(2): 109-116.
38. Hilyard, N. C., Collier, P. and Care, C. M. (1983), "Dynamic mechanical behavior of flexible foam cushion materials and its influence on ride comfort", *The UK informal Group Meeting on Human Response to Vibration*, the National Institute of Agricultural Engineering, Silsoe, Bedfordshire, England, 14-16 September.
39. Ebe, K. and Griffin, M. J. (1994), "Effect of polyurethane foam on dynamic sitting comfort", *Inter. Noise 94*, Pacifico Yokohama, Japan, 29-31 August.
40. Ebe, K. (1997), "Effect of thickness on static and dynamic characteristics of polyurethane foams", *The UK informal Group Meeting on Human Response to Vibration*, ISVR, University of Southampton, Southampton, England, 17-19 September.
41. Smith, S. D. (1994), "The effect of military aircraft seat cushion on human vibration response", *The UK informal Group Meeting on Human Response to Vibration*, The Institute of Naval Medicine, Alverstoke, Gosport, Hants, England, 19-21 September.
42. Crosby, M. and Karnopp, D. C. (1973), "The active damper-a new concept for shock and vibration control", *Shock Vibration. Bull.*, Part H, Washington D. C.
43. Hrovat, D., Margolis, D. L. and Hubbard, M. (1988), "An approach toward the optimal semiactive suspension", *Journal of Dynamics Systems, Measurement and Control*, 110(3): 288-296.
44. Young, K. M. A. and Morishita, S. (1999), "On the design and development of a

magneto-rheological mount”, *Vehicle System Dynamics*, 32(2-3): 199-216.

45. Margolis, D. L. (1982), “The response of active and semi-active suspensions to realistic feedback signals”, *Vehicle System Dynamics*, 11(5-6): 267-282.
46. Hwang, S., Heo, S., Kim, H. and Lee, K. (1997), “Vehicle dynamic analysis and evaluation of continuously controlled semiactive suspension using hardware-in-the-loop simulation”, *Vehicle System Dynamics*, 27(5-6): 423-434.
47. Mclellan, N. (1998), “On the development of a real-time embedded digital controller for heavy truck semiactive suspensions”, M. Sc. Thesis, Virginia Poly. Inst. and Stte. University, Blacksburg, VA, USA.
48. Bellizzi, S. and Bouc, R. (1995), “Adaptive sub-optimal parametric control for nonlinear stochastic systems: application to seamiactive isolators”, *Probabilistic Methods in Applied Physics*, pp. 223-238.
49. Choi, S. –B., Lee, B. –K., Nam, M. –H. and Cheong, C. –C. (2000), “Vibration control of a MR seat damper for commercial vehicles”, *Smart Structures and Materials 2000, Proceedings of SPIE*, 3985: 491-496.
50. Bouazara, M., Richarc, M. J. and Rakheja, S. (2006), “Safety and comfort analysis of a 3-D vehicle model with optimal non-linear active seat suspension”, *Journal of Terramechanics*, 43: 97-118.
51. Grimm, E. A., Huff, G. J. and Wilson, J. N. (1974), “An active seat suspension for off-road vehicles”, *Symposium on Computers, Electronics and Control*, 3: 265.
52. Stein, G. J. and Ballo, I. (1991), “Active vibration control system for the driver’s seat for off-road vehicles”, *Vehicle System Dynamics*, 20: 57-78.
53. Wu, J. D. and Chen, R. J. (2004), “Application of an active controller for reducing small-amplitude vertical vibration in a vehicle seat”, *Journal of Sound and Vibration*, 274: 939-951.
54. Guclu, R. (2003), “Active control of seat vibrations of a vehicle model using various suspension alternatives”, *Turkish J. Eng. Env. Sci.*, 27: 361-373.
55. McManus, S. J., St. Clair, K. A., Boileau, P.-E. and Rakheja, S. (2002), “Evaluation of the vibration and shock attenuation performance of a semi-active magnetorheological fluid damper”, *J. of Sound & Vibration*, 253(1): 313-327.
56. Choi, Y. T. and Wereley, N. M. (2003), “Mitigation of biodynamic response to vibratory and blast-induced shock loads using magnetorheological seat

suspensions”, 2003 ASME International Mechanical Engineering Congress, November, Washington, D.C., USA.

57. Rabinow, J. (1948), “The magnetic fluid clutch”, *AIEE Transaction*, 67: 1308-1315.
58. Carlson, J. D. (1994), “The promise of controllable fluids”, *Proc. of Actuator 94*, AXON Technologic Consult GmbH, pp. 266-270.
59. Carlson, J. D. and Weiss, K. D. (1994), “A growing attraction to magnetic fluids”, *Machine Design*, August, pp. 61-64.
60. Carlson, J. D., Catanzarite, D. M. and St. Clair, K. A. (1995), “Commercial magneto-rheological fluid devices”, *Proc. 5th Int. Conf. on ER Fluids, MR Fluids and Associated Tech.* U. Sheffield, UK.
61. Thomas Lord Research Center, Lord Corporation (1999), “Designing with MR fluids”, Engineering Note.
62. Chrzan, M. J. and Carlson, J. D. (2001), “MR fluid sponge devices and their use in vibration control of washing machines”, *International Society of Optical Engineering (SPIE)*, 4331: 370- 378.
63. Carlson, J. D. (2000), “Implementation of semi-active control using magneto-rheological fluids”, *Mechatronic System, Proceedings Volume from IFAC Conference*, Germany, pp. 973-978.
64. Dyke, S. J., Spencer Jr, B. F., Sain, M. K. and Carlson, J. D. (1998), “An experimental study of MR dampers for seismic protection”, *Smart Materials and Structures*, 7: 693-703.
65. Carlson, J. D., Catanzarite, D. M. and St Clair, K. A. (1995), “Commercial magneto-rheological fluid devices”, *5th Int. Conf. ER, MR Suspensions Assoc. Technol.*, Sheffield, England.
66. Bouc, R. (1966), “Solution periodique de l’equation de la ferro-resonance avec hysteresis”, *Comptes Rendus Acad. Hebd. Seances*, A263, pp. 497-499.
67. Bouc, R. (1967), “Forced vibration of mechanical system with hysteresis”, *Proceedings of 4th Conference on Nonlinear Oscillation*, Prague, Czechoslovakia.
68. Shames, I. H. and Cozzarelli, F. A. (1997), “Elastic and Inelastic Stress Analysis”, Taylor & Francis Inc. ISBN 1560326867.
69. Wang, E. R., Ma, X. Q., Rakheja S. and Su, C. -Y. (2002), “A general model of a

magneto-rheological controllable damper”, *9th conference of sound and vibration*, Orlando, USA.

70. Phillips, R. W. (1969), “Engineering applications of fluids with a variable yield stress”, Ph. D. thesis, Mech. Eng., U. Berkeley, California, USA.
71. Prager, W. (1961), “Introduction to Mechanics of Continua”, Ginn and Company, New York, ISBN 0486438090.
72. Stanway, R., Sproston, J. D. and EI-Wahed, A. K. (1996), “Application of electrorheological fluids in vibration control: a survey”, *Smart Materials and Structures*, 5(4): 464-482.
73. Spencer, B. F., Dyke, D. J., Sain, K. M. and Carlson, J. D. (1997), “Phenomenological model of a magneto-rheological damper”, *J. of Eng. Mech.*, ASCE, 123 (3): 230-238.
74. Li, W. H., Yao, G. Z., Chen, G., Yeo, S. H. and Yap, F. F. (2000), “Testing and steady state modeling of a linear MR damper under sinusoidal loading”, *Smart Materials and Structures*, 9: 95-102.
75. Kamath, G. M. and Wereley, N. (1997), “Nonlinear viscoelastic-plastic mechanism-based model of an electrorheological damper”, *J. of Guidance, Control and Dynamics*, 20(6): 1125-1132.
76. Pang, L., Kamath, G. M. and Wereley, N. M. (1998), “Dynamic characterization and analysis of magnetorheological damper behavior”, *SPIE Conf. on Passive Damping and Isolation*, 1-5 March, San Diego CA, 3327: 284-302.
77. Choi, S. B. and Lee, S. K. A. (2001), “hysteresis model for the field-dependent damping force of a magnetor-rheological damper”, *Journal of Sound and Vibration*, 245(2): 375-383.
78. Ma, X. Q., Wang, E. R., Rakheja, S. and Su, C. Y. (2002), “Modeling hysteretic characteristics of MR-fluid damper and model validation”, *41st IEEE Conf. on Decision and Control*, Dec. 10-13, Lasvegas, Nevada, USA, pp. 1675-1680.
79. Leva, A. and Piroddi, L. (2002), “NARX-based technique for the modeling of magneto-rheological damping devices”, *Smart Materials and structures*, 11: 79-88.
80. Tao, G. and Kokotovic, P. V. (1995), “Adaptive control of plants with unknown hysteresis”, *IEEE Transactions on Automatic Control*, 40(2): 200-212.
81. Su, C. -Y., Stepanenko, Y., Svoboda, J. and Leung, T. P. (2000), “Robust adaptive

- control of a class of nonlinear systems with unknown backlash-like hysteresis”, *IEEE Transactions on Automatic Control*, 45(12): 2427-2431.
82. Khalil, H. (2002), “Nonlinear System”, Prentice Hall, Inc., Upper Saddle River, NJ 07458.
 83. Hrovat, D. (1997), “Survey of advanced suspension developments and related optimal control applications”, *Automatics*, 33(10): 1781-1817.
 84. “MATLAB”, The Language of Technical Computing, Version 6.5.1., 199709 Release 13, @ 1984-2003, The MathWorks, Inc.
 85. Ballo, I. (1995), “Power requirement of active vibration control systems”, *Vehicle System Dynamics*, 24(9): 683-694.
 86. Karnopp, D. C., Crosby, M. J. and Harwood, R. A. (1974), “Vibration controlling semi-active generators”, *J. of Eng. For Industries*, 96(2): 619-626.
 87. Redfield, R. C. (1991), “Performance of low-bandwidth, semi-active damping concepts for suspension control”, *Vehicle Dynamic System*, 20: 245-267.
 88. Dyke, S. J., Spencer Jr., B. F., Sain, M. D. and Carlson, J. D. (1996), “Seismic response reduction using magnetorheological dampers”, *Proceedings of IFAC13th Triennial World Congress*, San Francisco, USA, pp. 145-150.
 89. Getpreecharsawas, J. and Lyshevski, S. E. (2002), “Modeling and analysis of flexible beams with surface-mounted PZT actuators”, *Proceedings of the 41st IEEE Conference on Decision and Control*, Las Vegas, Nevada, USA.
 90. Gong, J. Q., Guo, L., Lee, H. S. and Yao, B. (2002), “Modeling and cancellation of pivot nonlinearity in hard disk drive”, *Proceedings of the American Control Conference*, Anchorage, AK, USA.
 91. Tan, K. K., Lee, T. H. and Zhou H. X. (2001) “Micro-positioning of linear piezoelectric motors based on a learning nonlinear PID controller”, *IEEE/ASME Transaction. Mechatron*, 6:428-436.
 92. Tan, X. B. and Baras, J. S. (2002), “Modeling and control of a magnetostrictive actuator”, *Proceedings of the 41st IEEE Conference on Decision and Control*, Las Vegas, Nevada, USA.
 93. Smith, R. C., Salapaka, M. V., Hatch, A., Smith, J. and De, T. (2002), “Model development and inverse compensator design for high speed nonpositioning”, *Proceedings of the 41st IEEE Conference on Decision and Control*, Las Vegas,

Nevada, USA, pp. 3652-3657.

94. International Organization for Standardization (1997), "Evaluation of human exposure to whole-body vibration-part I: General requirements", ISO 2631/1.
95. International Organization for Standardization (2000), "Earth-moving Machinery – Laboratory Evaluation of Operator Seat Vibration", ISO7096.
96. Fairley, T. E. and Griffin, M. J. (1989), "The apparent mass of the seated human body: vertical vibration", *Journal of Biomechanics*, (22): 81-94.
97. Politis, H., Rakheja, S., Juras, D., Boileau, P. E. and Boutin, J. (2003), "Limits of application of human body dynamics in assessing vibration comfort of seats", *SAE 2003 World Congress & Exhibition, Session: Human Factors in Seating Comfort*, Detroit, MI, USA, SAE paper No. 2003-01-0953.
98. Wu, X., Rakheja, S. and Boileau, P. E. (1999), "Dynamic performance of suspension seats under vehicular vibration and shock excitations", *Transactions of SAE, Passenger Car Journal*, 108(6): 2398-2410.
99. Milliken, W. F. and Milliken, D. L. (1995), "Race Car Vehicle Dynamics", Society of Automotive Engineers, PA, USA, ISBN 1560915269.
100. Rakheja, S., Boileau, P. –E., Wang, Z. and Politis, H. (2003), "Performance Analysis of Suspension Seats Under High Magnitude Vibration Excitations: Part 1: Model Development and Validation", *Journal of Low Frequency Noise, Vibration and Active Control*, 22(4): 225-252.
101. Coermann, R. R. (1962), "The mechanical impedance of the human body in sitting and standing position at low frequencies", *Human Factors*, pp. 227-253.
102. Wereley, N. M., Pang, L. and Kamath, G. M. (1998), "Idealized hysteresis modeling of electro-rheological and magneto-rheological dampers", *Journal of Intelligent Material Systems and Structures*, 9: 642-649.
103. Carlson, J. D. and Sproston, J. L. (2000), "Controllable Fluids in 2000- Status of ER and MR Fluid Technology", *7th International Conference on New Actuator*, 19-21 June, Bermen, Germany, pp. 126-130.
104. Nakano, M., Yamamoto, H. and Jolly, M. R. (1999), "Dynamic viscoelasticity of a magneto-rheological fluid in oscillatory slit flow", *International Journal of Modern Physics*, 13: 2068-2076.
105. Warner, B. (1996), "An analytical and experimental investigation of high

- performance suspension dampers". Ph.D. Dissertation, Concordia University, Canada.
106. Wang, E. R., Ma, X. Q., Rakheja, S. and Su, C. -Y. (2002), "Modeling hysteretic characteristics of a MR-fluid damper," *Proc. of the Inst. of Mech. Engrs., Part D : J. of Automobile Engineering*, 217: 537-550.
 107. Dixon, J. C. (1999), "The Shock Absorber Handbook", SAE International Publisher, ISBN 0768000505.
 108. Wu, X., Rakheja, S. and Boileau, P. -E. (1998), "Study of human-seat interface pressure distribution under vertical vibration", *International Journal of Industrial Ergonomics*, 21: 433-449.
 109. Gunston, T. P. (2002), "Two methods of simulating a suspension seat cushion", *Proc. of the 37th UK Conf. on Human Responses to Vibration*, Loughborough University, 18-20 September.
 110. Patten, W. N. and Pang, J. (1998), "Validation of a nonlinear automotive seat cushion vibration model", *Vehicle systems Dynamics*, 30: 55-68.
 111. Rakheja, S., Boileau, P. -E. and Wang, Z. (2004), "Performance Analysis of Suspension Seats Under High Magnitude Vibration Excitations: Part II: Design Parameter Study", *Journal of Low Frequency Noise, Vibration and Active Control*, 23(1): 7-26.
 112. Hanselmann, H. (1993), "Hardware-in-the-loop simulation as a standard approach for development, cost optimization and production test", *SAE paper* No. 930207.
 113. Krohm, H. (1995), "Hardware-in-the-loop simulation for an electronic clutch management system, *SEA paper*, No. 950420.
 114. Besinger, F. H., Cebon, D. and Cole, D. J. (1995), "Damper models for heavy vehicle ride dynamics", *Vehicle System Dynamics*, 24(1): 35.